Development of Techniques to Quantify Chemical and Mechanical Modifications of Polymer Surfaces: Application to Chemical Mechanical Polishing

A Thesis
Presented to
The Academic Faculty

by

Jie Diao

In Partial Fulfillment
of the Requirements for the Degree of
Doctor of Philosophy in Chemical Engineering

School of Chemical and Biomolecular Engineering
Georgia Institute of Technology
December 2004

Development of Techniques to Quantify Chemical and Mechanical Modifications of Polymer Surfaces: Application to Chemical Mechanical Polishing

Approved by:

Dr. Dennis W. Hess, Advisor
School of Chemical and Biomolecular Engineering

Dr. Jeffrey F. Morris, Co-advisor
Levich Institute, City College of New York

Dr. Robert J. Samuels
School of Chemical and Biomolecular Engineering

Dr. Steven Danyluk
School of Mechanical Engineering

Dr. Clifford L. Henderson
School of Chemical and Biomolecular Engineering

Dr. Lawrence A. Bottomley
School of Chemistry & Biochemistry

Date Approved: November 2004

For my loving wife: Lan

ACKNOWLEDGEMENTS

First and foremost I would like to thank my research advisor, Dr. Dennis Hess for his guidance and insights throughout my stay at Georgia Tech. His extensive knowledge, work ethic and enthusiasm served as a constant source of inspiration. I would also like to thank my co-advisor, Dr. Jeff Morris for his support and useful advice. I am especially grateful for his continued accessibility to me despite our geographical separation over the last two years.

I am also indebted to the rest of my thesis committee (Dr. Lawrence Bottomley, Dr. Steven Danyluk, Dr. Clifford Henderson and Dr. Robert Samuels) for their involvement in my research and critical reading of my work. Dr. Bottomley gave me lots of useful suggestions on AFM probing of rubbed surfaces and thin film preparations. Dr. Danyluk offered valuable comments on my CMP experiments and kindly granted me access to polisher and profilometer in his laboratory. Dr. Henderson helped a lot in optical characterization of thin films and gave me the privilege to run CMP study on a latest QCM model. Dr. Samuels has not only been kind to share with me his expertise knowledge in polymer characterization and structure-property relationship, but also been consistently supportive for experimental work using the prism coupler in his laboratory. In addition I want to thank Dr. Charles Eckert for his encouragement, Dr. Sankar Nair for letting me access the infrared spectroscopy in his laboratory, Dr. Agaram Abhiraman (now the director of research at Hindustan Lever Research Centre) for useful discussions at the early stage of my thesis work, Dr. Robert Opila at University of Delaware for

critical reviewing of my angle resolved XPS results, Dr. Timothy Anderson at University of Florida for providing MOCVD samples and helping in SIMS depth profiling, Dr. David Allara at Pennsylvania State University for supplying computer codes for infrared spectrum simulation.

I am lucky to be in a great research group. I would like to thank all the past and present members of Hess group. The list includes: Dr. Galit Levitin, Ms. Karen Gao, Dr. Yiming Li, Dr. Matt Spuller, Dr. Ebony Mays, Mr. Satya Myneni, Mr. Chris Timmons, Mr. Sudeep Vaswani, Mr. Qian Luo, Mr. Ashwini Sinha, Mr. Prabhakar Tamirisa, Ms. Gelareh Shakourian and Mr. Ingu Song. I want to express my gratitude to all the graduate students and post doc fellows that have provided invaluable help, for both experimental work and discussion, in my thesis work. They are Ms. Hollie Reed, Dr. Ravi Tanikella, Mr. Lingbo Zhu, Mr. Zhenting Dai, Mr. Guoan Wang, Ms. Zhi Li, Dr. Tao Liu, Dr. Chunhong Zhou, Mr. Gary Ng, Mr. Inho Yoon, Mr. Andres Osorno, Dr. Sean Barstow, Dr. Kendra McCoy, Mr. Josh Stapleton (Pennsylvania State University), Mr. Omar Bchir (University of Florida), and Dr. Weontae Oh.

The thesis work was funded by Center for Surface Engineering and Tribology at Georgia Institute of Technology in the initial stages. Later financial support was provided through the Applied Materials Graduate Student Fellowship awarded by Applied Materials, Inc. (Santa Clara, CA). Dr. Tom Kropewnicki at Applied Materials has been involved in part of the thesis work supplying sample films and exchanging research ideas.

Finally I would like to thank my wife and my best friend Lan for her friendship, love and understanding. Sharing the last four years of my life with her has been a wonderful experience and I look forward to our many years ahead.

TABLE OF CONTENTS

LIST OF TABLES

LIST OF FIGURES

LIST OF ABBREVIATIONS

Abbreviation	Full Name	Appearance	
		Chapter	**Appendix**
AFM	atomic force microscopy	2,3,5	E
ARXPS	angle resolved x-ray photoelectron spectroscopy	2,3,4,6	A
ATR	attenuated total reflectance spectroscopy	2,5	
BCB	benzo-cyclo-butane	2	
BE	binding energy	3	B,C
BOE	buffered oxide etchant	6	
BPDA-PDA	poly (biphenyl dianhydride-p-phenylenediamine)	1,2,3,4,5	A,B,E
CMP	chemical mechanical polishing	1,2,3,4,5, 6	
CTE	coefficient of thermal expansion	2	
CVD	chemical vapor deposition	2	
DI water	deionized water	2,3,4	
DMTA	dynamic mechanical thermal analysis	2	
DSP	double-side polished	5	
DTGS	deuterated triglycine sulfide	3	
EAL	electron attenuation length		B,C
ER-IR	external reflectance infrared spectroscopy	2,4	
FLAC	fluorinated amorphous carbon	2	
FTIR	Fourier tranform infrared	2,3	
HSQ	hydrogen silsesquioxane	2	

Abbreviation	Full Name	Appearance	
		Chapter	Appendix
IC	integrated circuit	1,2	
ILD	interlayer dielectric	1,2	
IMFP	inelastic mean free path	4	B,C
IPA	iso-propanol	2,3,4	
IR	infrared	2,3,5,6	
KE	kinetic energy	3	B,C
low-k	low dielectric constant	1,2,6	
LPCVD	low pressure chemical vapor deposition	3	
MSQ	methyl silsesquioxane	2	
NDF	number of degrees of freedom	4	
NEXAFS	near-edge x-ray absorption fine structure spectroscopy	2,5	
NMP	N-methyl-2-pyrrolidone	2,3,5	
PAA	poly (amic acid)	2,3	
PAE	poly aryl ethers	2	
PE	polarizer efficiency		F
PECVD	plasma enhanced chemical vapor deposition	2	
PMDA-ODA	pyromellitimido-oxydianiline polyimide		B
PTFE	polytetrafluoroethylene	2	
RBS	Rutherford backscattering spectroscopy	2,4,6	
RDS	reflectance difference spectroscopy	5	
RIE	reactive ion etching	2,3	E
RTP	rapid thermal processor	3,4	

Abbreviation	Full Name	Appearance	
		Chapter	Appendix
SAXS	small-angle x-ray scattering	2	
SHG	second harmonic generation	5	
SiLK	silicon low-k	2	
SIMS	secondary ion mass spectroscopy	4,6	
SiON	oxygen doped silicon nitride	3,4,6	
SSE	sum of squared error	5	
TBAH	tetra-butyl ammonium hydroxide	2	
TE	transverse electric	3	E
T_g	glass transition temperature	2	
TGA	thermal gravimetric analysis	2	
TM	transverse magnetic	3	E
TMA	thermal mechanical analysis	2	
TMAH	tetra-methyl ammonium hydroxide	2	
TMFP	transport mean free path		B,C
UV-VIS	UV-VIS	5	
WAXD	wide angle x-ray diffraction	2,3	
X-PEEM	x-ray photoelectron emission microscopy	2,5	
XPS	x-ray photoelectron spectroscopy	2,3,4,6	B,C

SUMMARY

Replacement of aluminum interconnects with copper in the fabrication of microelectronic devices has led to the use of damascene integration approaches. Chemical mechanical polishing (CMP) is used to planarize surfaces in damascene processes to meet the stringent planarity requirements of photolithography. Incorporation of low dielectric constant (low-k) materials in microelectronic device fabrication requires a fundamental understanding of the material removal mechanism and microscopic scale chemo-mechanical interactions in CMP so that degradation of material properties and mechanical damage can be minimized. Little progress has been made in obtaining such understanding due to the inherent difficulties in quantifying chemical and mechanical changes near a low-k surface, since these usually occur within tens of nanometers of the surface.

This thesis is devoted to development of techniques to quantify chemical and mechanical influences during CMP near the surface of a low-k polymer film, poly (biphenyl dianhydride-p-phenylenediamine) (BPDA-PDA). To quantify chemical modifications during CMP, an iterative algorithm has been proposed to extract depth profiles based on Fick's second law of diffusion in a multi-element system from data supplied by angle resolved x-ray photoelectron spectroscopy (ARXPS). It has been demonstrated that the technique can be used to quantify the depth of chemical modification of BPDA-PDA surfaces treated with alkaline solutions. Polymer chains near the surface realign themselves during CMP and polarized infrared spectroscopy is chosen in this thesis to

quantify chain orientations induced by CMP to evaluate the mechanical influence. A theoretical framework based on a 4×4 matrix method for spectral simulation together with an oscillator model for BPDA-PDA has been used to obtain quantitative chain orientation information on a post-CMP BPDA-PDA sample by fitting simulated polarized infrared spectra to experimentally generated spectra. Verification of the oscillator model was established from the complex refractive indices of BPDA-PDA films, which were determined using a new method (R/T ratio method) developed in this thesis to extract complex refractive indices of films with biaxial symmetry from polarized transmission and reflection spectra.

CHAPTER 1
INTRODUCTION

1.1. Copper damascene process

As the minimum feature size of microelectronic devices reaches beyond the 130nm technology node, copper metallization has been readily adopted for interconnect technologies of advanced microelectronic devices. The move to copper metallization has been motivated primarily by better electrical conductivity and improved electromigration resistance relative to aluminum [1]. Adoption of copper has led to the prevalence of the dual damascene integration approach due to the inability to apply conventional subtractive patterning to copper metallization schemes [1].

There are two ways to perform a dual damascene process [2]. As shown in Figure 1-1a, in the single damascene approach, the interlayer dielectric (ILD) is first etched down to the previous metal layer, the via is filled, and excess copper is removed by chemical mechanical polishing (CMP). Next the interconnect recess is patterned and etched, and a second copper fill and CMP are carried out. Alternatively, in the dual damascene approach (Figure 1-1b), both the line and recess can be defined prior to copper deposition. Successful planarization while introducing minimal surface topography is essential to the construction of multilayer structures. As the only known technique that can meet surface planarity requirements of photolithography tools in the sub-0.5μm regime, CMP is a critical and enabling process step for successful Cu damascene

integration. As a result, over the past decade, CMP has emerged as the fastest-growing operation in the manufacture of semiconductor devices and integrated circuits (ICs).

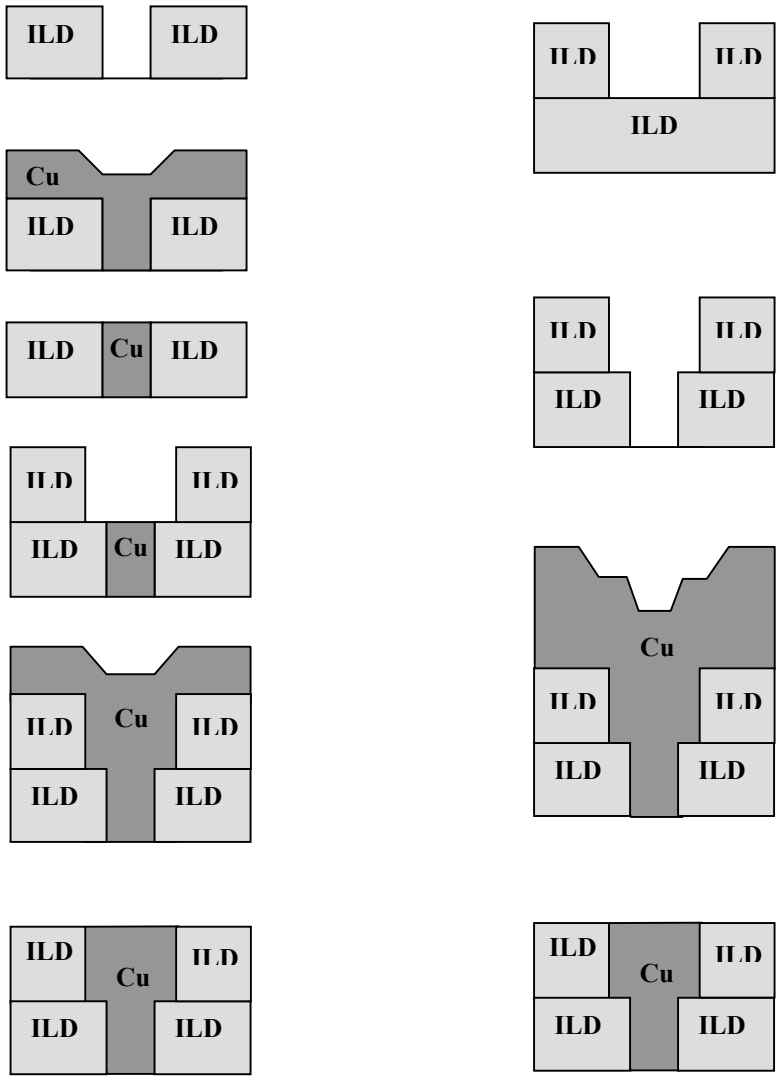

Figure 1-1 Two approaches for performing a dual damascene process (a) single damascene (b) dual damascene [2]

1.2. CMP process

CMP planarizes metal and dielectric surfaces through a combination of mechanical forces and chemical interactions. A schematic diagram of the CMP operation is shown in Figure 1-2. A slurry with abrasive material held in suspension is fed onto a polishing pad composed of a porous polymer. By moving the pad across the wafer in a circular, elliptical, or linear motion, wafer surface layers are removed and thus the surface polished. The polymer pad performs several functions, including uniform slurry transport, distribution and removal of reaction products, and the uniform application of applied pressure (mechanical force) across the wafer [3]. Typical process metrics for CMP include removal rate and within wafer uniformity.

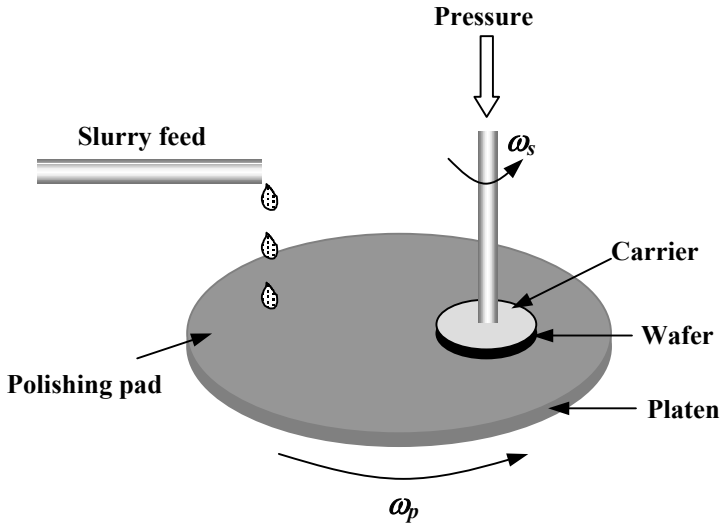

Figure 1-2 Schematic diagram of a typical CMP process [3]

CMP involves complex chemical and mechanical interactions with the film material being removed that depend on numerous interdependent parameters related to characteristics such as wafer topography, process consumables, and tool design. Wafer topography variables include pattern density and interconnect structure. Consumable parameters include slurry composition, flow characteristics, solution pH, physical and chemical characteristics of abrasive particles, material properties and topography of the polishing pad. Critical tool variables include down force (applied pressure) and linear velocity [1]. The total number of variables can exceed 20, making the process difficult to understand and control. The time-dependence of some of these variables causes further complexities in the process [3].

1.3. Challenges presented by low dielectric constant (low-k) materials

CMP technologies are well established for the 130nm technology node, developed primarily for planarization of Cu/SiO_2 systems; however, the rapid introduction of low dielectric constant (low-k) materials presents new challenges. CMP of Cu/low-k interconnect structures is particularly difficult due to significantly different mechanical and chemical properties of copper and low-k materials. Relative to dense SiO_2, low-k materials are mechanically weak and may contain significant porosity [1]. To protect the low-k ILD material during CMP, a barrier layer is usually deposited on top of the ILD (the embedded technique) and the polishing stopped as the barrier layer is reached. A specific amount of over-polish of the barrier is necessary to guarantee the removal of excess copper in the damascene process. However, in cases where the over-polish is severe, the low-k dielectric may be exposed to the slurry chemistry upon complete removal of the barrier layer [1]. Compared to the embedded technique, direct polishing of

low-k materials can significantly reduce the number of process steps. However, the development of CMP processes for direct polishing of low-k materials has been minimal, since direct CMP of low-k materials offers more severe challenges, because these materials are usually hydrophobic, chemically inert and mechanically soft [4].

1.4. Necessity for fundamental understanding of CMP

Despite the strategic importance and dramatic growth of CMP, the basic physical and chemical mechanisms of CMP are still poorly understood [5]. Most of the studies reported have focused on macroscopic scale investigations such as the influence of operational parameters and slurry chemistries on removal rate, within-wafer uniformity, and surface roughness of polished samples. Although such studies provide useful information for design and optimization of certain CMP processes, they contribute little to overall mechanistic understanding. The lack of fundamental understanding of the CMP process has resulted in heavy reliance upon empiricism in CMP process development and control.

Clearly, the complexity of CMP processes partly contributes to the slow progress in mechanistic studies of the process. There are at least two challenging areas to be explored before a complete microscopic understanding is possible. One is the three-body interaction among pad, wafer and slurry particles and the other is how materials are removed due to synergy between chemistry and mechanics. The former area has witnessed numerous research efforts including quantification of particle-particle and particle-wafer interactions [6] as well as visualization of the flow and pressure field in the gap between the pad and the wafer [7,8]. Little progress has been made in the latter area for low-k CMP. The goal of my Ph.D. thesis is to develop techniques to quantify

chemical and mechanical influences near low-k film surfaces during CMP in order to provide a technical platform for studying the synergy between chemistry and mechanics.

Figure 1-3 schematically shows the synergistic effects that can occur between chemistry and mechanics. Chemical effects may break bonds, change chemical composition near a surface or change surface hydrophilicity and hydrophobicity, causing a change of modulus, hardness or charge distribution near the surface; mechanical effects may reorient polymer chains, physically remove material, enhance local temperature or damage the polymer chain by shearing. The chemical mechanical interaction may result in altered removal rate and polishing uniformity, surface property changes, modification of bulk films and alteration in scratch density or depth. Process variables may change the final polishing results by interaction with either chemical or mechanical effects.

A widely accepted mechanism for material removal in CMP involves formation of a chemically modified surface due to interaction of slurry chemicals with the material and simultaneous mechanical wearing of the chemically modified surface layers by abrasives in the slurry. Quantitative information regarding the chemical modification and mechanical influence in CMP will facilitate the understanding of material removal mechanisms due to chemo-mechanical synergy.

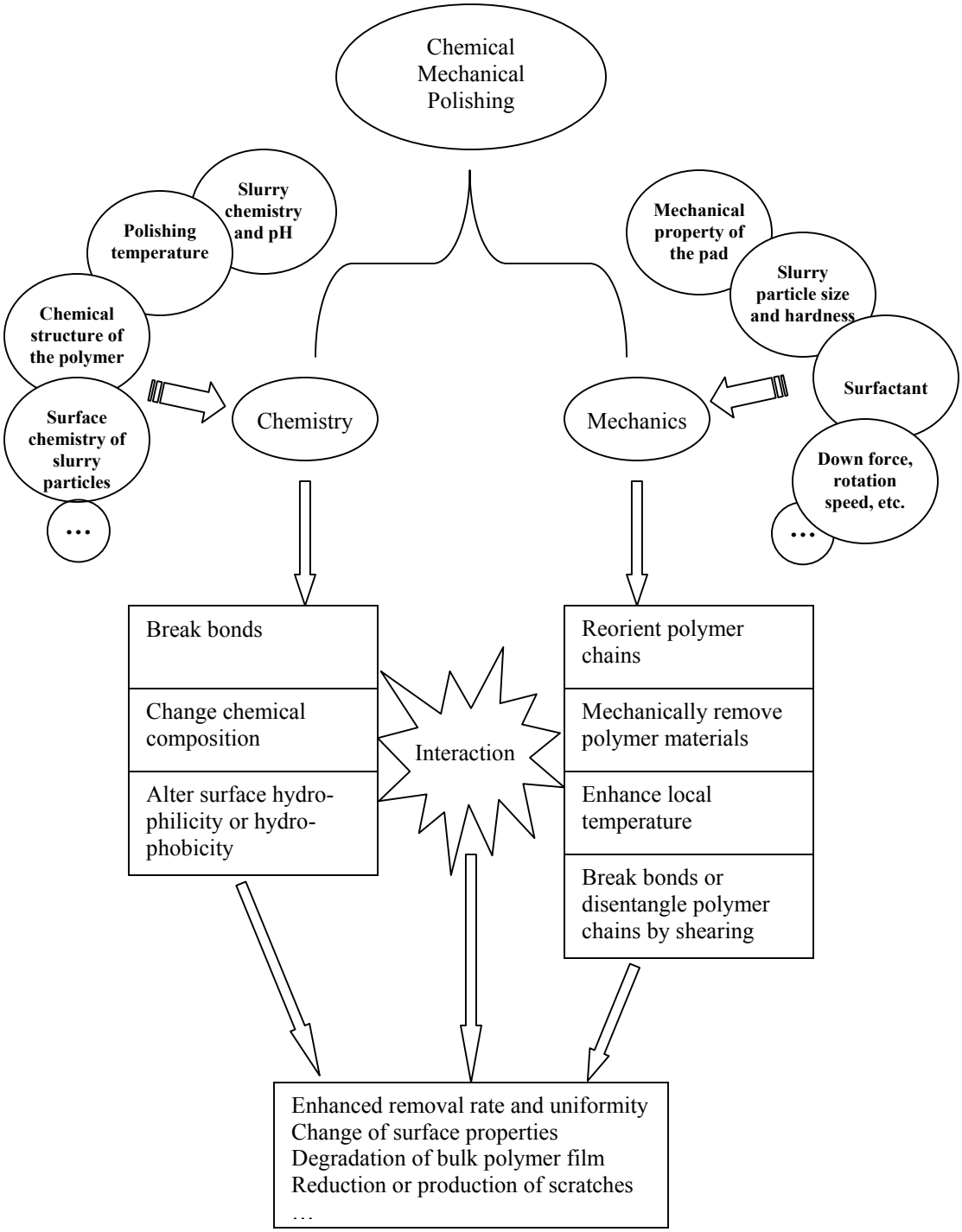

Figure 1-3 Schematic representation of synergistic effects in CMP

For polymeric low-k materials, when the film is subject to a shearing force, polymer chains in the surface and near surface layers will orient preferentially along a certain direction. The depth of mechanical influence (d_{ME}) can be defined as the depth of the region in which the polymer chain motion and orientation are significantly altered by the force exerted on the surface. Similarly, the depth of chemical modification (d_{CH}) can be defined as the depth of the region near the surface in which detectable changes in polymer properties by slurry chemistry occur. This thesis will address the development of techniques to quantify d_{CH} and d_{ME}.

A low-k polymer, poly (biphenyl dianhydride-p-phenylenediamine) (BPDA-PDA) has been chosen as the material to be studied because of its chemical stability and rigid backbone structure. BPDA-PDA has already been extensively studied; thus many of its chemical and physical properties have been well characterized. The rigidity of chains makes BPDA-PDA an ideal material for the study of chain reorientation under mechanical influence.

The thesis is organized as follows. In Chapter 2, previous investigations on low-k materials, low-k CMP and BPDA-PDA film characterization will be reviewed. Chapter 3 summarizes experimental techniques that are used in this thesis. In Chapter 4, a technique is described that was developed to quantify chemical modification depth using angle resolved x-ray photoelectron spectroscopy. In Chapter 5, a theoretical framework is proposed to quantify polymer chain reorientation using polarized infrared spectroscopy and a novel technique is developed to extract complex refractive indices of films with biaxial symmetry from polarized transmission and reflection spectra. Chapter 6 summarizes the thesis results and recommends future directions for research.

It should be noted that the techniques developed in this thesis can be applied to numerous fields in addition to CMP. For example, chemical or plasma modification of solid surfaces and rubbing induced chain orientation in liquid crystal polymers are well-known processes that could benefit from the application of methods developed in this work.

CHAPTER 2

LITERATURE REVIEW

2.1. A brief overview of low dielectric constant (low-k) materials

Reduction in the minimum feature size results in an increased number of components per chip, thus allowing more functionality and speed per unit area [6]. The signal propagation speed in an integrated circuit (IC) depends upon the gate delay and the interconnect delay. The gate delay and interconnect delay as a function of feature size is shown in Figure 2-1 [10].

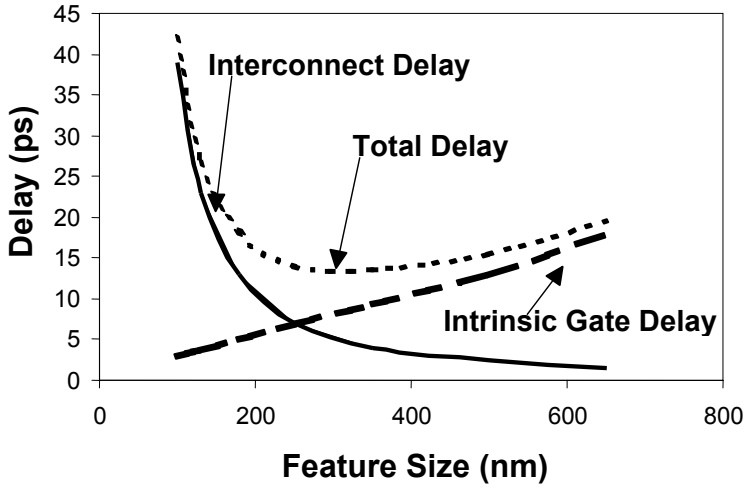

Figure 2-1 Total signal delay (sum of intrinsic gate delay and interconnect delay) increases with decrease in feature size [10]

As the feature size decreases, the intrinsic gate delay decreases, but the interconnect delay increases rapidly causing a total delay increase. Significant effort is being expended to reduce the interconnect delay. This delay depends on the "RC" time constant where "R" is the resistance of metal wires and "C" is the capacitance of the dielectric material [11,14]. RC time delay is given by

$$RC = \rho k \frac{l^2}{td} \tag{2-1}$$

where ρ, *k, l, d and t are* metal resistivity, insulator dielectric constant, length of metal lines, thickness of metal lines and thickness of insulator, respectively [11].

As the feature size is scaled down, the line thickness and the insulator thickness decrease, but the length of the metal lines remains nearly constant as a result of increasing chip complexity, thereby increasing the RC delay. This delay can be reduced by using low resistivity metals and low-k dielectrics [12]. Instead of aluminum and SiO_2 the interconnect schemes will become copper and a low-k material. Copper has several advantages over aluminum; low resistivity (<2μΩ-cm vs. >3μΩ-cm for aluminum alloys), superior resistance to electromigration and fewer processing steps. Capacitance of the dielectric can be reduced by using low-k materials [13].

Since the fabrication of multilevel structures requires hundreds of steps, it is important that the low-k materials can withstand all subsequent processing steps without degradation. Requirements for the low-k inter-layer dielectrics include [15]:

- Low dielectric constant (<3)
- High thermal and mechanical stability

- Resistance to processing chemicals
- Good adhesion to interconnect conductor materials
- Low moisture absorption
- Low cost

Some of the low-k dielectrics being considered for interlayer dielectric (ILD) applications include polytetrafluoroethylene (PTFE), poly (biphenyl dianhydride-p-phenylenediamine) (BPDA-PDA), poly aryl ethers (PAE), benzo-cyclo-butane (BCB), silicon low-k (SiLK), parylene, fluorinated amorphous carbon (FLAC) and hydrogen silsesquioxane (HSQ) [15]. Table 2-1 lists a number of key dielectric and thermomechanical properties for these materials. In addition to dielectric constant k, mechanical strength (as reflected by Young's modulus), coefficient of thermal expansion (CTE) and thermal stability (as indicated by the glass transition temperature (T_g) and weight loss in thermal gravimetric analysis (TGA)) are crucial properties for successful integration into conventional or damascene interconnect structures.

Table 2-1 Dielectric and thermomechanical properties of low-k thin films [15]

Material	k	Young's Modulus (GPa)	Lateral CTE 25-225°C (ppm/°C)	T_g (°C)	TGA % weight loss (425°C, 8h)
PTFE	1.92	0.5	135	250	0.6
BPDA-PDA	3.12	8.3	3.8	360	0.4
Crosslinked PAE	2.8-3.0	2.7	52	350	2.5
Fluorinated PAE	2.64	1.9	52	>400	Not observed
BCB	2.65	2.2	62	/	30
SiLK	2.65	2.3	54	/	2.1
Parylene-N	2.58	2.9	55-100+	425 (melt)	30
Parylene-F	2.18	4.9	33	/	0.8
FLAC	3.2	/	/	/	12.3
HSQ	2.8-3.0	7.1	20.5	/	Not observed

2.2. Literature review on low-k chemical mechanical polishing (CMP)

Many studies have been reported in the area of low-k CMP since the mid-90s. Table 2-2 summarizes investigations performed on low-k CMP since 1992.

From Table 2-2, it can be seen that research in low-k CMP has been quite diversified. The films studied include pure organic polymers, porous SiO_2, and carbon containing SiO_2-based materials (HSQ, MSQ, etc.), prepared either by spin-coating or plasma enhanced chemical vapor deposition (PECVD). Different slurries have also been used for low-k CMP, including silica based slurries [16,17,23,29,38-48,50,51,53-55,57,59], alumina based slurries [18-27,31,55,59], or slurries containing other oxide abrasives such as ZrO_2, CeO_2, MnO_2 or Mn_2O_3 [32-34,37-39,53,55]. This wide spectrum of materials reflects in part the fact that low-k CMP processes are not mature, but are still in its initial stage of development.

The effect of polishing pressure, platen speed and abrasive concentrations are routinely studied in almost all publications. These results are helpful for process design and operation, but they provide little insight into the fundamental chemical and transport aspects of the process.

Table 2-2 Study on low-k CMP in recent literature

Films studied	Characterization	Reference
Polyimide (PI2610, PI2611 or fluorinated polyimide DuPont 37B')	Film thickness, refractive index, surface topography, bulk film chemical structure, mobile ion content, electric properties, zeta potential	16-20
BCB and SiLK™	Film thickness, surface topography, surface chemistry, bulk film chemical structure	20-31
Polyarylene ether (FLARE™, Parylene-N)	Film thickness, surface topography, film hardness, adhesion strength	20, 25, 26, 32, 33
Fluorinated low-k materials	Film thickness, refractive index; dielectric constant; surface topography, surface chemistry, film hardness and modulus, adhesion strength;	20, 33-36
SiOC films: including carbon doped silicon dioxide, Methyl silsesquioxane (MSQ) Hydrogen silsesquioxane (HSQ) and organosilicate glasses	Film thickness, refractive index, dielectric constant, bulk film chemical structure, surface topography, surface chemistry, electrical properties	23, 28, 37-57, 58, 59

Abrasives play a very important role in CMP. Many different abrasives have been used and their effects on CMP studied. For instance, deep scratches were observed at the surface of PAE or fluorocarbon films when they were polished with a fumed silica slurry. However, no deep scratches were found at the surface when a MnO_2 slurry was used [33,34]. CMP of MSQ films demonstrated that the removal rate for different abrasives followed the trend Al_2O_3>ZrO_2>SiO_2. These observations were explained by the abrasive hardness and the electrostatic interaction between the polymer surface and abrasive [37,38].

The influence of surfactant on CMP processes has been extensively studied. Addition of tetra-methyl ammonium hydroxide (TMAH) to the slurry improved the wafer surface wettability and enhanced the polishing rate of polyimide films [17]. A "latency" period was observed for some slurries during CMP and this was attributed to the surfactant [22]. The investigators proposed that this was due to the time needed for the polymer film surface and the slurry particles to adsorb surfactant [22]. In Reference 38, the authors suggested that surfactants might influence the CMP process by modifying the surface interaction, charge status and polarity of the abrasive. The removal selectivity of organic spin-on-glass to SiO_2 has been adjusted by adding varying amounts of TMAH or tetra-butyl ammonium hydroxide (TBAH) to the slurry and this phenomenon was explained by the change of hydration on the oxide surface due to a change in hydrophobicity caused by TMAH, TBAH, or due to a change in chemical dissolution of the oxide surface by TMAH or TBAH [39]. Also, enhanced MSQ CMP removal rates were observed when TMAH was added into a commercial slurry (CABOT SS-25). The surface roughness of post CMP MSQ was also reduced when TMAH was added. This was believed to result

from the enhancement of hydration reactions due to adsorption of ammonium hydroxide onto the hydrophobic MSQ surface resulting in a local increase of pH [44,45]. The influence of TMAH addition into Al_2O_3 or SiO_2-based slurries on the polishing rate of BCB increased drastically when a small amount of TMAH was added to the slurries. The significant increase in removal rate was attributed to two factors: the polymer became more soluble in solutions containing surfactants and the wetting of the polymer surface by the slurry was enhanced by surfactants [21].

The hydrophilicity or hydrophobicity of low-k films also seems to play an important role during CMP. By changing the organic content (methyl groups) in MSQ films, the hydrophobocity or hydrophilicity of the film surface was changed; a more hydrophilic surface led to higher removal rate [38]. A lowering of CMP removal rate was attributed to incorporation of methyl groups which reduced the diffusion rate of water into the oxide [56]. The surface of a low-k film after CMP changed from hydrophobic to hydrophilic with increasing additive concentrations (no information on the additive was provided.) [60]. Finally, it has been demonstrated that an oxygen plasma treatment made the surface of MSQ more hydrophilic and therefore enhanced the MSQ CMP rate [42,43,46].

Degradation of bulk film properties is one of the major concerns of low-k CMP. However, after polishing, neither the leakage current density nor the dielectric constant of polyimide films were degraded [17]. These results are consistent with Fourier tranform infrared (FTIR) studies which suggested that the chemical structure of HSQ and MSQ films remained unchanged after CMP [38]. Likewise, dielectric properties of porous polysilazane films did not degrade after CMP [41]. With SiOC films, the post-CMP surface had the same chemical composition as the original SiOC bulk films [23]. Bulk

chemical bonding did not change after CMP of methyl-incorporated silicon oxide prepared by chemical vapor deposition (CVD) [47]. After polishing SiLK and porous SiLK films, no increase in dielectric constant was observed [28]. The electrical and mechanical integrity of low-k carbon doped oxide films were also maintained during CMP [49]. CMP had only a limited impact on the electrical properties of SiLK films because experimental evidence indicated that the chemical changes were located mainly near the polymer surface [29].

Some studies, however, have reported an increase in both leakage current and dielectric constant after CMP of HSQ films [40], and a degradation of electrical properties of post-CMP MSQ [44]. The leakage current of post CMP MSQ increased as much as one order of magnitude from that of pre-CMP MSQ; the dielectric constant of post CMP MSQ increased from the as-cured value of 2.60 to 2.86 [44]. Film surface chemistry could be modified during CMP; for BCB films, the modified depth was estimated to be around 70-100nm while for SiLK 10nm was reported [22]. CMP had a deep damaging effect on the TEOS film after 25nm of TEOS was removed from a 100nm film by CMP [50]. A remarkable increase in refractive index of fluorinated silicon oxide films after CMP has been observed if the fluorine concentration was greater than 5.8% in the film. The change in refractive index reflected a change in chemical bonding, which could have resulted from either accelerated chemical reactions or exacerbated moisture absorption during CMP [35].

Experimental results described in the above studies on abrasive-surface interactions, surfactant addition and surface hydrophilicity (or hydrophobicity) can be better explained if quantitative information is available concerning how surfaces are chemically modified;

a deeper understanding of degradation of low-k properties can be achieved if the intensity and scale of surface modification (either chemical or mechanical) can be quantified. However, there are few techniques readily available that can be directly applied to quantify chemical and mechanical changes near the surface of low-k materials during CMP. Although sputter depth profiling has been used by some investigators to estimate the depth of chemical modification [22], the explanation of the results is questionable due to the possibility of selective sputtering. This thesis will focus on the development of techniques that can be used to quantify chemical and mechanical influences near a polymeric low-k surface. The techniques will aid in achieving a deeper understanding of chemo-mechanical interaction during CMP and therefore provide insight into material removal and degradation mechanisms.

2.3. Literature review on BPDA-PDA research

BPDA-PDA is a low-k material that may be suitable for future generations of multilevel integrated circuit devices, because of its excellent thermal stability, superior mechanical properties, low CTE, high glass transition temperature, low moisture up-take, and low processing cost. Extensive studies have been performed to determine physical properties of BPDA-PDA films such as optical properties, dielectric properties, mechanical properties, residual stress and crystallinity; some of the studies will be summarized in the following paragraphs.

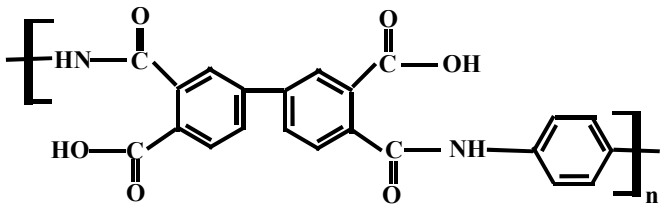

BPDA-PDA PAA precursor

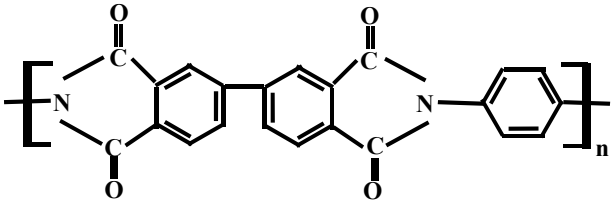

BPDA-PDA

Figure 2-2 Chemical structures of BPDA-PDA and its poly(amic acid) (PAA) precusor

BPDA-PDA is typically prepared through dehydration of its poly (amic acid) (PAA) precursor, which is soluble in N-methyl-2-pyrrolidone (NMP). Usually, PAA solution is first spin coated onto a silicon wafer or a glass slide and subsequently softbaked to remove most of the NMP solvent. The dehydration, also called imidization, is generally carried out in nitrogen at high temperature (>300°C). During imidization, PAA undergoes a ring closure process producing water as a by-product (Figure 2-2). Interaction between adjacent imide and benzene rings results in a rigid backbone structure and causes spontaneous molecular orientation during thermal imidization [61-63,80].

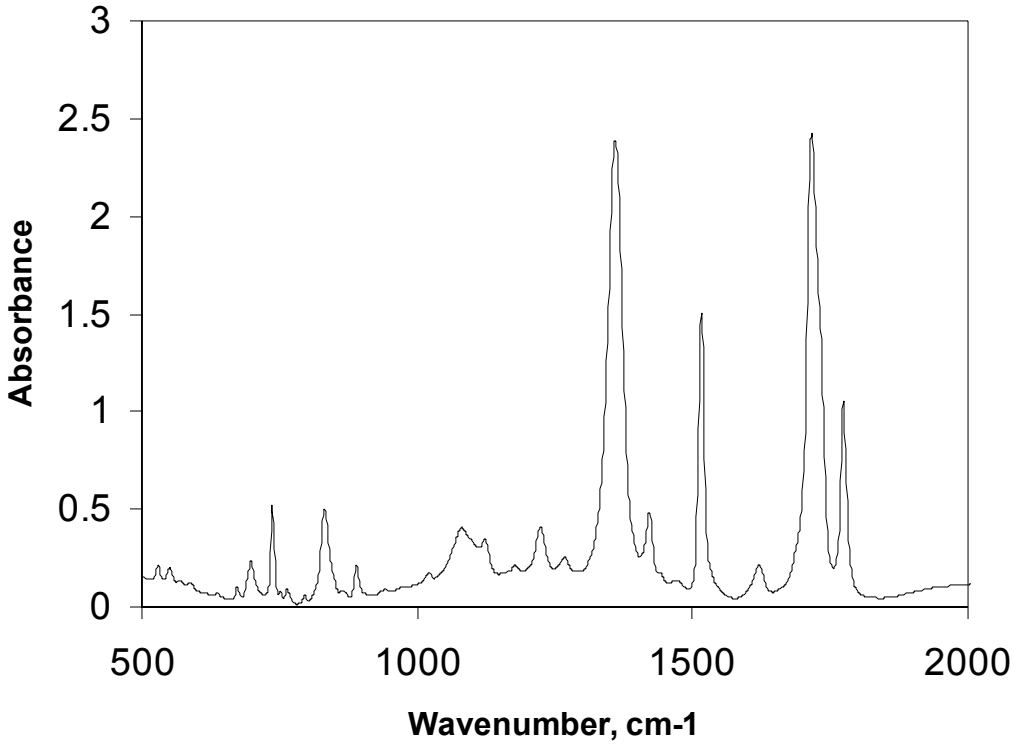

Figure 2-3 A typical infrared absorbance spectrum of a BPDA-PDA film

A typical infrared spectrum of a freestanding BPDA-PDA film is shown in Figure 2-3. Assignment of the more important vibrational modes is: 1774cm^{-1} [ν_s(C=O), Imide I], 1717 cm^{-1} [ν_{as}(C=O), Imide I], 1516 cm^{-1} [C=C tangential stretch of PDA ring, C=C$_{PDA}$] and 1360 cm^{-1} [C-N-C axial stretch., Imide II], and 738cm^{-1} [C-N-C bending out-of-plane, Imide IV] [64,65].

2.3.1. Optical properties and birefringence

In-plane ($n_{//}$) and through-plane ($n_{\perp}$) refractive indices of BPDA-PDA films at a particular wavelength are usually measured by a waveguide prism coupler (details can be found in Section 3.3.4.). They can also be obtained from attenuated total reflectance spectroscopy (ATR) using waveguide modes [70,96]. BPDA-PDA is known for its large optical anisotropy, which is clearly indicated by the data shown in Table 2-3.

In Table 2-3, refractive index and birefringence data are reported for both BPDA-PDA films synthesized in laboratory and those made from commercial PAA resins, e.g., DuPont PI2610. The film thickness varied from 2μm to 40μm. Average refractive index $\overline{n}$ and birefringence Δn are calculated from $\overline{n} = (2n_{//} + n_{\perp})/3$ and $\Delta n = n_{//} - n_{\perp}$, respectively.

Table 2-3 Values of refractive indices and birefringence of BPDA-PDA films reported in literature

Wavelength	$n_{//}$	$n_{\perp}$	Δn	$\overline{n}$	Reference
632.8nm	1.853	1.613	0.240	1.773	66
	1.8439	1.6202	0.2237	1.7693	67
	1.852	1.612	0.240	1.772	70
	1.8549	1.6125	0.2424	1.7741	75
	1.8507	1.6147	0.2360	1.7720	76,78
	1.74	1.62	0.12	1.70	80
	1.8425	1.6089	0.2336	1.7646	82
	1.8582	1.6110	0.2472	1.7758	84
	1.85	1.61	0.24	1.77	88
	1.8474	1.6141	0.2333	1.7696	85,95
	1.8297	1.6318	0.1979	1.7637	90
	1.856	1.614	0.242	1.775	96
1320nm	1.7825	1.5948	0.1877	1.7199	81

Different dependencies of optical anisotropy on the thickness of BPDA-PDA films have been reported. In one study, the large optical anisotropy of BPDA-PDA films was nearly independent of film thickness from 400nm to 4μm [70]; while another study reported the same independence for films from 2-10μm [84]. A decrease in birefringence with respect to BPDA-PDA film thickness from 4μm to 20μm has been reported [71,72]. Similarly, it was reported that birefringence remained constant in the thickness range 1-20μm but decreased drastically with thickness over the range 20-111μm [95]. The different dependence of optical anisotropy could result from the different curing strategies used by different researchers, since it has been reported that the curing process can affect optical properties of BPDA-PDA films [90,94]. Specifically, when a low heating rate (1°C/min) was during used in curing, the birefringence of the resulting BPDA-PDA films did not

depend on film thickness (from 3 to 50μm); however, for a fast heating rate (10°C/min), the birefringence decreased from 0.235 to 0.19 as film thickness increased from 3μm to 50μm [93].

BPDA-PDA films have also displayed a thermo-optic effect, which refers to variation of the refractive index due to temperature change (dn/dT). At a wavelength of 1.32μm, dn/dT did not depend on film thickness, but was affected by birefringence, residual stress and anisotropy during volume expansion [81].

2.3.2. Dielectric properties

The through-plane dielectric constant of BPDA-PDA films has been measured to be ~3 in the frequency range of 100-1MHz using a parallel plate capacitor structure; the in-plane dielectric constant was estimated to be ~3.7 [66]. The through-plane dielectric constant reported previously from a parallel plate capacitor measurement was 3.03; no dependence of dielectric constant on film thickness was observed [84].

2.3.3. Mechanical properties

Lateral (in-plane) Young's modulus, yield stress and tensile strength of BPDA-PDA films are usually derived from film stress-strain curves. Table 2-4 lists some of the reported values.

Table 2-4 Mechanical and thermo-mechanical properties of BPDA-PDA films*

Young's modulus (GPa)	Yield stress (MPa)	Tensile strength (MPa)	T_g (°C)	CTE (ppm/°C)	Reference
5.9	170	210	352	-	83
10.2	334	597	300-470	7.5	85
9.5-13	200-250	480-600	>400	5-7	92
~7	-	475-600	340	3	94
-	-	-	340	-	67
-	-	-	360	-	79
-	-	-	320	20	80
-	-	-	351	-	82
-	-	-	350	4.3	96

* All values reported were lateral (in-plane) values.

A dependence of the modulus on the curing history of BPDA-PDA films has been reported [73], as has a decrease in Young's modulus of BPDA-PDA film with an increase of film thickness from 5 to 40μm [93].

Through-plane modulus is more difficult to measure compared to its in-plane counterpart. High precision capacitance dilatometry has been used to measure the through-plane elastic modulus; the through-plane moduli of BPDA-PDA ranged from 0.05-1.1GPa as the film thickness increased from 4 to 20μm [72]. Loading and unloading curves of nanoindentation measurements were used to derive the average hardness of BPDA-PDA (0.453 GPa) and the through-plane modulus (16.6GPa) [80]; other studies gave different results (~0.7GPa and ~6.7GPa, respectively) [82]. The variation observed are likely due to different conditions used to prepare BPDA-PDA films.

2.3.4. Residual stress

Residual stress of 5MPa for BPDA-PDA films has been reported [85]. In another study, the stress in a fully cured BPDA-PDA film has been reported to be 7.5MPa, and the film showed moisture-induced residual stress relaxation when exposed to ambient air, 100% relative humidity at room temperature [67]. A thickness dependence of residual stress has also been observed: residual stress was ~6.5MPa for BPDA-PDA films ≤20μm thick but the stress increased steeply with thickness for films >20μm and leveled off at ~40MPa at thicknesses over 40μm. Curing history also appeared to have an effect on the residual stress in BPDA-PDA films [68,69]. For instance, residual stress varied between 2 and 10MPa for BPDA-PDA films cured at temperatures ranging from 300 to 400°C [94]. A systematic study on the effect of the film formation process on the residual stress in BPDA-PDA films revealed a wide range of residual stress: 4-43Mpa at room temperature depending on the history of softbake and imidization [75]. A correlation between lower residual stress and higher degree of in-plane chain orientation was established. To obtain a low stress film, solvents should be removed before the onset of imidization and a low heating rate (<5°/min) should be used [75].

2.3.5. Thermal stability, glass transition temperature and CTE

BPDA-PDA displays good thermal stability. It has a high decomposition temperature and T_g, as shown in Table 2-4. Most T_g values were obtained from dynamic mechanical thermal analysis (DMTA). BPDA-PDA does not go through a glass transition until the temperature is raised above 300°C. Furthermore, the thermal decomposition temperature has been reported to be 520°C (5% weight loss in thermo gravimetric analysis) [80].

Lateral, or in-plane, CTE is usually measured by thermal mechanical analysis (TMA); some of the in-plane CTE values reported are listed in Table 2-4. Similar to the modulus, through-plane CTE is more difficult to measure compared to in-plane CTE. The through-plane and in-plane BPDA-PDA CTE have been reported to be ~6ppm/°C and ~144ppm/°C, respectively [90]. Measurements of in-plane CTE using TMA and through-plane CTE using a differential capacitance technique have been reported [72]. The in-plane CTE increased from 5.3 to 7.3ppm/°C with an increase in film thickness from 2.5 to 21μm, while the through-plane CTE showed a slight decrease from 113 to 104ppm/°C [72]. Similar results have been reported by other investigators [87,92]. The through-plane CTE of BPDA-PDA films between 20 and 400°C have been measured using a laser spot scanning interferometer [86]. The through-plane CTE varied from 100ppm/°C at 20°C to 400ppm/°C at 400°C. The through-plane CTE became much larger than the in-plane CTE as the temperature exceeded T_g [86]. For BPDA-PDA films that were cured slowly (1°C/min), the increase of in-plane CTE with thickness was only minimal while for rapid curing (10°C/min), the in-plane CTE increased from 3.5ppm/°C to 19ppm/°C as the thickness increased from 5μm to 30μm[93]

2.3.6. Crystallinity

Wide angle x-ray diffraction (WAXD) patterns (both transmission and reflection modes) have been reported for freestanding BPDA-PDA films. The diffraction patterns revealed that the BPDA-PDA chain was highly extended along the chain and was well packed [67]. Structure anisotropy and high crystallinity were also demonstrated by other WAXD studies [67,73,74,76-80,82,83,85,87,89-94,96]. From the transmission WAXD pattern,

the overall crystallinity in BPDA-PDA films was estimated to be ~25% while from the reflection WAXD pattern the lateral crystallinity was ~18% [91]. The in-plane and through-plane mean intermolecular distances were estimated to be 0.481 and 0.482nm, respectively [76,78,85]. WAXD measurements on BPDA-PDA films cured at different temperatures indicated that the molecular packing order in BPDA-PDA film could be improved by raising curing temperature [68], or by decreasing curing rate [69].

Determination of the microstructure of BPDA-PDA films using small-angle x-ray scattering (SAXS) revealed a weak and broad peak [83]. The mean long intermolecular periodicity estimated from the peak maximum was 13.4nm [83], and a close value (15.6nm) was reported in another study [89].

2.3.7. Water absorption

Water absorption studies of different polyimide films reported a water vapor uptake (wt.%) of 1.46 for a fully cured BPDA-PDA film at 100% relative humidity at room temperature; the diffusion coefficient associated with the water vapor uptake was estimated to be ~$1.7\times10^{-10}$$cm^2$/s [76]. Similar results were reported by other researchers [77]. The activation energy of water diffusion in BPDA-PDA film was estimated to be 9.27kcal/mol [78]. Value of the diffusion coefficient was closely related to the in-plane orientation and mean intermolecular distance, whereas the water uptake was affected by the packing order [79].

2.3.8. Surface modifications

Modifications of the BPDA-PDA surface, either chemically or mechanically, is of great practical interest because such alterations can to be used to improve adhesion properties

and to achieve the desired chain orientation near the surface for liquid crystal display applications. Such modifications have been usually achieved by exposing BPDA-PDA surfaces to alkaline solutions, ion beams or mechanical rubbing.

BPDA-PDA samples have been treated with 1M KOH for 1-30 min at 50°C followed by a deionized (DI) water rinse and iso-propanol (IPA) rinse [99]. X-ray photoelectron spectroscopy (XPS) and external reflectance infrared spectroscopy (ER-IR) were used for surface characterization. Spectroscopic changes showed that the surface bacame potassium polyamate after KOH treatment and was further changed to polyamic acid after an HCl treatment. By measuring samples of different thicknesses using ellipsometry and determining the absorbance of certain bands by ER-IR, an estimation of the depth of modification was obtained; the modification depth for a 10 min reaction was estimated to be 21nm [99]. In another study by the same authors, the surface of BPDA-PDA was exposed to 1M KOH at 55°C for 1-20 min and the estimated depth of modification varied from 1.7nm to 22nm [100]. Rutherford backscattering spectroscopy (RBS) has been used to determine the modification depth of BPDA-PDA films in 1M KOH solutions at different temperatures. The modification depth was not significant at 40°C; at 60°C, ~60 min was needed for the modification depth to reach 100nm, while at 80°C the time required was ~12 min [101]; the activation energy for the modification process was estimated to be 68kJ/mol [101]. Surface chemistry and morphological changes of BPDA-PDA films treated with 1M KOH solutions at 80°C were determined with respect to reaction time by XPS, FTIR-ATR and atomic force microscopy (AFM) [102]. XPS spectra revealed that potassium polyamate structures were obtained simply by washing the KOH modified surface with IPA. When the treated surface was rinsed with water, the

surface could be partly converted into polyamic acid due to protonation of the carboxylate groups. AFM images revealed a high density of pinholes on the modified surfaces that was attributed to higher dissolution rate of amorphous regions on the BPDA-PDA surfaces [102].

XPS has been used to study the modification of BPDA-PDA films with argon, oxygen and nitrogen ion beams [97]. With argon beam irradiation, N and O atoms in the film are preferentially sputtered. For the oxygen and nitrogen beams, incorporation of O or N atoms into the films was observed at lower ion beam energies (<0.5keV); while for higher energy (3.0keV), selective sputtering dominated. Displacement of atoms in the polyimide structure and rearrangement of recoil atoms and incorporated atoms were observed [97]. Surface chemistry modification of BPDA-PDA by an argon ion beam and oxygen reactive ion etching (RIE) was characterized by XPS while angle resolved XPS (ARXPS) was used to estimate the modification depth [98]. The ARXPS measurement after argon ion beam modification showed little angle dependence; thus the modification depth was greater than 12nm. For RIE modified surfaces (30s treatment), some change was observed when the photoemission angle was greater than 70°, indicating a change in the outmost surface (~4nm). For 30 min RIE treatment, the modification depth was greater than 12nm [98].

When the BPDA-PDA surface is subject to mechanical rubbing, polymer chains near the surface will be preferentially aligned due to the external rubbing force. Near-edge x-ray absorption fine structure spectroscopy (NEXAFS) has been used to determine the average near-surface orientation of chains in a buffed BPDA-PDA film [103]. If the chain orientation was assumed to decay as a function of distance from the surface, becoming

random in the bulk, the 1/e alignment depth is estimated to be ~10nm [103]. A subsequent study demonstrated that x-ray photoelectron emission microscopy (X-PEEM), combined with NEXAFS, could be used to visualize surface orientation of BPDA-PDA films after rubbing [104]. The thickness of the realigned layer has been estimated to be 1.8-3nm from the dichroism in polarized infrared (IR) spectra [65]. AFM has also been used to study the rubbed BPDA-PDA film surfaces. Three dominant consequences of rubbing on the film topography were observed: scratches confined to the near surface of the film, tears that extended to the substrate, and strings of islands or droplets aligned parallel to the rubbing direction [105].

2.3.9. Summary

Various studies performed on BPDA-PDA films provide useful and comprehensive information on film properties. Many of the studies mentioned above will be cited throughout the thesis and will be used as justification for specific studies or for comparison purposes. To be more specific, information on mechanical properties, residual stress, thermal stability, water absorption and surface modification using RIE will serve as guidelines in preparing BPDA-PDA films for subsequent studies; information on optical properties, birefringence and crystallinity will be used in quantifying optical anisotropy; information on chemical modifications using alkaline solutions and mechanical modifications by rubbing will be cited in Chapter 4 and Chapter 5 for comparison purposes.

CHAPTER 3
EXPERIMENTAL

The purpose of this chapter is to summarize the experimental techniques that were used to prepare, modify and characterize various thin solid films during completion of this thesis. This chapter discusses the methods of poly (biphenyl dianhydride-p-phenylenediamine) (BPDA-PDA) film preparation, reactive ion etching (RIE) of BPDA-PDA films, chemical modification of BPDA-PDA surfaces using NaOH solutions, chemical mechanical polishing (CMP) of BPDA-PDA films, fabrication of copper-oxygen doped silicon nitride (SiON) dual layer film structure, high temperature diffusion and techniques used to characterize the surface and bulk properties of the films. These techniques include x-ray photoelectron spectroscopy (XPS), atomic force microscopy (AFM), Fourier tranform infrared (FTIR) spectroscopy, prism wave guide coupling technique, spectroscopic ellipsometry, profilometry and x-ray diffraction.

3.1. BPDA-PDA film preparation, etching and surface modification

3.1.1. Preparation of BPDA-PDA films on silicon wafers

BPDA-PDA resins (PI2610 or PI2611) were obtained from HD Microsystems, Inc., in the poly (amic acid) (PAA) form dissolved in N-methyl-2-pyrrolidone (NMP); the resins were used as received. Four-inch silicon wafers were spin coated (3000rpm) with an adhesion promoter (VM652 from HD Microsystems, Inc.) and heated on a hot plate at 110-130°C for 1 min, followed by PAA spin coating with spin speed varying between 1500 and 5000rpm. The films were soft baked at 90°C for 1.5 min and hard baked at

150°C for 1.5 min to remove some of the NMP solvent. Subsequently, the films were cured in a Lindburg furnace in nitrogen at 350°C for 30 min with a temperature ramp rate of 4°C/min. The number averaged molecular weight of the cured BPDA-PDA film is ~50,000. An infrared spectrum of a cured BPDA-PDA film is shown in Figure 2-3. Figure 3-1 shows the wide-angle x-ray diffraction (WAXD) results (reflection mode) on a BPDA-PDA film on silicon. In Figure 3-1, diffraction intensity in counts per second (CPS) is plotted versus 2θ (please see Section 3.3.7 for experimental details of WAXD). The diffraction pattern indicates that the BPDA-PDA film is largely amorphous and the vague shoulder peak at ~25° suggests a low level crystallinity (~7% based on peak deconvolution and data fitting).

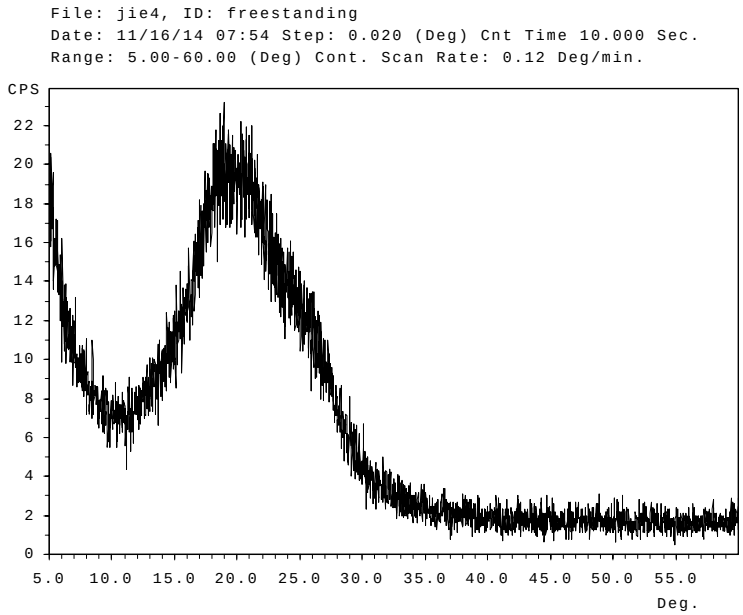

Figure 3-1 Wide-angle x-ray diffraction of a BPDA-PDA film on silicon

3.1.2. Preparation of freestanding BPDA-PDA films

Freestanding BPDA-PDA films were used for complex refractive determination with polarized infrared (IR) spectroscopy. To retain the stress level in the freestanding films as in films completely covering the silicon surface, the BPDA-PDA films were bound to the silicon at edges while being freestanding at the center, as shown in Figure 3-2.

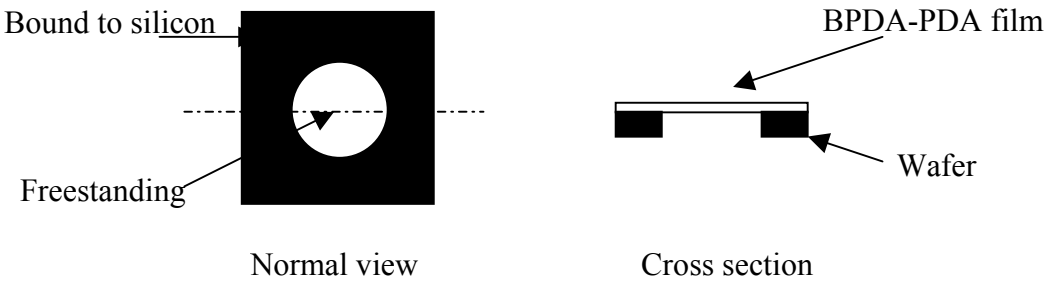

Figure 3-2 A freestanding BPDA-PDA film

A backside etching process was developed to fabricate the freestanding BPDA-PDA film. Following is a detailed description of the backside etching process.

1. ~150nm SiON was deposited on both sides of a 4-inch silicon wafer following the procedure described in Section 3.2.1.
2. Cr layers (~300nm) were deposited on both sides the wafer. The deposition was performed in a CVC DC sputtering system equipped with a 3" Cr target operating at a sputtering pressure of 6 mTorr. It took ~1200s to achieve a Cr thickness of ~300nm at a power of 350W (7% of a total power of 5000W);

3. The front side of the wafer was protected with a photoresist (PR1827 from Shipley) spin-coated at 3000rpm; the photoresist was baked on a hotplate at 120°C for 1 min;
4. A BPDA-PDA layer was spin coated on top of the Cr layer on the backside of the wafer and cured (Section 3.1.1); the spin speed was 2000rpm.
5. Another Cr layer (~300nm) was deposited on top of the BPDA-PDA layer on the backside of the wafer through DC sputtering.
6. The Cr layer was patterned by photolithography. PR1827 was spin coated at 3000rpm and baked on a hotplate at 120°C for 1 min. Photoresist exposure was carried out on a Karl Suss MA-6 mask aligner at a UV wavelength of 365nm. The exposure dose was 240mJ/cm^2. The resist was developed in Microposit 354 Developer (from Shipley) followed by hard bake on a hotplate at 120°C for 2 min. The Cr layer in the open areas was etched with a Cr etchant (CR-7S from Cyantek Corporation). PR1827 served as the etch mask.
7. BPDA-PDA in the open areas was etched for 15 min in a Plasma-Therm reactive ion etcher (see Section 3.1.3); during this etch, the entire PR1827 layer was removed. The Cr layer on top of the BPDA-PDA layer served as the etch mask. After BPDA-PDA patterning, the Cr layer on top of SiON in the open areas was exposed.
8. The Cr layer on top of the SiON in the open areas was removed with Cr-7S; simultaneously, the entire Cr layer on top of the BPDA-PDA layer was also completely removed;
9. An etch mask layer was fabricated for SiON RIE. Although BPDA-PDA could be used as the etch mask for SiON RIE, it was desirable to maintain the integrity of the BPDA-PDA film; thus a PR1827 layer was added on top of the BPDA-PDA to serve

as the etch mask. The mask and photolithography process described in Step 6 were used.

10. SiON in the open areas was etched for 6 min in the Plasma-Therm reactive ion etcher. The etching gas was a mixture of CHF_3 (45sccm) and O_2 (5sccm). The etching was carried out at 34°C and 40mTorr with an RF power of 200W.
11. The PR1827 on both sides of the wafer was removed with 1165A stripper from MicroChem Corp.
12. The front side of the wafer was rinsed thoroughly with acetone and iso-propanol (IPA). Then the front side was descummed in the Plasma-Therm reactive ion etcher. The etching gas was O_2 (40sccm). The etching was carried out at 34°C and 200mTorr with an RF power of 100W;
13. The target BPDA-PDA film was spin coated on top of the Cr layer on the front side of the wafer (see Section 3.1.1.);
14. The target BPDA-PDA film was protected with a photoresist (AZ4620 from Clariant) spin coated at 2000rpm; the photoresist was baked on a hotplate at 120°C for 1 min;
15. A 1:1:1 mixture of 49% (w.t.) HF and 70% (w.t.) HNO_3 and deionized (DI) water was used to etch silicon from the wafer backside in the open areas. The layer of 300nm DC sputtered Cr, which was inert to the HF+HNO_3 mixture, between the front side BPDA-PDA film and the silicon wafer, served to isolate the HF+HNO_3 mixture from the front side of the BPDA-PDA film during silicon wet etching. After silicon was etched away in the open areas, the Cr layer was removed using CR-7S. Thus the BPDA-PDA films in the open areas became freestanding.
16. The front-side AZ4620 layer was removed using acetone.

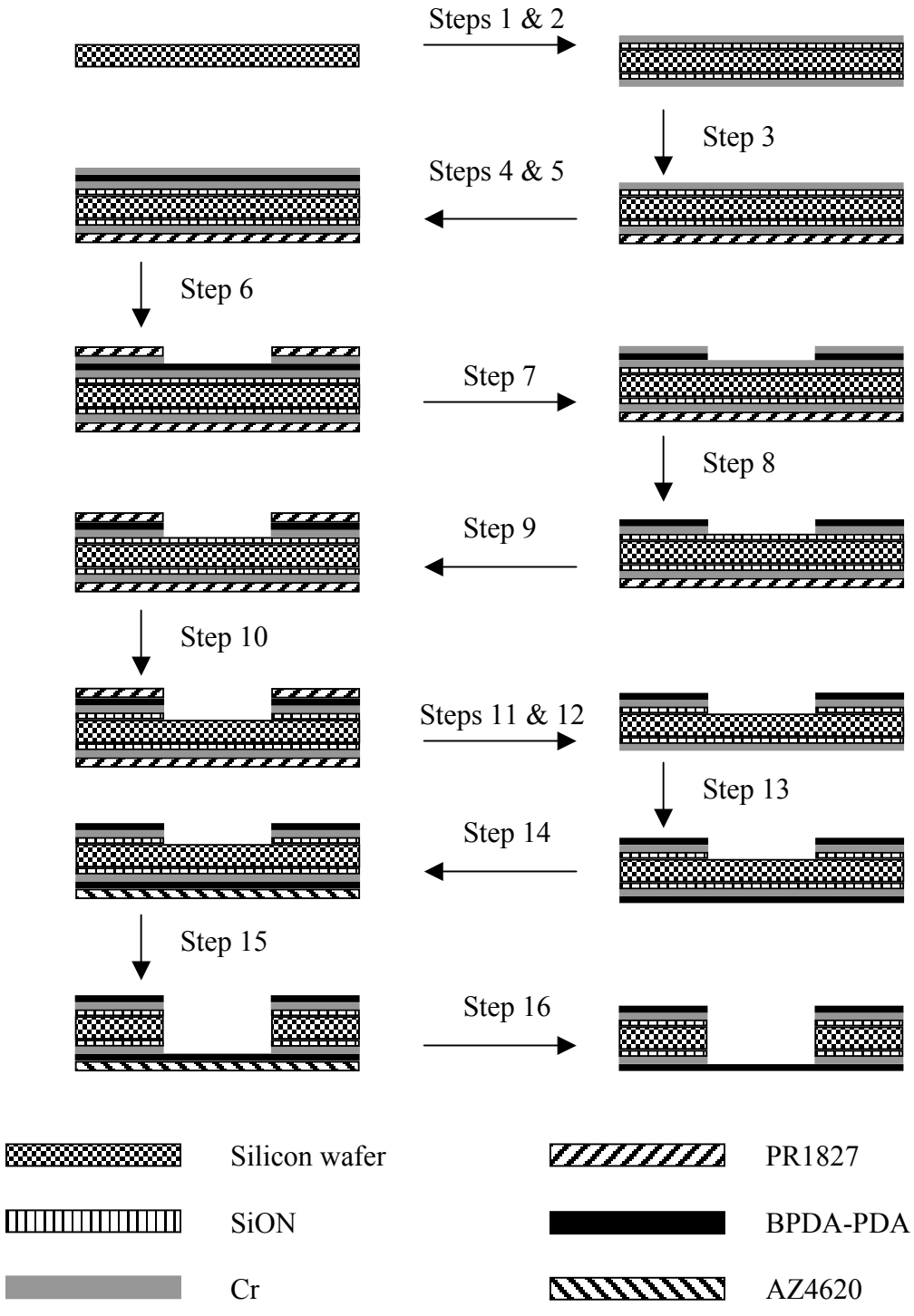

Figure 3-3 Fabrication of freestanding BPDA-PDA films by backside etching

Figure 3-3 schematically shows the freestanding film fabrication process. FTIR spectra revealed no detectable change of BPDA-PDA films due to treatment by either acetone or CR-7S.

3.1.3. RIE of BPDA-PDA films

RIE of the BPDA-PDA films was conducted in a Plasma-Therm reactive ion etcher with an 11-inch electrode. The etching gas was a mixture of CHF_3 (5sccm) and O_2 (45sccm). BPDA-PDA films were etched at 34°C and 200mTorr with an RF power of 350W.

3.1.4. Chemical modification of BPDA-PDA films with NaOH solutions

BPDA-PDA samples were treated with 0.2M or 1M NaOH aqueous solutions at room temperature for 1 min followed by a 10-second DI water rinse. For each sample, only about half of the sample area was exposed to NaOH solutions and DI water rinse. The purpose is to avoid contact of NaOH solution or DI water with the tweezers that was used to hold the sample in order to minimize contamination from the tweezers.

3.1.5. CMP of BPDA-PDA films

CMP of BPDA-PDA films was performed on a bench top Buehler Petrolap lapping machine. The lapping machine has a 12-inch diameter aluminum platen and the rotating speed is controllable to within ±1 rpm from 15 to 150 rpm. Polishing pads were bonded to the platen with adhesive backing. The lapping machine was modified slightly to accommodate a VersaLap 164 polishing fixture from South Bay Technology Inc. The VersaLap fixture accepts samples up to 4 inch in diameter and holds the sample via a vacuum chuck. During CMP, the polishing fixture was usually allowed to rotate freely as driven by the rotating platen; in unidirectional polishing, the polishing fixture was held

manually to prevent any motion. Down force was adjusted by adding weights onto the fixture.

Either an IC1000 or a Suba IV pad from Rodel, Inc. was used in CMP. The compressibility / hardness for IC1000 and SUBA IV pads are 2.25% / 57 (Shore D) and 15% / 61 (Shore A), respectively. A commercially available silica-based slurry (Klebosol 1501 from Rodel, Inc.) was used in CMP. The slurry uses KOH as the stabilizer and has a pH value of ~10.8. It contains ~30% (wt.) silica with an average particle size of ~50nm. The slurry flow rate was controlled and adjusted by a peristaltic pump. The polishing pad was conditioned each time before CMP by polishing a bare 4-inch silicon wafer for 5 min using DI water and for another 5 min using the slurry. During CMP, the polishing pad was conditioned in situ using a stainless steel conditioning ring. Table 3-1 lists typical conditions used for BPDA-PDA CMP and pre-CMP pad conditioning.

Table 3-1 Typical conditions used for BPDA-PDA CMP and for pre-CMP pad conditioning

	BPDA-PDA CMP	Pre-CMP pad conditioning
Platen rotation speed	30 rpm	30 rpm
Down force	2 psi (4-inch wafers) 10-15 psi (3cm×3cm square pieces)	2 psi
Slurry flow rate	50 ml/min	25 ml/min
Polishing time	1 min	5 min (DI water) + 5 min (slurry)

3.2. Copper diffusion in oxygen doped silicon nitride (SiON)

3.2.1. Cu-SiON dual layer structure fabrication

Silicon nitride films were deposited on 4-inch silicon wafers in a Tystar furnace at 800°C and 200mTorr by low pressure chemical vapor deposition (LPCVD). The flow rates of the two gaseous reactants, ammonia (NH_3) and dichlorosilane (SiH_2Cl_2), were 140 and 50sccm (standard cubic centimeters per minute), respectively. A 24-minute LPCVD run produces a silicon nitride film of ~150nm thick. The resultant silicon nitride films contain a small amount of oxygen (Section 4.4) and will be referred to as oxygen doped silicon nitride, or SiON, in this thesis.

A pure copper film was deposited onto the SiON in a CVC DC sputtering system equipped with an 8-inch Cu target operating at a sputtering pressure of 6 mTorr. Approximately 60 minutes were required to achieve a Cu thickness of 2μm at a power of 2000W (40% of a total power of 5000W). The wafers were broken to small pieces for subsequent high temperature diffusion studies.

3.2.2. High temperature diffusion

High temperature diffusion was carried out in an AET rapid thermal processor (RTP). The temperature of samples was raised to a preset value in seconds and maintain for different amounts of time. To prevent the copper layer from oxidizing, the RTP chamber was purged with forming gas (10% H_2 + 90% N_2) throughout the high temperature diffusion process. As the samples cooled to room temperature, half of the sample area was exposed to 70% nitric acid solution for 1 min followed by 1 min of a DI water rinse. The copper layer exposed to the HNO_3 solution was dissolved. Again, the purpose of etching only half of the sample was to avoid contact of HNO_3 solution or DI water with

the tweezers that was used to hold the sample to minimize contamination arising from the tweezers.

3.3. Characterization techniques

3.3.1. XPS

XPS is a surface sensitive technique for establishing chemical bonding information within the top few atomic layers (<20nm) of a surface [106]. Surface analysis is accomplished by irradiating a sample (in vacuum) with monoenergetic soft x-rays (energy hν < 10 keV) and analyzing the energy of the ejected electrons. The photons interact with atoms in the surface region, causing core electrons to be emitted by the photoelectric effect. The emitted electrons have kinetic energies (*KE*) given by

$$KE = h\nu - BE - \varphi \tag{3-1}$$

where $h\nu$ is the energy of the photon, *BE* is the binding energy of the atomic orbital from which the electron originates, and φ is the spectrometer work function [106]. Binding energy is the energy difference between the electron initial and final states (after the photoelectron has been ejected from the sample). Each element has a unique set of binding energies and therefore XPS can be used to identify chemical elements and determine their concentration in the surface. Variations in the elemental binding energies (the chemical shifts) arise from differences in the chemical bond strengths of compounds. These chemical shifts can be used to identify the chemical state of the material being analyzed. In angle resolved x-ray photoelectron spectroscopy (ARXPS), spectra are collected at various photoemission angles (referenced to the sample surface normal) by tilting the sample. Because the effective sampling depth decreases with a decrease in the

cosine of the photoemission angle, ARXPS can be used to extract information on the concentration depth profile of the sample [106].

In this thesis, all XPS spectra were collected using a Physical Electronics (PHI) Model 1600 XPS system equipped with a monochromator. The system used an Al Kα source ($h\nu$=1486.8eV). Ejected photoelectrons were detected by a hemispherical analyzer that provided high sensitivity and resolution. The operating pressure in the sampling chamber was below 5×10^{-9}Torr. All high resolution spectra were collected with a pass energy of 46.95eV. The step size and time/step were chosen to be 0.025eV and 100ms, respectively. Repeated measurements on one point demonstrated that the standard deviation of relative error in total photoelectron intensity was less than 0.25% under this condition. For ARXPS measurements, spectra were collected in such a way that the photoemission angle was varied from 70° to 20° at an interval of 5° (forward), and back from 20° to 70° at an interval of 5° (backward), and another sequence of forward and backward again.

3.3.2. AFM

AFM is a scanning probe technique in which a sharp tip positioned on a cantilever is scanned in a raster-pattern along a surface. Due to forces acting between the surface and tip the cantilever is deflected from its equilibrium position. The deflection is recorded as a function of time and thereby an image of the surface topography forms with close to atomic resolution [107].

In this thesis, A Digital Instruments Veeco atomic force microscope (AFM) was used in contact mode to measure the topography of the surface of BPDA-PDA films. All the

scans were performed over areas of 1 μm×1 μm with a DNP-1 type Nanoprobe SPM tip designed for Digital Instruments scanning probe microscopes. The resolution of all images acquired was 512 data points per scan line × 512 scan lines.

3.3.3. FTIR spectroscopy

FTIR analysis is a useful analytical tool for tracking chemical changes occurring in polymeric films [108]. This technique is based on the principle that molecules have vibrational energy transitions, which are sensitive to electromagnetic energy corresponding to the mid-infrared region (wavenumber between 4000 cm^{-1} and 400 cm^{-1}). When an infrared beam passes through a sample, certain frequencies are absorbed and are absent in the transmitted spectrum. The transmitted spectrum can be used to identify the presence of specific chemical bonds in the sample based on absorptions.

In this thesis, infrared spectra were collected with a Bruker Equinox 55 infrared spectrometer equipped with a deuterated triglycine sulfide (DTGS) detector. All spectra were taken at 2 cm^{-1} resolution, 512 scans in the wavenumber range of 400~6000 cm^{-1}. The polarization state of incident light was adjusted by using either a Harrick KRS-5 wire grid polarizer or a Perkin Elmer wire grid polarizer; two polarizers were used in series to increase the polarization efficiency in some measurements.

In addition to normal incidence transmission spectra collection, oblique incidence transmission and reflection collection was also made possible with a modified variable angle reflection stage, which allows switching between transmission and reflection spectra collection modes (Figure 3-4). In the transmission spectra collection mode, incident light passed through a circular optical aperture (8mm in diameter) on a scattering

platform and was reflected by a specular gold plate before entering the detector. Transmission background spectra were collected without the freestanding film on the optical aperture. The scattering platform was fabricated by using a piece of sand paper to scatter light outside the optical aperture area. In this way, the sampling area can be strictly controlled. A small shutter is placed in the path of light reflected by the film to prevent the light from entering the detector. In the reflection spectra collection mode, the freestanding film was positioned immediately below the scattering platform. Incident light in the optical aperture area was reflected by the film and entered the detector. Transmitted light hit the scattering platform and was scattered. Reflection background spectra were collected by replacing the freestanding film with the specular gold plate. Particular care was exercised in optical alignment to ensure that the identical area on a film was sampled when switching from transmission mode to reflection mode.

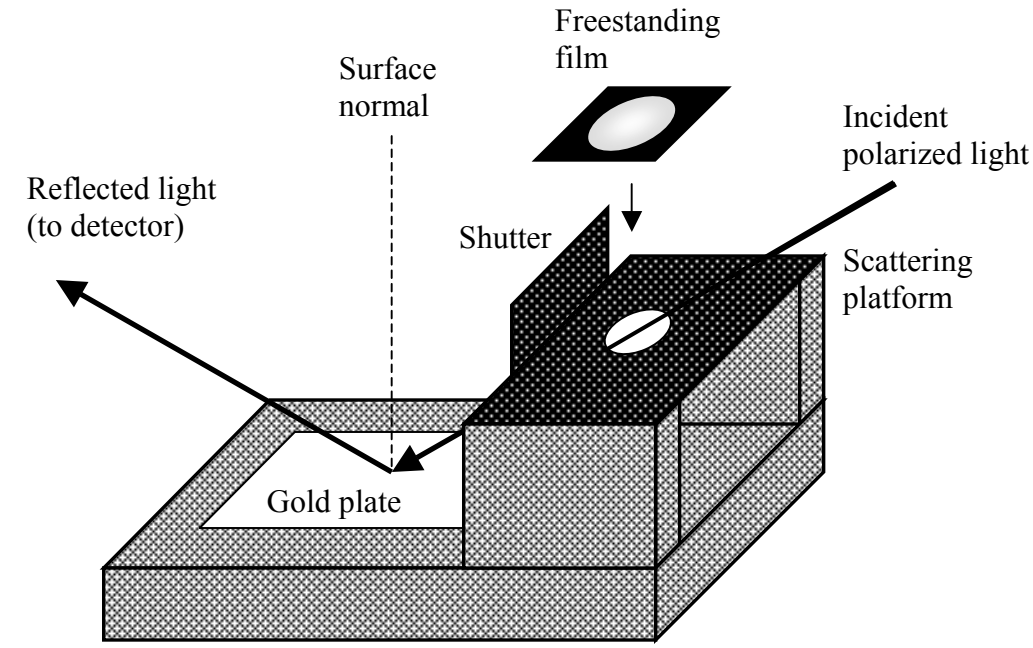

(a) Transmission spectra collection mode

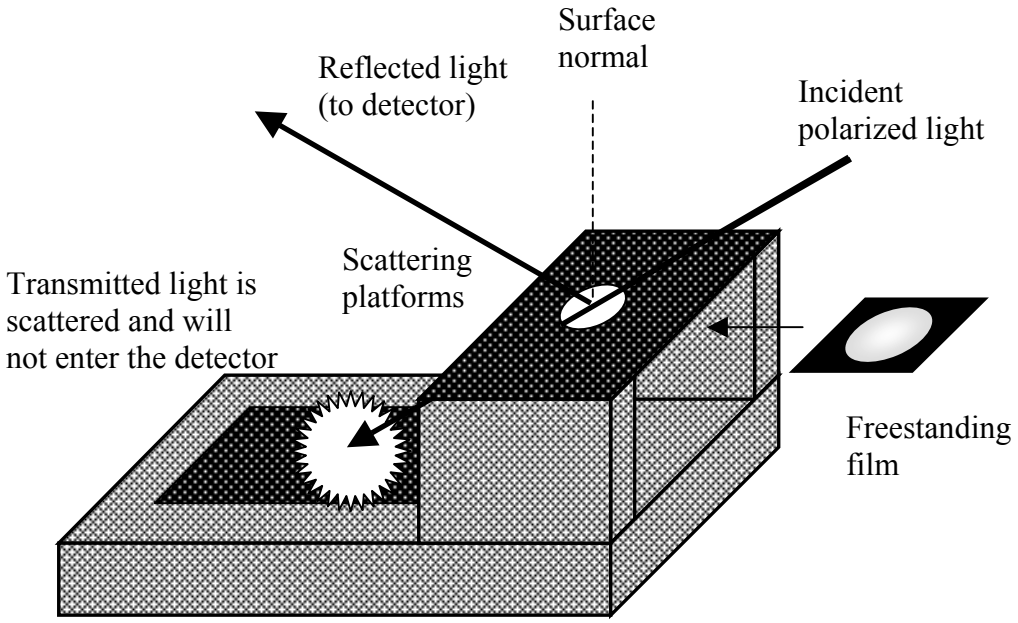

(b) Reflection spectra collection mode

Figure 3-4 Two different operation modes for the FTIR reflection configuration

3.3.4. Prism wave guide coupling technique

The wave-guide coupler technique can be used to infer orientation or crystallinity information by characterizing the three-dimensional optical properties of thin polymer films [109,110]. This method provides a non-destructive way to obtain the three principal refractive indices in a straightforward and efficient way. Figure 3-5 illustrates the geometry of the prism sample interface. The sample is held against the prism at a distance of a fraction of a wavelength. The light is incident at the base of the prism (of refractive index of n_p) at an angle γ_p. When γ_p is less than the critical angle, photons cross the air gap and enter the sample. The following equation relates the refractive indices of the prism and the sample.

$$n_p \sin\gamma_p = n_s \sin\gamma_s \tag{3-2}$$

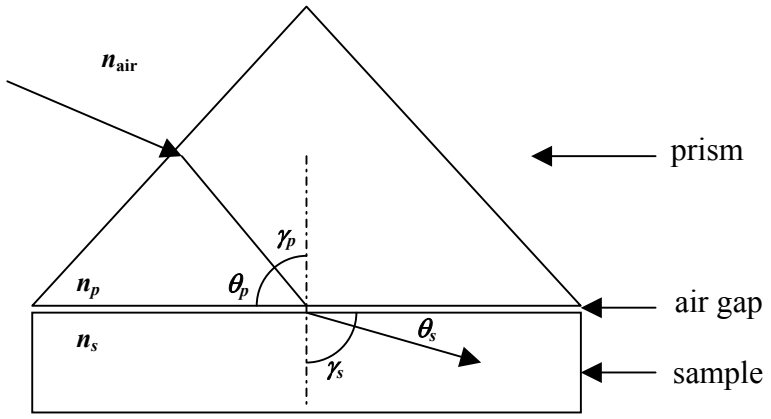

Figure 3-5 Geometry of the prism-sample interface of the prism coupler [109]

At certain angles of θ_s, called synchronous angles, the plane wave exactly duplicates its second reflection in the sample, the wave is guided along the sample, and a mode is present. The condition under which a particular θ_s is a synchronous angle is:

$$\sin\theta_s = \frac{m\lambda}{2d} \qquad m = 1,2,3\ldots \tag{3-3}$$

where m is the mode number, λ is the wave length, and d is the film thickness [109].

The wave-guiding theory can be utilized to measure the refractive indices and thickness of thin films. The sample refractive index may be calculated if two modes are known. If the sample is too thick (>15μm), it might be difficult in practice to distinguish different modes. When the prism wave-guide coupler is used to measure the three-dimensional refractive indices of a film sample, it is necessary for the incident laser beam to be linearly polarized so that the refractive indices in different directions can be obtained. Depending on the direction of the electric field with respect to the incident plane, the polarized light can be divided into TE (transverse electric) polarization and TM (transverse magnetic) polarization. The propagation direction of the incident beam and the normal direction of the surface on which the beam strikes defines the incident plane. If the TE wave is used in the prism coupler wave-guide, the excited film modes are called TE modes, otherwise if the TM wave is used, the excited film modes are called TM modes. TE modes yield the in-plane refractive index, and TM modes yield the through-plane refractive index of the film [109].

In this thesis, the refractive indices of cured polyimide films were measured in air using a Metricon Model 2010 prism coupler equipped with commercial laser sources of 632.8 nm

or 1550 nm wavelength. The resolution of the refractive index was ±0.0005 and that of the film thickness was ±0.3% over the 0.5-15μm thickness range.

3.3.5. Spectroscopic ellipsometry

Spectroscopic ellipsometry is used in this thesis to measure the thickness of some of the dielectric films. Spectroscopic ellipsometry measures the polarization and phase changes (Δ and Ψ) of polarized light reflected from a surface covered with a thin film over a range of wavelengths and angles. A model is constructed to simulate the sample (substrate and all thin films) and generate the theoretical Δ and Ψ for the sample. The generated data are compared with experimental data and sample parameters (such as film thickness and refractive index) are obtained through regression analysis [111].

In this thesis, spectroscopic measurements were performed on a Woollam variable angle spectroscopic ellipsometer with spectral range from 193 nm to 1700 nm. Measurements were taken at angles of 65°, 70°, and 75°. The data were fit with the Cauchy model in the spectral range from 700 nm to 1200 nm [111].

3.3.6. Profilometry

In this thesis, a Tencor Alpha Step stylus profilometer is also used to measure film thickness. In a stylus profilometer, a small radius stylus is drawn across a sample and deviations of the stylus are measured to give surface roughness similar to an AFM but with a much coarser tip size and greater tip pressure.

3.3.7. X-ray diffraction

WAXD measurements were used to characterize the crystallinity of the BPDA-PDA films. Measurements were performed on a SCINTAG X1 system and a Huber Seenan-Bohlin thin film diffractometer. The power settings of the X-ray were 45 kV and 40mA. The 2θ scanning range and continuous scanning rate were 5 - 60° and 0.12°/minute, respectively (θ is the diffraction angle).

CHAPTER 4

QUANTIFICATION OF CHEMICAL MODIFICATION DEPTH USING ANGLE RESOLVED X-RAY PHOTOELECTRON SPECTROSCOPY

In this chapter, a technique is developed to quantify chemical modification depth using angle resolved x-ray photoelectron spectroscopy (ARXPS). The chapter begins with a comprehensive literature review on different techniques that have been reported to extract chemical composition depth profiles using ARXPS. Subsequently, an iterative algorithm is proposed to extract depth profiles based on Fick's second law of diffusion in a multi-element system from data supplied by ARXPS. Parameters related to the concentration profiles are obtained by fitting the experimental angle-dependent photoelectron intensity fractions to predictions from the algorithm. Simulations using an infinite source diffusion model have been conducted to study the influence of errors in the raw data and to demonstrate the robustness of the algorithm. Chemical composition depth profiles resulting from high temperature diffusion near oxygen-doped silicon nitride surfaces are extracted from ARXPS using the algorithm to verify the correctness of the proposed algorithm. Finally, ARXPS is used to extract chemical composition depth profiles near surfaces of poly (biphenyl dianhydride-p-phenylenediamine) (BPDA-PDA) films modified with NaOH solutions. From the chemical composition depth profiles, quantitative information on the chemical modification depth can be obtained.

4.1. Literature review on depth profiling using ARXPS

The review is organized based mainly upon the depth-profile models that have been proposed, rather than on the algorithms that have been used for optimization. The articles reviewed are classified into 6 categories:

1. Articles dealing only with a thin overlayer on a substrate or a "patched" overlayer on a substrate
2. Articles using relatively simple depth profile models (e.g., exponential depth profile, step depth profile, etc.); some of the articles in this category may also have used models described in Category 1
3. Articles using depth profiles from diffusion models
4. Articles using multilayer models, including following multi-steps, multi-ramps and steps-ramps, as shown in Figure 4-1; these three models are quite similar.

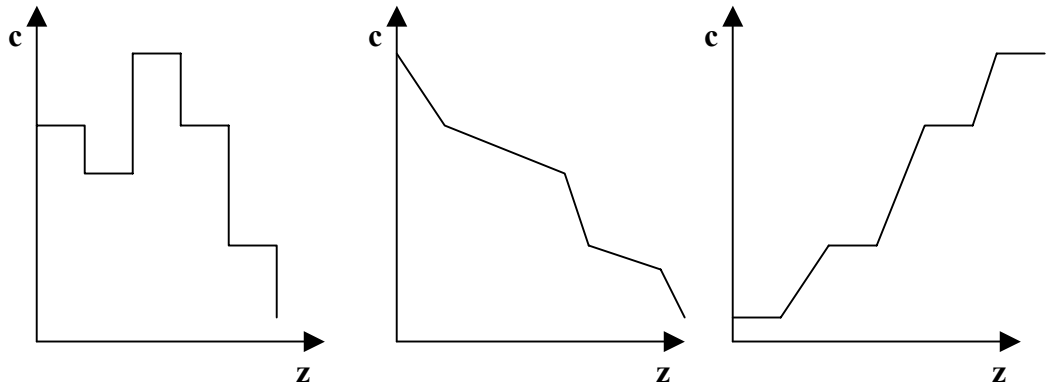

Figure 4-1 Different multilayer depth profiles

5. Articles using irregular profiles usually generated as a result of certain inversion algorithms, e.g., a linear combination of exponential functions
6. Review articles

In this review section, some of the typos or errors in the original articles are corrected based on current understanding. Most of nomenclature is kept the same as in the original article. However, some minor changes to the nomenclature are made where such change may help in comparing different articles. Different authors may prefer using θ to denote either the angle between electron traveling path and the surface (take-off angle) or the angle between electron traveling path and the surface normal (photoemission angle). Thus in this section, $\sin\theta$ and $\cos\theta$ convey the same information.

4.1.1. Thin overlayer models or "patched" overlayer models

Many researchers have used ARXPS data to retrieve thickness and composition information of a thin layer on a uniform substrate. These models and data analysis are relatively simple as described in the following examples.

Akhter *et al.* proposed a concentration profile in which one bonding state of an element has uniform concentration x_s in a layer of thickness t on a bulk material in which the concentration of the same bonding state is x_b [112]. The same model has also been mentioned in another paper [125]. Photoelectron intensity from atoms of a certain bonding state (I_{ca}) can be expressed as [112]:

$$I_{ca} = x_b I_c^{\infty} \exp[-t/(\lambda \sin\theta)] + x_s I_c^{\infty} \{1 - \exp[-t/(\lambda \sin\theta)]\} \quad (4\text{-}1)$$

where λ is the electron attenuation length and I_c^∞ is the total intensity from a semi-infinite sample. While intensity from atoms of other bonding states (I_{nc}) is:

$$I_{nc} = (1 - x_b) I_c^\infty \exp[-t/(\lambda \sin\theta)] + (1 - x_s) I_c^\infty \{1 - \exp[-t/(\lambda \sin\theta)]\} \quad (4\text{-}2)$$

$$I_{ca} + I_{nc} = I_c^\infty \quad (4\text{-}3)$$

The fractional concentration of atoms in the first bonding state (R) is:

$$R = I_{ca} / I_c^\infty = x_s - (x_s - x_b) \exp[-t/(\lambda \sin\theta)] = x_s - \Delta x \exp[-t/(\lambda \sin\theta)] \quad (4\text{-}4)$$

x_s, Δx and t/λ were obtained through curve fitting using R values; λ was obtained from literature values.

Ton-That developed an algorithm that allowed thickness determination for any uniform film of thickness ($t<3\lambda$) on a substrate using the relative peak intensities of two peaks, one of which is characteristic of the substrate and the other characteristic of the film, measured at different photoelectron take off angles [113]. The theory can be described in the following manner.

The intensity from element i (I_i) can be expressed as [113]:

$$I_i = \frac{I_i^0}{\lambda_i} \int_0^\infty X_i(z) \exp\left(-\frac{z}{\lambda_i \cos\theta}\right) dz \quad (4\text{-}5)$$

where I_i^0 is the intensity for an elemental bulk standard and $X_i(z)$ is the local concentration in mole fraction at depth z. For an element in the film (denoted by f) of thickness d:

$$I_f = \frac{I_f^0}{\lambda_f}\int_0^d X_f(z)\exp(-\frac{z}{\lambda_f \cos\theta})dz = I_f^0 X_f\left[1-\exp\left(-\frac{d}{\lambda_f \cos\theta}\right)\right] \quad (4\text{-}6)$$

For an element in the substrate (denoted by *s*):

$$I_s = \frac{I_s^0}{\lambda_s}\int_d^\infty X_s(z)\exp(-\frac{z}{\lambda_s \cos\theta})dz = I_s^0 X_s \exp\left(-\frac{d}{\lambda_s \cos\theta}\right) \quad (4\text{-}7)$$

By taking ratios:

$$\frac{I_f}{I_s} = K\left[\exp\left(\frac{d}{\lambda_s \cos\theta}\right) - \exp\left(\frac{d\lambda_f - d\lambda_s}{\lambda_s \lambda_f \cos\theta}\right)\right] \quad (4\text{-}8)$$

In Equation (4-8), $K=(I_f^0/I_s^0)(X_f/X_s)$ and could be calculated from either the atomic sensitivity factor of the film and substrate elements or could be experimentally determined from the bulk standards. The author further simplified the analysis by assuming: $\lambda_f \approx \lambda_s = \lambda$, so that:

$$\ln\left(\frac{I_f}{I_s}\frac{1}{K}+1\right) = \frac{d}{\lambda}\sec\theta \quad (4\text{-}9)$$

In Ref. 113, the method was demonstrated for polystyrene and polymethylmethacrylate films cast from chloroform solution by using the C 1s peak of the film and the Si 2s peak of the mica substrate. Literature values are use for *K* and λ.

Paynter studied the case in which the substrate material (S) was covered with a partial layer (L) (cover fraction *f*) of uniform thickness *t* and expressed the reduced intensity as:

$$\frac{I}{\phi T A \sigma \cos\theta} = f\left\{c_L\lambda_L[1-e^{-t/(\lambda_L\cos\theta)}]+c_S\lambda_S e^{-t/(\lambda_L\cos\theta)}\right\}+(1-f)c_S\lambda_S \quad (4\text{-}10)$$

where ϕ is the x-ray flux, T is the transmission/detector efficiency, A is the analysis area, and σ is the photoelectron emission [114]. With the reduced intensity known, f, c_L and t could be found from a least-square approach. λ_s and λ_L were obtained from literature values.

Palacio and Arranz ratiod two intensities, one from an element in the top layer and the other from another element in the substrate. Least square fitting was used to determine the thickness of the top layer or the thickness and cover fraction of the top layer for an island model [115]. Verpoort *et al.* ratiod the intensities from two different chemical states of one element, one (SiO_2) on the top layer and the other (Si) in the substrate, to calculate the thickness of the top layer [116]. There are also several other papers utilizing the same idea, that is, to obtain parameters (thickness of the film, electron attenuation length, etc.) by ratioing photoelectron intensities [117-123]. Different methods might use photoelectrons from different elements or different states of a single element, choose different take-off angles, or use different algorithms (analytically or through regression) to extract parameters from experimental data.

4.1.2. Alternative (simple) depth profile models

Fadley and Baird reviewed the field of ARXPS for surface analysis in 1974 [124].They mainly discussed how experimental factors, such as x-ray refraction and reflection, non-uniform x-ray flux and surface roughness, might influence ARXPS results. However, they discuss only briefly depth profile determination. In 1984, Fadley reviewed this field again, and suggested several possible specimen morphologies [125].

1. Semi-infinite homogeneous specimen, atomically clean surface;

2. Homogeneous specimen of thickness t, atomically clean surface;
3. Semi-infinite homogeneous specimen with uniform overlayer of thickness t;
4. Semi-infinite homogeneous substrate with a uniform, but patched overlayer of thickness t;
5. Semi-infinite homogeneous substrate with a very thin, non-attenuating overlayer;
6. An arbitrary concentration profile $\rho_k(z)$ of a given species in a semi-infinite substrate

For case 6, the author derived an expression for element intensities in a multilayer model in which the solid is divided up into an arbitrary number of layers (N) of equal thickness t. Case 6 will be described in more detail in "multi-layer model" section.

Nefedov considered many different kinds of possible depth composition profiles in the surface layer, including [126]:

1. The element is covered with a foreign film of thickness t;
2. The element is present only in the t thickness surface layer;
3. The concentration of the element decreases or increases linearly from n_0 to n_1 within the surface layer of thickness t and then remains constant;
4. The concentration of the element decreases exponentially;

The parameters were obtained by minimizing $\sum_i (f_{meas}(\theta_i) - f_{calc}(\theta_i))^2$. f was defined as:

$$f(\theta) = \frac{I}{A\sigma\lambda} = \frac{1}{\lambda \sin\theta}\int_0^\infty n(z)\exp(-\frac{z}{\lambda\sin\theta}) \qquad (4\text{-}11)$$

where n(z) is the element concentration at depth z, A the instrument factor and σ the photoionization cross-section.

Fischer *et al.* used a "trapezoidal" profile as follows [127]:

$$c(z)=\begin{cases} c_0 & 0 \le z \le a \\ \dfrac{c_0 - c}{a-b}(z-b)+c & a \le z \le b \\ c & b \le z \le \infty \end{cases} \tag{4-12}$$

The relative intensity r(θ) from elements A and B can be expressed as:

$$r(\theta) = R\frac{e^{-\frac{1}{\lambda_{c,A}\cos\theta}}\int_0^\infty c_A(z)\rho(z)e^{-\frac{1}{\lambda_A\cos\theta}}dz}{e^{-\frac{1}{\lambda_{c,B}\cos\theta}}\int_0^\infty c_B(z)\rho(z)e^{-\frac{1}{\lambda_B\cos\theta}}dz} \tag{4-13}$$

where $c(z)$ and $\rho(z)$ are concentration in weight fraction and mass densities, respectively. The parameters a, b and c_0 were found by minimizing $\sum_i (r_{meas}(\theta_i) - r_{calc}(\theta_i; a, b, c_0))^2$.

Grabherr *et al.* modeled the concentration depth profile $c_i(z)$ of element i as a polynomial of third order within the range $0 \le z \le z_m$ where z was the depth measured from the surface [128]. The further constraints $c_i(z_m)=b_i$, where b_i was the bulk concentration of the element i and $dc_i(z)/dz=0$ for $z=z_m$ reduced the number of unknown parameters to two per element. The differential quantity dN_i of photoelectrons emitted from the element i at depth z was described by:

$$dN_i = kA\frac{\Omega}{4\pi}\sigma_i S_i e_i L_i \frac{dz}{\cos\alpha}c_i(z)\exp(\frac{-z}{\lambda_i\cos\theta})\exp(\frac{-d}{\lambda_{i,c}\cos\theta}) \tag{4-14}$$

where k is a proportionality factor, A the effective flux of incident x-ray radiation, Ω the solid angle of photoelectronic detection, σ the photoabsorption cross-section, S_i the spectrometer transmission, e_i the detector efficiency, $\lambda_{i,c}$ the attenuation length in the

contamination layer, d the thickness of the contamination layer, α the incident angle of x-ray radiation, $L_i = 1 - \beta_i(3\cos^2\vartheta - 1)/4$ where β is the asymmetry parameter and ϑ the angle between the directions of the incident x-rays and the take-off of the photoelectrons. The equation was simplified to:

$$dN_i = \text{constant}\,\sigma_i \frac{1}{y} c_i(z) \exp(\frac{-z}{y}) dz \qquad y = \lambda\cos\theta \tag{4-15}$$

by assuming that all the λ's are equal. Equation (4-15) could be further simplified and integrated over the depth range:

$$N_i(y) = \text{constant}\,\sigma_i f(y) \tag{4-16}$$

where $f(y)$ is the integral resulting from the polynomial depth profile. The parameters were obtained by minimizing

$$\sum_{p=1}^{z}\left[\frac{N_{i,meas}(y_p)/\sigma_i}{\sum_{i=1}^{n} N_{i,meas}(y_p)/\sigma_i} - f_{i,calc}(y_p)\right]^2 \tag{4-17}$$

An Al-Li alloy was used to test the model.

Siuda approximated the concentration profile $n(z)$ with a polynomial with the degree lower than the number of take-off angles at which intenisties were measured [129]. The intensity was written as:

$$I(\theta_i) = C\int_0^\infty n(z)\exp(-\frac{z}{\lambda\cos\theta})dz \tag{4-18}$$

where C is a proportionality factor. Subsequently, $h_i=I(\theta_i)/C$, $p_i(z)=\exp(-z/\lambda\cos\theta)$ and $l_i=\lambda\cos\theta_i$, and $n(z)$ was approximated with a polynomial of degree q.

$$n(z) \cong a_0 + a_1 z + a_2 z^2 + \cdots + a_q z^q \tag{4-19}$$

So that after integration:

$$h_i = l_i a_0 + l_i^2 a_1 + \cdots + q! l_i^q a_q \tag{4-20}$$

The full set of equations was then written in a matrix form

$$\mathbf{h}=\mathbf{Pn} \tag{4-21}$$

Here $\mathbf{h}=[h_1, h_2, \ldots, h_m]$ was composed of normalized intensities, and $\mathbf{P}$ was defined by:

$$\mathbf{P} = \begin{bmatrix} l_1 & l_1^2 & l_1^3 & \ldots & l_1^q \\ l_2 & l_2^2 & l_2^3 & \ldots & l_2^q \\ \ldots & \ldots & \ldots & \ldots & \ldots \\ l_m & l_m^2 & l_m^3 & \ldots & l_m^q \end{bmatrix}$$

and $\mathbf{n}=[a_0, a_1, 2a_2, \ldots, q!a_q]$. $\mathbf{n}$ was solved by using a singular value decomposition method. This article only considered one element and no consideration was given to actual data analysis. The method was sensitive to the error in the raw data and it could only gave satisfactory results when the inaccuracy in the ARXPS intensities did not exceed 0.3%.

Ebel *et al.* compared ARXPS and XPS with ion sputtering to quantify depth profiles in Al-Li alloy [130]. In ARXPS data analysis, the authors assumed that the attenuation lengths for Li and Al are the same. Five kinds of depth profiles were used to fit the data:

1. Exponential depth profile:

$$c(z) = c_{bulk} + \Delta c \cdot e^{-kz} \tag{4-22}$$

2. Gaussian depth profile:

$$c(z) = c_{bulk} + \Delta c \cdot e^{-kz^2} \tag{4-23}$$

3. Linear depth profile:

$$c(z) = c_{bulk} + (D - z)\frac{\Delta c}{D} \quad \text{for } z < D\,; c(z) = c_{bulk} \quad \text{for } z \geq D \tag{4-24}$$

4. Rectangular depth profile:

$$c(z) = c_{bulk} + \Delta c \quad \text{for } z < D\,; c(z) = c_{bulk} \quad \text{for } z \geq D \tag{4-25}$$

5. Shifted Gaussian depth profile:

$$c(z) = c_{bulk} + \Delta c \cdot e^{-k(z+\delta)^2} \tag{4-26}$$

Intensities calculated from the depth profiles of two components (Al and Li) were ratiod and and the ratio (r) was used to designate the ratio. The parameters (Δc, k, D, δ) were obatined by minimizing $\Sigma(r_{meas}\text{-}r_{calc})^2$. In the calculation, atomic density and attenuation length were obtained from literature values.

Perruchot *et al.* used software (ARCtick 1.0) to reconstruct the depth profile of chemical species specified as the concentration at three depths with a regularization algorithm [131]. No details were provided about the algorithm. The model was a three piece-wise profile, which was discussed in Cumpson's 1995 review [164].

4.1.3. Diffusion models

Asami *et al.* determined diffusion coefficients (D) and mobilities of cations (μ) in passive films formed by anodization of amorphous Al-Cr-Mo and Al-Ti-Mg alloys by using ARXPS in combination with the generalized Fick's law [132]. However, there was no detailed discussion regarding how to extract depth profiles from the experimental data.

The depth profile (C) of a charged species i was derived based upon generalized Fick's law to yield:

$$C_i = J_i/(\mu_i E) + k_i \exp[\mu_i E(t-z)/D_i] \quad (4\text{-}27)$$

where J was the flow flux, E the electric field strength, t the passive film thickness and k the proportionality constant. In the calculation, the photoionization cross-sections were obtained from literature values. The mean free path of an electron with a specific kinetic energy was assumed to follow a universal curve expressed by $0.596\times(KE)^{0.5}$ where KE was the electron kinetic energy. The detailed data analysis method was described in other articles by Akiyama *et al* [133,134]. Simply it was assumed that :

$$a = k_i$$

$$b = \mu_i E / D_i \quad (4\text{-}28)$$

$$c = J_i/(\mu_i E)$$

As a result,

$$C_i = a\exp[b(t-x)] + c \quad (4\text{-}29)$$

C_i is Laplace transformed to obtain the intensity. The intensity contains three unknowns: a, b, and c. b was estimated separately based on the Einstein relation which relates the mobobility μ_i and diffusion coefficient D_I [133] Then a and c were obtained from a least square method. The values of attenuation length and thickness of the top contamination layer were obtained from literature values.

In Popovici *et al.*'s article, the experimental intensities (I_{meas}) were related to the take-off angle by:

$$\frac{I_{meas}(\theta)}{I_0} = \frac{1}{\lambda_{eff}} \int_0^\infty c(z) \exp(-z / \lambda_{eff}) dz \tag{4-30}$$

where $I_{meas}=I_0$ for $c(z)=1$. $\lambda_{eff}=\lambda_0 \sin\theta$ and λ_0=IMFP (inelastic mean free path) [135]. Also, the author used Fick's diffusion law to model the depth profile and the following formulae is the solution to the partial differential equation (limited source diffusion model):

$$c(z,t) = K\left[\exp(-(z-z_0)^2 / 4Dt) + \exp(-(z+z_0)^2 / 4Dt)\right] / \sqrt{Dt} \tag{4-31}$$

where D is the diffusivity and K is the proportionality factor. The author claimed that no analytical form for the Laplace transform of this solution should exist* and used a more tractable formula to approximate the profile:

$$c(z) = K'\left[\exp(-(z / P_1)^2)\right] \times \exp(P_2 z) \tag{4-32}$$

The Laplace transform of Equation (4-32) was used to fit the experimental data. For another more abundant species, the author used the expression

$$c(z) = K'' \exp(-(P_2 z / P_1) \tag{4-33}$$

to approximate the concentration profile. The diffusion constant D was finally determined from the slope $-1/4Dt$ of the lnc vs z^2 plot. This method was used to compare metal diffusion in copper/Teflon AF1600 and Al/Kapton systems.

* It should be noted that this claim is erroneous because the orignal solution does have an analytical form of the Laplace transform.

4.1.4. Multilayer models

"Multi-steps"

Fadley appproximated the intensity (N_k)from an arbitrary concentration profile $\rho_k(z)$ by a simple summation over atomic layers with spacing d at depths of $z_n=nd$ (n=1, 2,…,∞):

$$N_k(\theta) = I_0\Omega_0(E_k)A_0(E_k)D_0(E_k)\lambda_e(E_k) \times \frac{d\sigma_k}{d\Omega}\sum_{n=1}^{\infty}\rho_k(z_n)\exp(-\frac{z_n}{\lambda_e(E_k)\sin\theta}) \quad (4\text{-}34)$$

if the mean free path $\Lambda_e(E_k)$ can be assumed to be constant with depth z and thus independent of the composition change associated with $\rho_k(z)$ [125]. In equation (4-34), I_0 is the incident x-ray flux, Ω_0 is the effective solid angle, A_0 is the effective specimem area, D_0 is the dection efficiency, $d\sigma_k/d\Omega$ is the differential photoionization cross section, and E_k is the photoelectron energy. The results will be more complex if λ_e depends on z also as $\lambda_e(E_k, z)$:

$$N_k(\theta) = I_0\Omega_0(E_k)A_0(E_k)D_0(E_k)\lambda_e(E_k)\frac{d\sigma_k}{d\Omega} \times \sum_{n=1}^{\infty}\left\{\rho_k(z_n)\left[1-\exp(-\frac{d}{\lambda_e(E_k,z_n)\sin\theta})\right]\prod_{m=1}^{n-1,n>2}\exp(-\frac{d}{\lambda_e(E_k,z_n)\sin\theta}\right\} \quad (4\text{-}35)$$

In Pijolat and Hoolinger's model, the maximum sampling depth of the sample was divided into n equal and parallel layers where the current $I_A(\theta)$ of photoelectrons excited from the atoms A, measured in the direction of θ could be expressed as the sum of the intensities due to each layer modulated by the attenuation in the upper layers [136]. The mathematical expression used was:

$$I_A(\theta) = \sigma_A k(\theta) \sum_{j=1}^{M} \left\{ N_A(j) \left[1 - \exp(-\frac{x_0}{\lambda(j)\sin\theta}) \right] \times \prod_{k=1, j>1}^{j-1} \exp(-\frac{x_0}{\lambda(k)\sin\theta} \right\} \qquad (4\text{-}36)$$

where $N_A(j)$ is the atomic density in jth layer and x_0 is the thickness of each layer. σ_A is the photoelectron cross-section for the subshell considered, corrected by the asymmetry factor, and $k(\theta)$ is an instrumental factor depending on the x-ray flux and the sample-analyser geometry. To minimize experimental uncertainties, the relative intensities were used in place of absolute intensities and the $N_A(j)$'s were obtained by minimizing the function:

$$F = \sum_i [I_A(\theta)/I_B(\theta)|_{meas} - I_A(\theta)/I_B(\theta)|_{calc}]^2 \qquad (4\text{-}37)$$

Also, to reduce the number of parameters, a relation between N_A and N_B is assumed. Calculated value for the inelastic mean free path λ was used and the photoionization cross-section σ was estimated from tabulated values. $k(\theta)$ was estimated by measuring the angular dependent behavior of a homogeneous sample. In order to test the method, the concentration profiles of Ag-Al_2O_3 and SiO_2-Si interfaces and of the surface region of a Cu-Ni alloy were obtained.

Hazell *et al.* used the same multilayer model and intensity expression as did Fadley [137]. In their development, they used the sensitivity factor (*SF*) to replace the proportionality term.

$$I_A(\theta)/SF_A = \sum_{j=1}^{M} \left\{ N_A(j) \left[1 - \exp(-\frac{x_0}{\lambda(j)\sin\theta}) \right] \times \prod_{k=1, j>1}^{j-1} \exp(-\frac{x_0}{\lambda(k)\sin\theta} \right\} \qquad (4\text{-}38)$$

The apparent atomic composition C was expressed as:

$$C_A = (I_A / SF_A) / \sum_{x=1}^{n} I_x / SF_x \tag{4-39}$$

The parameters were found by minimizing

$$F = \sum_i [C_{A,meas} - C_{A,calc}]^2 \tag{4-40}$$

Cherkashinin used a regularization method in the numerical procedure [138] .He started with the form:

$$I_k(\theta) = AT_k C(\theta)\sigma_k(\beta)\lambda_k n_k \times \sum_{j=1}^{M} \left\{ N_j^k \left[1 - \exp(-\frac{x_0}{\lambda_j^k \sin\theta}) \right] \times \prod_{i=1, j>1}^{j-1} \exp(-\frac{x_0}{\lambda_i^k \sin\theta} \right\} \tag{4-41}$$

where A is a constant including the x-ray intensity and the surface area irradiated, $T_kC(\theta)$ is an instrument factor which depends on the photoelectron kinetic energy and the take-off angle, $\sigma_k(\beta)$ is the photoionization cross section and β is the asymmetry parameter. N_j^k was defined as an "effective" concentration in each layer j:

$$N_j^k = \lambda_j^k n_j^k / \lambda_k n_k \tag{4-42}$$

where λ_k and n_k are IMFP and atomic density for pure element k, respectively. By summing over all elements present in the sample:

$$\sum_k I_k(\theta) \frac{1}{T_k \sigma_k(\beta)\lambda_k n_k} = AC(\theta) \tag{4-43}$$

The following equation was obtained:

$$I_k(\theta)R(\theta, E) = \sum_{j=1}^{M} \left\{ N_j^k \left[1 - \exp(-\frac{x_0}{\lambda_j^k \sin\theta}) \right] \times \prod_{i=1, j>1}^{j-1} \exp(-\frac{x_0}{\lambda_i^k \sin\theta} \right\} \tag{4-44}$$

where $R(\theta,E)=\left|T_k\sigma_k(\beta)\lambda_k n_k\sum_\mu \frac{I_\mu(\theta)}{T_\mu\sigma_\mu(\beta)\lambda_\mu n_\mu}\right|^{-1}$ is the normalization coefficient depending on both the kinteic energy and the take-off angle of the photoelectrons. Normalization is carried out on the total intensity from every element.

The regularization algorithm works by minimizing the function:

$$\left\| I_{ex}(\theta)R_{ex}(\theta,E)-\sum_{j=1}^{M}\left\{N_j^k\left[1-\exp(-\frac{x_0}{\lambda(j)\sin\theta})\right]\times\prod_{k=1}^{j-1}\exp(-\frac{x_0}{\lambda(k)\sin\theta}\right\}\right\|^2 + \alpha\sum_{j=2}^{M}\left\|N_i^k-N_{j-1}^k\right\|^2 \qquad (4\text{-}45)$$

where α is the smoothing factor or the regularization parameter. For experimental data, T_k was defined as $T_k=E_k^{-0.7}$ where E_k is the photoelectron kinetic energy; σ_k and β were taken from literature values. λ for a pure materials took literature values and its value in a compound was calculated using a mixing rule. This numerical technique was tested on experimental data from two catalytic systems: C_2H_4/Pt(110) and CO/Ir(111). In fact, this method was the same as the one described in a 1991 article by Borodyansky and Abashkin [139]. Cherkashinin extended this approach to the situation in which the attenuation lengths are different for different species and proposed a method to find an optimal regularization constant.

Nefedov and Baschenko offered a detailed mathematical derivation for the relative intensities of two components in a binary system [140]. They divided the sample into a number of layers (M) and assumed that $I(\theta)$ could be expressed as the sum of the intensities from each layer modulated by the attenuation in the upper layers (each with

the same thickness d). The expression for $I(\theta)$ was very similar to those proposed in previous articles, with only minor differences in treating the Mth layer.

$$I_A(\theta) = K\sigma_A\lambda_A\left\{\sum_{j=1}^{M-1} N_A(j)\exp\left(\frac{-(j-1)d}{\lambda_A\cos\theta}\right)\left[1-\exp\left(\frac{-d}{\lambda_A\cos\theta}\right)\right] + N_A(M)\exp\left(\frac{-(M-1)d}{\lambda_A\cos\theta}\right)\right\} \quad (4\text{-}46)$$

where K is the instrument factor, σ_A is the photoionization cross-section, and N is the atomic concentration. As a result, determination of the concentration profile for the two-component sample from ARXPS data was reduced to the solution of a system of linear equations. Such a system could be solved by using the Gaussian elimination method with partial choice of the lead element. The results were extremely sensitive to errors in the raw data; thus physical limitations were put on the profile. Such limitations could be realized by performing certain mathematical manipulations on the linear systems and constraint conditions. Subsequently, the linear system was solved numerically. The difference between the two species was taken into account by an iteration process. The method was tested on ion-etched GaAs and a system comprising a Ag film on Al_2O_3.

Baschenko and Nefedov extended the method to a four-component system without essential changes to the algorithm [141]. Later Baschenko considered the case in which the attenuation length was dependent on composition. The algorithm was kept linear by introducing a new variable $N(j)=n(j)\sigma\lambda(j)$ so that all the methods invoked to solve the linear system could still be used [142].

Bussling and Holloway studied the deconvolution of concentration depth profiles for a binary system [143]. They approximated the detailed profiles as the sums of a

homogeneous bulk composition and a finite number of step depletions/accretions for a specific element.

$$C(x) = C_0 + \sum_{i=1}^{n} \Delta C_i U(i) \tag{4-47}$$

where $U(i)=U(z_{i-1}, z_i)$ is a unit step function in the interval (z_{i-1}, z_i). The parameters were obtained by minimizing the difference between the experimental relative intensities $R^*(\theta)$ [$R^*(\theta)=I(\theta)/ I_{total}$] and those calculated from the model. The sole constraint imposed was that the altered composition be confined by the physical limitations, i.e., zero to one. The expression for $R^*(\theta)$ for the proposed model is:

$$R^*(\theta) = p\pounds[C(z)] = C_0 + \sum_{i=1}^{n} \Delta C_i [\exp(-pz_{i-1}) - \exp(-pz_i)] \tag{4-48}$$

where $p=1/\lambda \sin\theta$. One of the most important assumptions here is that the inelastic mean free paths for the photoelectrons of the two species studied are equal. The same method was used in a 1988 article by Bussing *et al*. [144], a 1990 article by Flinn and McIntyre [145], and a 1992 article by Holloway and Bussing [146]. Althought the depth profile model is the same as previous ones, the resulting expression for intenisty is different. This result is due to the difference in the assumptions used in determining the Laplace transform.

Smith and Livesey first introduced the Maximum Entropy Method in ARXPS data analysis [147]. They started with the multilayer model in which the solid was divided into an arbitrary number of layers (N) of equal thickness t. The intensity of element j was given by:

$$I_j(\theta) = k_j \sum_{i=0}^{N} n_{j,i} \exp(-it/\lambda_j \cos\theta) \tag{4-49}$$

where $n_{j,i}$ is the atomic fraction composition of element j in the ith layer and k_j is the proportionality constant. The following parameters can then be defined:

$$C = \sum_k \frac{(I_k^{calc} - I_k^{meas})^2}{\sigma_k^2} \tag{4-50}$$

$$S = \sum_j \sum_i n_{j,i} - m_{j,i} - n_{j,i} \log(n_{j,i} / m_{j,i}) \tag{4-51}$$

where S is the entropy of the system and $m_{j,i}$ is the initial guess for $n_{j,i}$. Traditional methods only minimize C to obtain the parameters while the maximum entropy method minimizes:

$$Q = \alpha S - C/2 \tag{4-52}$$

where α is a Lagrange multiplier (also called a regularization constant). The same idea was examined in more detail in a 1994 paper by Livesey and Smith [148]. The advantages and disadvantages of this method have been reviewed by Cumpson in 1995 [164].

"Multi-ramps"

Jisl also studied a binary system and divided the surface region of the sample into flat layers parallel to the surface with equal thickness and used linear interpolation in these layers [149]. The author made some improvement to the algorithm by including the a priori information into the equation through a matrix transforming procedure and by solving the linear equation system with a regularization algorithm.

In Payton's 2002 article, the depth profile was described as one with a series of *j* inflection points [150].Variation with the photoemission angle of the intensity of a specific photoelectron peak is:

$$I(\theta) \propto c_1 \lambda \cos\theta + \sum_{i=1}^{j-1} \lambda^2 \cos^2\theta \frac{c_{i+1} - c_i}{z_{i+1} - z_i} \times (e^{\frac{-z_i}{\lambda \cos\theta}} - e^{\frac{-z_{i+1}}{\lambda \cos\theta}}) \quad (4\text{-}53)$$

where c_i is the concentration at the *i*th inflection point at depth z_i. The author claimed that the complexity of the profile that could be extracted was limited by the number of degrees of freedom, which was three for ARXPS. The values for the attenuation length used in the calculations were 3.4 nm for O 1s photoelectrons and 4.0 nm for C 1s photoelectrons. A nonlinear least-square optimization routine was used to vary the parameters in the model in order to minimize the sum of the squared differences between the results of the calculation and the experimental observations. The model was used to characterize the depth profile of oxygen in a polystyrene surface treated with a plasma.

Williams *et al.* proposed a novel simplex algorithm [151]. The author assumed polygonal profiles to a multielement analysis (this is the same as Paynter's model [150] and Jisl's model [149]) with the following constraints:

$$c_i(z) = c_i(M) \quad \text{for } z > (M-1)d \quad (4\text{-}54)$$

$$\sum_{i=1}^{n} v_i c_i(j) = \sum_{i=1}^{n} C_i(j) = 1 \quad \text{for } 1 \le j \le M \quad (4\text{-}55)$$

where v_i is the molar volume of element *i* and $C_i(j)=v_i c_i(j)$ is the elemental volume fraction. Williams *et al.* showed that the ratios of line intensities $R_i(\theta_k)=I_i(\theta_k)/I_n(\theta_k)$ should obey a matrix equation:

r=Qc (4-56)

The required constraints are that concentrations should always be positive and the sum of concentrations of elements of interest should be less than 1. The author used a least-square modified sequential simplex method to solve the equation by increasing the calculated residues if the constraints are violated. Several input parameters for each element are required for computation: the molar volume, the binding energy and the photoelectron cross section. The author claimed high depth resolution and robustness to experimental error. But one drawback with this method is that a substrate signal is required to provide a standard for the ratios.

In Iwasaki *et al.*'s article, the intensity was normalized such that [152]:

$$\begin{aligned} \bar{I}_A(\theta) &= \int_0^\infty \bar{N}_A(z')\exp(-sz')dz' \\ &= \int_0^{Z_B} \bar{N}_A(z')\exp(-sz')dz' + \int_{Z_B}^\infty C_A \exp(-sz')dz' \end{aligned} \quad (4\text{-}57)$$

where s=1/sinθ and z was scaled so that $z'=\lambda z$. Z_B represents a point sufficiently far from the surface that the bulk concentration C_A was reached. The second integral could be easily obtained provided that C_A and Z_B are known. The first integral was treated numerically using what is essentially a simple trapezoidal rule numerical integration technique. (This is equivalent to a piece-wise depth profile model.) The number of trapezoids was equal to the number of take-off angles (θ) for which XPS intensity data were collected. A system of linear equations resulted. In order to correct for instrumental factors encountered in intensity normalization, the intensity ratio $\bar{I}_{AB}(s) = \bar{I}_A(s)/\bar{I}_B(s)$ of two photoelectron peaks with similar kinetic energies was used and a relative depth

profile was obtained. Since the solutions to the linear equation set were quite unstable, the authors employed a constrained minimization of the function:

$$F[\overline{N}_A(z_i), \overline{N}_B(z_i)] = \sum_{j=1}^{n} \left[I_{AB}(s_j)_{meas} - I_{AB}(s_j)_{calc} \right]^2 I_{AB}(s_j)_{meas} \tag{4-58}$$

with constraints such as positive concentration and that the concentration of binary mixture should not exceed certain boundary values.

"Steps-ramps"

Paynter proposed a depth profile model with j steps, which can be viewed as a special case of the "multi-ramp" model [153]:

$$n(z) = \begin{cases} n_N & \text{for } z_{2N\text{-}2} \le z \le z_{2N-1} \\ n_N + (z - z_{2N-1}) \dfrac{n_{N+1} - n_N}{z_{2N} - z_{2N-1}} & \text{for } z_{2N\text{-}1} \le z \le z_{2N} \end{cases} \tag{4-59}$$

where N=1,…,j.

So that the intensity can be expressed as

$$I_A(\theta) = KF\lambda \sin\theta \times \left\{ n_1 + \sum_{N=1}^{j} \lambda \sin\theta \frac{n_{N+1} - n_N}{z_{2N} - z_{2N-1}} \times \left[\exp\left(\frac{-z_{2N-1}}{\lambda \sin\theta}\right) - \exp\left(\frac{-z_{2N}}{\lambda \sin\theta}\right) \right] \right\} \tag{4-60}$$

where F is the transmission function and K includes such factors as capture cross-section and emission efficiency. The author applied this method to a binary system and eliminated K by ratioing the intensities from the two components in the system.

4.1.5. Irregular depth profile models

Tyler *et al.* used a regularization method with non-negative contraints to generate depth profiles from ARXPS data [154].The normalized signal intenisty can be expressed as:

$$F_j(\theta) = F_j^*(\theta)\frac{\sin\phi}{\sigma_j \Psi \lambda_j} = \frac{A}{\lambda_j}\int_0^\infty n_j(z)\exp(\frac{-z}{\lambda_j \cos\theta})dz \qquad (4\text{-}61)$$

where $F_j^*(\theta)$ is the absolute signal intensity, ϕ the x-ray incident angle, σ_j the photoelectron cross-section, Ψ transmission function of the detector and A a constant including the efficiency of the detector, the sample area irradiated and the x-ray flux.

If a new term $\eta_j(z)$ is defined by:

$$\eta_j(z) = \frac{A}{\lambda_j} n_j(z) \qquad (4\text{-}62)$$

then

$$F_j(\theta) = \int_0^\infty \eta_j(z)\exp(\frac{-z}{\lambda_j \cos\theta})dz \qquad (4\text{-}63)$$

Traditional methods find the parameters by minimizing:

$$\varphi(\eta) = \left\| \int_0^\infty \eta(z)K(z,\theta)dz - F(\theta) \right\|^2 \qquad K(z,\theta) = \exp(\frac{-z}{\lambda \cos\theta}) \qquad (4\text{-}64)$$

While in the Tyler article, the target function is:

$$\varphi(\eta) = \left\| \int_0^\infty \eta(z)K(z,\theta)dz - F(\theta) \right\|^2 + \alpha \left\| \eta(z) \right\|^2 \qquad (4\text{-}65)$$

The additional term regularizes (or smooths) the solution and the constant α is called a smoothing parameter.

The minimum of φ is reached when the directional derivative is 0:

$$\nabla\varphi = \left[K(z,\theta)\int_0^\infty \eta(z)K(z,\theta)dz - F \right] + \alpha\eta(z) = 0 \tag{4-66}$$

If we express η as a linear combination of the kernal functions

$$\eta(z) = \max\left[0, \sum_{i=1}^{n} c_i K(z,\theta_i) \right] \tag{4-67}$$

then the equation can be transformed into matrix form:

$$(M + \alpha I)c = F \tag{4-68}$$

where

$$M_{ij} \cong \int_D K(z,\theta_i)K(z,\theta_j)dz \tag{4-69}$$

where D = all z such that $\eta \geq 0$

The solution was obtained by iteration. The process was repeated until:

$$\frac{\left\|(M + \alpha I)c - F\right\|}{\left\|F\right\|} \leq \varepsilon \tag{4-70}$$

The author also suggested a method to select an optimal α value.

Ro used a generalized solution based on the singular system approach for the characterization of ARXPS data to provide the depth profile function, $f(x)$, which minimize the function $\varphi(f(x))$ in the following equation [155]:

$$\varphi[f\{z\}] = \left\| \int_0^\infty f(z)\exp(-zp_n)dz - F(p_n) \right\|^2 \tag{4-71}$$

The measured intensity F of the photoelectron flux at the take off angle θ_n is given by

$$F'(\theta_n) = K\int_0^{\infty} f(z')\exp(\frac{-z'}{\lambda\sin(\theta_n)})dz' \tag{4-72}$$

where K is a normalization parameter. With $z=z'/\lambda$ and $p_n=1/\sin(\theta_n)$, the normalized intensity of photoelectron flux is:

$$F(p_n) = \int_0^{\infty} f(z)\exp(-zp_n)dz \tag{4-73}$$

The singular system of the Laplace transform is defined by α_k, $u_k(x)$ and v_k, where α_k is the kth singular value, $u_k(x)$ is the kth singular function and v_k is the kth singular factor. Using the singular system approach, the generalized solution, $f_g(x)$ is given by:

$$f_g(x) = \sum_{k=1}^{N'}\frac{1}{\alpha_k}\left[\sum_{n=1}^{N} w_n F(p_n)v_k(n)\right]u_k(x) \tag{4-74}$$

where N is the number of data points, N' is the number of linearly independent singular functions and w_n is the weight. The singular functions are represented as the linear combination of exponentially decreasing $\exp(-xp_n)$ functions:

$$u_k(x) = \frac{1}{\alpha_k}\left[\sum_{n=1}^{N} w_n v_k(n)\exp(-p_n x)\right] \tag{4-75}$$

The author studied the influences of several factors on the extraction of depth profiles from ARXPS data. Results indicated that the equiangular sampling scheme was more susceptible to the ill-posedness in the inverse operation of the Laplace transform and should be avoided. Random error in the data and the type of depth profiles were the most important parameters limiting the inversion of ARXPS data. This article only considered one element and worked with simulated data. No attempt was made to treat actual data.

Yih and Ratner proposed "Model B" based on ideas from inverse theory [156], and compared the results with a model (Model A) by Paynter (1981) [153]. The inverse problem was to find $m(x)$ from e for the following relation

$$e = \int m(x) f(x) dx \tag{4-76}$$

However,

$$m(x_0) = \int m(x) \delta(x - x_0) dx \tag{4-77}$$

where $\delta(x\text{-}x_0)$ is the Dirac delta function.

Suppose that the delta function can be approximated by following linear combination:

$$\delta(x - x_0) \cong \sum C_i f_i(x) \tag{4-78}$$

Then

$$m(x_0) = \int m(x) \sum C_i f_i(x) dx = \sum C_i \int m(x) f_i(x) dx = \sum C_i e_i \tag{4-79}$$

The key is to then find suitable C_i values.

For XPS, the normalized intenisty can be expressed as:

$$I(\theta) = K \int_0^\infty n(z) \exp(\frac{-z}{\lambda \cos\theta}) dz \tag{4-80}$$

Comparing with the above general theory,

$$m(z) = Kn(z) \tag{4-81}$$

$$f(z) = \exp(\frac{-z}{\lambda \cos\theta}) \tag{4-82}$$

and

$$Kn(z_0) = \sum_{i}^{A} C_i I(\theta_i) \tag{4-83}$$

Based on theories to approximate delta functions by a linear combination of functions, C_i can be calculated from a set of linear equations generated from z_0, $f(z)$ and experimental I values. Once the C_i's are obtained, $n_i(z_0)$ can be easily calculated and the depth profile can be obtained by calculating n_i at different z_0's.

As the authors indicated, the problem with Model B is that it is dependent on the number of take-off angles measured and on the choice of take-off angles. The greater the number of take-off angles measured, the better the delta function approximation. But when the number of take-off angles increases, it will not only increase the number of normal equations to be solved, it may also cause the determinant of the normal equation matrix to be near zero. Thus, either the entire equation set may be unsolvable, or a set of meaningless coefficient constants may be generated. Also, the model is very sensitive to the absolute value of spectral intensity. Small errors in the experimental data could result in a large variation in the depth profile. The authors suggested combination of Model B with the model put forward by Paynter in 1981 [153]. In addition, they believed that exact and unique construction of the actual depth profile from experimental data was extremely difficult because of the mathematical restrictions and physical assumptions inherent in each model. McCaslin and Young's method involves a basic numerical approach to the Laplace transform [157]. A transformation of variables yields the definite integral

$$\bar{I}_A(\theta) = I_A(\theta)/[\lambda K_A(\theta)] = \int_0^\infty \overline{N}_A(z)\exp(-sz)dz = \int_0^1 \overline{N}_A(-\ln z)z^{s-1}dz \tag{4-84}$$

where $K_A(\theta)$ takes into account of all the instrumental factors and $s=1/\sin\theta$.

This integral is subjected to a Gaussian quadrature approximation, so that

$$\bar{I}_A(s) = \sum_{i=1}^{n} w_i z_i^{s-1} \overline{N}_A(-\log z_i) \tag{4-85}$$

where the w_i and z_i are the tabulated values of the weights and roots for the shifted Legendre polynomial of degree n. A system of n linear equations may be obtained by letting s take on n different values, giving

$$\bar{I}_A(s) = \sum_{i=1}^{n} w_i z_i^{s-1} \overline{N}_A(-\log z_i) \tag{4-86}$$

A conventional matrix inversion technique (LU decomposition) was used to solve for the concentration values $N_A(-\log z_i)$. Because the linear system was not stable, the author also introduced a method to stabilize the solution.

4.1.6. Review articles

Seelmann-Eggebert and Richter discussed the limitations of ARXPS with regard to depth profiling of multicomponent (with different phases) systems [158]. They did not describe in detail the algorithms to recover the depth profile. Their emphasis was that the composition and the distribution of the phases constituting a sample could not be independently obtained by any approach of depth profiling which was based on the analysis of components only. The same experimental data could yield a set of possible phase combinations and corresponding depth profiles. In a later paper, Seelmann and Keller further studied how much information could be obtained from ARXPS [159]. With an assumed experimental error of 1%, the class of all possible ARXPS signal functions

was shown to be contained in a subspace spanned by just five basis functions. Therefore, the information obtainable for each single ARXPS signal is confined to a maximum of five parameters. Almost all ARXPS signals of a single component (except for a few very special cases) could be interpreted in terms of a depth profile consisting of just three zones with constant composition and with two optimized interface positions.

Tielsch and Fulghum compared two algorithms [160], one by Bussing and Holloway in 1985 [143] and the other by Tyler *et al.* in 1989 [154]. The results showed that the Bussing and Holloway method could reproduce sharp interfaces between the substrate and the overlayer while the Tyler's regularization method could not. The author did not discussed out the reason. In Cumpson's 1999 article, this topic was revisited and Cumpson pointed out that the regularization method tended to produce smooth profiles [167].

Gries reviewed several methods and pointed out the inherent insufficiency of the angle-resolved data for depth profiling and stated that the causes had not been sufficiently emphasized [161]. The author believed that angle-resolved intensity data alone almost never sufficed for a unique construction of the depth distribution; at least the shape of the depth distribution was required as an additional input quantity. The author proposed a method based on the Gries-Wybenga moment equation, or self-ratio procedure. (The original references are in German and I was not able to find them. So the technical details are not provided here.) The data input consisted of the ratios of a given signal measured at different take-off angles. The author considered two situations: a top layer (the species extends to the surface) and an over-layer situation (the species is completed buried) and each situation was divided into three sub-types: rectangular, rising-ramp and falling-

ramp. The author believed that such division was sufficient for most surface structures within information depth of ARXPS.

Tilinin *et al.* reviewed the literature methods for ARXPS depth profile reconstruction [162]. They started with a more general form to express the photoelectron intensity:

$$Y(\Omega, E) = \int_0^\infty dz c(z) \int_0^\infty dE_0 \int_{4\pi} d\Omega_0 S(E_0, \Omega_0) \Phi(z, \Omega, E \mid \Omega_0, E_0) \qquad (4\text{-}87)$$

where $c(z)$ is the concentration depth profile, $S(\Omega, E)$ is the initial angular and energy distribution of signal photoelectrons released in a unit volume of the sample per unit time and $\Phi(z, \Omega, E|\Omega_0, E_0)$ is a usual depth distribution function describing the probability for an electron generated at the depth z with the energy E_0 and moving initially in the direction Ω_0 to escape from the target in the direction Ω with the kinetic energy E. By introducing the probability $p(z,\Omega,E)$ for an electron created at a depth z to escape from a solid with a specific energy and momentum, they could rewrite the above equation in the form of a single integral:

$$Y(\Omega, E) = \int_0^\infty dz c(z) P(z, \Omega, E) \qquad (4\text{-}88)$$

The choice of the function P depends on the model used to describe electron solid interaction. In this article, most of the comments on currently available methods in reconstructing depth profiles were based on Cumpson's (1995) paper [164].

Opila's review focused on the maximum-entropy method [163]. The author pointed out three pitfalls of the method. First, irreproducible photoemission intensities can lead to physically meaningless composition depth profiles. Second, the choice of the value of the

regularization constant has a very strong influence on the results. Third, the maximum entropy method tends to have a built-in preference for sharpness.

Cumpson's 1995 article is probably the most comprehensive and incisive review of methods to reconstruct depth profiles from ARXPS data [164]. The author made an analogy between ARXPS data analysis and signal processing and discussed "information loss." Some formulae were derived in terms of Degree of Freedom and depth resolution. Following is a summary of the major points in this article.

1) Photoelectron intensity

The photoelectron intensity depends on the analysis area, which will change with the take-off angle for most XPS equipment. There are basically two methods of addressing this problem: a) ensure that the instrument is operated so that the analysis area is a constant or correct the area change for all take-off angles; b) cancel the area factor by attempting to calculate the depth profile from peak intensity ratios.

2) Information content.

ARXPS measurement from any specimen can be reproduced, to within experimental uncertainty, by a model depth-profile consisting of three delta-doped layers, chosen to have appropriate concentrations; the essential point is that three numbers are sufficient to completely describe the measurements. This number three is a quantitative measure of the amount of information present in ARXPS measurements. In the literature on inverse problems, this value is known as the generalized Shannon Number [165] or number of

degrees of freedom (NDF) [166]. The NDF will increase if experimental uncertainties are reduced.

Any algorithm with four or more adjustable parameters per element can never hope to produce a meaningful solution from the information in the measurement alone, unless the measured peak intensities have better than 0.29% precision. A fit of any simple parametric model containing only one or two adjustable parameters per element is likely to give more accurate values of those parameters than if they were measured from a depth profile plot obtained from any general inversion algorithm.

3) Accuracy and precision

The author claimed that it is precision, rather than accuracy, that has the most influence on the depth resolution. Systematic uncertainties usually dominate random ones in determining the accuracy of a typical XPS analysis. Since these uncertainties will be common to the set of angle-resolved measurements, the accuracy of the final depth profile will depend on the uncertainties, but no more so than in ordinary "single emission angle" XPS. Notable random uncertainties include the Poisson statistics of electron detection and x-ray source variability. (The variation of x-ray primary beam intensity cannot be completely removed by ratioing one peak intensity against another unless all the peaks of interest are acquired simultaneously.) Modern equipment has made the Poisson error insignificant as compared to other sources of error. 1% uncertainties in individual peak intensities formed a practical limit [164].

4) Comparison of published inversion algorithms

The author believes that if properly implemented, each of the currently available approaches means accepting essentially the same depth resolution. If enough is known about a specimen to use a simple fitting model, it will be the best solution, more accurate than using any other algorithm to calculate a depth profile. In any given application, the method preferred is that in which the extra constraints imposed by the algorithm are most transparent (especially to the reader of the research results). The simplicity and familiarity of the least-square fitting gives an advantage over more complex algorithms when judged by this criterion.

5) Sampling

Given the typical accuracy of XPS peak intensity measurements, there is little advantage in using more that 5 emission angles.

In a later paper, Cumpson discussed what kind of constraints could be applied to the regularization methods [167]. He proposed three side constraints, each of which will ensure a smooth depth profile:

1) Squared concentration: $\int c(z)^2 dz$

2) Squared concentration gradient: $\int [dc(z)/dz]^2 dz$

3) Squared concentration curvature: $\int [d^2 c(z)/dz^2]^2 dz$

A simulation showed that squared concentration minimization was the best constraint to apply when the species is not present in the bulk and squared concentration gradient minimization was the best constraint when dealing with a species known to have constant, non-zero concentration in the bulk.

4.1.7. Other articles and summary

In addition, several articles mentioned the use of ARXPS to study depth profiles. However, none of them described these methods in detail [168-177]. Despite numerous effects reported to extract various depth profiles, only limited attention has been given to extracting depth profiles resulting from an infinite or a limited source diffusion [180]. As mentioned above, Popovici *et al.* studied metal diffusion in polymer materials using ARXPS; in their investigation, the diffusion process was approximated as limited source diffusion governed by Fick's second law of diffusion [135]. However, the authors claimed that no analytical form for the Laplace transform existed and they therefore approximated the depth profile using a more tractable but less exact formula [135]. In the following sections of this chapter, it will be shown that analytical forms for the Laplace transform of the solutions to both limited source diffusion and infinite source diffusion do exist and can be used to extract depth profiles from ARXPS data. An algorithm that allows simultaneous determination of the depth profiles of two or more elements in a multi-element system will also be developed. The correctness of the algorithm will be verified through well-controlled high-temperature diffusion studies. The algorithm will be finally used to extract compositional depth profiles near a chemically modified BPDA-PDA surface.

4.2. Theory

4.2.1. Reconstruction of concentration depth profile from ARXPS data

The intensity of photoelectrons, I_A, of kinetic energy E_A from element A in a sample can be expressed as [178]:

$$I_A = \sigma_A^X(h\nu)D(E_A)\int_{\gamma=0}^{\pi}\int_{\phi=0}^{2\pi}L_A(\gamma)\int_{y=-\infty}^{\infty}\int_{x=-\infty}^{\infty}J_0(x,y,\delta)T(x,y,\gamma,\phi,E_A) \times\int_{z=0}^{\infty}N_A(x,y,z)\exp[-z/\lambda_M(E_A)\cos\theta]dzdxdyd\phi d\gamma \quad (4\text{-}89)$$

where $\sigma_A^X(h\nu)$ is the cross-section for emission of a photoelectron from the relevant inner shell X per atom of A by a photon of energy $h\nu$, $D(E_A)$ is the detection efficiency for each electron transmitted by the electron spectrometer, and the coordinates γ, ϕ, δ, x, y and z are given in Figure 4-2. $L_A(\gamma)$ is the angular asymmetry of the intensity of the photoemission from each atom, $J_0(x,y,\delta)$ is the flux of the x-ray characteristic line per unit area at point (x,y) on the sample, $T(x,y,\gamma,\phi,E_A)$ is the analyzer transmission and $N_A(x,y,z)$ is the atom density of A at (x,y,z), $\lambda_M(E_A)$ is the attenuation length of the characteristic XPS electrons of energy E_A from level X of element A in matrix M, and θ is the angle of emission of the electron from the surface normal (photoemission angle) [106,124,178]. Equation (4-89) is based on the following assumptions [106,124,178]:

1) x-ray reflection on the sample surface and x-ray attenuation within the detection depth of XPS can be neglected;
2) the surface of the specimen is smooth on an atomic scale;
3) the specimen is amorphous or finely polycrystalline within the analysis volume;
4) refraction and scattering of electrons upon leaving the specimen surface is negligible;

5) photoelectron attenuation within the specimen follows an exponential decay along the path length and elastic scattering of photoelectrons can be neglected;

6) photoelectron attenuation length is independent of θ.*

Equation (4-89) involves the integral of the product of the incident x-ray flux density and the spectrometer transmission over the surface coordinates of the sample emitting photoelectrons. The integrals over γ and ϕ account for the entrance solid angle of the spectrometer [178].

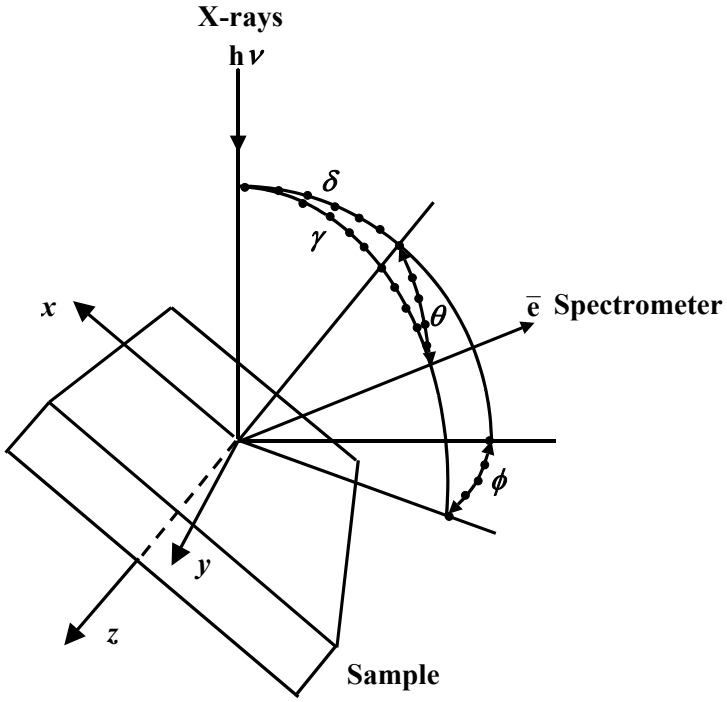

Figure 4-2 Geometry of the XPS analysis configuration, after Seah and Anthony [178]

* This assumption is commonly used for simplification purposes. In general, the electron attenuation length is a function of both photoemission angle and film thickness (or depth). For a detailed discussion, see Reference 179.

If we further assume that [164]:

7) the attenuation length of a photoelectron is independent of the composition of the material through which it passes;
8) the acceptance angle of the electron analyzer – the range of angles over which electrons will be detected – is very small;
9) the specimen composition is uniform in the *xy*-plane;
10) the algorithms used to evaluate the peak intensities can contend with widely varying relative intensities of poorly resolved peaks and widely varying matrix backgrounds without introducing systematic errors,

then the peak intensity I_A corresponding to a specific orbital of element A can be written as:

$$\begin{aligned} I_A &= \sigma_A^X D L_A(\gamma) J_0 T \int_{y=-\infty}^{\infty}\int_{x=-\infty}^{\infty}\int_{z=0}^{\infty} N_A(z)\exp\left[-z/\lambda_M^A\cos\theta\right]dzdydx \\ &= \sigma_A^X D L_A(\gamma) J_0 T A \int_{z=0}^{\infty} N_A(z)\exp\left[-z/\lambda_M^A\cos\theta\right]dz \\ &= (DJ_0T)A\sigma_A^X L_A(\gamma)\lambda_M^A \int_{z=0}^{\infty} N_A(z)\exp\left[-z/\lambda_M^A\cos\theta\right]d(z/\lambda_M^A) \end{aligned} \tag{4-90}$$

where A is the area of analysis on the specimen surface, DJ_0T is the instrument transmission/detection function. I_A can be measured using peak-fitting software, which is now widely available and often gives a direct numerical value for the "peak area" [164].

If in a particular XPS system, γ is a constant, then $L_A(\gamma)$ will not change during the measurement for electrons emitted from a certain orbital; likewise, D and T will also remain constant for electrons emitted from this orbital. Thus, the product ($D\,T\,\sigma_A{}^X L_A \lambda_M{}^A$) is a function of E_A only when the relative position of x-ray source and electron energy analyzer is fixed.

If the area of analysis is wholly defined by the detection area, then $A=A_0\sec\theta$, where A_0 is the analysis area at normal emission. If the XPS system analyzes the entire area of the specimen subjected to the primary x-ray beam, then $A=A_B\sec\delta$, where A_B is the projection area for the primary beam at normal incidence. However, it is also possible that the detection area is neither $A_0\sec\theta$ nor $A_B\sec\delta$, but rather falls somewhere between these two situations [164]. Nevertheless, the detection area will always be a function only of the geometry (θ and δ), provided that the analysis area of the detector and the x-ray beam size do not change during measurement. If J_n is the x-ray flux normal to the incident beam, then the x-ray flux, J_0 is given by $J_n\cos\delta$. In a system where the relative position between electron energy analyzer and the x-ray source is fixed, δ can be uniquely determined when θ is fixed. Thus the product (J_0A) is a function of θ only and will be denoted as $(J_0A)_\theta$ in the following discussion.

If we assume that the species concentrations within the sample are uniform and that N_1, N_2, …, N_n are the atomic densities for element 1, 2, …, n, respectively, then,

$$\begin{aligned} I_1(\theta) &= (DT\sigma^X L\lambda_M)^1 (J_0A)_\theta \int_{z=0}^{\infty} N_1 \exp\left[-z/\lambda_M^1 \cos\theta\right] d(z/\lambda_M^1) \\ &= (DT\sigma^X L\lambda_M)^1 N_1 (J_0A)_\theta \cos\theta \end{aligned} \tag{4-91}$$

Similarly,

$$\begin{aligned} I_2(\theta) &= (DT\sigma^X L\lambda_M)^2 N_2 (J_0A)_\theta \cos\theta \\ &\cdots \\ I_n(\theta) &= (DT\sigma^X L\lambda_M)^n N_n (J_0A)_\theta \cos\theta \end{aligned} \tag{4-92}$$

The corresponding atomic fractions ($c_i=N_i/\Sigma N_i$) can be also calculated from:

$$c_i(\theta) = \frac{I_i(\theta)/S_i}{\sum I_i(\theta)/S_i} \tag{4-93}$$

where S_i is the sensitivity factor for element i.

By comparing Equations (4-91) - (4-93), it is obvious that $(D\ T\ \sigma^X L\lambda_M)^i$ is proportional to S_i. If the proportionality constant is denoted by Q, then

$$(DT\sigma^X L\lambda_M)^i = QS_i \tag{4-94}$$

where Q is a constant for all elements in an individual measurement.

Thus Equation (4-90) can be rewritten as

$$I_A(\theta) = QS_A(J_0A)_\theta \int_{z=0}^{\infty} N_A(z)\exp\left[-z/\lambda_M^A \cos\theta\right] d(z/\lambda_M^A) \tag{4-95}$$

By setting $s=1/\cos\theta$ and $t=z/\lambda_M{}^A$, the above equation can be rewritten as

$$I_A(s) = QS_A(J_0A)_\theta \int_{t=0}^{\infty} N_A(\lambda_M^A t)\exp(-st)dt = QS_A(J_0A)_\theta \pounds\left[N_A(\lambda_M^A t); s\right] \tag{4-96}$$

ARXPS data directly yield $I_A(1/\cos\theta)$. Thus $N_A(z)$ can be derived from the inverse Laplace transform of $I_A(1/\cos\theta)/QS_A(J_0A)_\theta$. However, because the numerical inverse Laplace transform is difficult to obtain and the results are extremely sensitive to the data error, it is not possible to accurately reconstruct a depth profile using the direct inverse Laplace transform [164].

Another way to obtain $N_A(z)$, as we will describe below, is to assume a depth profile, perform a Laplace transform, compare the calculated $I_A(s)$ with experimental $I_A(s)$ and then obtain the parameters through least-squares regression. In the above derivation of

Equation (4-96), we did not consider reflection, diffraction or scattering (See assumptions 1, 2 and 3). The loss of electron intensity from reflection, diffraction or scattering can vary with geometric configuration. As a result, the experimentally measured electron intensities will differ from the theoretical values by a loss factor $F_{L\mathrm{A}}$, which is a function of both geometric configuration and photoelectron energy.

$$I_A(s)^{\mathrm{Exp}} = F_{LA} I_A(s) \tag{4-97}$$

If we assume that the percentage loss caused by reflection, diffraction or scattering is the same for all XPS photoelectrons for a certain geometric configuration, i.e., $F_{\mathrm{L}1}=F_{L2}=\ldots=F_{L\mathrm{n}}$, then there are two possible ways to account for the losses incurred.

One way is to eliminate the loss factors by taking the ratio of intensities of two elements before data fitting.

$$\frac{I_i(s)^{\mathrm{Exp}}}{I_j(s)^{\mathrm{Exp}}} = \frac{F_{Li} I_i(s)}{F_{Lj} I_j(s)} = \frac{I_i(s)}{I_j(s)} = \frac{QS_i(J_0 A)_\theta \pounds[N_i(\lambda_M^i t); s]}{QS_j(J_0 A)_\theta \pounds[N_j(\lambda_M^j t); s]} = \frac{S_i \pounds[N_i(\lambda_M^i t); s]}{S_j \pounds[N_j(\lambda_M^j t); s]} \tag{4-98}$$

A drawback of this method is that it doubles the number of parameters by introducing two sets of parameters in a single least-squares fitting calculation, which may complicate the data fitting process. (For binary systems, this is not a problem, because the concentration profile of one of the elements can be derived from that of the other one. Therefore, the number of parameters will not increase.)

Another way to account for the loss factors is to derive the concentration depth profile parameters in an iterative way.

From Equations (4-96) and (4-97),

$$\frac{I_i(s)^{\mathrm{Exp}}}{\sum I_i(s)^{\mathrm{Exp}}} = \frac{F_{Li} I_i(s)}{\sum F_{Li} I_i(s)} = \frac{I_i(s)}{\sum I_i(s)} \tag{4-99}$$

$$\frac{I_i(s)^{\mathrm{Exp}}}{\sum I_i(s)^{\mathrm{Exp}}} = \frac{QS_i(J_0 A)_\theta \pounds[N_i(\lambda_M^i t); s]}{\sum QS_i(J_0 A)_\theta \pounds[N_i(\lambda_M^i t); s]} = \frac{S_i \pounds[N_i(\lambda_M^i t); s]}{\sum S_i \pounds[N_i(\lambda_M^i t); s]} \tag{4-100}$$

Thus

$$S_i \pounds[N_i(\lambda_M^i t); s] = \frac{I_i(s)^{Exp}}{\sum I_i(s)^{Exp}} \sum S_i \pounds[N_i(\lambda_M^i t); s] \tag{4-101}$$

where S_i is known for a specific XPS system. $I_i(s)^{\mathrm{Exp}}$ can be obtained from angle-resolved measurements. A solution of Equation (4-101) can be obtained using the following iterative algorithm:

1) Start with a uniform concentration profile $N_i^k(z)$ (k=0)(no z dependence) and calculate $\sum S_i \pounds[N_i^k(\lambda_M^i t); s]$. Based on experimental $I_i(s)$ values, calculate $\{S_i \pounds[N_i(\lambda_M^i t); s]\}^{k+1}$ via Equation (4-101).
2) Assume a concentration profile $N_i(z)$ with no more than 3 parameters for each element i and obtain the parameters and concentration profile $N_i^{k+1}(z)$ for each i separately through least-squares fitting, i.e., minimize $(S_i \pounds[N_i^{k+1}(\lambda_M^i t); s] - \{S_i \pounds[N_i(\lambda_M^i t); s]\}^{k+1})^2$.
3) Compare $N_i^k(z)$ and $N_i^{k+1}(z)$ (or the corresponding parameters) to determine if convergence has been reached. If the values are not the same, start with $N_i^{k+1}(z)$ and repeat steps 1) and 2) until the concentration profile converges.

However, in order for this method to work, an estimate of λ_M values in the matrix is needed.

It should be noted that in Equation (4-101) $\sum \frac{I_i(s)^{Exp}}{\sum I_i(s)^{Exp}} = 1$. Therefore, in an *n*-component system, only intensity fractions from *n*-1 components are independent. In order to get physically realistic results, it is necessary to limit the degree of freedom of N_i to *n*-1. In a diffusion system, this is realized by keeping the total atomic concentration as a constant, i.e., $\sum N_i = N_{\text{Total}}$.

4.2.2. Diffusion models and concentration depth profiles

In the following derivation, we define *N* as the total atomic concentration and assume that *N* is uniform within the sample and does not change with time.

$$N_i(z) = Nc_i(z) \tag{4-102}$$

where c_i is the local concentration of *i* (in atomic fraction).

Two standard models are considered in the following development: infinite source diffusion and limited source diffusion. Fick's second law of diffusion is typically used to describe diffusion in solids [180]:

$$\frac{\partial c_i}{\partial t'} = D_i \nabla^2 c_i \tag{4-103}$$

where t' is the diffusion time and D_i the diffusion coefficient of *i*. For diffusion in only one dimension (*z* direction):

$$\frac{\partial c_i}{\partial t'} = D_i \frac{\partial^2 c_i}{\partial z^2} \tag{4-104}$$

For infinite source diffusion, the boundary and initial conditions are:

$$
\begin{aligned}
&c_i(z \geq 0, t' = 0) = c_{B,i} \\
&c_i(z = 0, t' > 0) = c_{S,i} + c_{B,i} \\
&c_i(z = \infty, t' > 0) = c_{B,i}
\end{aligned}
\tag{4-105}
$$

where $c_{B,i}$ is the bulk concentration of i and $c_{S,i}$ is the difference between surface concentration and bulk concentration of i.

The solution to Equation (4-104) for infinite source diffusion is [180]:

$$
c_i(z, t') = c_{B,i} + c_{S,i}\,\mathrm{erfc}\left[\frac{z}{\sqrt{4D_i t'}}\right] \tag{4-106}
$$

For limited source diffusion, the boundary and initial conditions are:

$$
\begin{aligned}
&c_i(z \geq 0, t' = 0) = c_{B,i} \\
&c_i(z = \infty, t' > 0) = c_{B,i} \\
&\int_0^\infty \left[c_i(z, t') - c_{B,i}\right] dz = V_i / N = M_i
\end{aligned}
\tag{4-107}
$$

where $c_{B,i}$ is the bulk concentration of i and V_i is the total amount of i that diffuses into the sample per unit area; V_i is a constant for limited source diffusion. For simplification purpose, V_i/N is expressed in a collected term M_i in Equation (4-107).

The solution of Equation (4-104) for limited source diffusion is:

$$
c_i(z, t') = c_{B,i} + \frac{M_i}{\sqrt{\pi D_i t'}} \exp\left(-\frac{z^2}{4D_i t'}\right) \tag{4-108}
$$

For a particular diffusion time t', let $\Delta_i = 1/\sqrt{4D_i t'}$ and $c'_{S,i} = M_i / \sqrt{\pi D_i t'}$.

Then, for infinite source diffusion

$$c_i(z) = c_{B,i} + c_{S,i}\text{erfc}(\Delta_i z) \tag{4-109}$$

while for limited source diffusion

$$c_i(z) = c_{B,i} + c'_{S,i}\exp(-\Delta_i^2 z^2) \tag{4-110}$$

Simpler concentration profiles have been reported previously. For the purpose of examples in this article, the following two, linear gradient and step models, will be used for comparison to the concentration profiles generated by diffusion models. Figure 4-3 shows the concentration depth profiles of the two models.

Table 4-1 summarizes the depth concentration profiles and analytical forms of $\pounds[N_i(\lambda_M^i t); s]$. Appendix A can be consulted for the detailed derivation.

Table 4-1 Different concentration profiles and corresponding Laplace transforms*

Model	Depth profile	$\pounds[N_i(\lambda_M^i t); s]$	M_{1i}	M_{2i}	M_{3i}
Infinite source	$c_i(z) = c_{B,i} + c_{S,i}\text{erfc}(\Delta_i z)$	$\frac{M_{1i}^{IS}}{s} + \frac{M_{2i}^{IS}}{s} e^{\frac{s^2}{(M_{3i}^{IS})^2}} \text{erfc}(\frac{s}{M_{3i}^{IS}})$	$N(c_{B,i} + c_{S,i})$	$-Nc_{S,i}$	$2\Delta_i\lambda_M^i$
Limited source	$c_i(z) = c_{B,i} + c'_{s,i}e^{-\Delta_i^2 z^2}$	$\frac{M_{1i}^{LS}}{s} + M_{2i}^{LS} e^{\frac{s^2}{(M_{3i}^{LS})^2}} \text{erfc}(\frac{s}{M_{3i}^{LS}})$	$Nc_{B,i}$	$\frac{\sqrt{\pi}Nc'_{S,i}}{2\Delta_i\lambda_M^i}$	$2\Delta_i\lambda_M^i$
Linear gradient	$c_i(z) = \begin{cases} c_{B,i} + c_{S,i} - \frac{z}{\Lambda_i} c_{S,i} & \text{when } 0 < z < \Lambda_i \\ c_{B,i} & \text{when } z > \Lambda_i \end{cases}$	$\frac{M_{1i}^{LG}}{s} + \frac{M_{2i}^{LG}}{s^2}(1 - e^{\frac{s}{M_{3i}^{LG}}})$	$N(c_{B,i} + c_{S,i})$	$-\frac{Nc_{S,i}\lambda_M^i}{\Lambda_i}$	$-\frac{\lambda_M^i}{\Lambda_i}$
Step	$c_i(z) = \begin{cases} c_{B,i} + c_{S,i} & \text{when } 0 < z < \Lambda_i \\ c_{B,i} & \text{when } z > \Lambda_i \end{cases}$	$\frac{M_{1i}^{ST}}{s} + \frac{M_{2i}^{ST}}{s} e^{\frac{s}{M_{3i}^{ST}}}$	$N(c_{B,i} + c_{S,i})$	$-Nc_{S,i}$	$-\frac{\lambda_M^i}{\Lambda_i}$

* The superscripts: IS, LS, LG and ST designate infinite source model, limited source model, linear gradient model and step model, respectively.

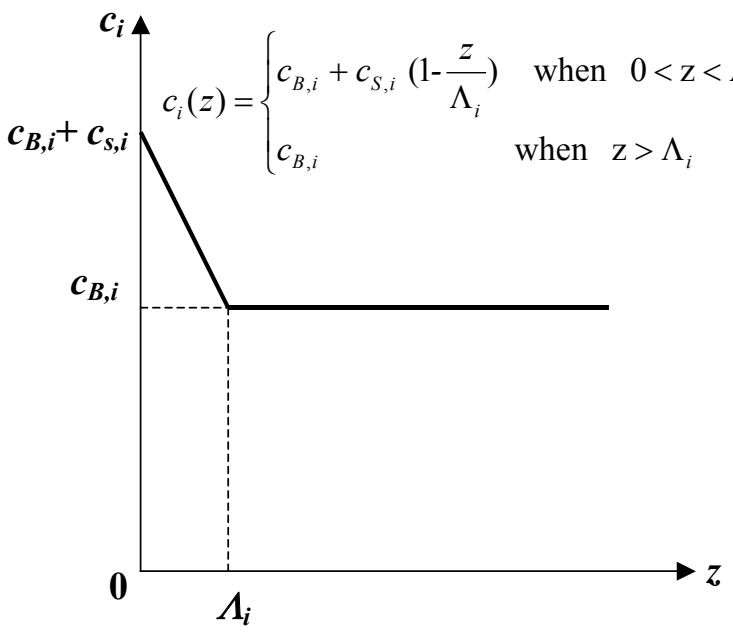

a) Linear gradient model

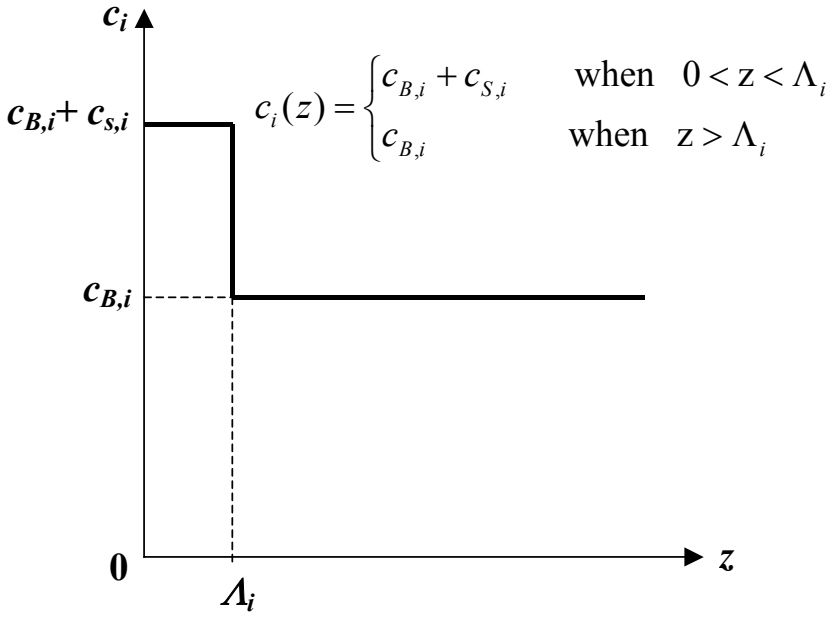

b) Step model

Figure 4-3 Concentration depth profiles represented by linear gradient model and step model

4.3. Simulation

4.3.1. Concentration depth profiles of different elements in BPDA-PDA

In the simulation, BPDA-PDA is chosen as the diffusion system. The three elements of interest are carbon, nitrogen and oxygen. Because hydrogen cannot be detected by XPS, we follow the common practice and neglect hydrogen atoms in all the following discussions [102].

In the diffusion model, different elements can diffuse separately; however, one constraint will always apply: the sum of the concentrations of all elements should be a constant if we assume that the total atomic concentration is constant within the sample. Thus among n elements, only the concentration profiles of n-1 elements are allowed to change independently during the regression. For the BPDA-PDA films, it follows that $c_C+c_N+c_O$=constant. In the following discussion, the concentration profiles of carbon and oxygen are chosen to vary independently in the regression. Because the N concentration profile is calculated from those of C and O, mathematically the N concentration will assume a different form and the procedure to obtain the N Laplace transform is also slightly different. Details regarding calculation of the Laplace transform of N concentration profiles can be found in Appendix A.3.

In the model description, N is the total atomic concentration within the sample. In the calculation, N is set equal to 1 for convenience because the absolute value of N will not affect the atomic fractions of individual elements.

4.3.2. Generation of data to test the algorithm

To test the algorithm, a set of raw data are generated from the following assigned parameters:

$c_{B,C}$=0.7856; $c_{S,C}$=-0.10; Δ_C=0.6 nm^{-1};

$c_{B,O}$=0.1430; $c_{S,O}$=0.06; Δ_O=1.0 nm^{-1};

The bulk concentration values for C and O ($c_{B,C}$ and $c_{B,O}$) are chosen based on the molecular structure of BPDA-PDA (Figure 2-2). Other parameters include:

Sensitivity factors: C: 0.292; N: 0.475; O: 0.713;

Electron attenuation length (in nm)*: C: 3.5668; N: 3.2793; O: 2.9514;

Appendix B should be consulted for the details of electron attenuation length calculations.

Table 4-2 ARXPS data generated from simulation for algorithm testing and error analysis

θ	1 / cos(θ)	$I_C/(I_C+I_N+I_O)$	$I_N/(I_C+I_N+I_O)$	$I_O/(I_C+I_N+I_O)$
15	1.035276	0.5975	0.1095	0.2930
20	1.064178	0.5969	0.1098	0.2933
25	1.103378	0.5960	0.1103	0.2937
30	1.154701	0.5948	0.1109	0.2943
35	1.220775	0.5934	0.1116	0.2951
40	1.305407	0.5916	0.1124	0.2960
45	1.414214	0.5893	0.1135	0.2971
50	1.555724	0.5866	0.1148	0.2986
55	1.743447	0.5831	0.1164	0.3005
60	2.000000	0.5788	0.1183	0.3029
65	2.366202	0.5733	0.1207	0.3060
70	2.923804	0.5661	0.1235	0.3104
75	3.863703	0.5565	0.1269	0.3166

* The significant number here is not an indication of the precision of the calculation.

The C and O concentration profiles are assumed to follow the infinite source diffusion model. The photoemission angle θ is assigned values from 15º to 75º at intervals of 5º. Table 4-2 shows the data generated from this simulation.

4.3.3. Three-parameter algorithm

Each element (C and O) has three parameters: c_B, c_s and Δ. These three parameters can be obtained from data in Table 4-2 through least-squares curve fitting and iteration as described in the Section 4.2. However, the final results depend sensitively on the initial values chosen for Δ. Since one of the main purposes of ARXPS data analysis is to estimate Δ, such an algorithm is not appropriate. Table 4-3 illustrates how the initial values of Δ influence the data fitting results.

Table 4-3 Regression results for three-parameter algorithm

Value	Initial	Final	Initial	Final	Initial	Final	Initial	Final
$c_{B,C}$	0.7856	0.7856	0.7856	0.7862	0.7856	0.7858	0.7856	0.7854
$c_{S,C}$	-0.1000	-0.1000	-0.1000	-0.1018	-0.1000	-0.1005	-0.1000	-0.0995
Δ_C	**0.6000**	**0.6006**	**0.6000**	**0.6001**	**0.6000**	**0.5999**	**0.6000**	**0.6013**
$c_{B,O}$	0.1430	0.1430	0.1430	0.1374	0.1430	0.1416	0.1430	0.1447
$c_{S,O}$	0.0600	0.0600	0.0600	0.0439	0.0600	0.0511	0.0600	0.0925
Δ_O	**1.0000**	**1.0000**	**0.2000**	**0.3892**	**0.7000**	**0.7119**	**2.0000**	**1.9638**
$c_{B,C}$	0.7856	0.7817	0.7856	0.7864	0.7856	0.7846	0.7856	0.7847
$c_{S,C}$	-0.1000	-0.1259	-0.1000	-0.0973	-0.1000	-0.1037	-0.1000	-0.1036
Δ_C	**1.0000**	**0.9685**	**0.2000**	**0.5562**	**0.7000**	**0.6590**	**1.0000**	**0.6578**
$c_{B,O}$	0.1430	0.1412	0.1430	0.1430	0.1430	0.1430	0.1430	0.1430
$c_{S,O}$	0.0600	0.0504	0.0600	0.0598	0.0600	0.0601	0.0600	0.0604
Δ_O	**0.6000**	**0.6737**	**1.0000**	**0.9954**	**1.0000**	**1.0010**	**1.0000**	**1.0091**

In a Laplace transform of the infinite source concentration profile, the Δ value appears in the error function and even small fluctuations in Δ will result in a large change in the total value of the target function. This might be the reason why the final results show such a strong dependence on the initial value of Δ in the three-parameter algorithm.

4.3.4. Two-parameter algorithm

One way to ensure that the algorithm is relatively insensitive to initial parameter values is to reduce the number of regression parameters. Among the three parameters: c_B, c_s and Δ, c_B can be obtained either from prior knowledge of the sample or from separate measurements on a sample with uniform composition. In this article, c_B takes the theoretical values calculated based on the chemical structure of BPDA-PDA: $c_{B,C}$=0.7856, $c_{B,N}$=0.0714 and $c_{B,O}$=0.1430. If the values of c_B are fixed during the regression, it will be much easier for the algorithm to converge to the correct values, as can be illustrated by the results shown in Table 4-4.

Table 4-4 Regression results for two-parameter algorithm

Value	Initial	Final	Initial	Final	Initial	Final	Initial	Final
$c_{B,C}$	0.7856	0.7856	0.7856	0.7856	0.7856	0.7856	0.7856	0.7856
$c_{S,C}$	**-0.1000**	**-0.1001**	**0.0800**	**-0.1001**	**-0.0600**	**-0.1001**	**0.0800**	**-0.1000**
Δ_C	**0.6000**	**0.6006**	**0.5000**	**0.6006**	**2.0000**	**0.6006**	**2.0000**	**0.5999**
$c_{B,O}$	0.1430	0.1430	0.1430	0.1430	0.1430	0.1430	0.1430	0.1430
$c_{S,O}$	**0.0600**	**0.0600**	**-0.1000**	**0.0600**	**0.1000**	**0.0600**	**-0.1000**	**0.0600**
Δ_O	**1.0000**	**0.9994**	**0.5000**	**0.9994**	**0.3000**	**0.9994**	**0.1000**	**1.0001**

4.3.5. Sensitivity of algorithm to error of c_B values (two-parameter algorithm)

Although there is little dependence of the final results of the two-parameter algorithm on the initial values, the accuracy of the final results will be determined to a large extent by accurate estimation of c_B. In most cases, the estimated c_B values are not free from error. Thus it is desirable to establish how the accuracy of c_B affects the final results.

Figure 4-4(a) and (b) show how the relative error in c_B value estimation influences final values of other parameters. In Figure 4-4(a), $c_{B,O}$ is fixed at the correct value 0.1430, while $c_{B,C}$ is varied around 0.7856; in Figure 4-4(b), $c_{B,C}$ is fixed at the correct value 0.7856, while $c_{B,O}$ is varied around 0.1430. Results are obtained with the two-parameter algorithm and relative errors are calculated with corresponding reference values: $c_{B,C}$=0.7856, $c_{S,C}$=-0.10, Δ_C=0.6nm^{-1}, $c_{B,O}$=0.1430, $c_{S,O}$=0.06, Δ_O=1.0nm^{-1}. The initial values of other parameters for the regression are: $c_{S,C}$ = -0.06, Δ_C = 2.0 nm^{-1}, $c_{S,O}$ = 0.10, Δ_O = 0.3 nm^{-1}.

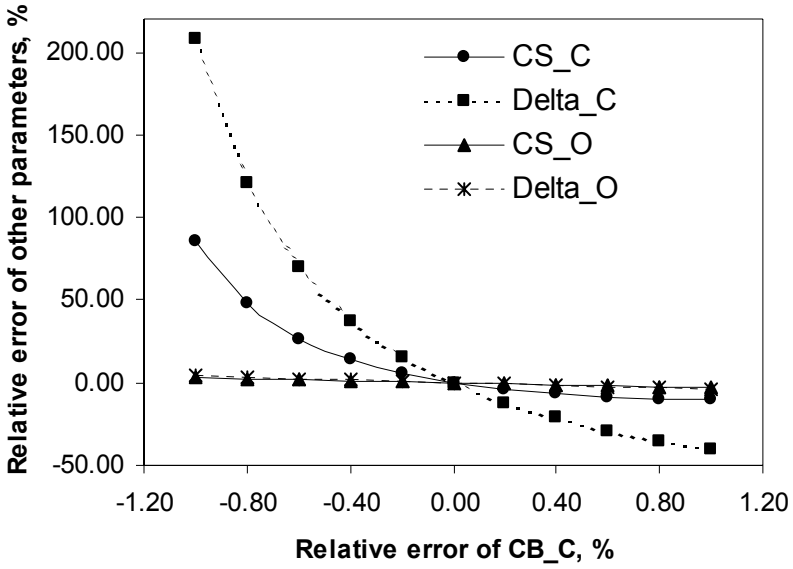

(a) $c_{B,O}$ fixed at 0.1430 and $c_{B,C}$ varied around 0.7856

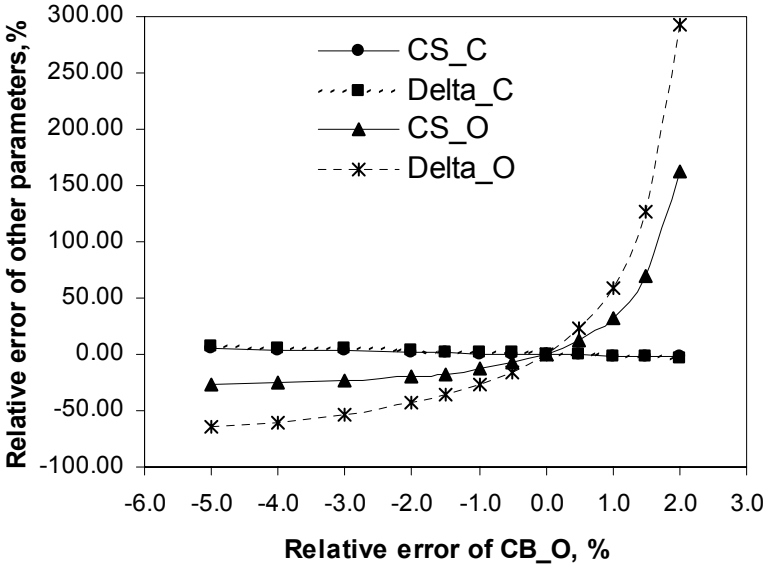

(b) $c_{B,C}$ fixed at 0.7856 and $c_{B,O}$ varied around 0.1430

Figure 4-4 Influence of the relative error in c_B on final values of other parameters

Clearly, the final values for simulation parameters of a specific element are quite sensitive to the estimation accuracy of the specific c_B value, but are not very sensitive to the estimation accuracy of the c_B value of the other element. Also, if the surface concentration of one element is lower than the bulk concentration, a negative error in the estimation of its c_B value results in a larger error compared to a positive error in the estimation of its c_B value; the converse is also true.

4.3.6. Sensitivity of algorithm to data error

To study the influence of error in the raw data on the final results, random error is introduced intentionally. In this study, several simplifications are made. The relative error in total photoelectron intensity (y) is defined as the error in intensity divided by the total intensity. y is assumed to follow either the uniform distribution (e.g., $f(y) = \frac{1}{0.02}, y \in [-0.01, 0.01]$ for a relative error of 1.0%) or the normal distribution (e.g., $f(y) = \frac{\exp(-y^2 / 2 \times 0.01^2)}{0.01\sqrt{2\pi}}$ for a relative error of 1.0%). If the theoretical C and O intensity fractions are $I_C/\Sigma I$ and $I_O/\Sigma I$, respectively, then the intensity fractions including error will be $I_C/\Sigma I + y$ and $I_O/\Sigma I + y$, respectively. Note that the relative errors for C and O photoelectron intensities are different. They are actually y divided by the corresponding relative intensity fractions. For example, for a sample containing 75% C and 15% O, if the relative error in total photoelectron intensity is 0.3%, the relative error in C photoelectron intensity will be 0.4% while the relative error in O photoelectron intensity will be 2.0%.

In the simulation, for each level of relative error in total electron intensity: 0.05%, 0.1%, 0.2%, 0.25%, 0.3% and 0.4%, 1000 sets of data with error following either distribution are generated. The average and standard deviation of parameters obtained from regression with the error-included data are then calculated. Table 4-5 summarizes the results (η designates average and σ designates standard deviation). In all regressions, $c_{B,O}$ is fixed at 0.1430 and $c_{B,C}$ is fixed at 0.7856. The initial values of other parameters for the regression are: $c_{S,C}$ = -0.06, Δ_C = 2.0 nm^{-1}, $c_{S,O}$ = 0.10, Δ_O = 0.3 nm^{-1}.

Table 4-5 Influence of raw data error on parameter estimation

a) For the case that the error of raw data follow uniform distribution

Relative error	σ of relative error*	$c_{S,C}$		Δ_C		$c_{S,O}$		Δ_O	
		η	σ	η	σ	η	σ	η	σ
0	0	-0.100	0	0.600	0	0.060	0	1.000	0
0.0005	0.00029	-0.100	0.002	0.601	0.014	0.060	0.002	0.999	0.040
0.0010	0.00058	-0.100	0.003	0.601	0.030	0.060	0.004	1.001	0.084
0.0020	0.00115	-0.100	0.007	0.601	0.060	0.061	0.008	1.020	0.179
0.0025	0.00144	-0.101	0.009	0.606	0.077	0.061	0.010	1.023	0.226
0.0030	0.00173	-0.101	0.010	0.609	0.091	0.062	0.012	1.033	0.267
0.0040	0.00231	-0.102	0.014	0.615	0.129	0.064	0.019	1.101	0.419

b) For the case that the error of raw data follow normal distribution

Relative error	σ of relative error	$c_{S,C}$		Δ_C		$c_{S,O}$		Δ_O	
		η	σ	η	σ	η	σ	η	σ
0	0	-0.100	0	0.600	0	0.060	0	1.000	0
0.0005	0.0005	-0.101	0.002	0.608	0.026	0.060	0.003	1.010	0.074
0.0010	0.0010	-0.102	0.006	0.615	0.050	0.061	0.007	1.032	0.152
0.0020	0.0020	-0.104	0.012	0.639	0.108	0.064	0.016	1.094	0.351
0.0025	0.0025	-0.103	0.015	0.628	0.133	0.067	0.026	1.148	0.594
0.0030	0.0030	-0.108	0.020	0.678	0.179	0.079	0.201	1.424	4.617
0.0040	0.0040	-0.112	0.032	0.709	0.288	0.121	0.419	2.361	9.290

* For a uniform distribution: $f(y) = 1/(2a)$, $y \in [b-a, b+a]$, the standard deviation of y is $a/\sqrt{3}$.

Clearly, for both uniform and normal distributions, the results are unacceptable when the standard deviation of relative error of total photoelectron intensities reaches 0.30%. Obviously, high quality data are required to reconstruct the concentration profile.

4.3.7. Robustness of the infinite source model

It is unlikely that actual concentration profiles in BPDA-PDA films will follow the infinite source model rigorously. Therefore, it is of practical interest to know how well the infinite source model works if a concentration profile follows another model such as the limited source model, the linear gradient model or the step model.

To test the robustness of the infinite source model when the concentration follows a different profile, a set of XPS data were generated from depth profiles based on a different model and were used to obtain the infinite source model parameters. A concentration profile following the infinite source model was then generated and compared with the original concentration profile.

Figure 4-5(a), (b) and (c) show comparisons between concentration profiles of limited source and infinite source models. Due to the good agreement of the results of these two models, concentration profiles display nearly complete overlap. In all regressions, $c_{B,O}$ is fixed at 0.1430 and $c_{B,C}$ is fixed at 0.7856. The initial values of other parameters for the regression are: $c_{S,C}$ = -0.06, Δ_C = 2.0 nm^{-1}, $c_{S,O}$ = 0.10, Δ_O = 0.3 nm^{-1}. Table 4-6 summarizes the simulation parameters and results.

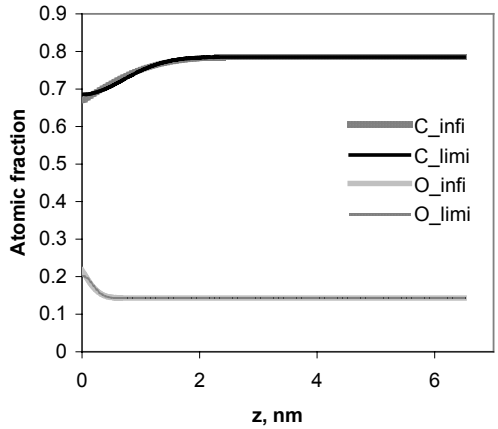

(a) Limited source model: $c_{B,C}$=0.7856, $c_{S,C}$=-0.10, Δ_C=1nm^{-1}, $c_{B,O}$=0.1430, $c_{S,O}$=0.06, Δ_O=4nm^{-1}

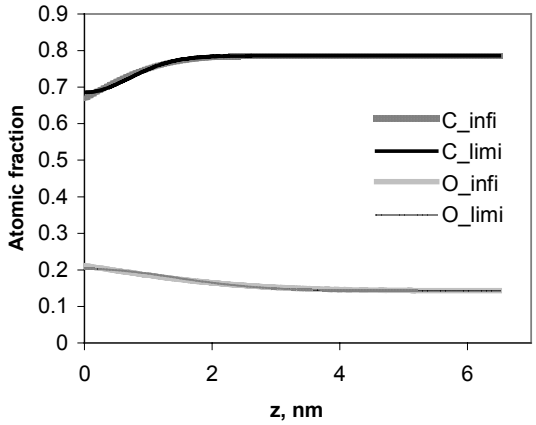

(b) Limited source model: $c_{B,C}$=0.7856, $c_{S,C}$=-0.10, Δ_C=1nm^{-1}, $c_{B,O}$=0.1430, $c_{S,O}$=0.06, Δ_O=0.5nm^{-1}

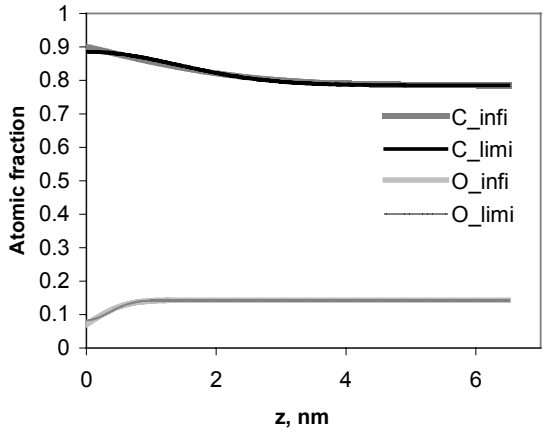

(c) Limited source model: $c_{B,C}$=0.7856, $c_{S,C}$=0.10, Δ_C=0.5nm^{-1}, $c_{B,O}$=0.1430, $c_{S,O}$=-0.06, Δ_O=2nm^{-1}

Figure 4-5 Comparison between concentration profiles of limited and infinite source model

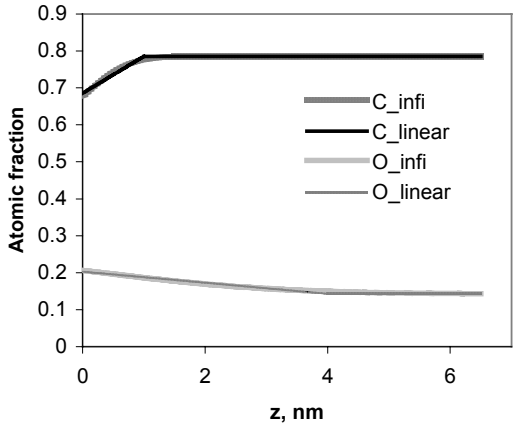

(a) Linear gradient model: $c_{B,C}$=0.7856, $c_{S,C}$=-0.10, Λ_C=1nm, $c_{B,O}$=0.1430, $c_{S,O}$=0.06, Λ_O=4nm

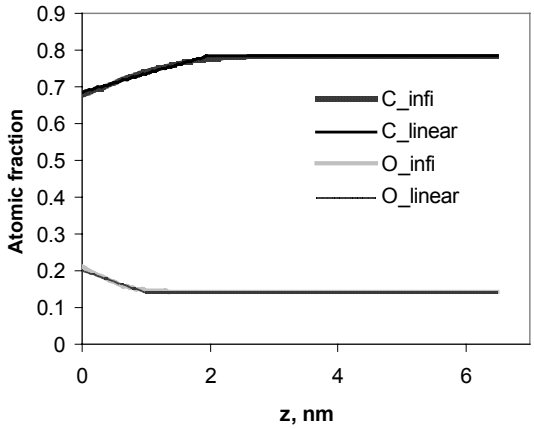

(b) Linear gradient model: $c_{B,C}$=0.7856, $c_{S,C}$=-0.10, Λ_C=2nm, $c_{B,O}$=0.1430, $c_{S,O}$=0.06, Λ_O=1nm

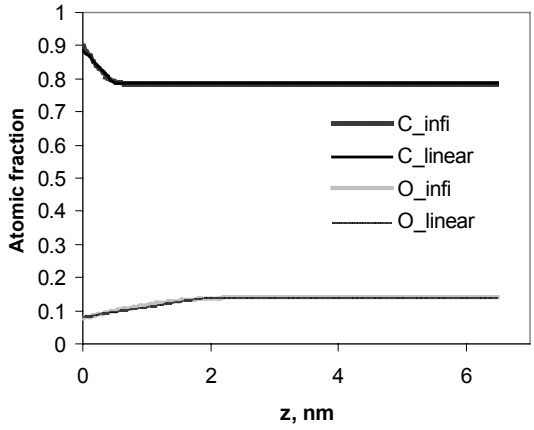

(c) Linear gradient model: $c_{B,C}$=0.7856, $c_{S,C}$=0.10, Λ_C=0.5nm, $c_{B,O}$=0.1430, $c_{S,O}$=-0.06, Λ_O=2nm

Figure 4-6 Comparison between concentration profiles of linear gradient and infinite source model

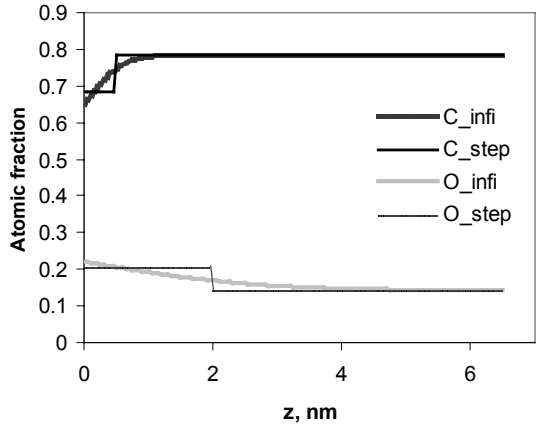

(a) Step model: $c_{B,C}$=0.7856, $c_{S,C}$=-0.10, Λ_C=0.5nm, $c_{B,O}$=0.1430, $c_{S,O}$=0.06, Λ_O=2nm

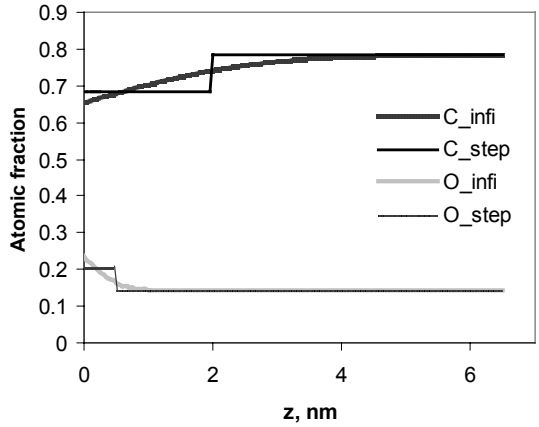

(b) Step model: $c_{B,C}$=0.7856, $c_{S,C}$=-0.10, Λ_C=2nm, $c_{B,O}$=0.1430, $c_{S,O}$=0.06, Λ_O=0.5nm

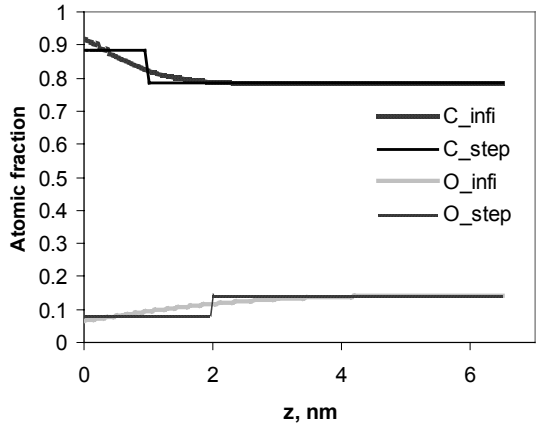

(c) Step model: $c_{B,C}$=0.7856, $c_{S,C}$=0.10, Λ_C=1nm, $c_{B,O}$=0.1430, $c_{S,O}$=-0.06, Λ_O=2nm

Figure 4-7 Comparison between concentration profiles of step model and infinite source model

Figure 4-6(a), (b) and (c) show comparisons between concentration profiles of linear gradient and infinite source models. Again, due to the good agreement of the results, concentration profiles display nearly complete overlap. In all regressions, $c_{B,O}$ is fixed at 0.1430 and $c_{B,C}$ is fixed at 0.7856. The initial values of other parameters for the regression are: $c_{S,C}$ = -0.06, Δ_C = 2.0 nm^{-1}, $c_{S,O}$ = 0.10, Δ_O = 0.3 nm^{-1}. Table 4-7 summarizes the simulation parameters and results.

Table 4-6 Summary of simulation results (limited vs. infinite source model)

		Preset parameters (limited source model)			Parameters from regression (infinite source model)		
		$c_{B,I}$	$c_{S,i}$	Δ_i, nm^{-1}	$c_{B,i}$	$c_{S,i}$	Δ_i, nm^{-1}
A	C	0.7856	-0.10	1	0.7856	-0.1185	0.7501
	O	0.1430	0.06	4	0.1430	0.0740	3.1454
B	C	0.7856	-0.10	1	0.7856	-0.1177	0.7426
	O	0.1430	0.06	0.5	0.1430	0.0687	0.3555
C	C	0.7856	0.10	0.5	0.7856	0.1151	0.3584
	O	0.1430	-0.06	2	0.1430	-0.0727	1.5426

Table 4-7 Summary of simulation results (linear gradient vs. infinite source model)

		Preset parameters (linear gradient model)			Parameters from regression (infinite source model)		
		$c_{B,i}$	$c_{S,i}$	Λ_i, nm	$c_{B,i}$	$c_{S,i}$	Δ_i, nm^{-1}
a	C	0.7856	-0.10	1	0.7856	-0.1101	1.2311
	O	0.1430	0.06	4	0.1430	0.0636	0.2868
b	C	0.7856	-0.10	2	0.7856	-0.1103	0.6149
	O	0.1430	0.06	1	0.1430	0.0679	1.2727
c	C	0.7856	0.10	0.5	0.7856	0.1106	2.4859
	O	0.1430	-0.06	2	0.1430	-0.0658	0.6099

Table 4-8 Summary of simulation results (step vs. infinite source model)

		Preset parameters (step model)			Parameters from regression (infinite source model)		
		$c_{B,i}$	$c_{S,i}$	Δ_i, nm	$c_{B,i}$	$c_{S,i}$	Δ_i, nm^{-1}
a	C	0.7856	-0.10	0.5	0.7856	-0.1361	1.5085
	O	0.1430	0.06	2	0.1430	0.0773	0.3395
b	C	0.7856	-0.10	2	0.7856	-0.1307	0.3484
	O	0.1430	0.06	0.5	0.1430	0.0914	1.7187
c	C	0.7856	0.10	1	0.7856	0.1372	0.7544
	O	0.1430	-0.06	2	0.1430	-0.0773	0.3389

The above comparisons demonstrate that the infinite source model can yield good approximations to the concentration profiles produced by limited source or linear gradient models.

Figure 4-7(a), (b) and (c) display comparisons between concentration profiles of step and infinite source models. In all regressions, $c_{B,O}$ is fixed at 0.1430 and $c_{B,C}$ is fixed at 0.7856, while the initial values of other parameters for the regression are: $c_{S,C}$ = -0.6, Δ_C = 2.0 nm^{-1}, $c_{S,O}$ = 0.10, Δ_O = 0.3 nm^{-1}. Table 4-8 summarizes the simulation parameters and results.

Although the infinite source model cannot fit the concentration profile of the step model as well as it does the limited source or the linear gradient models, the general trend is clearly correct.

4.4. Experimental verification of the two-parameter algorithm

Preliminary experiments have been carried out to verify the correctness of the algorithm proposed in Section 4.2. A direct approach will be to prepare a film with strictly controlled diffusion depth profile near the surface and compare the depth profile extracted from ARXPS data using the algorithm with that measured using another depth profiling technique of comparable depth resolution, such as secondary ion mass spectroscopy (SIMS) or Rutherford backscattering spectroscopy (RBS). Since no access exists at Georgia Tech to high resolution SIMS or RBS, an indirect approach is proposed in this section to produce diffusion depth profiles near a surface and perform initial verification of the correctness of the algorithm. The approach is based on the fact that Δ_i is inversely proportional to the square root of diffusion time (t') at a particular temperature: $\Delta_i = 1/\sqrt{4D_i t'}$. Therefore, for depth profiles resulting from diffusion for different times (t_1 and t_2, for instance) at the same temperature, the corresponding $\Delta_i(t_1)$ and $\Delta_i(t_2)$ should satisfy the following equation:

$$\frac{\Delta_i(t_1)}{\Delta_i(t_2)} = \frac{\sqrt{t_2}}{\sqrt{t_1}} \tag{4-111}$$

If the algorithm in Section 4.2 can generate correct depth profile parameters from ARXPS data, it should yield Δ_i values that satisfy Equation (4-111). In the following sections, a procedure is proposed to obtain desired diffusion profiles, depth profiles extracted from ARXPS are shown and corresponding Δ_i values are compared.

4.4.1. Generation of diffusion depth profiles near a surface

For a diffusion depth profile suitable for ARXPS study, most of the concentration change should be within the top 20 nm of the surface. An extended range of concentration change will be difficult to detect due to rapid attenuation of photoelectrons. Initial experimental studies revealed that nitrogen was depleted and oxygen enriched at the copper/oxygen doped silicon nitride (SiON) interface when the temperature was raised above 500°C (Section 3.2 should be consulted for the Cu-SiON dual layer structure fabrication). It is possible that impurities in copper, such as iron and nickel (both are typical impurity elements in copper sputtering targets), react with the SiON film and form metal nitrides or silicides [197,198]. Although the reason for N depletion and O enrichment is still not clear, the phenomena can be utilized to produce infinite source diffusion depth profiles for the proposed ARXPS study.

High temperature diffusion (500°C) was performed in a rapid thermal processor (RTP) on two copper covered SiON samples, one for 15 min and the other for 60 min. The RTP can heat samples from room temperature to 500°C in 10 seconds; cooling of the sample was through natural convection and ~1 min was required for the temperature to drop below 300°C. After high temperature diffusion, copper remaining on the SiON surface was subsequently removed with HNO_3 and the SiON surface probed by ARXPS.

4.4.2. Characterization of SiON film before copper deposition and high temperature diffusion

The two-parameter algorithm requires that the bulk concentrations of different elements in a film be known in advance. A SiON sample was examined by XPS before copper deposition and high temperature diffusion to determine the bulk concentrations. Due to

adsorption of air-borne carbonaceous species on sample surfaces, the SiON surface was contaminated before introduction into the XPS measurement chamber. Argon ion (Ar^+) sputtering was used to remove the contaminants before XPS measurements. Ion sputtering was resumed after each XPS measurement until the atomic concentrations did not vary with further sputtering. The final atomic concentrations measured by XPS are 0.525 for N, 0.080 for O and 0.395 for Si. As expected, no C was detected in the bulk of the SiON films. Before ion sputtering, ARXPS measurements were performed on the SiON in order to estimate the level of contamination based on a simple overlayer model. The $Si_{0.395}O_{0.08}N_{0.525}$ film is assumed to be covered uniformly with a carbonaceous layer (C_xO_{1-x}) of thickness d. Mathematical analysis for extracting x and d from ARXPS data can be found in Appendix A.4. x and d were estimated to be 0.37 and 0.3nm, respectively.

SiON samples without copper coverage were also placed side by side with copper covered samples during high temperature diffusion and treated with HNO_3. XPS measurements on these samples did not reveal significant changes to the SiON surface resulting from high temperature processing itself (without copper) or HNO_3 treatment. The variation of atomic concentrations of each specific element among these samples is less than 0.015.

4.4.3. Depth profiles near SiON surface after high temperature diffusion

The two-parameter algorithm was used to calculate parameters for depth profiles near the SiON surface after high temperature diffusion from ARXPS data and the results are summarized in Table 4-9. For SiON films with carbon contamination, it follows that $c_C+c_N+c_O+c_{Si}$=constant. In the following discussion, the concentration profiles of carbon,

oxygen and nitrogen are chosen to vary independently. Because the Si concentration profile is calculated from those of C, O and N, the Si concentration will mathematically assume a different form. The procedure to obtain the Si Laplace transform is similar to the one described in Appendix A.3. In all regressions, bulk atomic concentrations for C, N and O were fixed at 0, 0.525 and 0.080, respectively. Various initial values of C, N and O parameters were used in the regression; results were not sensitive to the choice of initial parameter values.

Table 4-9 Parameters for depth profiles near SiON surface after high temperature diffusion

	Diffusion at 500°C for 15 min			Diffusion at 500°C for 60 min		
	$c_{B,i}$	$c_{S,i}$	Δ_i, nm^{-1}	$c_{B,i}$	$c_{S,i}$	Δ_i, nm^{-1}
C	0	0.0679	0.695	0	0.0594	0.661
N	0.5250	-0.5945	0.130	0.5250	-0.5672	0.075
O	0.0080	0.6970	0.115	0.0080	0.6683	0.069

In Figure 4-8, comparisons are shown between the measured values of photoelectron intensity fractions and those generated from simulation based on parameters reported in Table 4-9. In Figure 4-8, solid and dotted curves represent photoelectron intensity fractions from simulation while scattered data points are experimentally measured values.

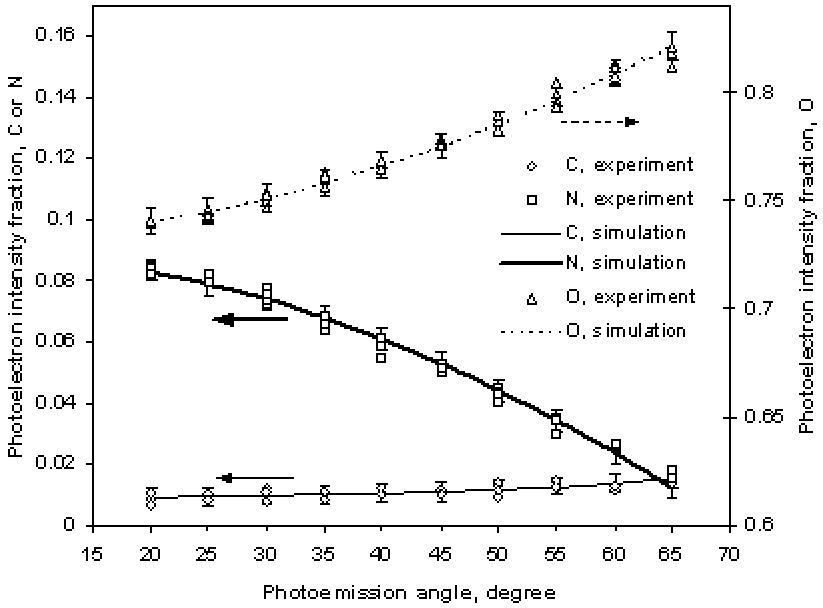

(a) Diffusion at 500°C for 15 min

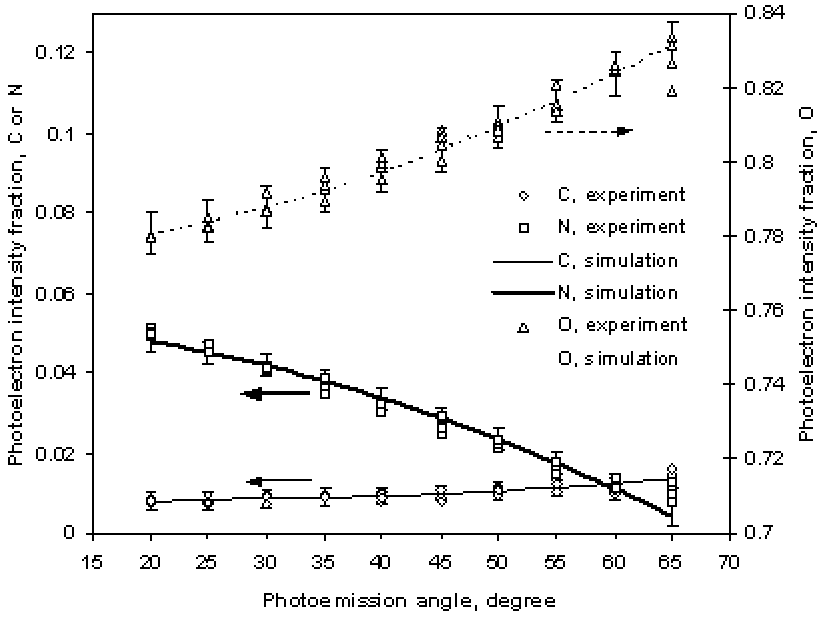

(b) Diffusion at 500°C for 60 min

Figure 4-8 Comparison between measured and simulated photoelectron intensity fractions for SiON films after high temperature diffusion

In Figure 4-8, for a specific sample, the span of error bars is $\pm 2\sigma_i$ for a particular element i; σ_i is the standard deviation of experimental error calculated from the following equation:

$$\sigma_i = \sqrt{\frac{\sum_{j=1}^{N_{angle}} \sum_{k=1}^{4} \left(I_{ijk} / \sum_{C,O,N,Si} I_{ijk} - \left(\sum_{k=1}^{4} I_{ijk} / \sum_{C,O,N,Si} I_{ijk} \right) / 4 \right)^2}{(4-1) \times N_{\text{angle}}}} \tag{4-112}$$

where i designates the particular element (C, N, O or Si), N_{angle} is the number of photoemission angles, 4 is the number of repetitions at each photoemission angle, and $I_{ijk} / \sum_{C,O,N,Si} I_{ijk}$ is the photoelectron intensity fraction for element i at the jth photoemission angle in the kth repetition. The denominator in the square root, $(4\text{-}1)\times N_{\text{angle}}$, is the number of degree of freedom for this calculation [199]. It can be seen that most experimental data fall within $\pm 2\sigma_i$ of the simulated curves.

Figure 4-9 shows and compares concentration depth profiles of different elements near the surface of the two SiON samples treated at 500°C for 15 min and 60 min. Clearly, if C depth profiles are modeled by infinite source diffusion, the C concentration will quickly drop near zero within ~1nm. Since most C is expected to be from air contamination, treating the C depth profile as an infinite source diffusion will incorporate some error in the reconstructed depth profiles, especially within the top 1nm, as indicated by the dotted line with arrows on both ends in Figure 4-9. This is probably the reason why N concentrations drop below zero in this specific region in the reconstructed depth profiles.

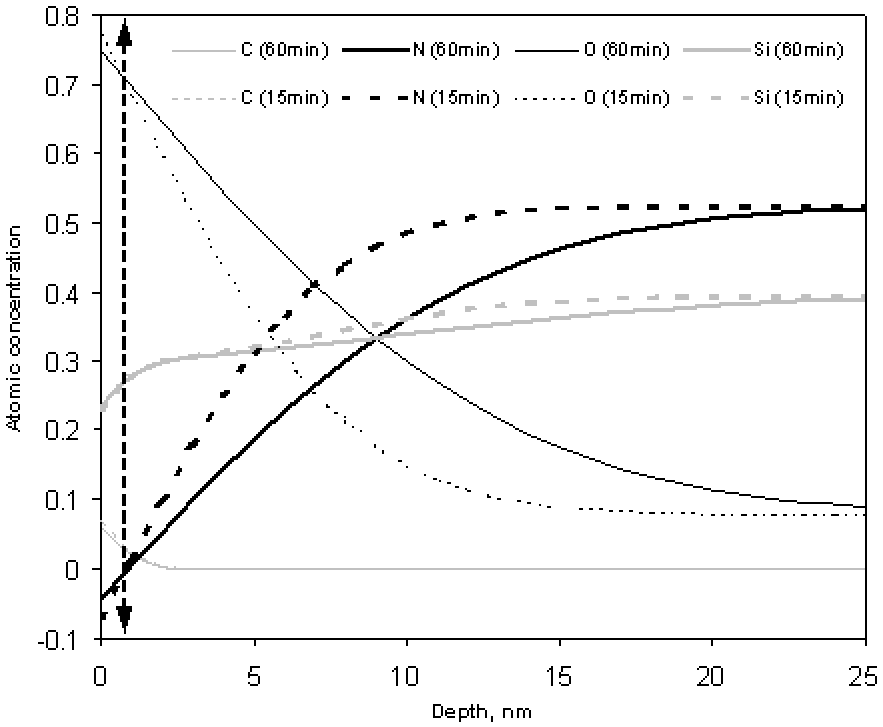

Figure 4-9 Comparison between measured and calculated photoelectron intensity fractions for SiON films after high temperature diffusion

It is obvious from Figure 4-9 that nitrogen is depleted and oxygen enriched near the surface. As a result, nitrogen diffuses from the bulk to the surface while oxygen diffuses in the opposition direction. Relatively, Si does not show significant diffusion. The length scale of diffusion for N and O shown by the 60 min curve is nearly double that of the 15 min curve. Quantitative comparison can be obtained by calculating $\frac{\Delta_i(60\,\text{min})}{\Delta_i(15\,\text{min})}$ values from the data in Table 4-9. The calculated values are 1.73 and 1.66 for nitrogen and oxygen, respectively. Although there is some discrepancy between the calculated values and the theoretical predictions (2 for both N and O from Equation (4-111)), the results are

satisfactory considering that surface contaminants exist and the simplifying assumption that the system follows a strict infinite source diffusion model.

A few models have been proposed to calculate the diffusivity of atomic oxygen in amorphous SiO_2 based on experimental data in the temperature range of 760-1200°C [200]. By extrapolating to 500°C, the diffusivity of O in SiO_2 is estimated to be between 10^{-22} and $10^{-20}m^2/s$. For comparison, the diffusivity of O at 500°C calculated from Δ_i for 60 min diffusion is $1.46\times10^{-20}m^2/s$. Thus, the high temperature study demonstrates that the proposed two-parameter algorithm can be used to quantify diffusion depth profiles near a surface from ARXPS data.

4.5. Quantification of chemical modification near BPDA-PDA surface using ARXPS

Initial chemical mechanical polishing (CMP) studies have shown that BPDA-PDA films polished with a commercial slurry (Klebosol 1501 from Rodel, Inc., pH=10.8) displayed no detectable change in film thickness after 15 min of CMP (platen rotation speed: 30rpm; down force: 2 psi; slurry flow rate: 50 ml/min). The pH value of the slurry was intentionally adjusted by adding NaOH; the polish rate was above 100nm/min for a slurry with pH>13. XPS measurements on BPDA-PDA films after CMP with the pH-adjusted slurry revealed a high level of C and Si contamination, which probably originated from proprietary surfactants, pad materials or silica particles remaining on the surface. Due to the lack of effective cleaning equipment to remove the contaminants, NaOH was used to replace the commercial slurry in order to study the chemical modification of BPDA-PDA surfaces. In CMP using basic slurries, most chemical attack originates from OH^- ions. Therefore, NaOH solutions with comparable pH values are expected to produce similar chemical effects as commercially available basic slurries. To quantify the chemical modification of BPDA-PDA by alkaline solutions, BPDA-PDA films were treated with 0.2M or 1M NaOH aqueous solutions at room temperature for 1 min. Both an untreated and a treated sample were measured with ARXPS and the composition depth profiles near the surface were extracted with the two-parameter algorithm. For treated samples, they were introduced into the XPS sampling chamber immediately (<20 min) after the treatment. XPS measurements were performed after the sample was positioned in the sampling chamber for 2 hours. The details of BPDA-PDA film preparation, chemical

modification and ARXPS measurements can be found in Sections 3.1.1, 3.1.4 and 3.3.1, respectively.

In ARXPS measurements, examination of the data taken during forward runs and backward runs did not reveal a detectable change in angle-dependent photoelectron intensity. This observation eliminates concerns regarding x-ray damage to the sample and also indicates little, if any, alteration of the depth profile during XPS measurements. A small amount of Na was detected on the treated sample with an atomic concentration of ~0.5%. Sodium was not included when the photoelectron intensity fractions of O, N and C were calculated, because sodium served the same role as hydrogen in that it could be bonded to carbonyl groups [99]. All calculations and reconstructed depth profiles using the experimental data were obtained by the two-parameter algorithm based on the infinite source diffusion model. In all regressions, $c_{B,O}$ was fixed at 0.1430 and $c_{B,C}$ at 0.7856. The initial values of other parameters for the regression were: $c_{S,C}$ = -0.06, Δ_C = 2.0 nm^{-1}, $c_{S,O}$ = 0.10, Δ_O = 0.3 nm^{-1}. For comparison, experimental data were also processed using the three-parameter algorithm. However, the parameters obtained with the three-parameter algorithm depended on the initial estimates, analogous to results described in Section 4.3.3.

4.5.1. Comparison between untreated and treated BPDA-PDA samples

ARXPS measurements were conducted on two blank samples (T00_1 and T00_2), two samples treated with 0.2M NaOH at room temperature for 1 min (T02_1, T02_2) and two samples treated with 1.0M NaOH at room temperature for 1 min (T10_1, T10_2). Table 4-10 shows the parameters obtained from regression analyses on experimental ARXPS data.

Table 4-10 Parameters from experimental ARXPS data

Parameters		T00_1	T00_2	T02_1	T02_2	T10_1	T10_2
C	$c_{B,i}$	0.7856	0.7856	0.7856	0.7856	0.7856	0.7856
	$c_{S,i}$	0.0095	0.0081	-0.0119	-0.0178	-0.0078	-0.0132
	Δ_i, nm^{-1}	0.3895	0.2985	0.4090	1.0485	0.0148	0.1564
O	$c_{B,i}$	0.1430	0.1430	0.1430	0.1430	0.1430	0.1430
	$c_{S,i}$	0.0039	0.0081	0.0243	0.0245	0.0188	0.0222
	Δ_i, nm^{-1}	0.3554	2.5125	0.4221	0.4726	0.1210	0.1464

Figure 4-10(a) and (b) show the reconstructed concentration depth profiles of carbon and oxygen, respectively, based on parameters in Table 4-10. The reconstructed depth profiles clearly show differences among the untreated samples, the samples treated with 0.2M NaOH and the samples treated with 1M NaOH. In the untreated samples, there is a small concentration gradient for both O and C, which could be due to data error or to carbonaceous species adsorbed on the sample surface. After NaOH treatment, a significant increase in O concentration and a small decrease in C concentration near the surface region are observed. It is evident that the outmost surface concentrations of oxygen and carbon are 0.163-0.167 and 0.768-0.778 after NaOH treatment. In addition, Figure 4-10 demonstrates that NaOH concentration has little influence on the O and C concentration on the outmost surface as compared to its influence on the penetration depth. This indicates that a reaction limit has been reached on the outmost surface. It is commonly accepted that polyimide converts to poly (amic acid) when it reacts with OH^- [99-102]. Therefore, the theoretical atomic concentrations for the poly (amic acid) -[-

$C_{22}O_6N_2H_{14}$-]- after conversion of BPDA-PDA are 0.733, 0.200 and 0.066 for C, O and N, respectively (H is not considered in the calculation). But not all BPDA-PDA will convert to poly (amic acid) even if it is treated with a strong base for prolonged times at even higher temperatures. Yu and Ko reported the stoichiometric formula of a treated BPDA-PDA surface ($C_{22}N_{1.42}O_{4.68}K_{0.96}$) after treatment with 1M KOH at 80^{o}C for 20 min followed by thorough rinsing with deionized (DI) water and iso-propanol (IPA) [102]. If we neglect K, the resulting atomic concentrations for C, O and N are 0.783, 0.167 and 0.050, respectively. These values are quite similar to the surface concentrations that we calculated from our NaOH-treated samples.

The NaOH concentration has a significant influence on the depth of chemical attack; treatment with 1M NaOH results in a deeper chemically modified region compared with that observed for 0.2M NaOH. While the agreement between concentration profiles of some of the samples treated under the same condition is not precise (especially between carbon profiles of T10_1 and T10_2), the general trend is obvious. Because accurate reconstruction of the depth profile requires high quality photoelectron intensity data with little error, there will inevitably be some uncertainty in the parameter values. More extensive scatter in photoelectron intensity fraction of carbon has been observed than with oxygen, which probably accounts for the larger variation observed for carbon profiles.

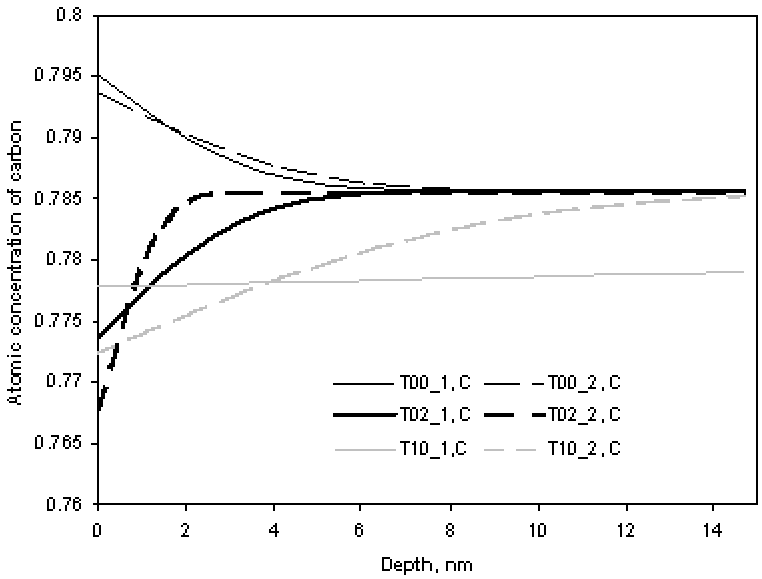

(a) Carbon

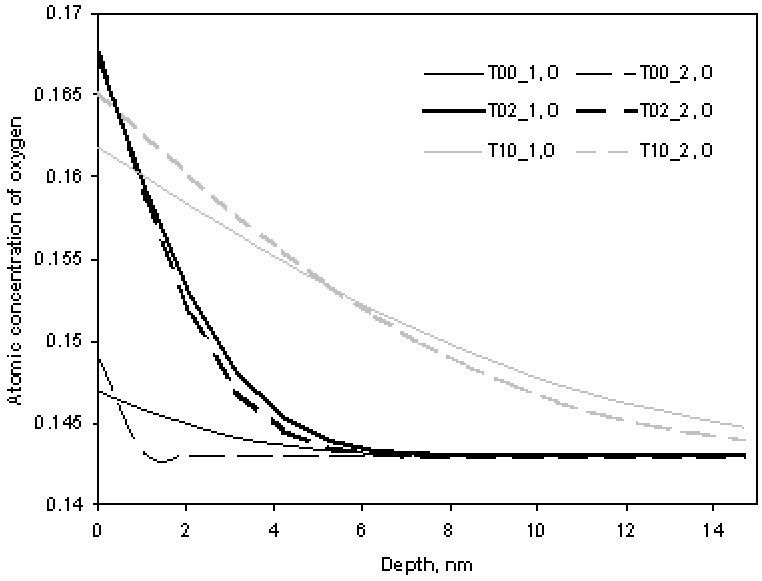

(b) Oxygen

Figure 4-10 Reconstructed depth profiles from ARXPS data

From Figure 4-10, the depth of polyimide chemical modification by 1M NaOH treatment is ~10 nm. Table 4-11 compares the modification depth in our study with previously recorded values. It should be noted that the modification depth reported in this thesis is based on an infinite source model while others have been based on a step model. Clearly, ARXPS can detect changes over a depth range less than that detected by external reflectance infrared spectroscopy (ER-IR) or RBS. For deep and intense chemical modifications, the concentration profile in the modified films will be approximated well with a step model because the near surface regions will undergo extensive modification and concentration changes with depth will be slow. In such cases, ER-IR and RBS are appropriate for quantification of the modification depth. For chemical modifications limited to ~10nm, it is very unlikely that the concentration profile will display a sudden step at a certain depth; thus depth profiles showing gradual changes, like the one based on infinite source diffusion model, will be preferred, and ARXPS is suitable for extracting the depth profiles.

Table 4-11 BPDA-PDA Modifications Depth Comparison

Base	Temperature	Treatment time	Modification depth	Reference
1M NaOH	22^{o}C	1 min	~10 nm	This thesis
1M KOH	40^{o}C	90 min	Not detectable by RBS	101
1M KOH	50^{o}C	20 min	20 nm	99
1M KOH	60^{o}C	60 min	100 nm	101
1M KOH	80^{o}C	12 min	100 nm	101

4.5.2. Change of depth profile with time

One of the samples (T10_1) was placed in the XPS sampling chamber for more than 3 days and profile measurements performed 2 hours and 72 hours after NaOH treatment. Table 4-12 lists the parameters obtained from regression analysis in these two cases.

Table 4-12 Parameters from experimental ARXPS data collected at different times (T10_2)

Parameters		2 hours after NaOH treatment	72 hours after NaOH treatment
C	$c_{B,i}$	0.7856	0.7856
	$c_{S,i}$	-0.0132	-0.0058
	Δ_i, nm^{-1}	0.1564	0.0340
O	$c_{B,i}$	0.01430	0.1430
	$c_{S,i}$	0.0222	0.0204
	Δ_i, nm^{-1}	0.1464	0.1786

Little change is observed in the oxygen depth profile with time. However, the change in carbon depth profiles is more pronounced. As mentioned previously, parameters obtained from carbon analysis have more error due to the error in raw data. In fact, the carbon concentration depth profile obtained for the T10_2 sample 72 hours after NaOH treatment matches closely the one for the T10_1 sample 2 hours after NaOH treatment. This result indicates that there should not be much change in the concentration depth profile near the surface of treated BPDA-PDA films during XPS measurement if the measurement is made immediately (within several hours) after the treatment.

4.5.3. Further discussion of data error

Compared to the depth profiles obtained from the high temperature diffusion studies in Section 4.4, depth profiles resulting from BPDA-PDA modification with NaOH is more sensitive in the sense that the difference between surface and bulk concentrations is smaller in the latter case although the length scale over which such differences occur is similar (10-20nm) in both cases. In order to resolve the depth profiles resulting from BPDA-PDA modification with NaOH, more strict control over data error is required. In the following, a brief discussion is given regarding how to reduce error in data collection to achieve the data quality required by ARXPS analysis (standard deviation of relative error of total photoelectron intensities should be less than 0.30%).

In XPS measurements, the step size and time/step are chosen such that the standard deviation of the relative error in total photoelectron intensity is less than 0.25% for repeated measurements at one location at a specific photoemission angle. In ARXPS measurements, the sample must be re-aligned to maximize signal intensity each time the photoemission angle θ is changed. In most cases, the previous sampling point will not be positioned at exactly the same location within the x-ray beam. It is thus difficult to guarantee that precisely the same area is sampled every time. Thus, point-to-point variation in surface roughness and composition may arise and increase the data error. Reference marks (usually these are pinholes or defects on the film surface that reflect light differently relative to other areas of the film) were used to guarantee that the same area is sampled every time. Since the mid-point of a straight line will not change with the observation angle, the sample position was adjusted during realignment so that under microscopic examination, the sampling point fell in the middle of the line established by

two separate reference marks. By doing so, data quality was indeed improved. Another common way of reducing data error is to perform repeated measurements and use average values. That is, if n variables all follow the same distribution, then the standard deviation of the average of the n variables is reduced by a factor of $\sqrt{n}$. This is the reason for performing ARXPS data collection with decreasing (forward) as well as increasing (backward) angle increments, and repeating these measurements several times.

Table 4-13 Estimation of random error in raw data

		T00_1		T10_1	
		C	O	C	O
Parameters	$c_{B,i}$	0.7856	0.1430	0.7856	0.1430
	$c_{S,i}$	-0.0656	0.0051	-0.0132	0.0222
	Δ_i, nm^{-1}	45.6049	0.0282	0.1564	0.1464
Standard deviation of $\varepsilon_{est,raw}$		0.0059		0.0045	
Standard deviation of $\varepsilon_{est,ave}$		0.0024		0.0019	

One way to investigate the data error is to reproduce the photoelectron intensity fractions based on parameters obtained from regression and estimate the data error by comparing the reproduced (or generated) results to the measured photoelectron intensity fractions, that is, $\varepsilon_{est}=(I/\Sigma I)_{calculated}-(I/\Sigma I)_{measured}$. Since four measurements are performed for each photoemission angle, ε_{est} can be obtained for both raw and averaged data, and are denoted as $\varepsilon_{est,raw}$ and $\varepsilon_{est,ave}$, respectively. The results of error estimation are shown in Table 4-13. Clearly, the standard deviation of $\varepsilon_{est,ave}$ is less than half that of $\varepsilon_{est,raw}$, which indicates that repeated measurements and data averaging reduce random error in the raw data.

4.6. Summary

This chapter demonstrates an approach to quantify the depth of chemical modification using a technique based on ARXPS. Section 4.1 presents a comprehensive literature review on different techniques that have been reported to extract chemical composition depth profiles from ARXPS data. In Section 4.2, an iterative algorithm is proposed to extract depth profiles based on Fick's second law of diffusion in a multi-element system from data supplied by ARXPS. Parameters related to the concentration profiles are obtained by fitting the experimental angle-dependent photoelectron intensity fractions to predictions from the algorithm. Section 4.3 describes the influence of errors in the raw data and demonstrates the robustness of the algorithm from simulations using an infinite source diffusion model. The correctness of the algorithm is verified in Section 4.4, where chemical composition depth profiles resulting from high temperature diffusion near oxygen-doped silicon nitride film surfaces are extracted from ARXPS. In Section 4.5, ARXPS is used to extract chemical composition depth profiles near surfaces of BPDA-PDA films modified with NaOH solutions. These studies clearly demonstrate that the technique developed in this chapter can be used to quantify the depth of chemical modification of BPDA-PDA surfaces treated with alkaline solutions. Furthermore, the methods developed should be general in their application to other systems (film/chemical component) of technological interest.

CHAPTER 5

QUANTIFICATION OF MECHANICAL INFLUENCE USING POLARIZED INFRARED SPECTROSCOPY

In this chapter, a method is described to quantify mechanical influence near poly (biphenyl dianhydride-p-phenylenediamine) (BPDA-PDA) surface during chemical mechanical polishing (CMP). Because polymer chains tend to realign when subject to external shear forces, the degree of polymer chain reorientation can be used to infer the magnitude of shear force that the polymer surface experiences during CMP. The chapter begins with a brief literature review on different methods that have been developed to quantify rubbing induced molecular alignment near polymer surface, followed by a detailed derivation of a theoretical framework of infrared (IR) spectral simulation, which will serve as a basis for extracting quantitative polymer chain reorientation information from polarized infrared spectra. Three-dimensional complex refractive indices of BPDA-PDA films are crucial in inferring polymer chain orientation. A new method to extract complex refractive indices of films with biaxial symmetry from polarized transmission and reflection spectra is described. Theoretical analysis demonstrates that the reflectance/transmittance ratio (R/T ratio) of two films of different thicknesses but with the same optical anisotropy is a simple function of refractive index (n) and extinction coefficient (k). For films with biaxial symmetry, components of n and k on symmetric axes can be extracted from either s- or p-polarized R/T ratios if the film thickness values are known. Finally, polarized IR spectra are collected on a BPDA-PDA film after CMP and the IR dichroism is used to quantify the depth of polymer chain reorientation.

5.1. Literature review on quantification of rubbing induced molecular alignment near polymer surface

Rubbing of a polymer surface with a dry cloth is a process very similar to chemical mechanical polishing. The main difference is the latter uses slurry to facilitate material removal. A lot of research has been carried out on the rubbing induced molecular alignment in polymer films. Although the main purpose of such studies is to understand the mechanism of molecular alignment related to liquid crystals or to test the abrasion resistance of polymer films, the results and techniques are relevant to CMP study considering the similarity between the two processes. In Section 2.3.8, studies on mechanical rubbing of BPDA-PDA surface has been briefly reviewed, different techniques such as near-edge x-ray absorption fine structure spectroscopy (NEXAFS) [103], x-ray photoelectron emission microscopy (X-PEEM) [104], atomic force microscopy (AFM) [105] and polarized IR spectroscopy [65] have been employed to determine, either quantitatively or semi-quantitatively, the rubbing induced molecular alignment near the surface. In these studies, typical load applied for rubbing was ~2g/cm^2 (or ~0.03 psi) and the dry cloth was moved at a speed of 30 cm/min relative to the BPDA-PDA surface over a distance up to 300 cm. The rubbing process could lead to the propagation of molecular alignment into the film for ~10nm.

In addition to BPDA-PDA films, studies on rubbing induced molecular alignment have also been performed on some other polymer films using different methods. Optical second harmonic generation (SHG) was used to study chain orientation on rubbed polyimide surfaces [189,190]. SHG is a highly surface specific technique, which provides information on surface molecular orientation based on different input/output polarization

combinations [189]. Optical phase retardation in a polymer layer induced during the rubbing treatment was utilized in studying the effect of various rubbing parameters on molecular reorientation of thin polyimide layers [189]. The observed phase retardation could be related to molecular reorientation in the polymer layer. Optical phase retardation was used together with infrared dichroism and SHG method to quantify the molecular reorientation near the surface [191,192]. Experiments showed that the penetration depth of the rubbing influence could be varied from less than 10nm to more than 60nm by variation in rubbing conditions [191]. Reflectance difference spectroscopy (RDS) was used to measure the in-plane optical anisotropy of rubbed polystyrene films and the molecular alignment of the rubbed films was determined from IR dichroism [193]. Sum-frequency generation vibrational spectroscopy is another surface sensitive technique that can be used to probe surface molecular orientation [194,195]. It is a second-order non-linear optical process and it is forbidden in media with inversion symmetry, but allowed at interfaces where the inversion symmetry is necessarily broken. Therefore, it is particularly sensitive to some interfacial structure between two media. It can provide information not only on the average molecular orientation and order parameter but also on the orientational distribution [194].

Based on availability of resources, polarized IR spectroscopy was chosen from above methods as the technique to quantify chain orientations induced by CMP to evaluate the mechanical influence. Quantitative chain orientation information can be obtained by fitting simulated spectra to experimental ones, which requires a theoretical framework for spectral simulation and information about vibrational modes of the material. The theoretical framework used in this thesis is based on a 4×4 matrix method and is

described in detail in Section 5.2. The vibrational modes of the material can be inferred from the complex refractive index spectra. Sections 5.3 and 5.4 develop a new method (R/T ratio method) to extract complex refractive indices of films with biaxial symmetry, e.g. BPDA-PDA, from polarized transmission and reflection spectra. Section 5.5 demonstrates how to use the polarized infrared spectra to extract quantitative information on mechanical influence during CMP.

5.2. IR Spectra Simulation

5.2.1. Maxwell's equations

Maxwell's equations are the most fundamental equations for electromagnetic wave propagation. The four equations are [181]:

$$\nabla \times \mathbf{E} + \frac{\partial \mathbf{B}}{\partial t} = 0 \tag{5-1}$$

$$\nabla \times \mathbf{H} - \frac{\partial \mathbf{D}}{\partial t} = \mathbf{J} \tag{5-2}$$

$$\nabla \cdot \mathbf{D} = q \tag{5-3}$$

$$\nabla \cdot \mathbf{B} = 0 \tag{5-4}$$

In these equations, **E** and **H** are the electric field vector (in volts per meter) and the magnetic field vector (in amperes per meter), respectively. The quantities **D** and **B** are called the electric displacement (in coulombs per square meter) and the magnetic induction (in webers per square meter), respectively. The quantities q and **J** are the electric charge (in coulombs per cubic meter) and current density (in amperes per square meter), respectively [181].

In IR spectral study, the electromagnetic radiation propagation usually takes place in regions of space where both charge density and current density are zero. Electromagnetic fields occurring in media in the absence of charges are called electromagnetic waves [181].

The Maxwell's equations consist of 8 scalar equations that relate a total of 12 variables, 3 for each of the 4 vectors **E**, **H**, **D** and **B**. A unique solution to these equations requires the

relationship between **B** and **H** and that between **E** and **D** be known. Such relationship is described by the so-called constitutive equations (or material equations),

$$\mathbf{D} = \boldsymbol{\varepsilon}\mathbf{E} = \varepsilon_0\mathbf{E} + \mathbf{P} \tag{5-5}$$

$$\mathbf{B} = \boldsymbol{\mu}\mathbf{H} = \mu_0\mathbf{H} + \mathbf{M} \tag{5-6}$$

where the constitutive parameters $\boldsymbol{\varepsilon}$ and $\boldsymbol{\mu}$ are tensors of rank 2 and are known as the dielectric tensor (or permittivity tensor) and the permeability tensor, respectively; **P** and **M** are electric and magnetic polarizations, respectively. The constant ε_0 is the permittivity of a vacuum and has a value of 8.854×10^{-12}F/m. The constant μ_0 is the permeability of a vacuum and by definition has the exact value of $4\pi\times10^{-7}$H/m [181].

5.2.2. Boundary conditions

To determine the reflectance and transmittance of electromagnetic radiation through a layered medium, it is important to know the continuity of some components of the field vectors at the dielectric interfaces between layers. Such continuity conditions can be described by the following four equations.

$$\mathbf{n}\cdot(\mathbf{B}_2 - \mathbf{B}_1) = 0 \tag{5-7}$$

$$\mathbf{n}\cdot(\mathbf{D}_2 - \mathbf{D}_1) = \sigma \tag{5-8}$$

$$\mathbf{n}\times(\mathbf{E}_2 - \mathbf{E}_1) = 0 \tag{5-9}$$

$$\mathbf{n}\times(\mathbf{H}_2 - \mathbf{H}_1) = \mathbf{K} \tag{5-10}$$

In the above four equations, the subscript 1 and 2 stand for the two media separated by the boundary. **n** is the unite normal to the surface directed from medium 1 into medium 2, σ is the surface charge density (in coulombs per square meter) and **K** is the surface

current density (in amperes per meter). In other words, the normal component of the magnetic induction **B** is always continuous, and the difference between the normal components of the electric displacement **D** is equal in magnitude to the surface charge density σ, the tangential components of the electric field vector **E** is always continuous at the boundary surface, and the difference between the tangential components of the magnetic field vector **H** is equal to the surface current density **K**. In IR spectral study, the surface charge density σ and the surface current density **K** usually both vanish.

5.2.3. Plane waves in homogeneous and anisotropic media

Plane-wave propagation in an anisotropic media is determined by the dielectric tensor ε that links the displacement vector and the electric vector:

$$\mathbf{D} = \boldsymbol{\varepsilon}\mathbf{E} \tag{5-11}$$

In following discussion, the Cartesian coordinate system is chosen such that the *z*-axis is normal to the interfaces.

In nonmagnetic (i.e., $\mu=\mu_0$) materials, this tensor is symmetric:

$$\varepsilon_{ij} = \varepsilon_{ji} \tag{5-12}$$

Because of its symmetric nature, it is always possible to find three mutually orthogonal axes in such a way that the off-diagonal elements vanish, leaving

$$\boldsymbol{\varepsilon} = \varepsilon_0 \begin{pmatrix} (n_{x'} - ik_{x'})^2 & 0 & 0 \\ 0 & (n_{y'} - ik_{y'})^2 & 0 \\ 0 & 0 & (n_{z'} - ik_{z'})^2 \end{pmatrix} = \begin{pmatrix} \varepsilon_{x'} & 0 & 0 \\ 0 & \varepsilon_{y'} & 0 \\ 0 & 0 & \varepsilon_{z'} \end{pmatrix} \tag{5-13}$$

where $\varepsilon_{x'}$, $\varepsilon_{y'}$ and $\varepsilon_{z'}$ are the principal dielectric constants and $n_{x'}$ -$ik_{x'}$, $n_{y'}$ -$ik_{y'}$ and $n_{z'}$ -$ik_{z'}$ are the principal complex indices of refraction. These directions (*x'*, *y'* and *z'*) are called the principle dielectric axes [181].

The orientations of the crystal axis are described by the Euler's angles ϑ, φ, ζ with respect to a fixed *xyz* coordinate. In the Euler rotation, axes instead of objects are rotated. By convention, Euler rotation transforms from the space axes to the body axes, as shown in Figure 5-1.

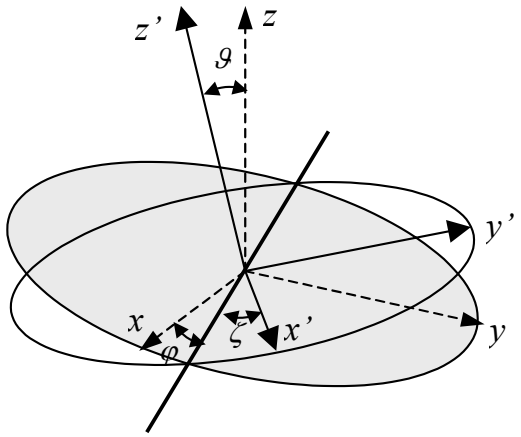

Figure 5-1 Euler rotation

The dielectric tensor in the *xyz* coordinate system is given by:

$$\boldsymbol{\varepsilon} = \mathbf{A}\begin{pmatrix} \varepsilon_{x'} & 0 & 0 \\ 0 & \varepsilon_{y'} & 0 \\ 0 & 0 & \varepsilon_{z'} \end{pmatrix}\mathbf{A}^{-1} \tag{5-14}$$

where **A** is the coordinate rotation matrix, given by:

$$\mathbf{A} = \begin{pmatrix} \cos\zeta\cos\varphi - \cos\vartheta\sin\varphi\sin\zeta & -\sin\zeta\cos\varphi - \cos\vartheta\sin\varphi\cos\zeta & \sin\vartheta\sin\varphi \\ \cos\zeta\sin\varphi + \cos\vartheta\cos\varphi\sin\zeta & -\sin\zeta\sin\varphi + \cos\vartheta\cos\varphi\cos\zeta & -\sin\vartheta\cos\varphi \\ \sin\vartheta\sin\zeta & \sin\vartheta\cos\zeta & \cos\vartheta \end{pmatrix} \tag{5-15}$$

To study propagation of electromagnetic wave along a general direction, we assume a monochromatic plane wave with an electric field vector:

$$\mathbf{E}\exp[i(\omega t - \mathbf{k}\cdot\mathbf{r})] \tag{5-16}$$

and a magnetic field vector

$$\mathbf{H}\exp[i(\omega t - \mathbf{k}\cdot\mathbf{r})] \tag{5-17}$$

where **k** is the wave vector $\mathbf{k}=(\omega/c)n\mathbf{s}$, with **s** as a unit vector in the direction of propagation, ω the frequency, c the speed of light in vacuum. The phase velocity c/n, or equivalently n, is to be determined. Substitution for **E** and **H** in Equations (5-16) and (5-17) into Equations (5-1) and (5-2) yields:

$$\mathbf{k}\times\mathbf{E} = \omega\mu\mathbf{H} \tag{5-18}$$

$$\mathbf{k}\times\mathbf{H} = -\omega\boldsymbol{\varepsilon}\mathbf{E} = -\omega\mathbf{D} \tag{5-19}$$

Elimination of H from equations (5-18) and (5-19) leads to:

$$\mathbf{k}\times(\mathbf{k}\times\mathbf{E}) + \omega^2\mu\boldsymbol{\varepsilon}\mathbf{E} = 0 \tag{5-20}$$

For electromagnetic wave propagation in a layered structure shown in Figure 5-2, The wave vector **k** can be described in terms of X, Y and Z components termed α, β, and γ, respectively, for convenience. Since each layer is assumed homogeneous, α and β remain constant throughout the layered media. Therefore, the two components (α, β) of the

propagation vector are chosen as the dynamical variables characterizing the electromagnetic waves propagating in the layered media.

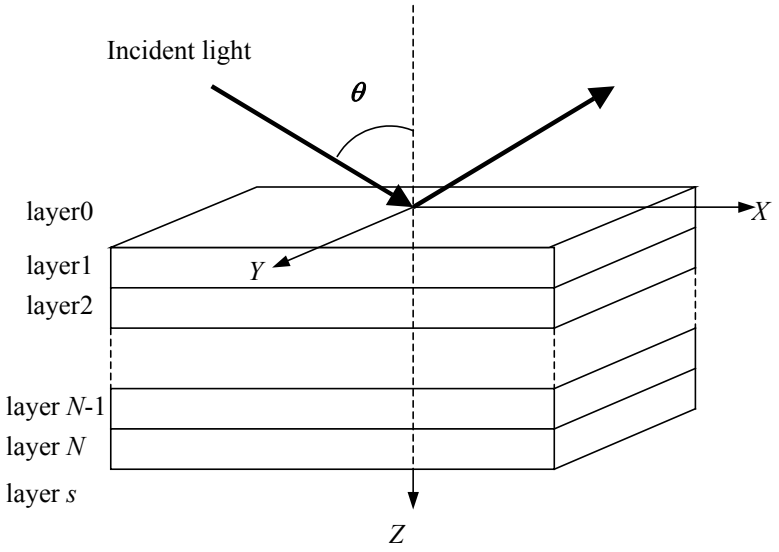

Figure 5-2 Geometry of electromagnetic wave propagation in a layered structure

Given α and β, the z component γ is determined directly from equation (5-20), or equivalently,

$$\begin{pmatrix} \omega^2\mu\varepsilon_{xx} - \beta^2 - \gamma^2 & \omega^2\mu\varepsilon_{xy} + \alpha\beta & \omega^2\mu\varepsilon_{xz} + \alpha\gamma \\ \omega^2\mu\varepsilon_{yx} + \alpha\beta & \omega^2\mu\varepsilon_{yy} - \alpha^2 - \gamma^2 & \omega^2\mu\varepsilon_{yz} + \beta\gamma \\ \omega^2\mu\varepsilon_{zx} + \alpha\gamma & \omega^2\mu\varepsilon_{zy} + \beta\gamma & \omega^2\mu\varepsilon_{zz} - \alpha^2 - \beta^2 \end{pmatrix} \times \begin{pmatrix} E_x \\ E_y \\ E_z \end{pmatrix} = 0 \quad (5\text{-}21)$$

In order to have a non-trivial plane-wave solution, the determinant of the matrix in Equation (5-21) must vanish, that is,

$$\det\begin{pmatrix} \omega^2\mu\varepsilon_{xx}-\beta^2-\gamma^2 & \omega^2\mu\varepsilon_{xy}+\alpha\beta & \omega^2\mu\varepsilon_{xz}+\alpha\gamma \\ \omega^2\mu\varepsilon_{yx}+\alpha\beta & \omega^2\mu\varepsilon_{yy}-\alpha^2-\gamma^2 & \omega^2\mu\varepsilon_{yz}+\beta\gamma \\ \omega^2\mu\varepsilon_{zx}+\alpha\gamma & \omega^2\mu\varepsilon_{zy}+\beta\gamma & \omega^2\mu\varepsilon_{zz}-\alpha^2-\beta^2 \end{pmatrix}=0 \qquad (5\text{-}22)$$

This results in a quartic equation in γ which yields four roots γ_σ, σ=1,2,3,4. These roots may be either real or complex. Since all the coefficients of this quartic equation are real, complex roots are always in conjugate pairs.

The electric field of the plane electromagnetic waves can thus be written as

$$\mathbf{E}=\sum_{\sigma=1}^{4} A_\sigma \mathbf{p}_\sigma \exp\left[i(\varpi t-\alpha x-\beta y-\gamma_\sigma z)\right] \qquad (5\text{-}23)$$

where

$$\mathbf{p}_\sigma = N_\sigma \begin{pmatrix} (\omega^2\mu\varepsilon_{yy}-\alpha^2-\gamma_\sigma^2)(\omega^2\mu\varepsilon_{zz}-\alpha^2-\beta^2)-(\omega^2\mu\varepsilon_{yz}+\beta\gamma_\sigma)^2 \\ (\omega^2\mu\varepsilon_{yz}+\beta\gamma_\sigma)(\omega^2\mu\varepsilon_{xz}+\alpha\gamma_\sigma)-(\omega^2\mu\varepsilon_{xy}+\alpha\beta)(\omega^2\mu\varepsilon_{zz}-\alpha^2-\beta^2) \\ (\omega^2\mu\varepsilon_{xy}+\alpha\beta)(\omega^2\mu\varepsilon_{yz}+\beta\gamma_\sigma)-(\omega^2\mu\varepsilon_{xz}+\alpha\gamma_\sigma)(\omega^2\mu\varepsilon_{yy}-\alpha^2-\gamma_\sigma^2) \end{pmatrix} \qquad (5\text{-}24)$$

In Equation (5-24), N_σ's are the normalization constants such that $\mathbf{p}_\sigma \cdot \mathbf{p}_\sigma = 1$.

5.2.4. Matrix method

The materials are assumed to be non-magnetic so that μ=constant throughout the whole layered medium. The dielectric permittivity tensor ε in the *xyz* coordinates is given by

$$\boldsymbol{\varepsilon}=\begin{cases} \boldsymbol{\varepsilon}(0) & z<z_0 \\ \boldsymbol{\varepsilon}(1) & z_0<z<z_1 \\ \boldsymbol{\varepsilon}(2) & z_1<z<z_2 \\ \vdots & \\ \boldsymbol{\varepsilon}(N) & z_{N-1}<z<z_N \\ \boldsymbol{\varepsilon}(s) & z_N<z \end{cases} \qquad (5\text{-}25)$$

The electric field distribution within each homogeneous anisotropic layer can be expressed as a sum of those four partial waves [Equation(5-23)]. The complex amplitudes of these four partial waves constitute the components of a column vector. The electromagnetic field in the *n*th layer of the anisotropic layered medium can thus be represented by a column vector $A_\sigma(n)$, σ=1, 2, 3, 4. The electric field distribution in the same *n*th layer can be written as:

$$\mathbf{E}(n) = \sum_{\sigma=1}^{4} A_\sigma(n)\mathbf{p}_\sigma \exp\{i[\omega t - \alpha x - \beta y - \gamma_\sigma(n)(z - z_n)]\} \tag{5-26}$$

The column vectors are not independent of each other. They are related through the continuity conditions at the interfaces. As a matter of fact, only one vector (or any four components of four different vectors) can be arbitrarily chosen. The magnetic field distribution is obtained using Maxwell's equations and is given by:

$$\mathbf{H}(n) = \sum_{\sigma=1}^{4} A_\sigma(n)\mathbf{q}_\sigma \exp\{i[\omega t - \alpha x - \beta y - \gamma_\sigma(n)(z - z_n)]\} \tag{5-27}$$

$$\mathbf{q}_\sigma(n) = \frac{c\mathbf{k}_\sigma(n)}{\omega\mu} \times \mathbf{p}_\sigma(n) \tag{5-28}$$

$$\mathbf{k}_\sigma(n) = \alpha\mathbf{x} + \beta\mathbf{y} + \gamma_{\sigma(x)}\mathbf{z} \tag{5-29}$$

Imposing the continuity of E_x, E_y, H_x and H_y at the interface z=z_{n-1} leads to:

$$\sum_{\sigma=1}^{4} A_\sigma(n-1)\mathbf{p}_\sigma(n-1)\cdot\mathbf{x} = \sum_{\sigma=1}^{4} A_\sigma(n)\mathbf{p}_\sigma(n)\cdot\mathbf{x}\exp[i\gamma_\sigma(n)t_n] \tag{5-30}$$

$$\sum_{\sigma=1}^{4} A_\sigma(n-1)\mathbf{p}_\sigma(n-1)\cdot\mathbf{y} = \sum_{\sigma=1}^{4} A_\sigma(n)\mathbf{p}_\sigma(n)\cdot\mathbf{y}\exp[i\gamma_\sigma(n)t_n] \tag{5-31}$$

$$\sum_{\sigma=1}^{4} A_\sigma(n-1)\mathbf{q}_\sigma(n-1)\cdot\mathbf{x} = \sum_{\sigma=1}^{4} A_\sigma(n)\mathbf{q}_\sigma(n)\cdot\mathbf{x}\exp\left[i\gamma_\sigma(n)t_n\right] \tag{5-32}$$

$$\sum_{\sigma=1}^{4} A_\sigma(n-1)\mathbf{q}_\sigma(n-1)\cdot\mathbf{y} = \sum_{\sigma=1}^{4} A_\sigma(n)\mathbf{q}_\sigma(n)\cdot\mathbf{y}\exp\left[i\gamma_\sigma(n)t_n\right] \tag{5-33}$$

where $t_n=z_n-z_{n-1}$, $n=1,2,...,N$.

Equations (5-30) - (5-33) can be rewritten as a matrix equation:

$$\begin{pmatrix} A_1(n-1) \\ A_2(n-1) \\ A_3(n-1) \\ A_4(n-1) \end{pmatrix} = \mathbf{D}^{-1}(n-1)\mathbf{D}(n)\mathbf{P}(n)\begin{pmatrix} A_1(n) \\ A_2(n) \\ A_3(n) \\ A_4(n) \end{pmatrix} \tag{5-34}$$

where

$$\mathbf{D}(n) = \begin{pmatrix} \mathbf{x}\cdot\mathbf{p}_1(n) & \mathbf{x}\cdot\mathbf{p}_2(n) & \mathbf{x}\cdot\mathbf{p}_3(n) & \mathbf{x}\cdot\mathbf{p}_4(n) \\ \mathbf{y}\cdot\mathbf{q}_1(n) & \mathbf{y}\cdot\mathbf{q}_2(n) & \mathbf{y}\cdot\mathbf{q}_3(n) & \mathbf{y}\cdot\mathbf{q}_4(n) \\ \mathbf{y}\cdot\mathbf{p}_1(n) & \mathbf{y}\cdot\mathbf{p}_2(n) & \mathbf{y}\cdot\mathbf{p}_3(n) & \mathbf{y}\cdot\mathbf{p}_4(n) \\ \mathbf{x}\cdot\mathbf{q}_1(n) & \mathbf{x}\cdot\mathbf{q}_2(n) & \mathbf{x}\cdot\mathbf{q}_3(n) & \mathbf{x}\cdot\mathbf{q}_4(n) \end{pmatrix} \tag{5-35}$$

$$\mathbf{P}(n) = \begin{pmatrix} \exp\left[i\gamma_1(n)t_n\right] & 0 & 0 & 0 \\ 0 & \exp\left[i\gamma_2(n)t_n\right] & 0 & 0 \\ 0 & 0 & \exp\left[i\gamma_3(n)t_n\right] & 0 \\ 0 & 0 & 0 & \exp\left[i\gamma_4(n)t_n\right] \end{pmatrix} \tag{5-36}$$

The matrices $\mathbf{D}(n)$ are called dynamical matrices because they depend only on the direction of polarization of those four partial waves. The dynamical matrices are defined in a way such that they are block diagonalized when the mode coupling disappears. This requires that A_1 and A_2 are the amplitudes of the plane waves of the same mode (polarization) such that the plane wave with amplitude A_1 propagates in the direction with a positive Z component, whereas the plane wave with amplitude A_2 propagates in the

direction with a negative Z component. Likewise, A_3 and A_4 are the amplitudes of the plane wave of the same mode, propagating in directions with positive and negative Z components, respectively. The matrices $\mathbf{P}(n)$ are called propagation matrices. The transfer matrix is defined as:

$$\mathbf{T}_{n-1,n} = \mathbf{D}^{-1}(n-1)\mathbf{D}(n)\mathbf{P}(n) \tag{5-37}$$

for n=1,...,N. Since there is no thickness value for the last layer (s), the definition of transfer matrix is slightly different:

$$\mathbf{T}_{N,s} = \mathbf{D}^{-1}(N)\mathbf{D}(s) \tag{5-38}$$

Equation (5-34) can thus be written as

$$\begin{pmatrix} A_1(n-1) \\ A_2(n-1) \\ A_3(n-1) \\ A_4(n-1) \end{pmatrix} = \mathbf{T}_{n-1,n} \begin{pmatrix} A_1(n) \\ A_2(n) \\ A_3(n) \\ A_4(n) \end{pmatrix} \tag{5-39}$$

The matrix equation that related $A(0)$ and $A(\mathrm{s})$ is therefore given by

$$\begin{pmatrix} A_1(0) \\ A_2(0) \\ A_3(0) \\ A_4(0) \end{pmatrix} = \mathbf{T}_{0,1}\mathbf{T}_{1,2}\mathbf{T}_{2,3}\cdots\mathbf{T}_{N-1,N}\mathbf{T}_{N,s} \begin{pmatrix} A_1(s) \\ A_2(s) \\ A_3(s) \\ A_4(s) \end{pmatrix} \tag{5-40}$$

Figure 5-3 is a schematic representation of Equation (5-40). Because s is the last phase, there is no backward wave, there are only two non-zero terms for $A_1(s) \sim A_4(s)$. Since the intensity of electromagnetic wave is proportional to AA^* (or square of modulus of A), the reflectance and transmittance spectra can be readily calculated.

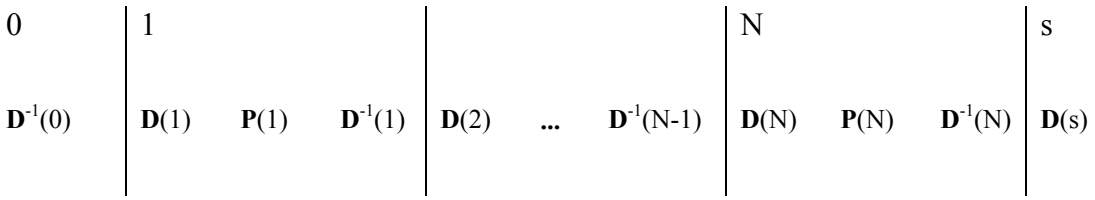

Figure 5-3 Schematic representation of the matrix method

The reflectance and transmittance spectra of a layered structure are solely determined by the material properties (dielectric constant, or equivalently, complex refractive indices) and layer thicknesses, properties of electromagnetic wave (wavelength) and system geometry (the incident angle). In practice, the wavelength range is usually determined by the specific spectrometer and the system geometry chosen by the experimenter. The polarized transmittance (or reflectance) spectra can be used to derive the thickness of a mechanically modified layer if the complex refractive indices of the modified layer are known beforehand. The complex refractive indices of the modified layer can be calculated given a specific physical model of modification if quantitative information on all molecular vibration modes of interest is available.

The following section is devoted to a newly developed method (R/T ratio method) that can be used to extract complex refractive indices of films with biaxial symmetry and further to obtain quantitative information on the molecular vibration modes.

5.3. R/T ratio method

Considerable interest exists in experimentally determining the refractive index (n) and the extinction coefficient (k), or complex refractive index (n-ik), of biaxially or uniaxially symmetric films [201-207]. Several techniques are currently available to determine anisotropic complex refractive indices of thin films such as prism coupling techniques [201,202], spectroscopic ellipsometry [203-205], attenuated total reflection spectroscopy (ATR) [206] and methods based on transmission and reflection spectra [207].

In prism coupling measurements, a thin film is contacted with a prism and the reflected intensity of light through the prim changes with incident angle as a result of guided propagation of light in the thin film. The dependence of reflectivity on incident angle of s- and p-polarized light can be used to derive anisotropic n and k values [201,202]. In spectroscopic ellipsometry, the difference in the phase of reflected or transmitted s- and p-polarized light and the ratio between the changes in amplitude are measured and the anisotropic n and k are obtained by fitting the simulated data to the measured values [111]. In data fitting, a model describing the relation between n, k and the wavelength is usually assumed [111,204,205]. In ATR spectroscopy, n and k are calculated from the reflectivity data under total reflection mode. A model describing the relation among n, k and the wavelength must be assumed [206]. In addition to the above techniques, methods that use transmission or reflection spectra to extract anisotropic complex refractive indices will be of special interest since collection of transmission and reflection spectra is routine in many laboratories. For instance, a procedure has been developed to obtain the in-plane and out-of-plane refractive indices of a uni-axially oriented film from a normalized transmission spectrum at normal incidence and a p-polarized reflection

spectrum at grazing incidence, respectively [207]. The procedure used a matrix formalism to simulate spectra of anisotropic multilayer systems and the Kramers-Kronig relationship to describe the interdependence of n and k. The film thickness was obtained from spectroscopic ellipsometry measurements and was subsequently used in the spectral simulation [207].

The prism coupling technique can be used to extract n and k without assuming a relationship between n and k. However, it is limited to the extraction of n and k at specific laser wavelengths such as 632.8nm, 1550nm, etc. Other methods can generate continuous n and k spectra over a wavelength range. Although theoretically these methods can extract n and k on a wavelength-wise basis without assuming a relationship between n and k, they usually use an assumed relationship between n and k so that the number of parameters is greatly reduced and the solution to the n and k spectra can be obtained using a reasonable amount of computing time. The assumption of a relationship between n and k demands preliminary knowledge about the physics of the film. In this section, a new reflectance/transmittance ratio method is proposed to extract the complex refractive indices of absorbing freestanding films with biaxial symmetry from transmission and reflection spectra at oblique incidence. This method can generate the complex refractive index spectra from a series of films of different thicknesses but with the same optical anisotropy. The inherent mathematic simplicity of this method enables extraction of n and k on a wavelength-wise basis without assuming a relationship between n and k.

5.3.1. R/T ratio formula

For a system consisting only of a freestanding film in air (Figure 5-4), the total number of layers will be 3, and $A_1(0)$, $A_2(0)$ and $A_1(2)$ are specified as the complex amplitudes of the

incident, reflected and transmitted p-polarized light, respectively; $A_3(0)$, $A_4(0)$ and $A_3(2)$ are specified as the complex amplitudes of the incident, reflected and transmitted s-polarized light, respectively. Transmittance (T_p) and reflectance (R_p) of p-polarized light can be calculated from [182]:

$$T_p = \frac{|A_1(2)|^2}{|A_1(0)|^2} \tag{5-41}$$

$$R_p = \frac{|A_2(0)|^2}{|A_1(0)|^2} \tag{5-42}$$

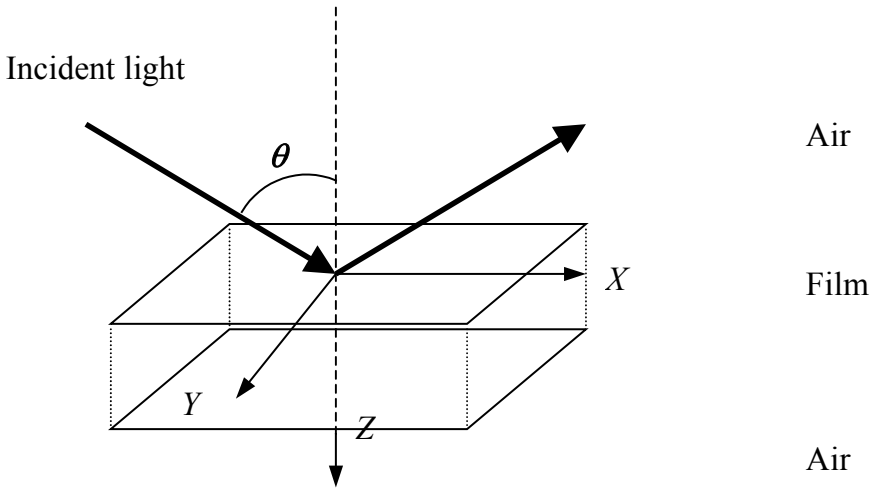

Figure 5-4 Geometry of light propagation in a freestanding film in the air

Similarly, transmittance (T_s) and reflectance (R_s) of s-polarized light can be calculated from:

$$T_s = \frac{|A_3(2)|^2}{|A_3(0)|^2} \tag{5-43}$$

$$R_s = \frac{|A_4(0)|^2}{|A_3(0)|^2} \tag{5-44}$$

In the following, we assume that the film is absorbing and is biaxial (with the symmetry axes coinciding with *X*, *Y* and *Z* axes) and use n_x, n_y, n_z and k_x, k_y, k_z to denote the *X*, *Y* and *Z* components of *n* and *k*, respectively. Let n_0 be the refractive index of air, *t* the film thickness, ω the frequency of incident light and *c* the speed of light in vacuum. If the light is incident from vacuum (or air) in the *XZ* plane with an incident angle of θ (Figure 5-4), T_p and R_p can be calculated from the following two equations (Appendix D):

$$1/T_p = \left|(\frac{1}{2}+\frac{H}{4}+\frac{1}{4H})\exp[i\gamma_1(1)t]+(\frac{1}{2}-\frac{H}{4}-\frac{1}{4H})\exp[-i\gamma_1(1)t]\right|^2 \tag{5-45}$$

$$1/R_p = \left|\frac{(\frac{1}{2}+\frac{H}{4}+\frac{1}{4H})\exp[i\gamma_1(1)t]+(\frac{1}{2}-\frac{H}{4}-\frac{1}{4H})\exp[-i\gamma_1(1)t]}{(\frac{H}{4}-\frac{1}{4H})\exp[i\gamma_1(1)t]-(\frac{H}{4}-\frac{1}{4H})\exp[-i\gamma_1(1)t]}\right|^2 \tag{5-46}$$

where

$$H = \frac{n_0^2\sqrt{(n_z-ik_z)^2-\sin^2\theta}}{(n_x-ik_x)(n_z-ik_z)\sqrt{n_0^2-\sin^2\theta}} \tag{5-47}$$

and

$$\gamma_1(1) = (\omega/c)\frac{(n_x-ik_x)}{(n_z-ik_z)}\sqrt{(n_z-ik_z)^2-\sin^2\theta} \tag{5-48}$$

Likewise, T_s and R_s can be calculated from the following two equations:

$$1/T_s = \left|(\frac{1}{2}+\frac{G}{4}+\frac{1}{4G})\exp[i\gamma_3(1)t]+(\frac{1}{2}-\frac{G}{4}-\frac{1}{4G})\exp[-i\gamma_3(1)t]\right|^2 \tag{5-49}$$

$$1/R_s = \left|\frac{(\frac{1}{2}+\frac{G}{4}+\frac{1}{4G})\exp[i\gamma_3(1)t]+(\frac{1}{2}-\frac{G}{4}-\frac{1}{4G})\exp[-i\gamma_3(1)t]}{(\frac{G}{4}-\frac{1}{4G})\exp[i\gamma_3(1)t]-(\frac{G}{4}-\frac{1}{4G})\exp[-i\gamma_3(1)t]}\right|^2 \tag{5-50}$$

where

$$G = \frac{\sqrt{{n_0}^2-\sin^2\theta}}{\sqrt{(n_y-ik_y)^2-\sin^2\theta}} \tag{5-51}$$

and

$$\gamma_3(1) = (\omega/c)\sqrt{(n_y-ik_y)^2-\sin^2\theta} \tag{5-52}$$

The ratios between R and T for p- and s-polarized light can be expressed as:

$$R_p/T_p = \left|(\frac{H}{4}-\frac{1}{4H})\right|^2 \times \left|\exp[i\gamma_1(1)t]-\exp[-i\gamma_1(1)t]\right|^2 \tag{5-53}$$

and

$$R_s/T_s = \left|(\frac{G}{4}-\frac{1}{4G})\right|^2 \times \left|\exp[i\gamma_3(1)t]-\exp[-i\gamma_3(1)t]\right|^2 \tag{5-54}$$

respectively. For two films of different thicknesses (t_1 and t_2) but with the same optical anisotropy, identical H, G and γ values occur for the same incident angle. Therefore:

$$\frac{(R_p/T_p)_{t=t_1}}{(R_p/T_p)_{t=t_2}} = \frac{\left|\exp[i\gamma_1(1)t_1]-\exp[-i\gamma_1(1)t_1]\right|^2}{\left|\exp[i\gamma_1(1)t_2]-\exp[-i\gamma_1(1)t_2]\right|^2} \tag{5-55}$$

and

$$\frac{(R_s / T_s)_{t=t_1}}{(R_s / T_s)_{t=t_2}} = \frac{\left|\exp[i\gamma_3(1)t_1] - \exp[-i\gamma_3(1)t_1]\right|^2}{\left|\exp[i\gamma_3(1)t_2] - \exp[-i\gamma_3(1)t_2]\right|^2} \tag{5-56}$$

$\gamma_3(1)$ is a complex number and contains both real and imaginary parts. Equation (5-56) can be used to calculate $\gamma_3(1)$ if s-polarized reflection and transmission spectra of three films with known but different thicknesses (two R/T ratios) are available. As the value of $\gamma_3(1)$ is determined, n_y and k_y can be calculated from Equation(5-52). In addition, n_x and k_x values can be calculated from the s-polarized reflection and transmission spectra when the sample film is rotated 90 degrees about the Z axis. Similarly, $\gamma_1(1)$ can be obtained from reflection and transmission spectra of p-polarized light. If n_x, k_x are already known, n_z and k_z can be calculated from Equation (5-48). To improve the accuracy of calculated n and k values, polarized reflection and transmission spectra of more than three films (all with different thicknesses but with the same optical anisotropy) can be collected and γ can be obtained by data fitting with known values of $\frac{\left\|\exp[i\gamma t_1] - \exp[-i\gamma t_1]\right\|}{\left\|\exp[i\gamma t_m] - \exp[-i\gamma t_m]\right\|}$, m=2,3,….

In practice, the step of obtaining γ values can be eliminated; n and k values can be generated directly from the data fitting process. In the following discussions, this method of obtaining n and k when t is known will be designated R/T ratio method.

Since the R/T ratio method uses the light intensity ratio, error resulting from incident light scattering is reduced because it is expected that the loss of intensity due to scattering will influence both the reflected and the transmitted light intensities in a similar manner. This fact also implies that the method does not require an accurate background for

reflection spectra since intensities are ratioed. In practice, to obtain sufficiently accurate absolute reflection spectra, either a calibrated mirror (which may have a short shelf life) or a carefully designed experimental configuration is required [183]. In addition, effects caused by absorption of atmospheric water and carbon dioxide will not cause significant error provided that the humidity and CO_2 content in the air do not change significantly during data collection. Therefore, purging or evacuation of the sample chamber is not required.

However, the primary advantage of the R/T ratio method is its mathematic simplicity which enables extraction of *n* and *k* spectra using a reasonable amount of computing time while no model or relationship for *n* and *k* is needed to obtain; this distinguishes R/T ratio method from other methods currently used on thin solid films. Implementation of the method requires that the three principle axes of the dielectric function can be identified without ambiguity and that one of the principle axes must be normal to the film surface (in *Z* direction) with the remaining two in the *X*-direction and *Y*-direction, respectively. In addition, a series of freestanding films with different thicknesses but with the same anisotropy must be available.

Both the R/T ratio method and the prism coupling technique can extract anisotropic complex refractive indices of thin films without assuming a model or relationship for *n* and *k*. Both methods are based on the theory of electromagnetic wave propagation in layered media and both uses least square data fitting to obtain *n* and *k* values. The prism coupling technique can generate *n* and *k* at the wavelength of the light source used by the prism coupler (either a laser source or an arc lamp) while the R/T ratio method can generate *n* and *k* spectra in a wavelength range. Compared to the prism coupling

technique, the R/T ratio method is mathematically simpler and offers a great computational advantage. The R/T ratio method can generate *n* and *k* spectra in a wavelength range in a reasonable amount of time using personal computers. Since the prism coupling technique usually uses a laser source, it samples a small area comparable to the beam size of the laser. Also, it utilizes the dependence of reflected intensity on incident angle to calculate *n* and *k*. The incident angle can be measured with a high accuracy. As a result, a high level precision is expected for *n* and *k* values extracted from the prism coupling technique. Therefore, *n* and *k* values at certain wavelengths provided by the prism coupling technique can serve as good basis for comparison to *n* and *k* spectra extracted by the R/T ratio method. However, the prism coupler that is accessible can only operate at three wavelengths (543, 633, and 1550 nm) where the BPDA-PDA films are transparent.

5.3.2. Data collection and analysis

When applying the R/T ratio method, the film thickness must be known. Although film thickness can be determined by numerous methods, the thickness value should be obtained by a method in which the entire illuminated area is used in thickness determination. Previous ultraviolet-visible (UV-VIS) and IR absorption studies have indicated that BPDA-PDA films are transparent in the wavelength range between 1.5μm and 2.5μm (corresponding to ~6600-4000cm^{-1}) and show little dispersion in refractive index [66]. Therefore, the total wavelength range was extended to the near infrared (up to 6000cm^{-1}, which is the upper limit of the spectrometer) for infrared spectra collection and the transmission spectra between 4500 and 6000cm^{-1} were used to extract the film thickness. The wavelength range between 4000 and 4500cm^{-1} was excluded to minimize

the influence of water vapor absorption near 4000cm^{-1}. A detailed description of the thickness determination of transparent anisotropic films using polarized transmission spectra can be find in Section 5.4. Theoretically, only R and T at three different thicknesses, corresponding to two different thickness pairs, are required to calculate n and k. However, because both reflectance and transmittance can be close to zero due to either film absorption or interference, R/T ratios may involve a small number in the denominator at some wavelengths, which can introduce significant errors into the calculated n and k values. To ensure more accurate results, R and T spectra at five different thicknesses were collected so that R/T ratios with four independent thickness pairs can be used to determine n and k. Optimal n and k values are determined by minimizing the following target function $g(n,k)$:

$$g(n,k)=\sum_{l=1}^{4}\left(\frac{(R/T)_{a_l,measured}/(R/T)_{b_l,,measured}}{\left|\exp\left(i\gamma t_{a_l}\right)-\exp\left(-i\gamma t_{a_l}\right)\right|^2/\left|\exp\left(i\gamma t_{b_l}\right)-\exp\left(-i\gamma t_{b_l}\right)\right|^2}-1\right)^2 \qquad (5\text{-}57)$$

where l is the sequence number of the thickness pairs, and a_l and b_l denote the first film and second film in the lth pair. $\gamma=\gamma_1$ for p-polarized light; $\gamma=\gamma_3$ for s-polarized light. For five films of different thicknesses, there are many possible pair combinations. To reduce experimental error, pairings that give the largest ranges for $(R/T)_{a_l,measured}/(R/T)_{b_l,,measured}$ at most wavelengths should be chosen. Table 5-1 lists the film pairs used to calculate R/T ratios in this paper.

Table 5-1 Film pairing for R/T ratio calculation with spectra collected at 45° incident angle*

Sequence number of film pair, l	t_{al}, μm	t_{bl}, μm
1	3.50 (3.47)	1.79 (1.80)
2	3.32 (3.28)	2.36 (2.30)
3	2.89 (2.81)	2.36 (2.30)
4	2.36 (2.30)	1.79 (1.80)

* Values in parentheses are the values used for calculations with spectra collected at 56° incident angle

With four R/T ratios, a search for n and k can be performed by any classic minimum searching method, such as the simplex method [184] in a Matlab 6.x function "fminsearch". An initial guess of n and k must be supplied at each wavelength for the simplex method. Because both n and k are continuous functions with respect to wavelength, n and k values obtained at a particular wavelength will be a viable initial guess for n and k calculation at an adjacent wavelength. However, in practice, we have found that use of n and k values at an adjacent wavelength as initial guesses does not yield stable iteration. If the results at one wavelength are incorrect due to measurement error, an incorrect initial guess will be entered into the calculation at the next wavelength and this may cause the search algorithm to converge at incorrect n and k values, which will be supplied as the initial guess for the next wavelength. The domino effect makes the algorithm unstable. In our calculations, we use a primitive searching scheme described as follows. Because both n and k are expected to fall in well-defined ranges, such as $n \in [0, 4]$ and $k \in [0, 2]$, we determine the optimal n and k values by meshing the rectangle representing $[0 \le n \le 4, 0 \le k \le 2]$ on the nk plane and finding the mesh point that gives the smallest $g(n,k)$. Computationally, both n and k were increased at a step size of 0.002.

Thus at each wavelength, $g(n,k)$ was evaluated and compared for 2.0×10^6 times. The computation was not particularly intensive such that a desktop computer equipped with a 1.7GHz processor and 512M random access memory yielded results in ~12 hours for the spectral range 1000~2000cm^{-1} with a resolution of 2cm^{-1}. Compared with the simplex searching algorithm, the algorithm we used was slower but more stable. Due to experimental error, at some wavelength, the resulting n and k show scatter from adjacent n and k points. Because both n and k should be continuous functions of wavelength with no abrupt change in values, n and k values that caused apparent discontinuities are excluded from final n and k plots.

5.3.3. Discussion

5.3.3.1. n and k spectra extracted from R/T ratios at 45° incident angle

Figure 5-5 shows the n and k spectra extracted from R/T ratios calculated from reflection and transmission spectra collected at 45° incident angle. The wavelength range of 1200-1900cm^{-1} is chosen for convenience in comparing results with literature values (see below). Scattering of n and k values is evident in the absorbing wavelength range. As discussed above, scattering is expected because in the absorbing wavelength range, either T or R or both will become very small due to film absorption; the detection error for weak signals can increase and a small numerical value on the denominator in R/T can cause large errors. It is also obvious that the data scattering is more serious for n_z and k_z relative to n_x and k_x. Since n_x and k_x are supplied as known values when calculating n_z and k_z using Equation (5-48), any calculation error in n_x and k_x will propagate to n_z and k_z.

Figure 5-6 compares R/T ratios reconstructed from the n and k spectra in Figure 5-5 to experimentally measured R/T ratios. To make the figures easier to view, only the R/T

ratio from one thickness pair (t_1=2.357μm, t_2=1.788μm) is shown. The match between reconstructed and measured R/T ratios is generally excellent. Again, because R_s/T_s ratios are determined solely by n_x and k_x while R_p/T_p ratios are functions of n_x, k_x, n_z and k_z, it is apparent that the match is not as good for R_p/T_p ratios.

As mentioned in the Section 5.3.2., both n and k should be continuous functions of wavelength and no abrupt change in their values is expected. Thus, n and k values that cause apparent discontinuities are deleted from the n and k plots. Figure 5-7 shows the resultant n and k spectra after these discontinuous points are excluded from Figure 5-5. Consistent with the data in Figure 5-6, n_z and k_z also show more scattering in Figure 5-7. Missing of the peak for C=C tangential stretch of the PDA ring at 1516 cm^{-1} in k_z spectra indicates that BPDA-PDA repeat units lie in planes parallel to film surface (see Figure 5-17 in Section 5.5.2); peaks appearing in k_x spectra are all for vibrational modes that are supposed to lie in the repeat unit plane (1360, 1516, 1714 and 1774 cm^{-1}); the peak at ~1723 cm^{-1} in k_z spectra is probably from the out-of-plane component of ν_{as}^{*}(C=O) [65].

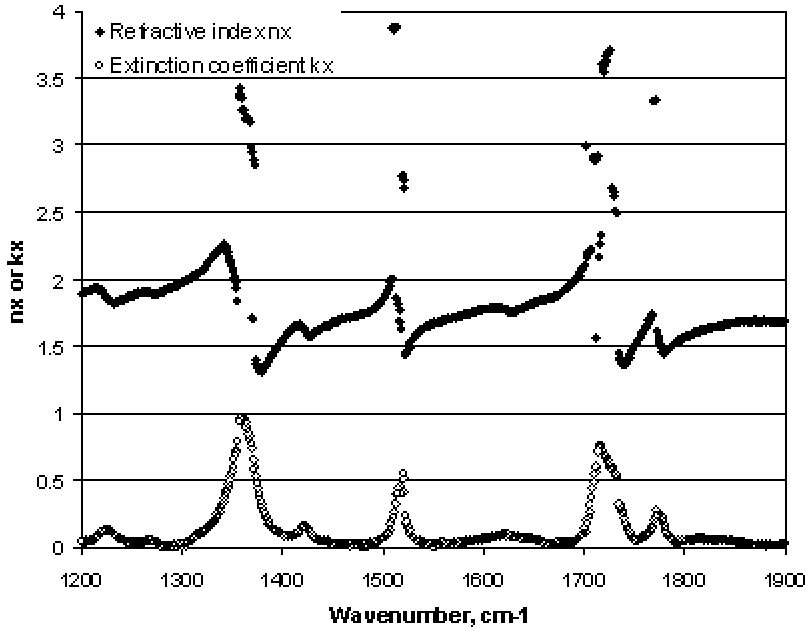

(a) n_x and k_x

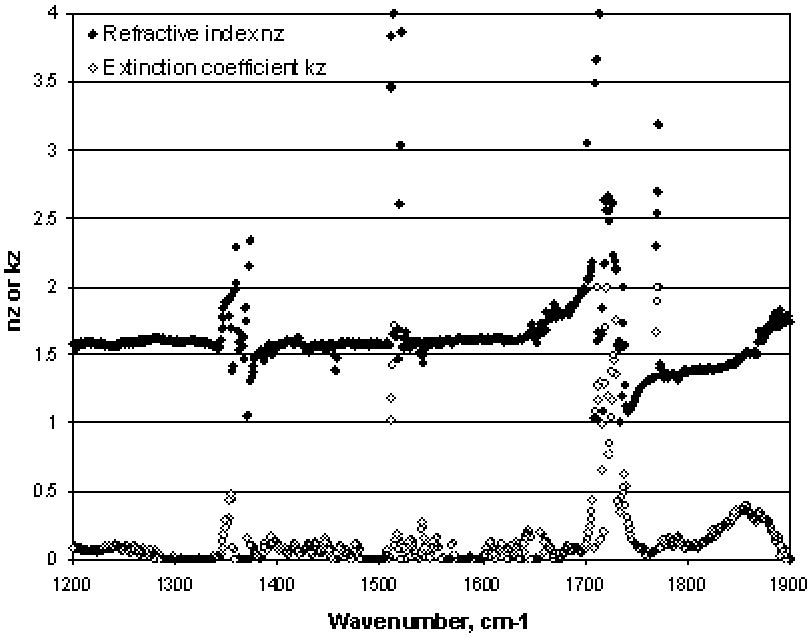

(b) n_z and k_z

Figure 5-5 *n* and *k* spectra extracted from R/T ratios at 45° incident angle (no points excluded)

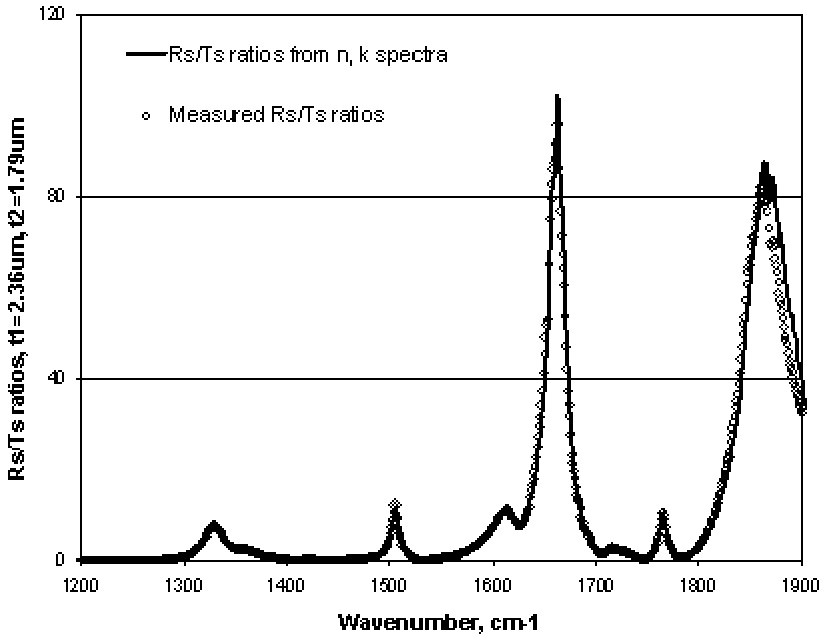

(a) R/T ratios for s-polarized light (t_1=2.36μm, t_2=1.79μm)

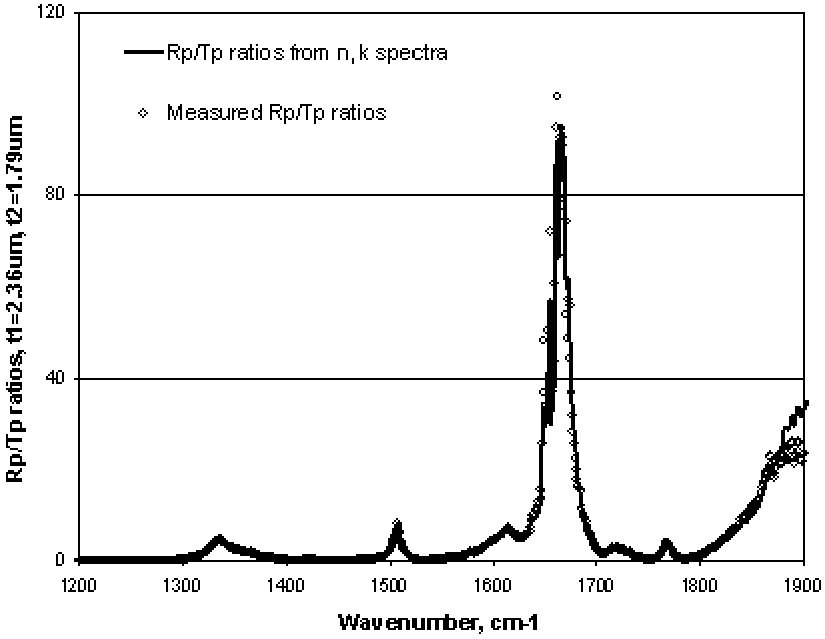

(b) R/T ratios for s-polarized light (t_1=2.36μm, t_2=1.79μm)

Figure 5-6 Comparison between measured R/T ratios and R/T ratios generated from the *n* and *k* spectra in Figure 5-5

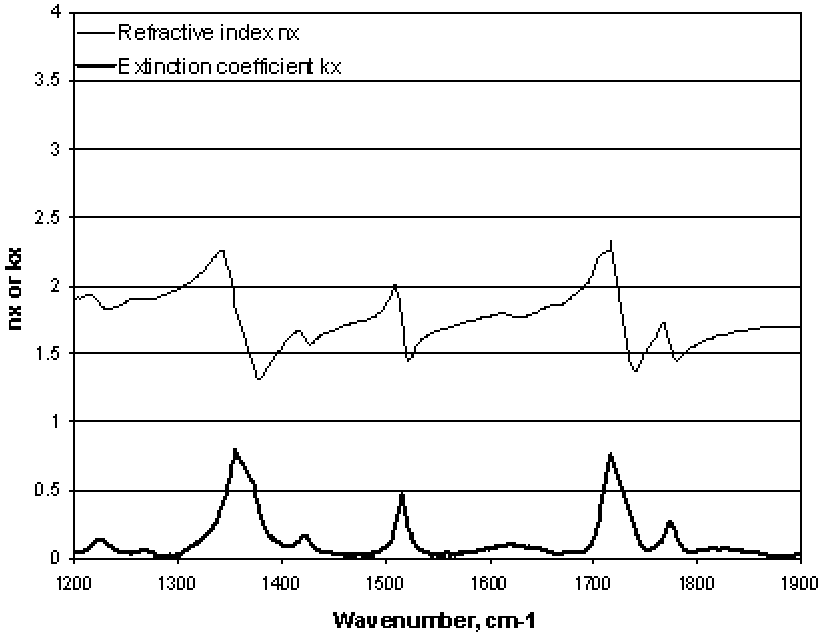

(a) n_x and k_x

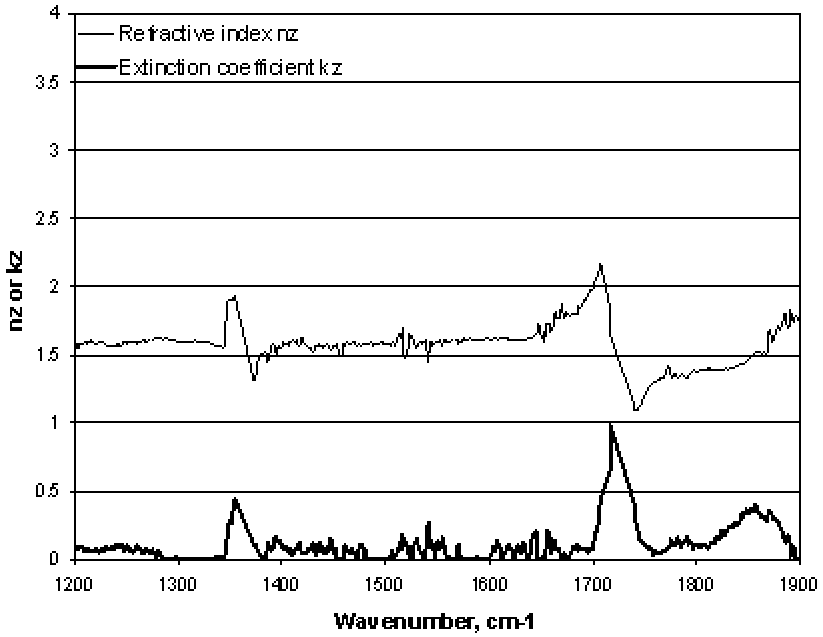

(b) n_z and k_z

Figure 5-7 *n* and *k* spectra extracted from R/T ratios at 45° incident angle (discontinuous points excluded)

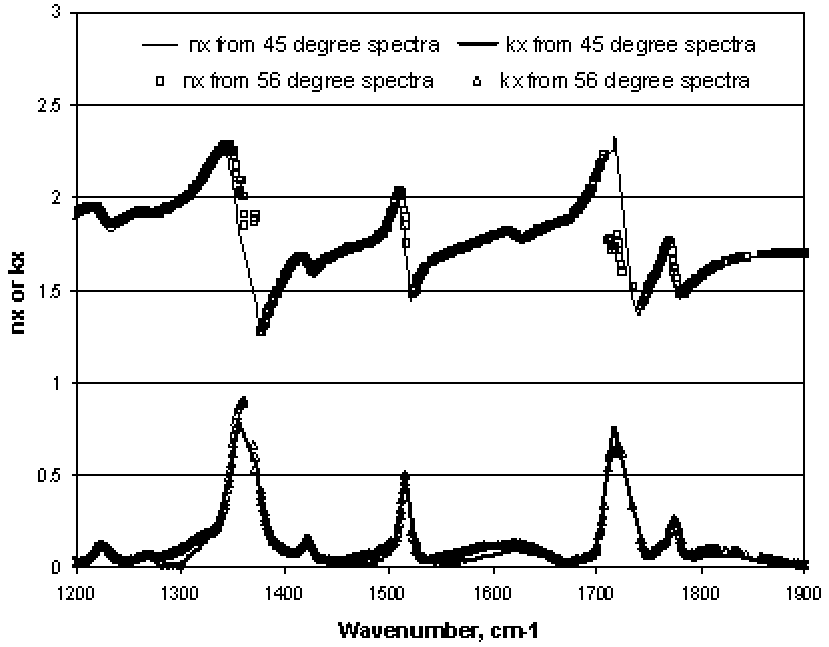

(a) n_x and k_x

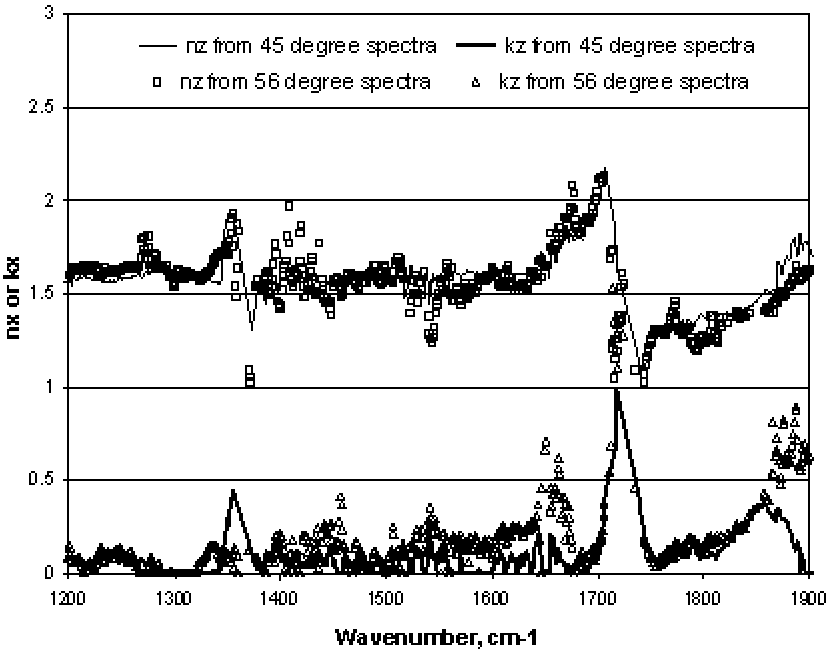

(b) n_z and k_z

Figure 5-8 Comparison between *n* and *k* spectra extracted from R/T ratios at 45° incident angle and R/T ratios at 56° degree incident angle (discontinuous points excluded)

5.3.3.2. n and k spectra extracted from R/T ratios at 56° incident angle

Reflection and transmission spectra were also collected at an incident angle of 56° and were used to calculate *n* and *k* spectra. The same thickness pairings were used as for 45° incident angle in Table 5-1. However, the thickness values were extracted from the transmission spectra collected at 56° incident angle and there were minor differences between the thickness values used for 45° and 56° incident angle. The thickness values obtained for the 56° incident angle are indicated in parentheses in Table 5-1. Section 5.4 presents a detailed discussion on the thickness differences. Figure 5-8 compares the resultant *n* and *k* spectra calculated from R/T ratios at 45° and 56° incident angles; in Figure 5-8, discontinuous points have been excluded. Clearly, the results at the two incident angles generally match well, although the results at 56° incident angle show more scattering, especially for the n_z and k_z spectra.

If the reflection and transmission spectra are error free, *n* and *k* can be extracted equally well from data collected at any incident angle between 0° and 90°. However, due to the existence of measurement error, accuracy of the resultant *n* and *k* will be dependent on the incident angle. In the following, we briefly discuss the influence of incident angle on *n* and *k* extraction. Generally speaking, for the same incident intensity, both the transmitted and reflected intensity will change as the incident angle changes. Since the incident intensity will always be the sum of transmitted intensity, reflected intensity and light absorption by the film, the transmitted intensity and the reflected intensity are expected to display a negative correlation for wavelength ranges where the absorption is not very strong. That is, when transmitted intensity increases, the reflected intensity will decrease, and vice visa. To reduce the error in R/T, neither R nor T should be too close to

0. Therefore, an optimal incident angle range may exist that provides good signal/noise ratio for both R and T. For n_x and k_x, ideal incident angles will be those that provide good signal/noise ratio for both R_s and T_s. The situation is more complicated for n_z and k_z since the achievement of good signal/noise ratio for both R_p and T_p is compromised by the need to limit the propagation of error of n_x and k_x on n_z and k_z. Rearranging Equation (5-48) yields,

$$n_z - ik_z = \frac{\sin\theta}{\sqrt{1 - \frac{\gamma_1^2(1)}{(\omega/c)^2}\frac{1}{(n_x - ik_x)^2}}} \tag{5-58}$$

Equation (5-58) indicates that the relative influence of (n_x-ik_x) on n_z and k_z values is reduced if the magnitude of $\gamma_1(1)$ decreases. From Equation (5-48), the magnitude of $\gamma_1(1)$ decreases with an increase of incident angle. The influence of errors in n_x and k_x on n_z and k_z values is minimized at grazing incidence (θ=90°). As a result, optimal incident angle for n_z and k_z should be the largest incident angle that provides satisfactory signal/noise ratio for both R_p and T_p.

5.3.3.3. Simulation based on previous publications

Previous investigations have constructed n_x and k_x spectra for BPDA-PDA films based on an oscillator model and the Kramers-Kronig relation [64,65]. The n_x and k_x spectra were reconstructed from a computer code kindly supplied by the authors of References 64 and 65. Figure 5-9 compares the reconstructed n_x and k_x spectra with those reported in Figure 5-7. For this calculation, four vibrational modes: (1774cm^{-1} [ν_s(C=O), Imide I], 1717 cm^{-1} [ν_{as}(C=O), Imide I], 1516 cm^{-1} [C=C tangential stretch of PDA ring, C=C_{PDA}] and 1360 cm^{-1} [C-N-C axial str., Imide II]) and an isotropic term were considered [64,65]. The in-

plane principle value of $n_x^{\infty} = 1.80$ is used based upon prism coupler measurement results at 1550nm (see Section 5.4). The measured n_x and k_x values match well with the values predicted by simulation. Therefore, this model is chosen in Section 5.5 for construction of n and k spectra of a preferentially aligned BPDA-PDA layer. Unfortunately, no literature values are currently available to verify the accuracy of n_z and k_z spectra.

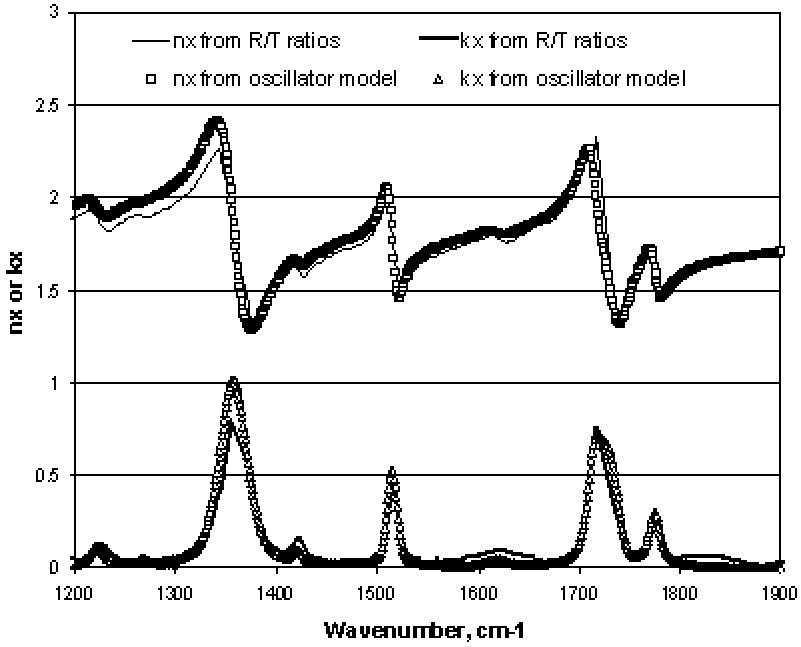

Figure 5-9 Comparison between *n* and *k* spectra extracted from R/T ratios at 45° incident angle and those generated from simulation based on an oscillator model [64,65]

5.3.3.4. Discussion on influence of variation in film thickness

In addition to experimental error on intensity measurements, sample non-uniformity also affects the accuracy of the calculated *n* and *k* values. Although uniform optical anisotropy

has been established across the sample film, film thickness can vary significantly as can be seen in Section 5.4 and Appendix E. All the above calculations are based on the average thickness across the sample area without considering the thickness variation. It is important to estimate the error due to neglect of thickness variation in calculation.

The thickness variation influences film transmittance and reflectance through a convolution with the non-uniformity in intensity of incident radiation. If we assume that the percentage of radiation intensity striking an area with thicknesses falling within the range [t, $t+dt$] can be represented by $f'(t)dt$, then,

$$\int_{t_{\min}}^{t_{\max}} f'(t)dt = 1 \tag{5-59}$$

where t_{min} and t_{max} are the minimum and maximum thickness in the illuminated sample. $f'(t)$ is called the intensity weighted thickness distribution function (Section 5.4). For a total intensity (I) of radiation striking the sample, the transmittance after thickness variation correction ($T_{\Delta t}$) is

$$T_{\Delta t} = \frac{\int_{t_{\min}}^{t_{\max}} I \cdot f'(t) \cdot T(t)dt}{I} = \int_{t_{\min}}^{t_{\max}} f'(t) \cdot T(t)dt \tag{5-60}$$

where $T(t)$ is the transmittance if the sample has a uniform thickness t. Similarly, the reflectance after thickness variation correction ($R_{\Delta t}$) is

$$R_{\Delta t} = \int_{t_{\min}}^{t_{\max}} f'(t) \cdot R(t)dt \tag{5-61}$$

Generally,

$$\frac{R_{\Delta t}}{T_{\Delta t}} = \frac{\int_{t_{\min}}^{t_{\max}} f'(t) \cdot R(t) dt}{\int_{t_{\min}}^{t_{\max}} f'(t) \cdot T(t) dt} \neq \frac{R(\bar{t})}{T(\bar{t})} \tag{5-62}$$

where $\bar{t}$ is the intensity weighted average thickness (Section 5.4). If $R_{\Delta t}$ and $T_{\Delta t}$, which are transmittance and reflectance collected over an area with thickness variation, and $\bar{t}$, which is determined from the polarized transmission spectra in the transparent wavelength range, are used to determine n and k, errors are inevitable as indicated by the inequality in Equation (5-62). In the following, we present a brief discussion on how thickness variation across the sample film affects error in calculated n and k values and how such error can be reduced.

For simplification purpose, the sample film is assumed to be isotropic (n_x=n_z, k_x=k_z) and $f'(t)$ is assumed to follow uniform distribution:

$$f'(t) = \frac{1}{2\Delta t} \tag{5-63}$$

where Δt=($t_{\max}$-$t_{\min}$)/2 is the intensity weighted half thickness span (Section 5.4). All simulations are for 1500cm^{-1} and an incident angle of 45°. Given a certain pair of n_x and k_x, $R_{\Delta t}$ and $T_{\Delta t}$ of s- and p-polarized light of three films with intensities weighted average thicknesses of 3.0, 2.4 and 1.8μm are calculated from Equations (5-60) and (5-61) by numerical integration. The intensity weighted half thickness span for the three films are assumed to be the same. Experimental error is not considered and $R_{\Delta t}$ and $T_{\Delta t}$ are used as input to extract n and k. The method described in the Section 5.3.2 is used to extract n_x, k_x, n_z and k_z values. The thickness pairings are shown in Table 5-2a. In simulation, n_x is

varied between 1 and 3 at a step size of 0.05 while k_x is varied between 0 and 2 at a step size of 0.05. The error in n or k is calculated by subtracting the true value from the extracted value. To expedite the computation, the "mesh-and-search" algorithm that was used for experimental data is not used. Instead, the Matlab function "fminsearch" is used in searching for optimal solutions because the given pair of n_x and k_x is expected to be a good initial guess in the absence of experimental error.

Table 5-2 Film pairing for simulation study on the influence of thickness variation

(a) The case of three films

Sequence number of film pair, l	t_{al}, μm	t_{bl}, μm
1	3.0	2.4
2	2.4	1.8

(b) The case of five films

Sequence number of film pair, l	t_{al}, μm	t_{bl}, μm
1	3.0	2.7
2	2.7	2.4
3	2.4	2.1
4	2.1	1.8

Figure 5-10a-d show how errors of n_x, k_x, n_z and k_z change over the square defined by [$1 \le n \le 3$, $0 \le k \le 2$] for Δt=0.01μm, respectively. Figure 5-11 and Figure 5-12 show corresponding figures for Δt=0.05μm and Δt=0.10μm, respectively. It can be seen that the errors of n_z and k_z are larger than n_x and k_x, as expected. The propagation of error from n_x to n_z and k_z is obvious in some areas. The error of k is relatively larger if k=0. This is due to the fact that if a film is transparent and uniform in thickness, the transmittance will

approach 100% for some n at a specified wavelength and incident angle as a result of light interference. However, if thickness variation exists, transmittance will never reach 100% (Section 5.4), with an effect similar to absorption. This will result in positive error in calculated k values. When $k>0$, the effect of decreased transmittance caused by thickness variations will be dwarfed by the absorption by the film so that the error in calculated k values will not be as significant as $k=0$. For $\Delta t=0.01\mu m$, most of calculated n and k values have errors below 0.01. Errors of n and k undergo substantial increase as Δt increases from 0.01μm to 0.05μm and to 0.10μm. The n and k errors for $\Delta t=0.05\mu m$ and $\Delta t=0.10\mu m$ are >0.1 in many areas on the nk plane. Obviously, sample thickness variation is critical in determining the accuracy of calculated n and k values.

In Section 5.3.2, to reduce the influence of experimental error, we proposed the use of five films with difference thicknesses (four R/T ratios). Using five films, as compared to three films, also reduces the influence of thickness variation on the errors in calculated n and k values. A similar simulation study to that described above has been performed. Five films with intensity weighted average thicknesses of 3.0, 2.7, 2.4, 2.1 and 1.8μm are used. For all five films, $\Delta t=0.05\mu m$. The thickness pairings are shown in Table 5-2b and the simulation results are shown in Figure 5-13. Compared to Figure 5-11, the errors in Figure 5-13 for both n and k values are significantly smaller. Except for regions where k is close to 0 or n is close to 1, errors for n_x, k_x and n_z are smaller than 0.01 while the error in k_z is smaller than 0.05. Therefore, if sample thickness variation is large, more films with different thicknesses should be used in order to improve the accuracy of calculated n and k values.

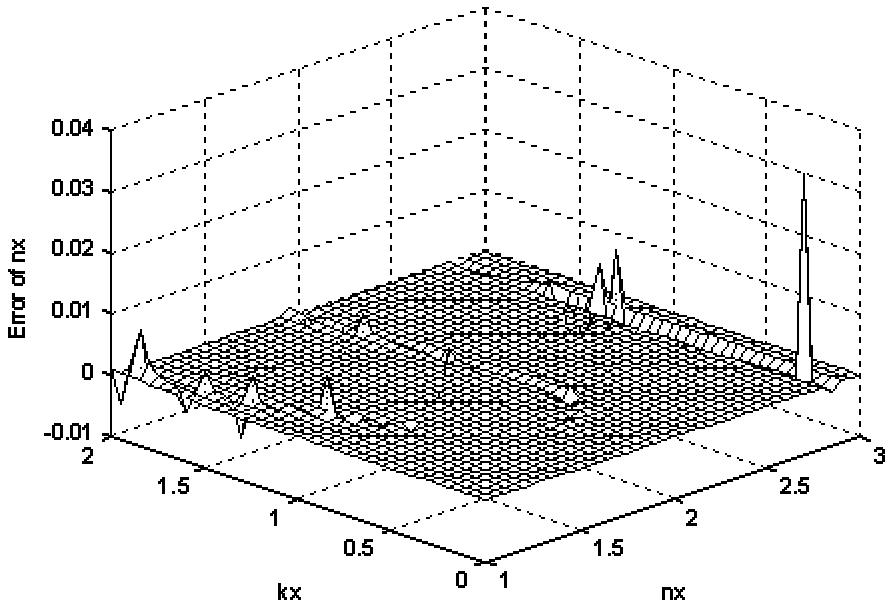

Figure 5-10(a) Error of n_x

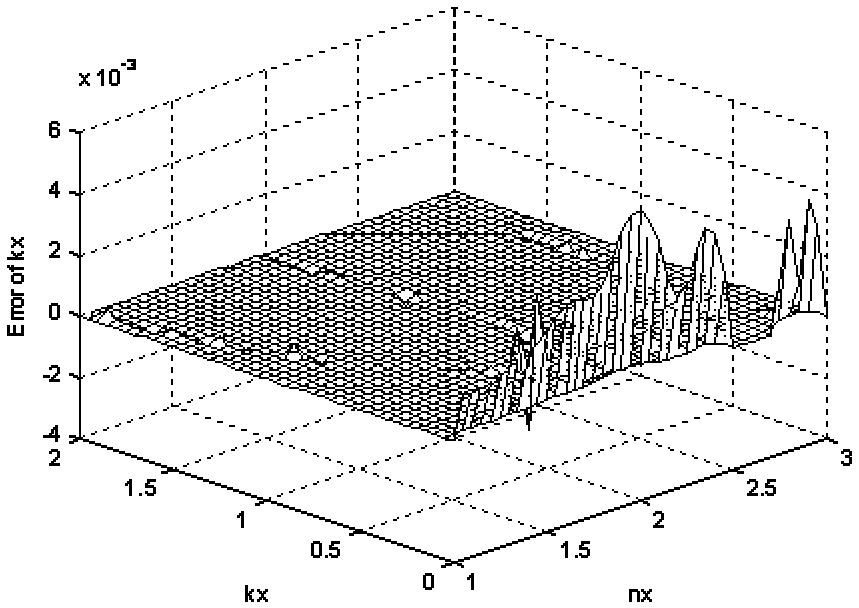

Figure 5-10 (b) Error of k_x

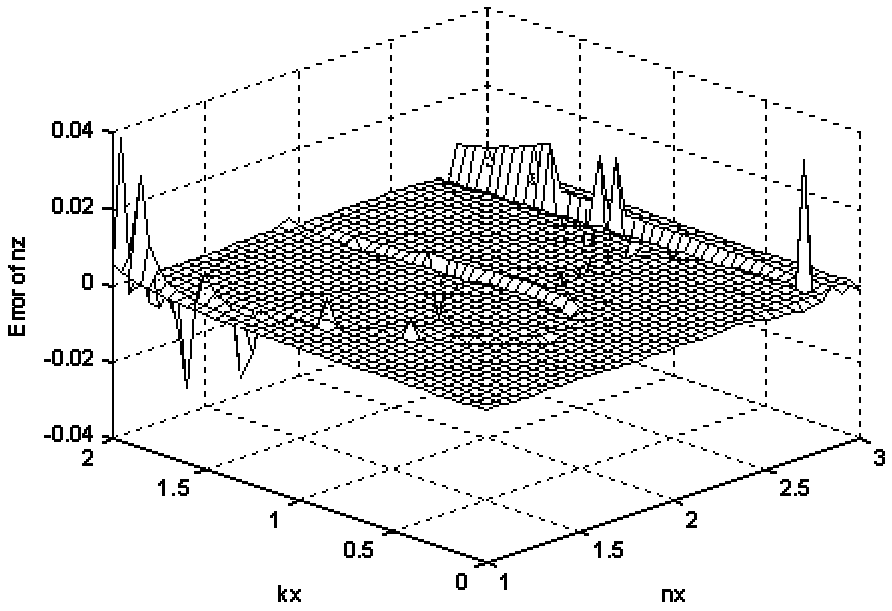

Figure 5-10 (c) Error of n_z

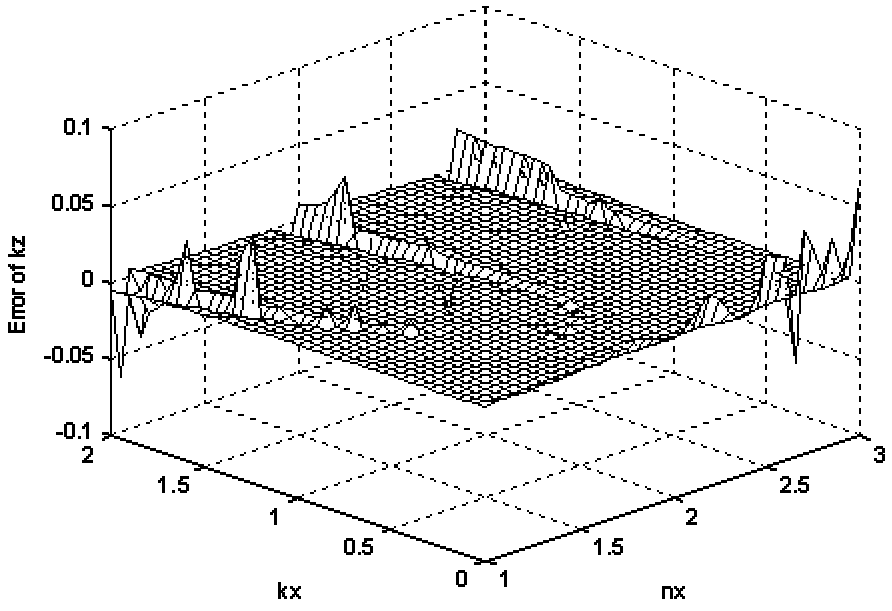

Figure 5-10 (d) Error of k_z

Figure 5-10 The influence of thickness variation (Δt=0.01μm) on calculation error of n and k (For three films: t_1=3.0μm, t_2=2.4μm, t_3=1.8μm)

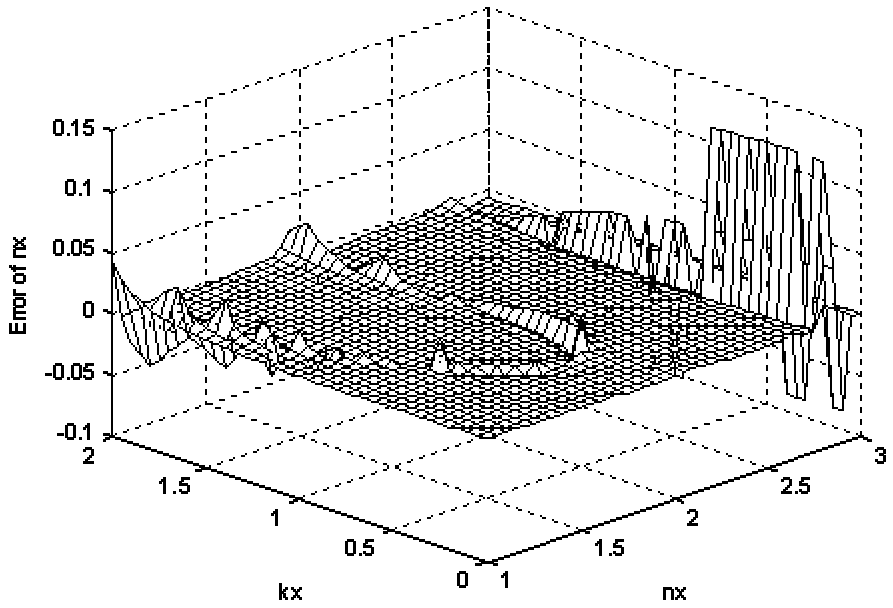

Figure 5-11(a) Error of n_x

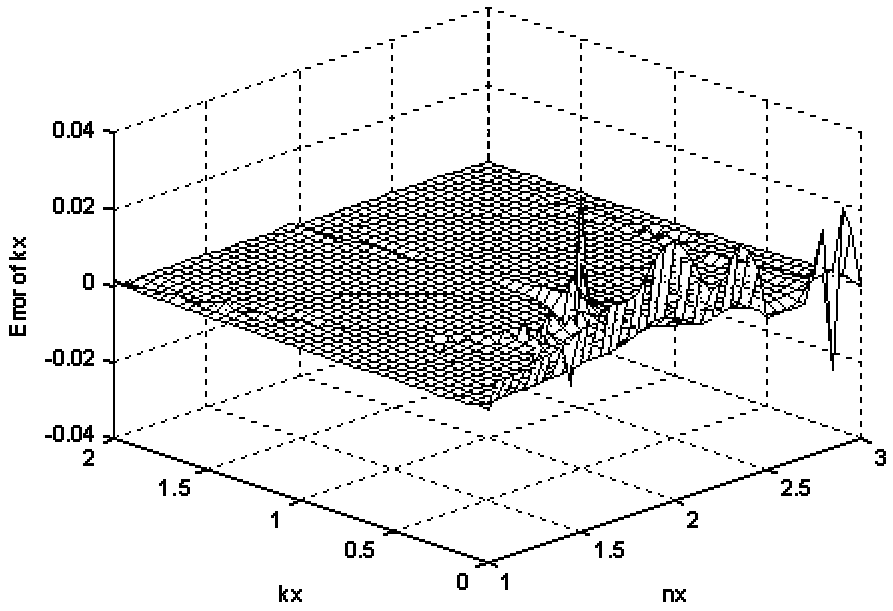

Figure 5-11 (b) Error of k_x

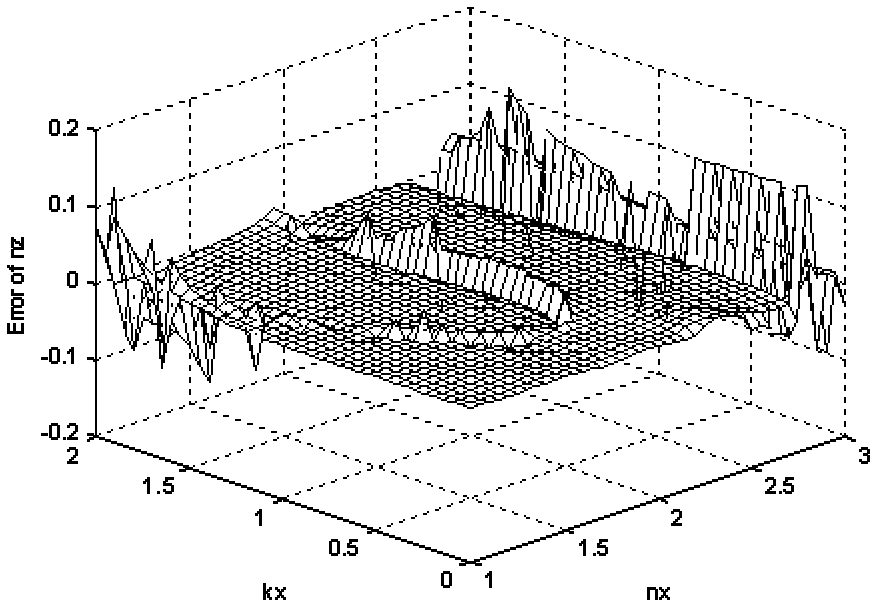

Figure 5-11(c) Error of n_z

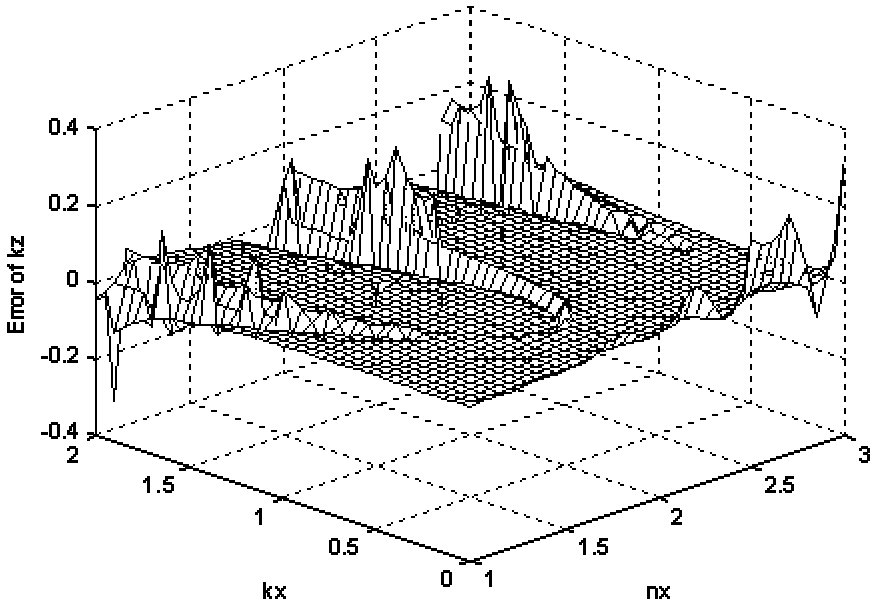

Figure 5-11(d) Error of k_z

Figure 5-11 The influence of thickness variation (Δt=0.05μm) on calculation error of n and k (For three films: t_1=3.0μm, t_2=2.4μm, t_3=1.8μm)

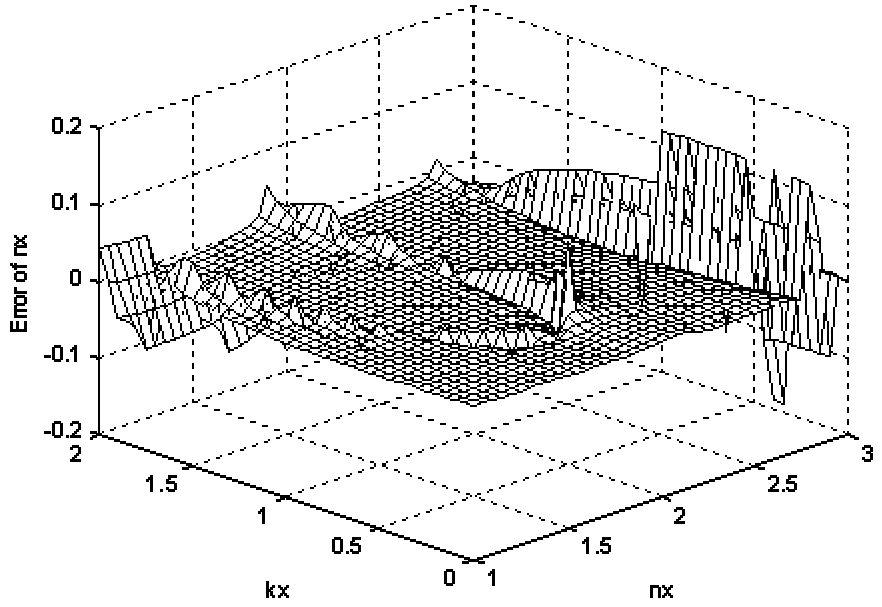

Figure 5-12(a) Error of n_x

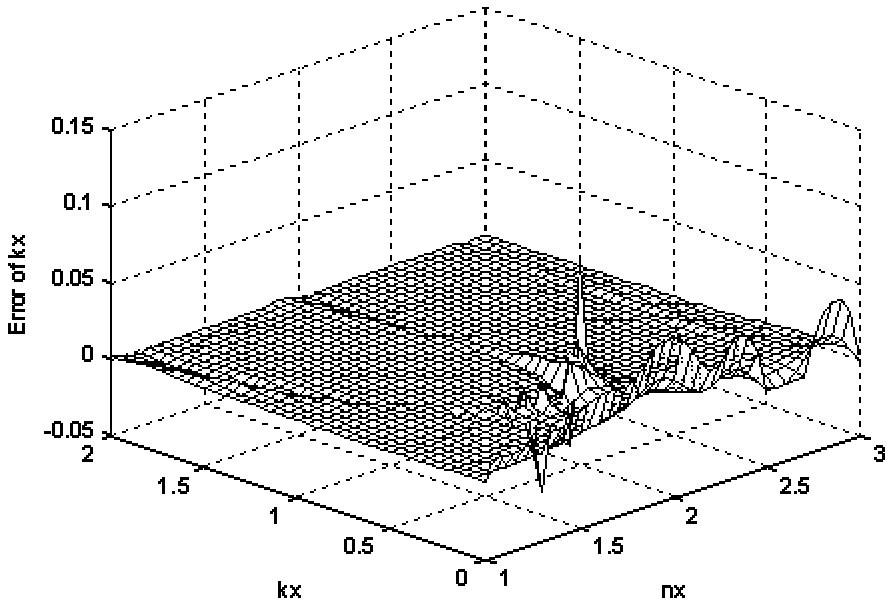

Figure 5-12(b) Error of k_x

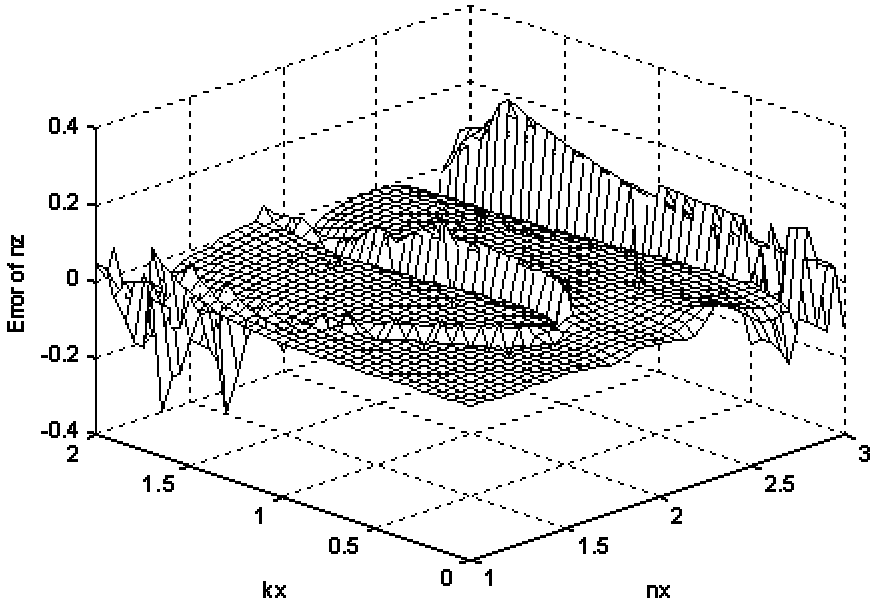

Figure 5-12(c) Error of n_z

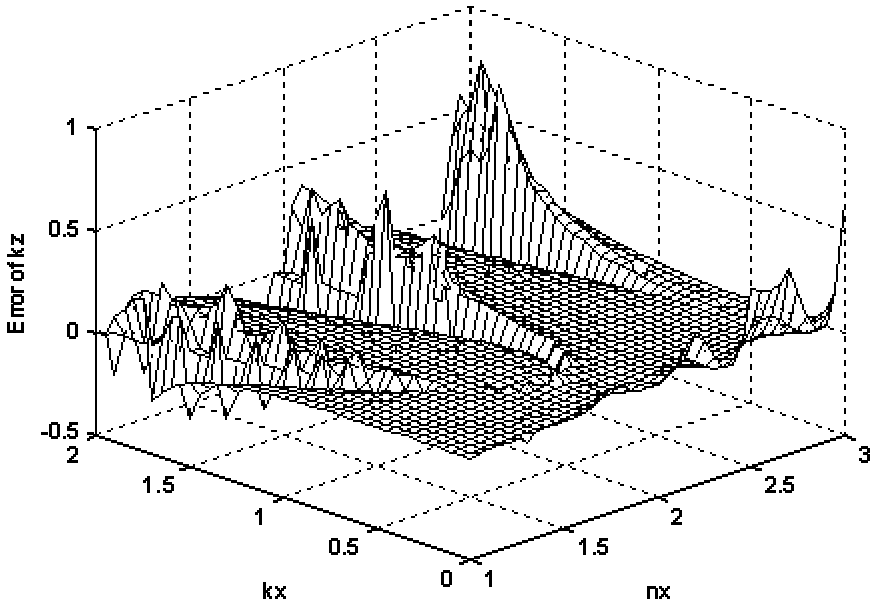

Figure 5-12(d) Error of k_z

Figure 5-12 The influence of thickness variation (Δt=0.10μm) on calculation error of *n* and *k* (For three films: t_1=3.0μm, t_2=2.4μm, t_3=1.8μm)

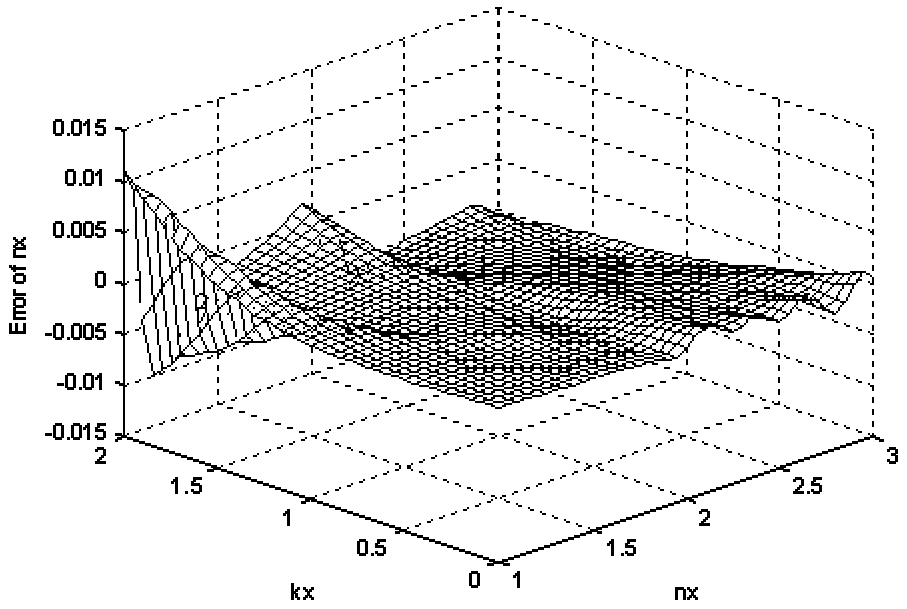

Figure 5-13(a) Error of n_x

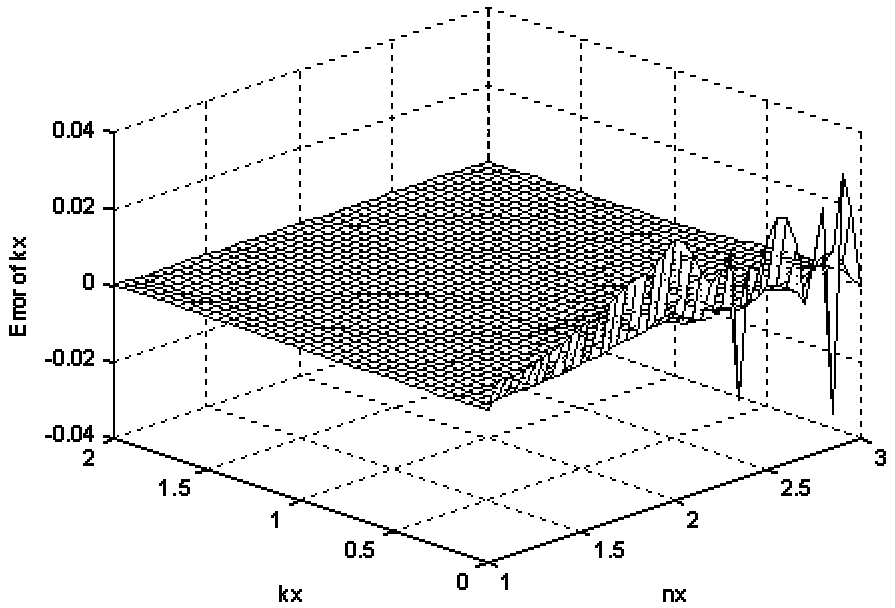

Figure 5-13(b) Error of k_x

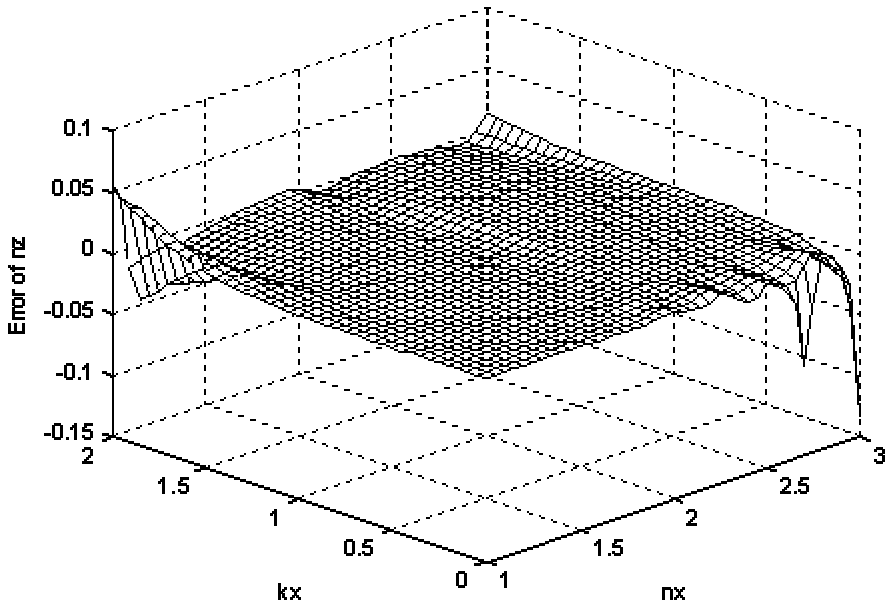

Figure 5-13(c) Error of n_z

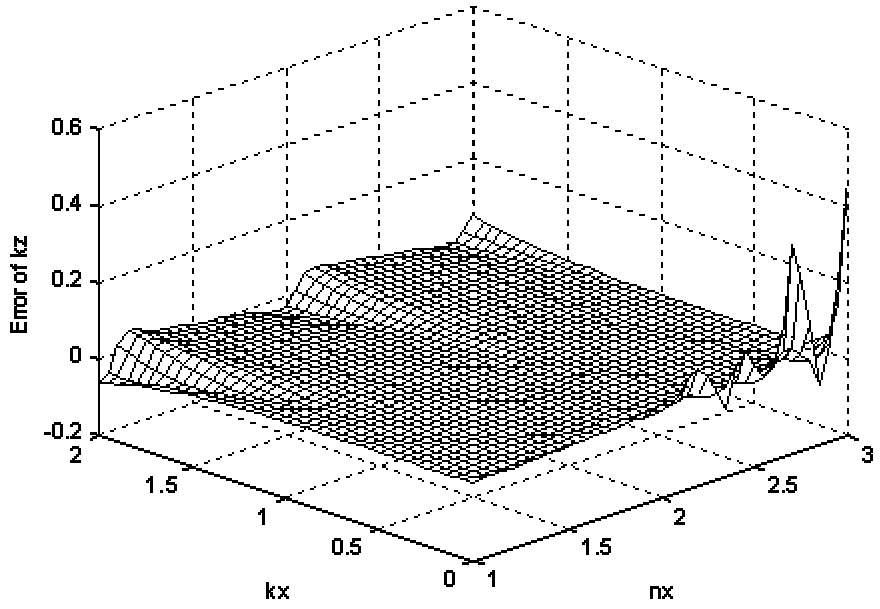

Figure 5-13(d) Error of k_z

Figure 5-13 The influence of thickness variation (Δt=0.05μm) on calculation error of *n* and *k* (For five films: t_1=3.0μm, t_2=2.7μm, t_3=2.4μm, t_4=2.1μm, t_5=1.8μm)

In addition to non-uniformity in sample thickness, errors in intensity measurement of reflectance or transmittance will also lead to error in the n and k spectra extracted from the R/T ratio method. It is important to evaluate the influence of error associated with R/T ratios on the accuracy of resultant n and k values. Some initial sensitivity analysis has been performed to show how the extracted n and k values respond to R/T ratio errors. The details of the sensitivity analysis can be found in Appendix G. From simulation results shown in Tables G-1 to G-4, following conclusions can be drawn.

1) When incident angle is small (θ =15°), maximum error in calculated n_z and k_z values can be very large; even for the case of ±1% error in R/T ratio, the errors in calculated n_z and k_z can exceed 0.1. When θ =45° or 75°, in most cases, the errors in calculated n_z and k_z are well within ±0.1. This is expected because as θ becomes smaller, the system approaches normal incidence while normal incidence is the extreme case in which no information in the z direction will be contained in the spectra.

2) Generally, as the R/T ratio error decreases, the errors in calculated n and k values will also decrease; the trend, however, is not strictly followed. The errors in calculated n and k depend on the wavelength, but not very strongly.

3) The occurrence of "worst case", in which the errors in calculated values become significantly larger, appears not to be solely related to the designated n and k values. It depends on the error level of R/T ratios as well. For example, at 1500cm^{-1} wavenumber and θ =45°, for an R/T ratio error level of 1%, largest error in k_z occurs for n_x=1.3, k_x=0, n_z=1.1 and k_z=1, while for an R/T ratio error level of -1%, largest error in k_z occurs for n_x=1.3, k_x=0, n_z=1.1 and k_z=0.

4) When θ =45° or 75°, for an R/T ratio error level of ±1%, the errors in calculated n_x and k_x values are within ±0.04, in most cases within ±0.02, while the errors in calculated n_z and k_z values are within ±0.10, in most cases within ±0.05; for an R/T ratio error level of ±2%, the errors in calculated n and k values are still within ±0.05 in most cases, but they can reach beyond ±0.1.

5.4. Extraction of film thickness from spectra in the transparent region

In this section, a technique is proposed to determine both anisotropic refractive indices and thickness of a film with biaxial symmetry based on polarized transmission spectra collected at oblique incidence over a wavelength range where the film is transparent and shows little dispersion in refractive indices. Methods are indicated to correct the errors caused by imperfect polarization of incident radiation and thickness variation across the sampling area. The technique was used to determine film thickness for the R/T ratio method described in Section 5.3.

5.4.1. Transmittance and reflectance of p-polarized and s-polarized light

By setting $k_x = k_y = k_z = 0$ in Equations (5-45) and (5-49), we can obtain T_s and T_p for a biaxial transparent film:

$$T_p = \frac{1}{1 + (4C^2 - 1)\sin^2\left(\frac{\omega n_x \sqrt{n_z^2 - \sin^2\theta}}{c n_z} t\right)} \tag{5-64}$$

$$T_s = \frac{1}{1 + (4D^2 - 1)\sin^2\left(\frac{\omega \sqrt{n_y^2 - \sin^2\theta}}{c} t\right)} \tag{5-65}$$

where

$$C = \frac{n_0^2 \sqrt{n_z^2 - \sin^2\theta}}{n_x n_z \sqrt{n_0^2 - \sin^2\theta}} + \frac{n_x n_z \sqrt{n_0^2 - \sin^2\theta}}{n_0^2 \sqrt{n_z^2 - \sin^2\theta}} \tag{5-66}$$

$$D = \frac{\sqrt{n_0^2 - \sin^2\theta}}{\sqrt{n_y^2 - \sin^2\theta}} + \frac{\sqrt{n_y^2 - \sin^2\theta}}{\sqrt{n_0^2 - \sin^2\theta}} \tag{5-67}$$

5.4.2. Correction for polarizer efficiency

Experimental errors will be introduced to the polarized transmission spectra if the incident light polarization is not perfect. It is important that the influence of imperfect polarization on transmittance be properly addressed and related errors be corrected. In the following discussion, $I_{//}$ denotes the intensity of polarized light parallel to the polarizer electric vector direction and $I_{\perp}$ denotes the intensity of polarized light perpendicular to the polarizer electric vector direction. Note that both $I_{//}$ and $I_{\perp}$ refer to intensities after the light passes through the polarizer but before striking the sample. q is defined as the fraction of polarized light intensity parallel to the polarizer electric vector direction,

$$q = \frac{I_{//}}{I_{//} + I_{\perp}} \tag{5-68}$$

q is a function of both the polarization state of incoming infrared radiation and the polarization efficiency of the polarizer. (Appendix F presents a more detailed discussion on the relation between q and polarizer efficiency). For light passing an ideal polarizer, q=1; for randomly polarized light, q=0.5. If the polarizer used for spectra collection is not perfect, the measured transmittance for s-or p-polarized light will generally be a mixture of transmittance from both s-polarized and p-polarized light. Thus the measured transmittance for s- and p-polarized light can be expressed by:

$$T_{s,measured} = \frac{I_{//}T_s + I_{\perp}T_p}{(I_{//} + I_{\perp})} = qT_s + (1-q)T_p \tag{5-69}$$

$$T_{p,measured} = \frac{I_{//}T_p + I_{\perp}T_s}{(I_{//} + I_{\perp})} = qT_p + (1-q)T_s \tag{5-70}$$

If the polarization state of incoming infrared radiation is well characterized and the dependence of polarizer efficiency on wavelength is known, T_s and T_p can be extracted from $T_{s,measured}$ and $T_{p,measured}$ using Equations (5-69) and (5-70). In practice, the dependence of polarizer efficiency on wavelength can be obtained through calibration. However, due to reflections from the mirror sets in the spectrometer, the incoming infrared radiation is not randomly polarized prior to striking the polarizer; as a result, the polarization state is generally unknown. Therefore, estimation of q is difficult. If the experimental error caused by q is not properly taken into account, significant error may result when the polarized transmission spectra are used to extract physical characteristics of the film. In the following, we propose a technique to eliminate errors caused by q by invoking a simple algebraic manipulation. Adding Equation (5-69) to (5-70) yields:

$$T_{p,measured} + T_{s,measured} = T_p + T_s \tag{5-71}$$

Equation (5-71) indicates that the influence of q will be eliminated if the sum of p- and s-polarized transmittance is used in calculation.

5.4.3. Correction for sample thickness variation

If the sample is uniform in thickness and if no refractive index dispersion exists over the wavelength range, the polarized transmittance should exhibit exact periodic oscillation with respect to wavelength as indicated by Equations (5-64) and (5-65). The transmittance is also expected to be equal to 1 at certain wavelengths. However, if the thickness varies across the sample area, the oscillation will not be ideally periodic and the transmittance is unlikely to reach a value of 1 at any wavelength. This deviation from

ideality can cause significant error in determining the refractive index and thickness if the thickness variation is not taken into account.

In practice, the influence of thickness variation will be convoluted with the non-uniformity in intensity of incident radiation. If $f(t)$ denotes the thickness distribution function in the illuminated sample area, i.e., if the percentage of film area with thicknesses falling within the range $[t, t+dt]$ can be represented by $f(t)dt$, then

$$\int_{t_{\min}}^{t_{\max}} f(t)dt = 1 \tag{5-72}$$

where t_{min} and t_{max} are the minimum and maximum thickness in the illuminated sample area, respectively. For commercial infrared spectrometers, radiation from the infrared source after reflections from a series of mirrors is not likely to have uniform intensity across the illuminated area. If we assume that the percentage of radiation intensity striking an area with thicknesses falling within the range $[t, t+dt]$ can be represented by $f'(t)dt$, then,

$$\int_{t_{\min}}^{t_{\max}} f'(t)dt = 1 \tag{5-73}$$

In the following discussion, $f'(t)$ is called the intensity weighted thickness distribution function. If the intensity of incoming radiation is not uniform, $f(t)$ and $f'(t)$ will be different. For a total intensity (I) of radiation striking the sample, the transmittance after thickness variation correction ($T_{\Delta t}$) will be

$$T_{\Delta t} = \frac{\int_{t_{\min}}^{t_{\max}} I \cdot f'(t) \cdot T(t)dt}{I} = \int_{t_{\min}}^{t_{\max}} f'(t) \cdot T(t)dt \tag{5-74}$$

where $T(t)$ is the transmittance if the sample has a uniform thickness t. According to Equation (5-74), it is the intensity weighted thickness distribution function instead of the actual thickness distribution function that determines the measured transmittance. Experimental determination of $f'(t)$ may be difficult given the fact that thickness variation and intensity non-uniformity of incident radiation are linked. In this paper, we correct the transmittance error caused by $f'(t)$ by making the simple assumption that $f'(t)$ is a uniform distribution function:

$$f'(t) = \frac{1}{t_{\max} - t_{\min}} \qquad t_{\min} < t < t_{\max} \tag{5-75}$$

Substitution of Equations (5-64) and (5-75) into (5-74) gives:

$$\begin{aligned} T_{p,\Delta t} &= \int_{t_{\min}}^{t_{\max}} f'(t) \cdot T_p(t) dt \\ &= \int_{t_{\min}}^{t_{\max}} \frac{1/(t_{\max} - t_{\min})}{1 + (4C^2 - 1)\sin^2(\frac{\omega n_x \sqrt{n_z^2 - \sin^2\theta}}{cn_z} t)} dt \\ &= \frac{\arctan\left[2C\tan(\frac{\omega n_x \sqrt{n_z^2 - \sin^2\theta}}{cn_z} t_{\max})\right]}{2C\frac{\omega n_x \sqrt{n_z^2 - \sin^2\theta}}{cn_z}} - \frac{\arctan\left[2C\tan(\frac{\omega n_x \sqrt{n_z^2 - \sin^2\theta}}{cn_z} t_{\min})\right]}{2C\frac{\omega n_x \sqrt{n_z^2 - \sin^2\theta}}{cn_z}} \end{aligned} \tag{5-76}$$

Similarly,

$$
\begin{aligned}
T_{s,\Delta t} &= \int_{t_{\min}}^{t_{\max}} f'(t)\cdot T_s(t)dt \\
&= \int_{t_{\min}}^{t_{\max}} \frac{1/(t_{\max}-t_{\min})}{1+(4D^2-1)\sin^2(\dfrac{\omega\sqrt{n_y-\sin^2\theta}}{c}t)}dt \\
&= \frac{\arctan\left[2D\tan(\dfrac{\omega\sqrt{n_y^2-\sin^2\theta}}{c}t_{\max})\right]}{2D\dfrac{\omega\sqrt{n_y^2-\sin^2\theta}}{c}} - \frac{\arctan\left[2D\tan(\dfrac{\omega\sqrt{n_y^2-\sin^2\theta}}{c}t_{\min})\right]}{2D\dfrac{\omega\sqrt{n_y^2-\sin^2\theta}}{c}}
\end{aligned}
\qquad (5\text{-}77)
$$

It should be pointed out that function "arctan" only has values within the range [-π/2, π/2]; thus in Equations (5-76) and (5-77), at certain wavelengths, the acrtan function will be discontinuous (sudden change from π/2 to -π/2, or from -π/2 to π/2). Because such discontinuities in the first term and the second term are unlikely to occur at the same wavelength, calculations can be adjusted by adding or subtracting π from the first term to make $T_{\Delta t}$ a continuous function with respect to wavelength.

5.4.4. Data collection and analysis

It has been widely reported that BPDA-PDA films exhibit uni-axial optical anisotropy [66,70,84]. A previous UV-VIS and IR absorption study suggested that BPDA-PDA films are transparent in the wavelength range between 1.5μm and 2.5μm (corresponding to ~6600-4000cm^{-1}) and show little dispersion in refractive index [66]. In the following, both thickness and anisotropic refractive indices are extracted from the transmission spectra between 4500 and 6000cm^{-1}. The wavelength range between 4000 and 4500cm^{-1} has been excluded in order to minimize the influence of water vapor absorption near 4000cm^{-1} on the transmission spectra.

Since spin coated BPDA-PDA films exhibit uni-axial optical anisotropy, equality of n_x and n_y values were assumed in all calculations. The dispersion of refractive indices in the wavelength range between 4500 and 6000cm^{-1} was neglected. It was further assumed that $f'(t)$ would follow the uniform distribution function described by Equation (5-75); the four unknown parameters (n_x, n_z, $t_{\max}$ and $t_{\min}$) were determined from the s- and p-polarized transmission spectra using least squares regression. The parameters $\bar{t}$ and Δt, defined by Equations (5-78) and (5-79), replaced the two parameters $t_{\max}$ and $t_{\min}$.

$$\bar{t} = \frac{t_{\max} + t_{\min}}{2} \tag{5-78}$$

$$\Delta t = \frac{t_{\max} - t_{\min}}{2} \tag{5-79}$$

$\bar{t}$ and Δt can be viewed as intensity weighted average thickness and intensity weighted half thickness span. A Matlab 6.x function "fminsearch" was used to find the optimal parameters by minimizing the following target function $g(n_x, n_z, \bar{t}, \Delta t)$ [184].

$$g(n_x, n_z, \bar{t}, \Delta t) = \sum \left(T_{p,\Delta t} + T_{s,\Delta t} - T_{p,measured} - T_{s,measured} \right)^2 \tag{5-80}$$

which is the sum of squared error over the wavelength range. $T_{p,\Delta t}$ and $T_{s,\Delta t}$ were determined from Equations (5-76) and (5-77), respectively.

For comparison purposes, two additional target functions: $g'(n_x, n_z, \bar{t}, \Delta t)$ and $g''(n_x, n_z, \bar{t})$ were defined as:

$$g'(n_x, n_z, \bar{t}, \Delta t) = \sum \left[\left(T_{p,\Delta t} - T_{p,measured} \right)^2 + \left(T_{s,\Delta t} - T_{s,measured} \right)^2 \right] \tag{5-81}$$

and

$$g''(n_x, n_z, \bar{t}) = \sum \left(T_p + T_s - T_{p,measured} - T_{s,measured} \right)^2 \tag{5-82}$$

respectively, where $T_{p,\Delta t}$, $T_{s,\Delta t}$, T_p and T_s were calculated from Equations (5-76), (5-77), (5-64) and (5-65), respectively. Determination of $n_x, n_z, \bar{t}$ and Δt by minimizing $g'(n_x, n_z, \bar{t}, \Delta t)$ corresponds to the inclusion of thickness variation but neglect of imperfect polarization, while determination of $n_x, n_z, \bar{t}$ by minimizing $g''(n_x, n_z, \bar{t})$ corresponds to inclusion of imperfect polarization while neglecting thickness variation.

In the following discussion, refractive indices and film thicknesses measured by the prism coupler and profilometer (thickness only) are also reported for comparison purposes. It is worth mentioning that the prism coupler technique utilizes a high quality laser source and samples an area approximately equal to the size of the laser beam (~1mm) so that excellent accuracy is possible. For the method described in this section, unless an intense radiation source is used and the sampling area is small, it is very difficult to achieve the accuracy obtainable with the prism coupler. It is estimated that the error for n_x, n_z and $\bar{t}$ will be ±0.05, ±0.1 and ±0.1μm, respectively. All refractive indices and film thicknesses (in μm) determined with the transmission spectra are reported to the second decimal point. Refractive indices obtained by the prism coupler are reported to the third decimal point. Because the thickness can vary up to several tenths of a micron across the sample, all thickness values (in μm) from the prism coupler and profilometer are reported to the second decimal point.

5.4.4.1. Corrections for imperfect polarization

Both the Harrick KRS-5 wire grid polarizer and the Perkin Elmer wire grid polarizer possess high polarization efficiency in the mid infrared range (>0.95 at 2000cm^{-1}). The polarizer efficiency is lower in the wavelength range between 4500 and 6000cm^{-1}. Therefore, significant error can result unless corrections are made for imperfect polarization. A common method of enhancing polarization efficiency is to use two polarizers in series and align their electric vector directions parallel to each other. Figure 5-14 compares the transmission spectra collected with the Harrick polarizer only ($T_{s,H}$, $T_{p,H}$, T_s+$T_{p,H}$) and with the Harrick and the Perkin Elmer polarizer in series($T_{s,H+P}$, $T_{p,H+P}$, T_s+$T_{p,H+P}$). The difference between $T_{s,H}$ and $T_{s,H+P}$ (or between $T_{p,H}$ and $T_{p,H+P}$) is apparent. The mixing of signals between T_s and T_p with the Harrick polarizer only is more significant as compared to that with two polarizers in series. However, the sum of T_s and T_p is relatively insensitive to whether one or two polarizers are used, which validates Equation (5-71).

Table 5-3 shows the results of refractive index and thickness calculations when only the Harrick polarizer was used and when the Harrick and Perkin Elmer polarizers were used in series. For comparison, measurement results on the same sample by the prism coupler and profilometer are also shown in Table 5-3. Appendix E shows that the refractive indices are uniform (within ±0.001) across a film on a single wafer although the film thickness can differ up to 0.4μm for an average thickness of 3μm. Thus, the refractive index values measured by the prism coupler are the accurate values for comparison to the calculated n_x and n_z, while either the thickness measured by the prism coupler or the profilometer can be used as estimated references for a calculated $\bar{t}$. Clearly, for

measurements with the Harrick polarizer only, if no correction for imperfect polarization is made, the calculated refractive indices and thickness values can differ significantly from those obtained by the prism coupler and profilometer. If the imperfect polarization is corrected, results with the Harrick polarizer only and with the two polarizers in series are very close; calculated n_x and $\bar{t}$ values match those from the prism coupler and profilometer measurements better than the calculated n_z values. This is understandable because the interference pattern displayed by T_s in Figure 5-14 is more obvious than that displayed by T_p. As shown by Equations (5-64) and (5-65), T_s is solely determined by n_x while T_p is determined by both n_z and n_x. Therefore, the calculated n_x values are expected to be more accurate than the calculated n_z values.

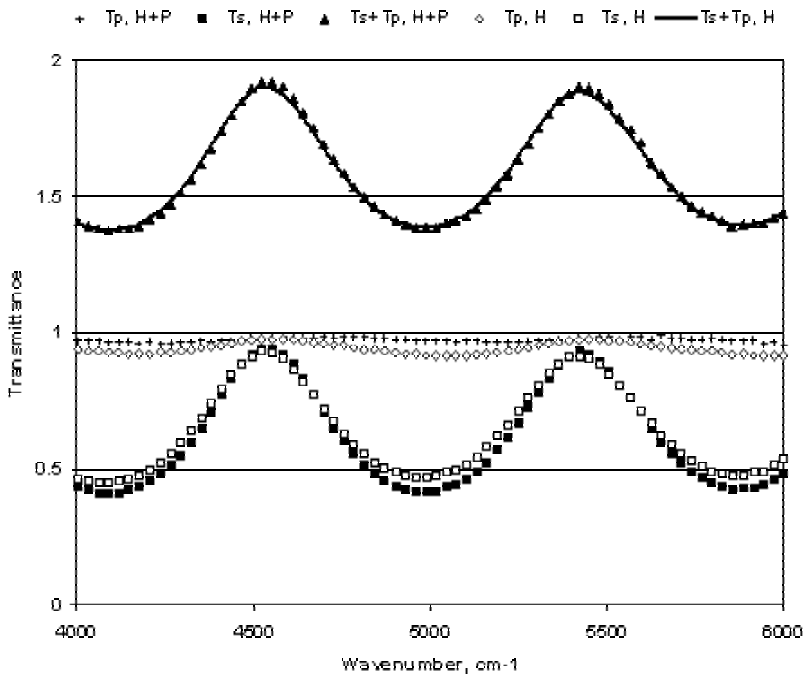

Figure 5-14 Comparison between transmission spectra collected with a Harrick polarizer only and with a Harrick and a Perkin Elmer polarizer used in series (spectra are collected at 56° incident angle on identical sample area)

Table 5-3 Effect of imperfect polarization on calculated optical constants and film thickness (from transmission spectra at 56° incident angle on sample film #1)

Polarizer	Correction for imperfect polarization?	Target function	Calculation results			
			n_x	n_z	$\bar{t}$,μm	Δt, μm
Harrick only	Yes	$g(n_x, n_z, \bar{t}, \Delta t)$	1.80	1.52	3.46	0.09
	No	$g'(n_x, n_z, \bar{t}, \Delta t)$	1.70	1.18	3.74	0.11
Harrick and Perkin Elmer in series	Yes	$g(n_x, n_z, \bar{t}, \Delta t)$	1.80	1.52	3.47	0.08
	No	$g'(n_x, n_z, \bar{t}, \Delta t)$	1.77	1.52	3.54	0.08
Prism coupler results	/	/	1.779	1.598	3.54	/
Profilometer results	/	/	/	/	3.50	/

From Table 5-3, it can also be seen that when two polarizers are used in series, the calculation results are essentially independent of whether the imperfect polarization was corrected or not. This is a result of improved polarization efficiency with two polarizers in series. By reconstructing the T_s and T_p spectra with calculated $n_x, n_z, \bar{t}$ and Δt values, an estimate of the polarizer efficiency in the 4500-6000cm^{-1} wavelength range could be obtained: ~0.88 for the Harrick polarizer and ~0.97 for the two polarizers in series. Although additional polarizers in series can improve the polarization efficiency, this will also significantly reduce the incident radiation intensity due to polarizer absorption and reflection, which may result in lower signal/noise ratio for the intensity measurements. Therefore, the polarization efficiency and intensity signal/noise ratio must be carefully balanced. It is recommended that the correction for imperfect polarization be made even if high polarizer efficiency can be obtained because any misalignment between the polarizer electric vector direction and *Y* (or *Z*) axis will have a similar effect to that of an imperfect polarizer.

5.4.4.2. Corrections for sample thickness variation

As discussed in Appendix E, color fringes are observed across a 4-inch wafer after spin coating and curing of a BPDA-PDA film, which is an indication of thickness non-uniformity. The thickness generally decreases from the center to the edge of the wafer; the thickness variation is more significant near the edge of the wafer. Profilometer measurements were performed on 2cm×2cm pieces cut from the wafer and the maximum thickness variation was as high as 0.3μm (from 3.35μm to 3.65μm). The sampling areas in transmission spectra collection are circles with a diameter of ~1cm; therefore, the thickness variation can be as large as 0.15μm (or Δt=0.7~0.8μm). The reactive ion etching rates of BPDA-PDA may also be different across the samples, which may increase or decrease the thickness variation caused by the spin coating process. It is thus important that thickness variation be considered and appropriately corrected.

Table 5-4 Refractive indices and film thickness determined with and without correction for thickness variation (from transmission spectra at 45° incident angle)

#	Correction for thickness variation?	Target function	Calculation results				Prism coupler			Profilometer
			n_x	n_z	$\bar{t}$,μm	Δt, μm	n_x	n_z	t,μm	t,μm
1	Yes	$g(n_x,n_z,\bar{t},\Delta t)$	1.78	1.56	3.50	0.08	1.779	1.598	3.54	3.50
	No	$g''(n_x,n_z,\bar{t})$	1.77	1.48	3.54	/				
2	Yes	$g(n_x,n_z,\bar{t},\Delta t)$	1.78	1.56	3.32	0.05	1.779	1.599	3.21	3.40
	No	$g''(n_x,n_z,\bar{t})$	1.78	1.52	3.34	/				
3	Yes	$g(n_x,n_z,\bar{t},\Delta t)$	1.80	1.53	2.89	0.05	1.780	1.600	2.79	2.87
	No	$g''(n_x,n_z,\bar{t})$	1.79	1.49	2.90	/				
4	Yes	$g(n_x,n_z,\bar{t},\Delta t)$	1.78	1.51	2.36	0.03	1.779	N/A*	2.15	2.22
	No	$g''(n_x,n_z,\bar{t})$	1.77	1.49	2.36	/				
5	Yes	$g(n_x,n_z,\bar{t},\Delta t)$	1.79	1.50	1.79	0.04	N/A[a]	N/A*	N/A*	1.65
	No	$g''(n_x,n_z,\bar{t})$	1.78	1.45	1.80	/				

* The data were not available because the films are too thin for the prism coupler to generate enough modes for accurate parameter determination.

Table 5-4 shows the refractive indices and film thicknesses for sample films #1 to #5 with thickness variation corrected and uncorrected. The calculated average thickness values do not change significantly with or without the thickness variation correction. However, the calculated n_x and n_z values, and especially n_z values, are less accurate if the thickness variation is not corrected. The calculated Δt values fall into the range of 0.03-0.07μm, which is comparable to the expected thickness variation magnitude. Again, it is important to note that Δt is the intensity weighted half thickness span for a simplified distribution model described by Equation (5-75).

From Table 5-4, it can also be seen that as the films become thinner, the calculated n_z values deviate further from the true values. We attribute this to experimental error related to thickness change. Interference patterns for thick films usually show at least one complete cycle in the wavelength range (Figure 5-14); the periodicity exhibited by the complete interference wave will aid the computer search algorithm to converge on the correct thickness and refractive index values. However, as the films become thinner, only incomplete cycles are obtained, which leads to more error in determining the periods of oscillation and ultimately the refractive index and thickness values. Oscillation in interference patterns of p-polarized light is not as obvious as that in interference patterns of s-polarized light. Therefore, the lack of a complete wave will have a larger impact on p-polarized light relative to s-polarized light; the error in calculated n_z values thus becomes more significant as the films become thinner.

5.4.4.3. Results from different incident angles

Table 5-5 shows the results of refractive index and thickness calculation based on transmission spectra of sample #1 collected at difference incident angles: 0°, 45° and 56°. At 0° incident angle, the difference between s- and p-polarized light disappears and only T_s is considered in calculating the transmittance; therefore, only n_x values are reported. These results indicate that the calculated refractive index and thickness values do not change significantly with incident angle. As the incident angle changes, the relative position of the sample in the light path changes and the thickness will be weighted differently by the incident intensity. Therefore, small changes in the intensity weighted thickness and half thickness span are expected. Also, a change in incident angle leads to a change in the magnitude of oscillation in the interference patterns of both s- and p-polarized light, which influences the accuracy of the calculation. Films #1 and #6 are in different areas on the wafer but went through identical processing steps. For comparison, the calculation results based on transmission spectra of sample #6 collected at 45° and 56° incident angles are also shown in Table 5-5. As expected, the refractive index and thickness values obtained for film #6 are similar to those for film #1.

Table 5-5 Refractive indices and film thickness determined from transmission spectra collected at different incident angles

Sample #	Incident angle	Target function	Calculation results			
			n_x	n_z	$\bar{t}$,μm	Δt, μm
1	0°	$g(n_x, n_z, \bar{t}, \Delta t)$*	1.78	/	3.51	0.07
	45°	$g(n_x, n_z, \bar{t}, \Delta t)$	1.78	1.56	3.50	0.08
	56°	$g(n_x, n_z, \bar{t}, \Delta t)$	1.80	1.52	3.47	0.08
6	45°	$g(n_x, n_z, \bar{t}, \Delta t)$	1.79	1.57	3.50	0.06
	56°	$g(n_x, n_z, \bar{t}, \Delta t)$	1.77	1.50	3.51	0.08

* For 0° incident angle, n_z will have no effect on the transmittance. Therefore, only T_s will be considered in the target function. The polarization state of incident radiation will not influence the transmittance because of the in-plane isotropy of the film.

5.5. Quantification of mechanical influence during CMP with infrared spectroscopy

In this section, a BPDA-PDA film is subject to unidirectional polishing, whereby a small piece of a BPDA-PDA film sample is fixed (not rotating) while only the pad is rotating. Because the size of the BPDA-PDA sample is small relative to the pad, the relative motion between the sample and the pad can be approximated as unidirectional. Due to the mechanical influence of the pad on the film, polymer chains near the BPDA-PDA surface will be preferentially aligned along the polishing direction. If preferential alignment occurs, dichroism will be observed in a normal incidence transmission spectrum; the dichroism can be used to quantify the depth of preferential orientation based on a physical model of the polishing process and spectral simulation.

5.5.1. Dichroism of BPDA-PDA films after CMP

A double-side polished (DSP) silicon wafer was spin-coated (2000rpm) with N-methyl-2-pyrrolidone (NMP) diluted PI2611 resin (13% solid content by weight) (Section 3.1.1). A small square (~3cm×3cm) was cut from the wafer and was subject to unidirectional polishing for 1 min following procedures described in Section 3.1.5. The sample was fixed by manually holding the VersaLap fixture during CMP and the down force exerted on the sample was estimated to be 10-15 psi (pounds per square inch). The platen rotation speed and slurry flow rate are 30 rpm and 50 ml/min, respectively. Polarized transmission spectra collected on the BPDA-PDA film on the DSP wafer at normal incidence before and after CMP are shown in Figure 5-15. In Figure 5-15, A_{90} and A_0 are used to indicate

absorbance spectra collected when the polishing direction of the sample is aligned perpendicular and parallel to the infrared polarization direction, respectively.

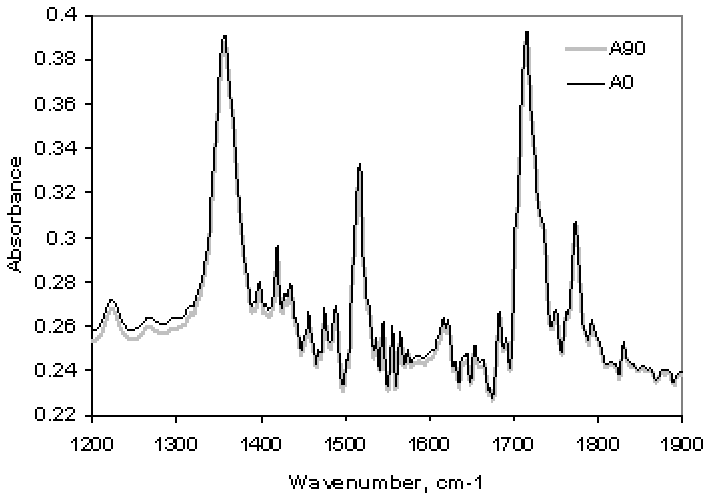

(a) Before CMP

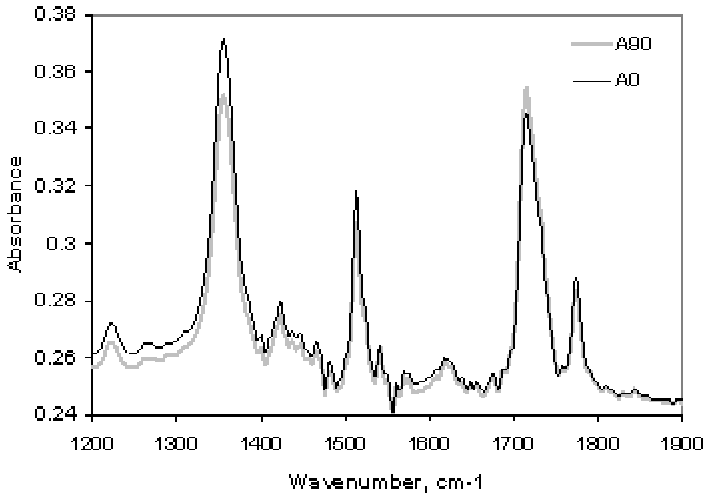

(b) After CMP

Figure 5-15 Polarized IR spectra of a BPDA-PDA film on a DSP wafer collected at normal incidence

From Figure 5-15, it is obvious that for the film before CMP, the infrared absorbance does not depend on the angle between the IR polarization direction and the polishing direction; after CMP, differences are noted between absorbance intensities when the polishing direction is aligned perpendicular and parallel to the infrared polarization direction. The difference (A_{90}-A_0), or dichroism, is plotted against wavelength in Figure 5-16.

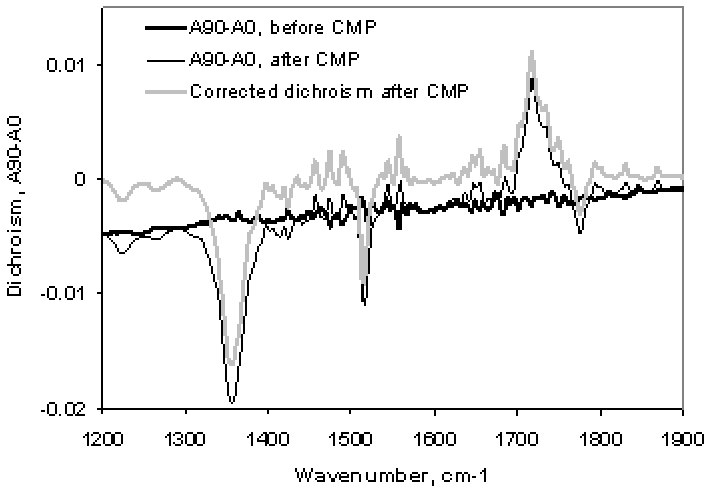

Figure 5-16 IR dichroism of the BPDA-PDA film before and after CMP

Theoretically speaking, the dichroism before CMP should be zero; however, the dichroism for the BPDA-PDA film before CMP (thicker black curve) deviates slightly from zero (Figure 5-16). The reason for such a deviation is not clear. Nevertheless, in Section 5.5.3, the thicker black curve will be treated as a baseline and be subtracted from the thinner black curve and the corrected dichroism (thicker gray curve) after CMP will

be used to minimize the influence of the deviation in quantifying the depth of chain reorientation.

5.5.2. Molecular model of BPDA-PDA

Figure 5-17 reproduces a previously published schematic diagram of the planar stacking structure of BPDA-PDA films [64].

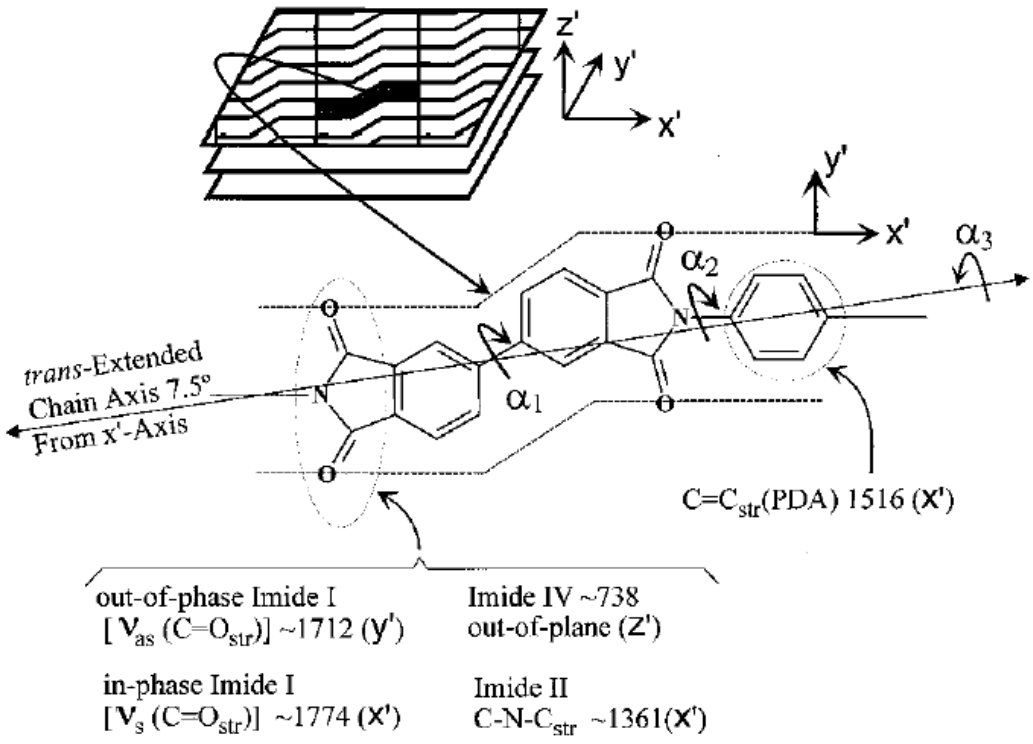

Figure 5-17 Schematic diagram of the planar stacking structure of BPDA–PDA films, after Hietpas and Allara [64]

In Figure 5-17, the diagnostic vibrational modes used for structural analysis and their transition dipole directions relative to the molecular coordinates are indicated. The validity of the assignment of vibrational modes has been verified in Section 5.3. The chain axis is taken as the director through an all-trans zigzag repeat unit. It should be noted that there is an angle (7.5°) between the chain axis and the X' axis. Therefore, if all the BPDA-PDA backbones are aligned parallel to the incident IR polarization direction, vibrational modes in the X' axis, such as those at 1361, 1516 and 1774cm^{-1}, will be major contributors to the absorbance spectra; if all the BPDA-PDA backbones are aligned perpendicular to the incident IR polarization direction, the absorption from all vibrational modes in the Y' axis, such as the one at 1712cm^{-1}, will dominate. This statement is consistent with the observed dichroism of the BPDA-PDA after CMP. In Figure 5-16, A_{90}-A_0 is negative around 1361, 1516 and 1774cm^{-1} and becomes positive around 1712cm^{-1}.

5.5.3. Quantification of depth of mechanical influence through simulation

To quantify the depth of mechanical influence, or the depth of preferential chain reorientation from infrared dichroism, the following two simplifying assumptions are made:

1) The all-trans zigzag repeat unit is the only conformation of all BPDA-PDA molecules in the film and the repeat unit lies perfectly in the X'-Y' plane before and after CMP;

and

2) There is a clear demarcation between the surface layer subject to mechanical influence and the bulk film; in the bulk film, all BPDA-PDA molecules assume random in-plane

orientation; in the surface layer, the chain axis of **ALL** BPDA-PDA molecules are aligned parallel to the polishing direction; the thickness of this surface layer is treated as the depth of mechanical influence in this thesis; this assumption is consistent with a statement by other investigators that the top layer was almost instantaneously oriented to a maximum value when a specific polyimide film was rubbed against a cotton velvet cloth [191].

Based on the two assumptions, the BPDA-PDA film sample after CMP can be described as a triple layer structure: DSP silicon wafer/bulk BPDA-PDA film/surface layer. The following procedure was thus used to determine the thickness of the surface layer.

First, *n* and *k* spectra of silicon, in-plane isotropic BPDA-PDA film and preferentially aligned surface layer were constructed in the wavelength range between 1200 and 1900cm^{-1}; only in-plane components (X and Y) of *n* and *k* spectra were needed for calculating infrared dichroism at normal incidence. Crystalline silicon is transparent between 1200 and 1900cm^{-1} and shows little dispersion in *n* spectra [196]. Therefore, in simulation, *n* and *k* values of the DSP wafer were fixed at 3.42 and 0, respectively [196]. The same computer code reported in Section 5.3.3.3 was used to reconstruct *n* and *k* spectra of both the bulk BPDA-PDA film and the surface layer. Similarly, the four vibrational modes: (1774cm^{-1} [ν_s(C=O), Imide I], 1717 cm^{-1} [ν_{as}(C=O), Imide I], 1516 cm^{-1} [C=C tangential stretch of PDA ring, C=C$_{PDA}$] and 1360 cm^{-1} [C-N-C axial str., Imide II]) and an isotropic term were considered [64,65]. For the bulk BPDA-PDA film, the in-plane principle value of $n_x^\infty = n_y^\infty = 1.80$ was used based upon prism coupler measurement results at 1550nm (Section 5.4). For the surface layer, it is difficult to

obtain n_x^∞ and n_y^∞ values because of difficulties associated with the fabrication of films with all chain axes aligned in one direction in a plane. Therefore, it is assumed that for a perfectly aligned BPDA-PDA film, n_y^∞ will assume the same value as n_z^∞, which is 1.60 (Section 5.4). Since $\overline{n}^\infty$ will remain constant, n_x^∞ will be 2.00. The angle between the chain axis and X' axis in Figure 5-17 was also taken into account in constructing the *n* and *k* spectra of the surface layer.

Second, the matrix method described in Section 5.2 was used to simulate propagation of an electromagnetic wave in the layered structure for given thickness values of different layers. Dichroism (A_{90}-A_0) can be calculated from the following Equation:

$$A_{90} - A_0 = -\log_{10}(T_{90}) + \log_{10}(T_0) \tag{5-83}$$

where T_{90} and T_0 are the transmittances when the polishing direction of the sample is aligned perpendicular and parallel to infrared polarization direction, respectively. The thicknesses of the DSP wafer and the bulk film were measured to be ~500μm and ~0.20μm and were used in simulation. Influence from error in the thicknesses of the DSP wafer and bulk BPDA-PDA film will cancel when calculating dichroism with Equation (5-83) and thereby will not result in significant error. The resultant dichroism spectrum was compared with the corrected experimental dichroism spectrum in Figure 5-16 and the sum of squared error (SSE) over all wavenumbers was calculated.

Finally, the thickness of the surface layer was varied from 1 to 50 nm at an interval of 0.1nm. Spectral simulation was carried out for each surface layer thickness and SSE

values at all surface layer thicknesses compared. The surface layer thickness yielding the minimum SSE was determined as the depth of mechanical influence.

Matlab 6.x was used for all spectral simulations. From the corrected experimental dichroism spectrum in Figure 5-16, the depth of mechanical influence was determined to be 5.6nm. Figure 5-18 compares the corrected experimental dichroism with simulated dichroism for a surface layer thickness of 5.6nm. The simulated dichroism curve shows some oscillation and this is a result of interference from the DSP wafer substrate. Since there is inevitable non-uniformity in the thickness of a wafer substrate, such oscillation was not captured by the infrared spectrometer. Generally, the agreement between the experimental and the simulated curves is satisfactory.

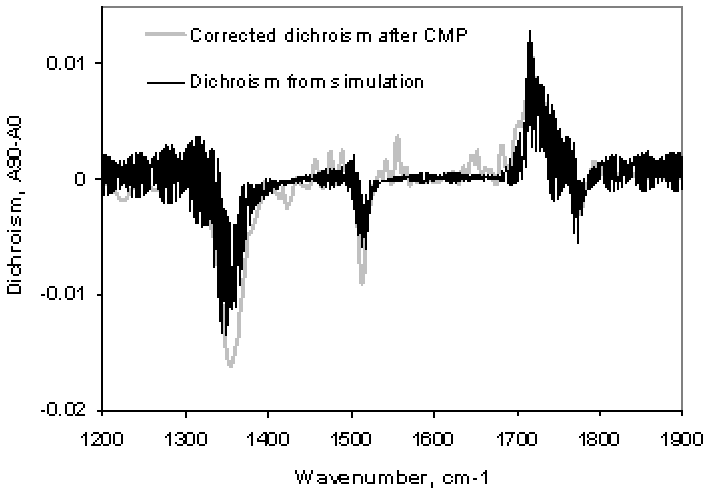

Figure 5-18 Comparison between corrected dichroism after CMP and dichroism from simulation

5.6. Summary

Polarized infrared spectroscopy was used to quantify chain orientations induced by the polishing process to evaluate the mechanical influence. Quantitative chain orientation information can be obtained by fitting simulated spectra to experimental ones, which requires a theoretical framework for spectral simulation and information about vibrational modes of the material. In this chapter, a theoretical framework for spectral simulation based on a 4×4 matrix method has been described; a new method (R/T ratio method) has been developed to extract complex refractive indices of films with biaxial symmetry, e.g. BPDA-PDA, from polarized transmission and reflection spectra. The complex refractive index spectra were used to verify the validity of a previously reported oscillator model [64], which is based upon the planar stacking structure in BPDA-PDA films and spectroscopic assignment of vibrational modes. With the 4×4 matrix method and the oscillator model, it has been demonstrated that the polarized infrared spectra can be used to quantify mechanical influence on a BPDA-PDA film as a result of CMP.

CHAPTER 6
SUMMARY AND FUTURE WORK

This chapter presents a brief summary of studies accomplished in this thesis and recommends directions for future research.

6.1. Summary

Despite the strategic importance and dramatic growth of chemical mechanical polishing (CMP), basic physical and chemical mechanisms of CMP are still poorly understood. Most of the studies reported have focused on macroscopic scale investigations such as the influence of operational parameters and slurry chemistries on removal rate, within wafer uniformity, and surface roughness of polished samples. Although such studies provide useful information for design and optimization of certain CMP processes, they contribute little to overall mechanistic understanding.

A widely accepted mechanism for material removal in CMP involves formation of a chemically modified surface due to interaction of slurry chemicals with the material and simultaneous mechanical wearing of the chemically modified surface layers by abrasives in the slurry. Quantitative information regarding the chemical modification and mechanical influence in CMP will facilitate the understanding of material removal mechanisms due to chemo-mechanical synergy. This thesis is devoted to development of techniques to quantify chemical and mechanical influences near low dielectric constant (low-k) film surfaces during CMP.

For polymeric low-k materials, when the film is subject to a shearing force, polymer chains in the surface and near surface layers orient preferentially along a certain direction. The depth of mechanical influence can be defined as the depth of the region in which the polymer chain motion and orientation are significantly altered by the force exerted on the surface. Similarly, the depth of chemical modification can be defined as the depth of the region near the surface in which detectable changes in polymer properties by slurry chemistry occur. Poly (biphenyl dianhydride-p-phenylenediamine) (BPDA-PDA) has been chosen as the low-k polymeric material to demonstrate the effectiveness of the techniques developed in this thesis to quantify chemical and mechanical influences during CMP.

The depth of chemical modification can be readily obtained if the concentration depth profile near a chemically modified surface is known. In this thesis, an iterative algorithm is proposed to extract depth profiles based on Fick's second law of diffusion in a multi-element system from data supplied by angle resolved x-ray photoelectron spectroscopy (ARXPS). Parameters related to the concentration profiles are obtained by fitting the experimental angle-dependent photoelectron intensity fractions to predictions from the algorithm. The use of photoelectron intensity fractions instead of absolute photoelectron intensities eliminates error due to changes in absolute photoelectron intensities resulting from the change of system geometries in angle-resolved experiments. Simulations using an infinite source diffusion model have been conducted to study the influence of errors in the raw data and to demonstrate the robustness of the algorithm. The correctness of the algorithm is established by extracting and comparing chemical composition depth profiles resulting from high temperature diffusion within oxygen doped silicon nitride

films. ARXPS data have been used to extract chemical composition depth profiles near surfaces of BPDA-PDA films modified with NaOH solutions. It has been clearly demonstrated that the technique can be used to quantify depth of chemical modification of BPDA-PDA surfaces with alkaline solutions.

Because polymer chains tend to realign when subject to external shear forces, the degree of polymer chain reorientation can be used to infer the magnitude of the force that the polymer surface experiences during polishing. Quantitative chain reorientation information can be obtained by fitting simulated infrared spectra to experimental ones if information is available on vibrational modes of the polymer.

Three-dimensional complex refractive indices of BPDA-PDA films are crucial in determining the assignment of vibrational modes in the infrared (IR) range. In this thesis, a new method to extract complex refractive indices of films with biaxial symmetry from polarized transmission and reflection spectra is described. Theoretical analysis demonstrates that the reflectance/transmittance ratio (R/T ratio) of two films of different thicknesses but with the same optical anisotropy is a simple function of the refractive index (n) and extinction coefficient (k). For films with biaxial symmetry, components of n and k on symmetric axes can be extracted from either s- or p-polarized R/T ratios if the film thickness values are known. The R/T ratio method is used to extract anisotropic complex refractive indices of BPDA-PDA films. The resultant n and k spectra compare well with simulations based on a previously reported oscillator model [64], which is based upon the planar stacking structure in BPDA-PDA films and spectroscopic assignment of vibrational modes. Simulation studies also revealed that the accuracy of n

and k spectra is most affected by data error in reflection and transmission spectra collection and thickness variation across sample films.

Based on the oscillator model and a theoretical framework developed for spectral simulation, polarized infrared spectra have been used to successfully quantify the mechanical influence on a BPDA-PDA film during CMP. Techniques developed in this thesis can be used to quantify either chemical modification or mechanically induced chain orientation in other fields such as chemical or plasma modification of solid surfaces and rubbing of polymer surfaces for liquid crystal display applications.

6.2. Future work

In this thesis, emphasis has been placed on the demonstration that ARXPS and polarized IR spectroscopy can be used to quantify chemical and mechanical modifications of BPDA-PDA surfaces during CMP. There are still many issues to be resolved before these techniques can be systematically applied to CMP and yield accurate results. The following are some suggestions for future improvements and new research directions.

6.2.1. Direct proof of the correctness of the two-parameter algorithm

In Section 4.4, the correctness of the two-parameter algorithm has been tested indirectly by extracting and comparing depth profiles resulting from diffusion for different times. Direct comparison between a depth profile extracted from ARXPS and that measured by secondary ion mass spectroscopy (SIMS) or Rutherford backscattering spectroscopy (RBS) of high depth-resolution can not only prove the correctness of the algorithm, but can also evaluate the accuracy of depth profiles extracted from ARXPS. The oxygen doped silicon nitride (SiON) samples with surface profiles resulting from high temperature treatments (Section 4.4) should be analyzed by SIMS to obtain depth profiles. The SIMS depth profiles of SiON are expected to serve as a good basis for comparison with those extracted from ARXPS.

6.2.2. Simulation study on evolution of concentration profile near a chemically modified BPDA-PDA surface

A basic assumption made in extracting concentration depth profiles near chemically modified BPDA-PDA surfaces is that the profiles follow an infinite source diffusion model. The real chemical modification process is a combination of diffusion and chemical reaction; the infinite source diffusion model is only an approximation. In

addition, the ARXPS measurements are made hours after the chemical treatment. It is possible that diffusion and chemical reaction continue to change the depth profiles during the period between chemical treatment and ARXPS measurement until all reactants are consumed and no further changes to the profiles occur. Therefore, the depth profiles extracted from ARXPS are the final profiles, and are not necessarily identical to the ones developed during the chemical treatment (or during CMP). The latter, of course, are of more practical interest. Since x-ray photoelectron spectroscopy (XPS) always requires a specific amount of time, usually more than 30 min, for sample loading and chamber pump-down, it is impossible to collect ARXPS data on surfaces immediately after chemical treatment. The problem of relating the final profiles from ARXPS to the profiles during CMP can be approached by modeling and simulation. The change of depth profiles after samples are removed from the slurries can be modeled as a diffusion-reaction process without further supply of chemical reactants and the evolution of the depth profiles and their corresponding angle dependent photoelectron intensity with respect to time can be obtained from numerical simulation using previously reported diffusivities [76] and reaction constants [101]. If the chemical modification is treated as an irreversible reaction, the depth profiles will not change with time after all reactants are consumed. Therefore, a relation between final depth profiles and depth profiles during CMP can be established and can be used to infer the latter from the former.

6.2.3. Improvement on R/T ratio method

As shown in Section 5.3, data scatter is still a concern for the R/T ratio method. The following two improvements can be made to enhance data quality.

1) Incorporation of another IR detector and sampling circuit into the spectrometer and redesigning the sampling mechanism so that simultaneous collection of reflection and transmission spectra will ensure that both reflection and transmission spectra are from the identical area on the sample. This redesign will reduce errors associated with sample non-uniformity and misalignment of samples when the spectrometer is switched between reflection and transmission modes.

2) Increase the intensity of the infrared source to improve signal to noise ratio. As mentioned in both Sections 5.3 and 5.4, the convolution between thickness variation and non-uniformity of incident infrared radiation results in an inaccuracy of *n* and *k* spectra calculated from measured R/T ratios if there is thickness variation across the sampling area. The adverse effect of the convolution can be reduced if a smaller area can be sampled without compromising the signal to noise ratio of measured infrared intensity. An infrared source of higher intensity is required so that a smaller sampling area can produce sufficient transmission or reflection intensity for accurate infrared detection.

Freestanding film samples were prepared using the backside etching procedure described in Section 3.1.2. Although the procedure has been successfully used to obtain freestanding BPDA-PDA films, it requires a significant amount of experimental work as well as aggressive chemistries (HF/HNO_3). Simplification of the sample preparation process is possible on a different substrate other than Si if the substrate can be patterned and removed using chemistries that do not attack the freestanding film or commercial photoresists. Thus many steps currently needed to protect the freestanding film or fabricate etch masks can be eliminated. Some recommended substrates include silicate glasses, which can be etched with buffered oxide etchant (BOE), and polished salt plates

(for example, NaCl), which can be dissolved in water. Care must be exercised when using these two substrates to minimize the influence of undercut in the etching process.

6.2.4. Systematic study on chemical and mechanical modification of polymer surfaces during CMP

How process variables (down force, rotation speed of platen, polishing temperature, etc.) and slurry characteristics (pH, slurry particle size, etc.) influence chemical or mechanical modification of polymer surfaces during CMP can be systematically studied using techniques developed in this thesis. Because of the small length scale (~10nm) associated with the modification, strict control over contamination and careful design of experiments are crucial to obtaining accurate and meaningful information. The post-CMP surface must be thoroughly cleaned to removal slurry particles and surfactants. Any slurry particles or surfactants remaining on the surface will contribute to unwanted photoelectron intensities during XPS measurements. Slurry particles left on the surface can also scatter x-rays or photoelectrons during XPS measurements and thus deteriorate data quality. Surfactants may also absorb in the infrared range and introduce noise in infrared spectra. Experiments must be carefully designed so that temperature variations, difference in wafer substrate or sample handling procedures (e.g., sample cleaning, transfer, etc.) do not lead to errors in comparison of samples. Usually, it is desired that samples be prepared on the same wafer, stored under the same conditions, polished and measured on the same day. If some experiments must be carried out with known changes in process conditions, blank samples should be included in related measurements so that the influence caused by process condition variation can be evaluated.

APPENDIX A

CONCENTRATION PROFILES AND CORRESPONDING LAPLACE TRANSFORMS

A.1. Derivation of several Laplace transform formulae

a) Laplace transform: $f(t) = \exp(-A^2t^2)$

$$\begin{aligned} £\left[\exp(-A^2t^2)\right] &= \int_0^{+\infty} e^{-st}e^{-A^2t^2}\,dt \\ &= \int_0^{+\infty} e^{-A^2t^2-st}\,dt \\ &= e^{\frac{s^2}{4A^2}}\int_0^{+\infty} e^{-A^2t^2-st-\frac{s^2}{4A^2}}\,dt \\ &= e^{\frac{s^2}{4A^2}}\int_0^{+\infty} e^{-(At+\frac{s}{2A})^2}\,dt \end{aligned} \tag{A-1}$$

Let $v = At + \dfrac{s}{2A}$ and if A>0:

$$e^{\frac{s^2}{4A^2}}\int_0^{+\infty} e^{-(At+\frac{s}{2A})^2}\,dt = e^{\frac{s^2}{4A^2}}\int_{\frac{s}{2A}}^{+\infty}\frac{e^{-v^2}dv}{A} = \frac{e^{\frac{s^2}{4A^2}}}{A}\int_{\frac{s}{2A}}^{+\infty} e^{-v^2}\,dv = \frac{\sqrt{\pi}}{2A}e^{\frac{s^2}{4A^2}}\operatorname{erfc}(\frac{s}{2A}) \tag{A-2}$$

Or if A<0:

$$\begin{aligned} e^{\frac{s^2}{4A^2}}\int_0^{+\infty} e^{-(At+\frac{s}{2A})^2}\,dt &= e^{\frac{s^2}{4A^2}}\int_{\frac{s}{2A}}^{-\infty}\frac{e^{-v^2}dv}{A} = \frac{e^{\frac{s^2}{4A^2}}}{A}\int_{-\frac{s}{2A}}^{+\infty} e^{-(-v')^2}d(-v') \qquad (v' = -v) \\ &= \frac{\sqrt{\pi}}{-2A}e^{\frac{s^2}{4A^2}}\operatorname{erfc}(\frac{s}{-2A}) \end{aligned} \tag{A-3}$$

The results can be written in a simpler form as:

$$£\left[\exp(-A^2t^2)\right] = \frac{\sqrt{\pi}}{2|A|}e^{\frac{s^2}{4|A|^2}}\operatorname{erfc}(\frac{s}{2|A|}) \tag{A-4}$$

b) Laplace transform: $f(t) = \text{erfc}(At)$

Definition of complementary error function

$$\text{erfc}(x) = 1 - \text{erf}(x) = \frac{2}{\sqrt{\pi}} \int_x^{+\infty} e^{-u^2} du \tag{A-5}$$

Since erfc is only defined for positive values and t is positive in Laplace transform, A must be positive in this case.

$$\begin{aligned}
\pounds[\text{erfc}(At)] &= \int_0^{+\infty} e^{-st} \frac{2}{\sqrt{\pi}} \int_{At}^{+\infty} e^{-u^2} du dt \\
&= \frac{2}{\sqrt{\pi}} \left[-\frac{1}{s} \int_0^{+\infty} \int_{At}^{+\infty} e^{-u^2} du de^{-st} \right] \\
&= -\frac{1}{s} \frac{2}{\sqrt{\pi}} \left[e^{-st} \int_{At}^{+\infty} e^{-u^2} du \Big|_0^{+\infty} - \int_0^{+\infty} e^{-st} \frac{d \int_{At}^{+\infty} e^{-u^2} du}{dt} dt \right] \\
&= -\frac{1}{s} \frac{2}{\sqrt{\pi}} \left[0 - 1 \cdot \int_0^{+\infty} e^{-u^2} du - \int_0^{+\infty} e^{-st} (-e^{-A^2 t^2}) A dt \right] \\
&= -\frac{1}{s} \frac{2}{\sqrt{\pi}} \left[-\frac{\sqrt{\pi}}{2} + A \int_0^{+\infty} e^{-A^2 t^2 - st} dt \right] \\
&= -\frac{1}{s} \frac{2}{\sqrt{\pi}} \left[-\frac{\sqrt{\pi}}{2} + A \frac{\sqrt{\pi}}{2} \frac{e^{\frac{s^2}{4A^2}}}{A} \text{erfc}\left(\frac{s}{2A}\right) \right] \\
&= \frac{1}{s} - \frac{1}{s} e^{\frac{s^2}{4A^2}} \text{erfc}\left(\frac{s}{2A}\right)
\end{aligned} \tag{A-6}$$

c) Laplace transform: $f(t)=\begin{cases} A-Bt & \text{when } 0 < t < D \\ C & \text{when } t > D \end{cases}$

$$
\begin{aligned}
\pounds[f(t)] &= \int_0^\infty e^{-st} f(t)dt \\
&= \int_0^D (A-Bt)e^{-st}dt + \int_D^\infty Ce^{-st}dt \\
&= A\int_0^D e^{-st}dt - B\int_0^D te^{-st}dt + C\int_D^\infty e^{-st}dt \\
&= A\frac{1}{s}(1-e^{-Ds}) + \frac{B}{s}De^{-Ds} - \frac{B}{s^2}(1-e^{-Ds}) + \frac{C}{s}e^{-Ds} \\
&= \frac{A}{s} - \frac{B}{s^2} + (\frac{BD}{s} - \frac{A}{s} + \frac{B}{s^2} + \frac{C}{s})e^{-Ds}
\end{aligned}
\tag{A-7}
$$

d) Laplace transform: $f(t)=\begin{cases} A & \text{when } 0 < t < D \\ C & \text{when } t > D \end{cases}$

Substitute B=0 to expression in (A-7):

$$
\begin{aligned}
\pounds[f(t)] &= \frac{A}{s} - \frac{0}{s^2} + (\frac{0\cdot D}{s} - \frac{A}{s} + \frac{0}{s^2} + \frac{C}{s})e^{-Ds} \\
&= \frac{A}{s} - (\frac{A}{s} - \frac{C}{s})e^{-Ds}
\end{aligned}
\tag{A-8}
$$

A.2. Laplace transforms $\pounds[N_i(\lambda_M^i t);s]$ for different concentration profiles

In the following derivations, the superscripts: IS, LS, LG and ST designate infinite source diffusion model, limited source diffusion model, linear gradient model and step model, respectively.

a) Infinite source diffusion model:

$$c_i(z) = c_{B,i} + c_{S,i}\text{erfc}(\Delta_i z) \tag{A-9}$$

$$
\begin{aligned}
\pounds[N_i(\lambda_M^i t);s] &= \pounds[Nc_i(\lambda_M^i t);s] = N\pounds[c_i(\lambda_M^i t);s] \\
&= N\pounds[c_{B,i} + c_{S,i}\operatorname{erfc}(\Delta_i \lambda_M^i t);s] \\
&= N\{\frac{c_{B,i}}{s} + \frac{c_{S,i}}{s}[1 - e^{\frac{s^2}{4(\Delta_i\lambda_M^i)^2}}\operatorname{erfc}(\frac{s}{2\Delta_i\lambda_M^i})]\} \\
&= \frac{N(c_{B,i}+c_{S,i})}{s} - \frac{Nc_{S,i}}{s}e^{\frac{s^2}{4(\Delta_i\lambda_M^i)^2}}\operatorname{erfc}(\frac{s}{2\Delta_i\lambda_M^i}) \\
&= \frac{M_{1i}^{IS}}{s} + \frac{M_{2i}^{IS}}{s}e^{\frac{s^2}{(M_{3i}^{IS})^2}}\operatorname{erfc}(\frac{s}{M_{3i}^{IS}})
\end{aligned}
\tag{A-10}
$$

where $M_{1i}^{IS} = N(c_{B,i} + c_{S,i})$

$M_{2i}^{IS} = -Nc_{S,i}$

$M_{3i}^{IS} = 2\Delta_i\lambda_M^i$

b) Limited source diffusion model:

$$
c_i(z) = c_{B,i} + c_{s,i}^{'}e^{-\Delta_i^2 z^2} \tag{A-11}
$$

$$
\begin{aligned}
\pounds[N_i(\lambda_M^i t);s] &= \pounds[Nc_i(\lambda_M^i t);s] = N\pounds[c_i(\lambda_M^i t);s] \\
&= N\pounds[c_{B,i} + c_{S,i}^{'}\exp[-(\Delta_i\lambda_M^i t)^2];s] \\
&= N[\frac{c_{B,i}}{s} + \frac{\sqrt{\pi}c_{S,i}^{'}}{2\Delta_i\lambda_M^i}e^{\frac{s^2}{4(\Delta_i\lambda_M^i)^2}}\operatorname{erfc}(\frac{s}{2\Delta_i\lambda_M^i})] \\
&= \frac{Nc_{B,i}}{s} + \frac{\sqrt{\pi}Nc_{S,i}^{'}}{2\Delta_i\lambda_M^i}e^{\frac{s^2}{4(\Delta_i\lambda_M^i)^2}}\operatorname{erfc}(\frac{s}{2\Delta_i\lambda_M^i}) \\
&= \frac{M_{1i}^{LS}}{s} + M_{2i}^{LS}e^{\frac{s^2}{(M_{3i}^{LS})^2}}\operatorname{erfc}(\frac{s}{M_{3i}^{LS}})
\end{aligned}
\tag{A-12}
$$

where $M_{1i}^{LS} = Nc_{B,i}$

$M_{2i}^{LS} = \dfrac{\sqrt{\pi}Nc'_{S,i}}{2\Delta_i\lambda_M^i}$

$M_{3i}^{LS} = 2\Delta_i\lambda_M^i$

c) Linear gradient model:

$$c_i(z) = \begin{cases} c_{B,i} + c_{S,i}(1 - \dfrac{z}{\Lambda_i}) & \text{when } 0 < z < \Lambda_i \\ c_{B,i} & \text{when } z > \Lambda_i \end{cases} \tag{A-13}$$

$$\begin{aligned} &\pounds[N_i(\lambda_M^i t); s] = \pounds[Nc_i(\lambda_M^i t); s] = N\pounds[c_i(\lambda_M^i t); s] \\ &= N\left[\frac{c_{B,i} + c_{S,i}}{s} - \frac{\dfrac{\lambda_M^i}{\Lambda_i} c_{S,i}}{s^2} + \left(\frac{\dfrac{\lambda_M^i}{\Lambda_i} c_{S,i} \times \dfrac{\Lambda_i}{\lambda_M^i}}{s} - \frac{c_{B,i} + c_{S,i}}{s} + \frac{\dfrac{\lambda_M^i}{\Lambda_i} c_{S,i}}{s^2} + \frac{c_{B,i}}{s}\right) e^{-\frac{\Lambda_i}{\lambda_M^i} s} \right] \\ &= N\left[\frac{c_{B,i} + c_{S,i}}{s} - \frac{\lambda_M^i c_{S,i}}{\Lambda_i s^2} + \frac{\lambda_M^i c_{S,i}}{\Lambda_i s^2} e^{-\frac{\Lambda_i}{\lambda_M^i} s} \right] \\ &= \frac{M_{1i}^{LG}}{s} + \frac{M_{2i}^{LG}}{s^2}\left(1 - e^{\frac{s}{M_{3i}^{LG}}}\right) \end{aligned} \tag{A-14}$$

where $M_{1i}^{LG} = N(c_{B,i} + c_{S,i})$

$$M_{2i}^{LG} = -\frac{Nc_{S,i}\lambda_M^i}{\Lambda_i}$$

$$M_{3i}^{LG} = -\frac{\lambda_M^i}{\Lambda_i}$$

d) Step model:

$$c_i(z) = \begin{cases} c_{B,i} + c_{S,i} & \text{when } 0 < z < \Lambda_i \\ c_{B,i} & \text{when } z > \Lambda_i \end{cases} \tag{A-15}$$

$$
\begin{aligned}
\pounds[N_i(\lambda_M^i t);s] &= \pounds[Nc_i(\lambda_M^i t);s] = N\pounds[c_i(\lambda_M^i t);s] \\
&= N\left[\frac{c_{B,i}+c_{S,i}}{s} - (\frac{c_{B,i}+c_{S,i}}{s} - \frac{c_{B,i}}{s})e^{-\frac{\Lambda_i}{\lambda_M^i}s}\right] \\
&= N\left[\frac{c_{B,i}+c_{S,i}}{s} - \frac{c_{S,i}}{s}e^{-\frac{\Lambda_i}{\lambda_M^i}s}\right] \\
&= \frac{M_{1i}^{ST}}{s} + \frac{M_{2i}^{ST}}{s}e^{\frac{s}{M_{3i}^{ST}}}
\end{aligned}
\tag{A-16}
$$

where $M_{1i}^{ST} = N(c_{B,i} + c_{S,i})$

$M_{2i}^{ST} = -Nc_{S,i}$

$M_{3i}^{ST} = -\frac{\lambda_M^i}{\Lambda_i}$

A.3. Laplace transform for N concentration profile in poly (biphenyl dianhydride-p-phenylenediamine) (BPDA-PDA)

The nitrogen concentration profile can be expressed as:

$$N_N(z) = N - N_O(z) - N_C(z) \tag{A-17}$$

The nitrogen concentration Laplace transform ($z = \lambda_M^N t$) is:

$$
\begin{aligned}
\pounds[N_N(\lambda_M^N t);s] &= \pounds[N - N_O(\lambda_M^N t) - N_C(\lambda_M^N t);s] \\
&= \pounds[N;s] - \pounds[N_O(\lambda_M^N t);s] - \pounds[N_C(\lambda_M^N t);s] \\
&= \frac{N}{s} - \pounds[N_O(\lambda_M^N t);s] - \pounds[N_C(\lambda_M^N t);s]
\end{aligned}
\tag{A-18}
$$

Since Table 4-1 lists only the formula for concentration profiles that follow one of the four concentration profiles, the subscripts for N and the superscripts for λ are the same (i). For the nitrogen concentration profile, $\pounds[N_O(\lambda_M^N t);s]$ and $\pounds[N_C(\lambda_M^N t);s]$ must be

known, in which the subscripts for N and the superscripts for λ are different. $\pounds[N_i(\lambda_M^j t);s]$ can be obtained by replacing λ_M^i with λ_M^j in the corresponding $\pounds[N_i(\lambda_M^i t);s]$ formula. For example, consider the infinite source diffusion model. For O and C,

$$N_N(z) = N[1 - c_{B,O} - c_{S,O}\text{erfc}(\Delta_O z) - c_{B,C} - c_{S,C}\text{erfc}(\Delta_C z)] \tag{A-19}$$

$$\pounds[N_O(\lambda_M^O t);s] = \frac{N(c_{B,O}+c_{S,O})}{s} - \frac{Nc_{S,O}}{s} e^{\frac{s^2}{(2\Delta_O\lambda_M^O)^2}} \text{erfc}(\frac{s}{2\Delta_O\lambda_M^O}) \tag{A-20}$$

$$\pounds[N_O(\lambda_M^N t);s] = \frac{N(c_{B,O}+c_{S,O})}{s} - \frac{Nc_{S,O}}{s} e^{\frac{s^2}{(2\Delta_O\lambda_M^N)^2}} \text{erfc}(\frac{s}{2\Delta_O\lambda_M^N}) \tag{A-21}$$

$$\pounds[N_C(\lambda_M^C t);s] = \frac{N(c_{B,C}+c_{S,C})}{s} - \frac{Nc_{S,C}}{s} e^{\frac{s^2}{(2\Delta_C\lambda_M^C)^2}} \text{erfc}(\frac{s}{2\Delta_C\lambda_M^C}) \tag{A-22}$$

$$\pounds[N_C(\lambda_M^N t);s] = \frac{N(c_{B,C}+c_{S,C})}{s} - \frac{Nc_{S,C}}{s} e^{\frac{s^2}{(2\Delta_C\lambda_M^N)^2}} \text{erfc}(\frac{s}{2\Delta_C\lambda_M^N}) \tag{A-23}$$

Therefore,

$$\begin{aligned}
&\pounds[N_N(\lambda_M^N t);s] \\
&= \pounds[(N - N_O(\lambda_M^N t) - N_C(\lambda_M^N t);s] \\
&= \pounds[N;s] - \pounds[N_O(\lambda_M^N t);s] - \pounds[N_C(\lambda_M^N t);s] \\
&= \frac{N}{s} - \frac{N(c_{B,O}+c_{S,O})}{s} + \frac{Nc_{S,O}}{s} e^{\frac{s^2}{(2\Delta_O\lambda_M^N)^2}} \text{erfc}(\frac{s}{2\Delta_O\lambda_M^N}) \\
&- \frac{N(c_{B,C}+c_{S,C})}{s} + \frac{Nc_{S,C}}{s} e^{\frac{s^2}{(2\Delta_C\lambda_M^N)^2}} \text{erfc}(\frac{s}{2\Delta_C\lambda_M^N})
\end{aligned} \tag{A-24}$$

In the Laplace transform of the nitrogen concentration profile, the dependence of nitrogen concentration on the other two species is reflected by parameters $c_{B,C}$, $c_{S,C}$, Δ_O and Δ_C, while the characteristics of nitrogen itself is reflected by λ_M^N .

For other forms of the depth profile, the Laplace transform of nitrogen concentration profiles can be obtained in the same way.

A.4. Mathematics for obtaining overlayer model parameters from angle resolved x-ray photoelectron spectroscopy (ARXPS) data

The system to be studied consists of a uniform C_xO_{1-x} layer covering a $Si_aO_{(1-a-b)}N_b$ film.

The mathematic expressions for C, O and Si composition depth profiles are:

$$c_C(z) = \begin{cases} x & \text{when } 0 < z < \text{d} \\ 0 & \text{when } z > \text{d} \end{cases} \tag{A-25}$$

$$c_O(z) = \begin{cases} 1-x & \text{when } 0 < z < \text{d} \\ 1\text{-}a\text{-}b & \text{when } z > \text{d} \end{cases} \tag{A-26}$$

$$c_{Si}(z) = \begin{cases} 0 & \text{when } 0 < z < \text{d} \\ a & \text{when } z > \text{d} \end{cases} \tag{A-27}$$

$$c_N(z) = \begin{cases} 0 & \text{when } 0 < z < \text{d} \\ b & \text{when } z > \text{d} \end{cases} \tag{A-28}$$

From Table 4-1, the corresponding Laplace transforms are:

$$£\left[N_C(\lambda_M^C t); s\right] = \frac{Nx}{s} - \frac{Nx}{s} e^{-sd/\lambda_M^C} \tag{A-29}$$

$$£\left[N_O(\lambda_M^O t); s\right] = \frac{N(1-x)}{s} - \frac{N(a+b-x)}{s} e^{-sd/\lambda_M^O} \tag{A-30}$$

$$£\left[N_N(\lambda_M^N t);s\right]=\frac{bN}{s}e^{-sd/\lambda_M^N} \tag{A-31}$$

and

$$£\left[N_{Si}(\lambda_M^{Si} t);s\right]=\frac{aN}{s}e^{-sd/\lambda_M^{Si}} \tag{A-32}$$

The experimental photoelectron intensity fraction for element i can be related to the composition depth file by Equation (4-100); after the photoelectron intensities are measured experimentally, the composition depth profile parameters such as *d* and *x* can be obtained through data-fitting using Equation (4-100). It should be noted that the four expressions $(\frac{I_i(s)^{Exp}}{\sum I_i(s)^{Exp}})$ for C, O, Si and N are not independent because $\sum\frac{I_i(s)^{Exp}}{\sum I_i(s)^{Exp}}=1$. Therefore, only photoelectron intensity fractions of three of the four elements are needed in data fitting. In calculation, photoelectron intensity fractions of C, O and N are used, that is, the two parameters, *x* and *d*, are found by minimizing the following target function $F(x,d)$:

$$F(x,d)=\sum_{j=C,O,N}\left(\frac{I_j(s)^{Exp}}{\sum_{i=C,O,N,Si}I_i(s)^{Exp}}-\frac{S_j£\left[N_j(\lambda_M^j t);s\right]}{\sum_{i=C,O,N,Si}S_i£\left[N_i(\lambda_M^i t);s\right]}\right)^2 \tag{A-33}$$

APPENDIX B

CALCULATION OF ELECTRON ATTENUATION LENGTH IN POLY (BIPHENYL DIANHYDRIDE-P-PHENYLENEDIAMINE) (BPDA-PDA)

The electron attenuation length (EAL) is calculated using NIST Electron Effective-Attenuation-Length Database Version 1.0. (EEALD 1.0) [185].

The inputs required by the software include:

1. IMFP (inelastic mean free path) and TMFP (transport mean free path): "database" is chosen as the source

2 Electron kinetic energy (*KE*)

KE can be calculated from binding energy (*BE*) using the following equation:

$$KE = h\nu - BE - \varphi \qquad \text{(B-1)}$$

where $h\nu$ is the photon energy and φ is the spectrometer work function.

The specific x-ray photoelectron spectroscopy (XPS) system in our laboratory (PHI Model 1600) uses Al Kα radiation, $h\nu$=1486.8eV and the work function φ is 3.7eV. *KE* and *BE* values for photoelectrons from C, N and O are shown in Table B-1.

Table B-1 *KE* and *BE* of photoelectrons

Element	Subshell	Electron Binding Energy (eV)	Electron Kinetic Energy (eV)
C	1s	284.4	1198.7
N	1s	401.7	1081.4
O	1s	533.4	949.7

3. The asymmetric parameter

Values of the photoionization asymmetric parameter for XPS with Mg and Al Kα x-rays for the indicated elements and subshells are obtained from Table A.1 in Reference 185 and are summarized in Table B-2.

Table B-2 Photoionization asymmetric parameters

Element	Subshell	Binding Energy (eV)	β	
			Mg x-rays	Al x-rays
C	1s	284.4	2.00	2.00
N	1s	401.7	2.00	2.00
O	1s	533.4	2.00	2.00

4. Stoichiometry coefficients and number of valence electrons per molecules

For BPDA-PDA, the chemical formula is $-[-C_{22}O_4N_2H_{10}-]_n-$.

Recommended values for the number of valence electrons per atom for each element in calculating IMFP from TPP-2M predictive IMFP are given in Table B.1 in Reference 185.

They are: H: 1 C: 4 N: 5 O: 6

Thus the number of valence electrons per monomer ($C_{22}O_4N_2H_{10}$) is 132.

5. Density of the solid material

Density of BPDA-PDA film is 1.4g/cm^3.

6. Band gap of BPDA-PDA

To the author's knowledge, the band gap energy of BPDA-PDA is not available in literature references. Only the band gap energy for pyromellitimido-oxydianiline polyimide (PMDA-ODA) is available and the value is 7.1eV [186]. PMDA-ODA has a similar chemical structure to BPDA-PDA.

Table B-3 EAL values for quantitative analysis (in nm)

C 1s	δ=5°, ϕ=85°	δ=45°, ϕ=45°	δ=85°, ϕ=5°
4eV	3.1959	3.2226	3.2273
7eV	3.5340	3.5668	3.5725
10eV	4.1248	4.1696	4.1774

N 1s	δ=5°, ϕ=85°	δ=45°, ϕ=45°	δ=85°, ϕ=5°
4eV	2.9362	2.9631	2.9678
7eV	3.2464	3.2793	3.2851
10eV	3.7881	3.8331	3.8410

O 1s	δ=5°, ϕ=85°	δ=45°, ϕ=45°	δ=85°, ϕ=5°
4eV	2.6400	2.6670	2.6717
7eV	2.9183	2.9514	2.9572
10eV	3.4042	3.4495	3.4574

Table B-3 lists the simulation results using the NIST database software. Three band gap energies are chosen to study the sensitivity of EAL with respect to the band gap energy. Three geometry settings (combination of δ and ϕ) are chosen.

It can be seen that EAL is not as sensitive to the geometric setting as it is to the band gap. The error of calculated EAL values can be as large as 20% if the band gap deviates from 7eV by ±3eV. As is evident from the modeling and the algorithm, it is the ratios (or the relative values) of EAL between different photoelectrons that will determine the exact shape of the concentration profiles for different species. The absolute values of EAL will establish how the concentration profiles scale in the depth direction. Table B-4 shows the EAL ratios of N 1s and O 1s to C 1s. It is obvious that the ratios are insensitive to both the choice of experimental geometry and the band gap value. EAL values for a band-gap energy of 7eV are used (δ=45^o, ϕ=45^o) in this thesis.

Table B-4 EAL ratios

N 1s/C 1s	δ=5^o, ϕ=85^o	δ=45^o, ϕ=45^o	δ=85^o, ϕ=5^o
4eV	0.91874	0.919475	0.919592
7eV	0.918619	0.919396	0.919552
10eV	0.918372	0.919297	0.919471

O 1s/C 1s	δ=5^o, ϕ=85^o	δ=45^o, ϕ=45^o	δ=85^o, ϕ=5^o
4eV	0.826058	0.827593	0.827844
7eV	0.825778	0.827464	0.827768
10eV	0.825301	0.827298	0.827644

APPENDIX C

CALCULATION OF ELECTRON ATTENUATION LENGTH IN SILICON NITRIDE

As in Appendix B, the electron attenuation length (EAL) is also calculated using NIST Electron Effective-Attenuation-Length Database Version 1.0. (EEALD 1.0) [185].

The inputs required by the software include:

1. IMFP (inelastic mean free path) and TMFP (transport mean free path): "database" is chosen as the source

2 Electron kinetic energy (*KE*)

KE and binding energy (*BE*) values for photoelectrons from C, N, O and Si are shown in Table C-1.

Table C-1 *KE* and *BE* of photoelectrons

Element	Subshell	Electron Binding Energy (eV)	Electron Kinetic Energy (eV)
C	1s	284.4	1198.7
N	1s	401.7	1081.4
O	1s	533.4	949.7
Si	$2p_{3/2}$	99.3	1383.8

3. The asymmetric parameter

Values of the photoionization asymmetric parameter for x-ray photoelectron spectroscopy (XPS) with Mg and Al Kα x-rays for the indicated elements and subshells are obtained from Table A.1 in [185] and are summarized in Table C-2.

Table C-2 Photoionization asymmetric parameters

Element	Subshell	Binding Energy (eV)	β	
			Mg x-rays	Al x-rays
C	1s	284.4	2.00	2.00
O	1s	533.4	2.00	2.00
N	1s	401.7	2.00	2.00
Si	$2p_{3/2}$	99.3	1.11	1.03

4. Stoichiometry coefficients and number of valence electrons per molecules

For silicon nitride, the chemical formula is Si_3N_4.

Recommended values for the number of valence electrons per atom for each element in calculating IMFP from TPP-2M predictive IMFP are given in Table B.1 in Reference 185.

They are: Si: 4 N: 5

Thus the number of valence electrons per molecule is 32.

5. Density of the solid material

Density of Si_3N_4 is 3.1g/cm^3 [2].

6. Band gap of Si_3N_4

The band gap of Si_3N_4 is 5eV [2]

Table C-3 lists the simulation results using the NIST database software. Three geometry settings (combination of δ and θ) are chosen.

Table C-3 EAL values for quantitative analysis (in nm)

Element	Subshell	δ=5^o, θ=85^o	δ=45^o, θ=45^o	δ=85^o, θ=5^o
C	1s	2.5280	2.5803	2.5896
N	1s	2.3189	2.3706	2.3799
O	1s	2.0806	2.1317	2.1408
Si	$2p_{3/2}$	2.8822	2.9454	2.9566

It can be seen that EAL is not very sensitive to the geometric setting. EAL values for δ=45^o and θ=45^o are used in all calculations.

APPENDIX D

DERIVATION OF R/T RATIO FORMULA

As shown in Figure 5-4, if the light is incident from vacuum (or air) in the *XZ* plane with an incident angle of θ, then $\alpha=(\omega/c)\sin\theta$, $\beta=0$. Equation (5-22) thus becomes:

$$\det\begin{pmatrix} (\omega/c)^2(n_x-ik_x)^2-\gamma^2 & 0 & \alpha\gamma \\ 0 & (\omega/c)^2(n_y-ik_y)^2-\alpha^2-\gamma^2 & 0 \\ \alpha\gamma & 0 & (\omega/c)^2(n_z-ik_z)^2-\alpha^2 \end{pmatrix}=0 \qquad \text{(D-1)}$$

In deriving Equation (D-1), the relation $c=1/\sqrt{\mu\varepsilon_0}$ is used. The solutions to Equation (D-1) are:

$$\gamma_{1,2}=\pm\sqrt{(\omega/c)^2(n_x-ik_x)^2-\frac{(n_x-ik_x)^2}{(n_z-ik_z)^2}\alpha^2} \qquad \text{(D-2)}$$

$$\gamma_{3,4}=\pm\sqrt{(\omega/c)^2(n_y-ik_y)^2-\alpha^2} \qquad \text{(D-3)}$$

In the following discussion, we specify γ_1 and γ_3 as the two roots with positive real parts; these two roots correspond to the two partial waves propagating in the positive *Z* direction. For γ_1, substitution of Equation (D-2) into Equation (D-1) yields:

$$\begin{pmatrix} (\omega/c)^2(n_x-ik_x)^2-\gamma_1^2 & 0 & \alpha\gamma_1 \\ 0 & (\omega/c)^2(n_y-ik_y)^2-\alpha^2-(\omega/c)^2(n_x-ik_x)^2+\frac{(n_x-ik_x)^2}{(n_z-ik_z)^2}\alpha^2 & 0 \\ \alpha\gamma_1 & 0 & (\omega/c)^2(n_z-ik_z)^2-\alpha^2 \end{pmatrix}\begin{pmatrix} E_x \\ E_y \\ E_z \end{pmatrix}=0 \qquad \text{(D-4)}$$

If

$$\alpha^2\frac{(n_z-ik_z)^2-(n_x-ik_x)^2}{(\omega/c)^2(n_z-ik_z)^2}\neq(n_y-ik_y)^2-(n_x-ik_x)^2 \qquad \text{(D-5)}$$

it can be concluded from Equation (D-4) that:

$$E_y = 0$$
$$\frac{E_x}{E_z} = \frac{-(\omega/c)^2(n_z - ik_z)^2 + \alpha^2}{\alpha\gamma_1} \tag{D-6}$$

It is worth pointing out that rearranging Equation (D-2) leads to:

$$\frac{(\omega/c)^2(n_z - ik_z)^2 - \alpha^2}{\alpha\gamma_1} = \frac{\alpha\gamma_1}{(\omega/c)^2(n_x - ik_x)^2 - \gamma_1^2} \tag{D-7}$$

Thus we can define $\mathbf{p}_1^{'}$ and unit vector $\mathbf{p}_1$ as:

$$\mathbf{p}_1^{'} = \begin{pmatrix} -(\omega/c)^2(n_z - ik_z)^2 + \alpha^2 & 0 & \alpha\gamma_1 \end{pmatrix}^T \tag{D-8}$$

$$\mathbf{p}_1 = \frac{\mathbf{p}_1^{'}}{\left|\mathbf{p}_1^{'}\right|} = \begin{pmatrix} \dfrac{-(\omega/c)^2(n_z - ik_z)^2 + \alpha^2}{\left|\mathbf{p}_1^{'}\right|} & 0 & \dfrac{\alpha\gamma_1}{\left|\mathbf{p}_1^{'}\right|} \end{pmatrix}^T = \begin{pmatrix} p_{11} \\ 0 \\ p_{13} \end{pmatrix} \tag{D-9}$$

where

$$p_{11} = \frac{-(\omega/c)^2(n_z - ik_z)^2 + \alpha^2}{\left|\mathbf{p}_1^{'}\right|}$$
$$p_{13} = \frac{\alpha\gamma_1}{\left|\mathbf{p}_1^{'}\right|} \tag{D-10}$$

Subsequently,

$$\mathbf{q}_1 = \frac{c}{\omega\mu}\mathbf{k}_1 \times \mathbf{p}_1 = \frac{c}{\omega\mu}\begin{pmatrix} \alpha \\ 0 \\ \gamma_1 \end{pmatrix} \times \begin{pmatrix} p_{11} \\ 0 \\ p_{13} \end{pmatrix} = \begin{pmatrix} 0 \\ \dfrac{c}{\omega\mu}(\gamma_1 \cdot p_{11} - \alpha \cdot p_{13}) \\ 0 \end{pmatrix} \tag{D-11}$$

Similarly, for $\gamma_2 = -\gamma_1$, we have:

$$\mathbf{p}_2^{'} = \left(-(\omega/c)^2(n_z - ik_z)^2 + \alpha^2 \quad 0 \quad -\alpha\gamma_1\right)^T \tag{D-12}$$

$$\mathbf{p}_2 = \frac{\mathbf{p}_2^{'}}{\left|\mathbf{p}_2^{'}\right|} = \left(\frac{-(\omega/c)^2(n_z - ik_z)^2 + \alpha^2}{\left|\mathbf{p}_2^{'}\right|} \quad 0 \quad \frac{-\alpha\gamma_1}{\left|\mathbf{p}_2^{'}\right|}\right)^T = \begin{pmatrix} p_{21} \\ 0 \\ p_{23} \end{pmatrix} \tag{D-13}$$

where

$$\begin{aligned} p_{21} &= \frac{-(\omega/c)^2(n_z - ik_z)^2 + \alpha^2}{\left|\mathbf{p}_2^{'}\right|} \\ p_{23} &= \frac{-\alpha\gamma_1}{\left|\mathbf{p}_2^{'}\right|} \end{aligned} \tag{D-14}$$

and

$$\mathbf{q}_2 = \frac{c}{\omega\mu}\mathbf{k}_2 \times \mathbf{p}_2 = \frac{c}{\omega\mu}\begin{pmatrix} \alpha \\ 0 \\ -\gamma_1 \end{pmatrix} \times \begin{pmatrix} p_{21} \\ 0 \\ p_{23} \end{pmatrix} = \begin{pmatrix} 0 \\ \frac{c}{\omega\mu}(-\gamma_1 \cdot p_{21} - \alpha \cdot p_{23}) \\ 0 \end{pmatrix} \tag{D-15}$$

In the above expressions: $\left|\mathbf{p}_1^{'}\right| = \left|\mathbf{p}_2^{'}\right|$, $p_{11} = p_{21}$ and $p_{13} = -p_{23}$.

For γ_3, substitution of Equation (D-3) into Equation (D-1) yields:

$$\begin{pmatrix} (\omega/c)^2(n_x - ik_x)^2 - \gamma_3^2 & 0 & \alpha\gamma_3 \\ 0 & 0 & 0 \\ \alpha\gamma_3 & 0 & (\omega/c)^2(n_z - ik_z)^2 - \alpha^2 \end{pmatrix} \begin{pmatrix} E_x \\ E_y \\ E_z \end{pmatrix} = 0 \tag{D-16}$$

From Equation (D-16):

$$\begin{pmatrix} (\omega/c)^2(n_x - ik_x)^2 - \gamma_3^2 & \alpha\gamma_3 \\ \alpha\gamma_3 & (\omega/c)^2(n_z - ik_z)^2 - \alpha^2 \end{pmatrix} \begin{pmatrix} E_x \\ E_z \end{pmatrix} = 0 \tag{D-17}$$

The inequality in Equation (D-5) is equivalent to:

$$\det\begin{pmatrix} (\omega/c)^2(n_x - ik_x)^2 - \gamma_3^2 & \alpha\gamma_3 \\ \alpha\gamma_3 & (\omega/c)^2(n_z - ik_z)^2 - \alpha^2 \end{pmatrix} \neq 0 \tag{D-18}$$

which implies that

$$E_x = E_z = 0 \tag{D-19}$$

Thus we can choose $\mathbf{p}_3$ as:

$$\mathbf{p}_3 = \begin{pmatrix} 0 \\ 1 \\ 0 \end{pmatrix} \tag{D-20}$$

Therefore,

$$\mathbf{q}_3 = \frac{c}{\omega\mu}\mathbf{k}_3 \times \mathbf{p}_3 = \frac{c}{\omega\mu}\begin{pmatrix} \alpha \\ 0 \\ \gamma_3 \end{pmatrix} \times \begin{pmatrix} 0 \\ 1 \\ 0 \end{pmatrix} = \begin{pmatrix} -\frac{c}{\omega\mu}\gamma_3 \\ 0 \\ \frac{c}{\omega\mu}\alpha \end{pmatrix} \tag{D-21}$$

Similarly, for $\gamma_4 = -\gamma_3$, we have:

$$\mathbf{p}_4 = \begin{pmatrix} 0 \\ 1 \\ 0 \end{pmatrix} \tag{D-22}$$

and

$$\mathbf{q}_4 = \frac{c}{\omega\mu}\mathbf{k}_4 \times \mathbf{p}_4 = \frac{c}{\omega\mu}\begin{pmatrix} \alpha \\ 0 \\ -\gamma_3 \end{pmatrix} \times \begin{pmatrix} 0 \\ 1 \\ 0 \end{pmatrix} = \begin{pmatrix} \frac{c}{\omega\mu}\gamma_3 \\ 0 \\ \frac{c}{\omega\mu}\alpha \end{pmatrix} \tag{D-23}$$

In deriving $\mathbf{p_1}$-$\mathbf{p_4}$, the inequality expressed in Equation (D-5) is assumed. However, it is easy to verify that the expressions for $\mathbf{p_1}$-$\mathbf{p_4}$ are still valid even if:

$$\alpha^2 \frac{(n_z - ik_z)^2 - (n_x - ik_x)^2}{(\omega/c)^2 (n_z - ik_z)^2} = (n_y - ik_y)^2 - (n_x - ik_x)^2 \tag{D-24}$$

Thus

$$\begin{aligned}
\mathbf{D} &= \begin{pmatrix} \mathbf{x}\cdot\mathbf{p}_1 & \mathbf{x}\cdot\mathbf{p}_2 & \mathbf{x}\cdot\mathbf{p}_3 & \mathbf{x}\cdot\mathbf{p}_4 \\ \mathbf{y}\cdot\mathbf{q}_1 & \mathbf{y}\cdot\mathbf{q}_2 & \mathbf{y}\cdot\mathbf{q}_3 & \mathbf{y}\cdot\mathbf{q}_4 \\ \mathbf{y}\cdot\mathbf{p}_1 & \mathbf{y}\cdot\mathbf{p}_2 & \mathbf{y}\cdot\mathbf{p}_3 & \mathbf{y}\cdot\mathbf{p}_4 \\ \mathbf{x}\cdot\mathbf{q}_1 & \mathbf{x}\cdot\mathbf{q}_2 & \mathbf{x}\cdot\mathbf{q}_3 & \mathbf{x}\cdot\mathbf{q}_4 \end{pmatrix} \\
&= \begin{pmatrix} p_{11} & p_{21} & 0 & 0 \\ \frac{c}{\omega\mu}(\gamma_1 \cdot p_{11} - \alpha \cdot p_{13}) & \frac{c}{\omega\mu}(-\gamma_1 \cdot p_{21} - \alpha \cdot p_{23}) & 0 & 0 \\ 0 & 0 & 1 & 1 \\ 0 & 0 & -\frac{c}{\omega\mu}\gamma_3 & \frac{c}{\omega\mu}\gamma_3 \end{pmatrix} \\
&= \begin{pmatrix} \mathbf{D}_{UL} & \mathbf{O} \\ \mathbf{O} & \mathbf{D}_{LR} \end{pmatrix}
\end{aligned} \tag{D-25}$$

where

$$\mathbf{D}_{UL} = \begin{pmatrix} p_{11} & p_{21} \\ \frac{c}{\omega\mu}(\gamma_1 \cdot p_{11} - \alpha \cdot p_{13}) & \frac{c}{\omega\mu}(-\gamma_1 \cdot p_{21} - \alpha \cdot p_{23}) \end{pmatrix} \tag{D-26}$$

$$\mathbf{D}_{LR} = \begin{pmatrix} 1 & 1 \\ -\frac{c}{\omega\mu}\gamma_3 & \frac{c}{\omega\mu}\gamma_3 \end{pmatrix} \tag{D-27}$$

$$\mathbf{O} = \begin{pmatrix} 0 & 0 \\ 0 & 0 \end{pmatrix} \tag{D-28}$$

and

$$\mathbf{P} = \begin{pmatrix} \exp[i\gamma_1 t] & 0 & 0 & 0 \\ 0 & \exp[-i\gamma_1 t] & 0 & 0 \\ 0 & 0 & \exp[i\gamma_3 t] & 0 \\ 0 & 0 & 0 & \exp[-i\gamma_3 t] \end{pmatrix} = \begin{pmatrix} \mathbf{P}_{UL} & \mathbf{O} \\ \mathbf{O} & \mathbf{P}_{LR} \end{pmatrix} \tag{D-29}$$

where

$$\mathbf{P}_{UL} = \begin{pmatrix} \exp[i\gamma_1 t] & 0 \\ 0 & \exp[-i\gamma_1 t] \end{pmatrix} \tag{D-30}$$

$$\mathbf{P}_{LR} = \begin{pmatrix} \exp[i\gamma_3 t] & 0 \\ 0 & \exp[-i\gamma_3 t] \end{pmatrix} \tag{D-31}$$

In the above expressions, subscripts UL and LR are used to denote "upper left" and "lower right", respectively. The inverse of **D** is:

$$\mathbf{D}^{-1} = \begin{pmatrix} \mathbf{D}_{UL}^{-1} & \mathbf{O} \\ \mathbf{O} & \mathbf{D}_{LR}^{-1} \end{pmatrix} \tag{D-32}$$

For a layered structure of air(0)-film(1)-air(2),

$$\begin{pmatrix} A_1(0) \\ A_2(0) \\ A_3(0) \\ A_4(0) \end{pmatrix} = \mathbf{M} \begin{pmatrix} A_1(2) \\ A_2(2) \\ A_3(2) \\ A_4(2) \end{pmatrix} = \mathbf{D}^{-1}(0)\mathbf{D}(1)\mathbf{P}(1)\mathbf{D}^{-1}(1)\mathbf{D}(2) \begin{pmatrix} A_1(2) \\ A_2(2) \\ A_3(2) \\ A_4(2) \end{pmatrix} \tag{D-33}$$

Because phase 0 and phase 2 are both air:

$$\mathbf{D}(0) = \mathbf{D}(2) \tag{D-34}$$

Also, because phase 2 is the last layer, there are no backward waves.

$$A_2(2) = A_2(4) = 0 \tag{D-35}$$

Now Equation (D-33) can be written as:

$$\begin{aligned}
\begin{pmatrix} A_1(0) \\ A_2(0) \\ A_3(0) \\ A_4(0) \end{pmatrix} &= \mathbf{D}^{-1}(0)\mathbf{D}(1)\mathbf{P}(1)\mathbf{D}^{-1}(1)\mathbf{D}(0)\begin{pmatrix} A_1(2) \\ 0 \\ A_3(2) \\ 0 \end{pmatrix} \\
&= \begin{pmatrix} \mathbf{D}_{UL}^{-1}(0) & \mathbf{O} \\ \mathbf{O} & \mathbf{D}_{LR}^{-1}(0) \end{pmatrix}\begin{pmatrix} \mathbf{D}_{UL}(1) & \mathbf{O} \\ \mathbf{O} & \mathbf{D}_{LR}(1) \end{pmatrix}\begin{pmatrix} \mathbf{P}_{UL}(1) & \mathbf{O} \\ \mathbf{O} & \mathbf{P}_{LR}(1) \end{pmatrix}\begin{pmatrix} \mathbf{D}_{UL}^{-1}(1) & \mathbf{O} \\ \mathbf{O} & \mathbf{D}_{LR}^{-1}(1) \end{pmatrix}\begin{pmatrix} \mathbf{D}_{UL}(0) & \mathbf{O} \\ \mathbf{O} & \mathbf{D}_{LR}(0) \end{pmatrix}\begin{pmatrix} A_1(2) \\ 0 \\ A_3(2) \\ 0 \end{pmatrix} \\
&= \begin{pmatrix} \mathbf{D}_{UL}^{-1}(0)\mathbf{D}_{UL}(1)\mathbf{P}_{UL}(1)\mathbf{D}_{UL}^{-1}(1)\mathbf{D}_{UL}(0) & \mathbf{O} \\ \mathbf{O} & \mathbf{D}_{LR}^{-1}(0)\mathbf{D}_{LR}(1)\mathbf{P}_{LR}(1)\mathbf{D}_{LR}^{-1}(1)\mathbf{D}_{LR}(0) \end{pmatrix}\begin{pmatrix} A_1(2) \\ 0 \\ A_3(2) \\ 0 \end{pmatrix}
\end{aligned} \tag{D-36}$$

Equation (D-36) can be written as two separate equations:

$$\begin{pmatrix} A_1(0) \\ A_2(0) \end{pmatrix} = \mathbf{D}_{UL}^{-1}(0)\mathbf{D}_{UL}(1)\mathbf{P}_{UL}(1)\mathbf{D}_{UL}^{-1}(1)\mathbf{D}_{UL}(0)\begin{pmatrix} A_1(2) \\ 0 \end{pmatrix} \tag{D-37}$$

and

$$\begin{pmatrix} A_3(0) \\ A_4(0) \end{pmatrix} = \mathbf{D}_{LR}^{-1}(0)\mathbf{D}_{LR}(1)\mathbf{P}_{LR}(1)\mathbf{D}_{LR}^{-1}(1)\mathbf{D}_{LR}(0)\begin{pmatrix} A_3(2) \\ 0 \end{pmatrix} \tag{D-38}$$

Because $\gamma_{1,2}$ and $\gamma_{3,4}$ correspond to p- and s-polarized light, respectively, Equations (D-37) and (D-38) can be used to calculate the transmittance and reflectance of p- and s-polarized light, respectively. Here we start with s-polarized light. For propagation in air:

$$\gamma_3(0) = (\omega/c)\sqrt{n_0^2 - \sin^2\theta} \tag{D-39}$$

Thus:

$$\mathbf{D}_{LR}(0)=\begin{pmatrix} 1 & 1 \\ -\frac{1}{\mu}\sqrt{n_0^2-\sin^2\theta} & \frac{1}{\mu}\sqrt{n_0^2-\sin^2\theta} \end{pmatrix} \tag{D-40}$$

$$\mathbf{D}_{LR}^{-1}(0)=\begin{pmatrix} 1/2 & -\frac{\mu}{2\sqrt{n_0^2-\sin^2\theta}} \\ 1/2 & \frac{\mu}{2\sqrt{n_0^2-\sin^2\theta}} \end{pmatrix} \tag{D-41}$$

For propagation in the film,

$$\gamma_3(1)=(\omega/c)\sqrt{(n_y-ik_y)^2-\sin^2\theta} \tag{D-42}$$

Thus:

$$\mathbf{D}_{LR}(1)=\begin{pmatrix} 1 & 1 \\ -\frac{1}{\mu}\sqrt{(n_y-ik_y)^2-\sin^2\theta} & \frac{1}{\mu}\sqrt{(n_y-ik_y)^2-\sin^2\theta} \end{pmatrix} \tag{D-43}$$

$$\mathbf{D}_{LR}^{-1}(1)=\begin{pmatrix} 1/2 & -\frac{\mu}{2\sqrt{(n_y-ik_y)^2-\sin^2\theta}} \\ 1/2 & \frac{\mu}{2\sqrt{(n_y-ik_y)^2-\sin^2\theta}} \end{pmatrix} \tag{D-44}$$

$$\mathbf{P}_{LR}(1)=\begin{pmatrix} \exp[i\gamma_3(1)t] & 0 \\ 0 & \exp[-i\gamma_3(1)t] \end{pmatrix} \tag{D-45}$$

$$\begin{pmatrix} A_3(0) \\ A_4(0) \end{pmatrix} = \mathbf{D}_{LR}^{-1}(0)\mathbf{D}_{LR}(1)\mathbf{P}_{LR}(1)\mathbf{D}_{LR}^{-1}(1)\mathbf{D}_{LR}(0)\begin{pmatrix} A_3(2) \\ 0 \end{pmatrix}$$

$$= \begin{pmatrix} \frac{1}{2}(1+\frac{\sqrt{(n_y-ik_y)^2-\sin^2\theta}}{\sqrt{n_0{}^2-\sin^2\theta}}) & \frac{1}{2}(1-\frac{\sqrt{(n_y-ik_y)^2-\sin^2\theta}}{\sqrt{n_0{}^2-\sin^2\theta}}) \\ \frac{1}{2}(1-\frac{\sqrt{(n_y-ik_y)^2-\sin^2\theta}}{\sqrt{n_0{}^2-\sin^2\theta}}) & \frac{1}{2}(1+\frac{\sqrt{(n_y-ik_y)^2-\sin^2\theta}}{\sqrt{n_0{}^2-\sin^2\theta}}) \end{pmatrix}$$

$$\times \begin{pmatrix} \frac{1}{2}(1+\frac{\sqrt{n_0{}^2-\sin^2\theta}}{\sqrt{(n_y-ik_y)^2-\sin^2\theta}})\exp[i\gamma_3(1)t]A_3(2) \\ \frac{1}{2}(1-\frac{\sqrt{n_0{}^2-\sin^2\theta}}{\sqrt{(n_y-ik_y)^2-\sin^2\theta}})\exp[-i\gamma_3(1)t]A_3(2) \end{pmatrix} \quad \text{(D-46)}$$

$$= \begin{pmatrix} \left\{(\frac{1}{2}+\frac{G}{4}+\frac{1}{4G})\exp[i\gamma_3(1)t]+(\frac{1}{2}-\frac{G}{4}-\frac{1}{4G})\exp[-i\gamma_3(1)t]\right\}A_3(2) \\ \left\{(\frac{G}{4}-\frac{1}{4G})\exp[i\gamma_3(1)t]-(\frac{G}{4}-\frac{1}{4G})\exp[-i\gamma_3(1)t]\right\}A_3(2) \end{pmatrix}$$

where

$$G = \frac{\sqrt{n_0{}^2-\sin^2\theta}}{\sqrt{(n_y-ik_y)^2-\sin^2\theta}} \quad \text{(D-47)}$$

Subsequently,

$$1/T_s = \left|(\frac{1}{2}+\frac{G}{4}+\frac{1}{4G})\exp[i\gamma_3(1)t]+(\frac{1}{2}-\frac{G}{4}-\frac{1}{4G})\exp[-i\gamma_3(1)t]\right|^2 \quad \text{(D-48)}$$

$$1/R_s = \left|\frac{(\frac{1}{2}+\frac{G}{4}+\frac{1}{4G})\exp[i\gamma_3(1)t]+(\frac{1}{2}-\frac{G}{4}-\frac{1}{4G})\exp[-i\gamma_3(1)t]}{(\frac{G}{4}-\frac{1}{4G})\exp[i\gamma_3(1)t]-(\frac{G}{4}-\frac{1}{4G})\exp[-i\gamma_3(1)t]}\right|^2 \quad \text{(D-49)}$$

For p-polarized light in air:

$$\gamma_1(0) = (\omega/c)\sqrt{n_0^2 - \sin^2\theta} \tag{D-50}$$

Thus:

$$\mathbf{D}_{UL}(0) = p_{11}(0)\begin{pmatrix} 1 & 1 \\ \dfrac{n_0^2}{\mu\sqrt{n_0^2 - \sin^2\theta}} & -\dfrac{n_0^2}{\mu\sqrt{n_0^2 - \sin^2\theta}} \end{pmatrix} \tag{D-51}$$

$$\mathbf{D}_{UL}^{-1}(0) = \frac{1}{p_{11}(0)}\begin{pmatrix} 1/2 & \dfrac{\mu\sqrt{n_0^2 - \sin^2\theta}}{2n_0^2} \\ 1/2 & -\dfrac{\mu\sqrt{n_0^2 - \sin^2\theta}}{2n_0^2} \end{pmatrix} \tag{D-52}$$

where $p_{11}(0)$ is the value of p_{11} in the air as defined in Equation (D-10).

For propagation in the film,

$$\gamma_1(1) = (\omega/c)\frac{(n_x - ik_x)}{(n_z - ik_z)}\sqrt{(n_z - ik_z)^2 - \sin^2\theta} \tag{D-53}$$

Thus:

$$\mathbf{D}_{UL}(1) = p_{11}(1)\begin{pmatrix} 1 & 1 \\ \dfrac{(n_x - ik_x)(n_z - ik_z)}{\mu\sqrt{(n_z - ik_z)^2 - \sin^2\theta}} & -\dfrac{(n_x - ik_x)(n_z - ik_z)}{\mu\sqrt{(n_z - ik_z)^2 - \sin^2\theta}} \end{pmatrix} \tag{D-54}$$

$$\mathbf{D}_{UL}^{-1}(1) = \frac{1}{p_{11}(1)}\begin{pmatrix} 1/2 & \dfrac{\mu\sqrt{(n_z - ik_z)^2 - \sin^2\theta}}{2(n_x - ik_x)(n_z - ik_z)} \\ 1/2 & -\dfrac{\mu\sqrt{(n_z - ik_z)^2 - \sin^2\theta}}{2(n_x - ik_x)(n_z - ik_z)} \end{pmatrix} \tag{D-55}$$

$$\mathbf{P}_{UL}(1) = \begin{pmatrix} \exp[i\gamma_1(1)t] & 0 \\ 0 & \exp[-i\gamma_1(1)t] \end{pmatrix} \tag{D-56}$$

where $p_{11}(1)$ is the value of p_{11} in the film as defined in Equation (D-10).

$$
\begin{aligned}
\begin{pmatrix} A_1(0) \\ A_2(0) \end{pmatrix} &= \mathbf{D}_{UL}^{-1}(0)\mathbf{D}_{UL}(1)\mathbf{P}_{UL}(1)\mathbf{D}_{UL}^{-1}(1)\mathbf{D}_{UL}(0)\begin{pmatrix} A_1(2) \\ 0 \end{pmatrix} \\
&= \begin{pmatrix} \frac{1}{2}\left(1+\frac{(n_x-ik_x)(n_z-ik_z)\sqrt{n_0^2-\sin^2\theta}}{n_0^2\sqrt{(n_z-ik_z)^2-\sin^2\theta}}\right) & \frac{1}{2}\left(1-\frac{(n_x-ik_x)(n_z-ik_z)\sqrt{n_0^2-\sin^2\theta}}{n_0^2\sqrt{(n_z-ik_z)^2-\sin^2\theta}}\right) \\ \frac{1}{2}\left(1-\frac{(n_x-ik_x)(n_z-ik_z)\sqrt{n_0^2-\sin^2\theta}}{n_0^2\sqrt{(n_z-ik_z)^2-\sin^2\theta}}\right) & \frac{1}{2}\left(1+\frac{(n_x-ik_x)(n_z-ik_z)\sqrt{n_0^2-\sin^2\theta}}{n_0^2\sqrt{(n_z-ik_z)^2-\sin^2\theta}}\right) \end{pmatrix} \\
&\times \begin{pmatrix} \frac{1}{2}\left(1+\frac{n_0^2\sqrt{(n_z-ik_z)^2-\sin^2\theta}}{(n_x-ik_x)(n_z-ik_z)\sqrt{n_0^2-\sin^2\theta}}\right)\exp\left[i\gamma_1(1)t\right]A_1(2) \\ \frac{1}{2}\left(1-\frac{n_0^2\sqrt{(n_z-ik_z)^2-\sin^2\theta}}{(n_x-ik_x)(n_z-ik_z)\sqrt{n_0^2-\sin^2\theta}}\right)\exp\left[-i\gamma_1(1)t\right]A_1(2) \end{pmatrix} \\
&= \begin{pmatrix} \left\{\left(\frac{1}{2}+\frac{H}{4}+\frac{1}{4H}\right)\exp\left[i\gamma_1(1)t\right]+\left(\frac{1}{2}-\frac{H}{4}-\frac{1}{4H}\right)\exp\left[-i\gamma_1(1)t\right]\right\}A_1(2) \\ \left\{\left(\frac{H}{4}-\frac{1}{4H}\right)\exp\left[i\gamma_1(1)t\right]-\left(\frac{H}{4}-\frac{1}{4H}\right)\exp\left[-i\gamma_1(1)t\right]\right\}A_1(2) \end{pmatrix}
\end{aligned}
\tag{D-57}
$$

where

$$
H = \frac{n_0^2\sqrt{(n_z-ik_z)^2-\sin^2\theta}}{(n_x-ik_x)(n_z-ik_z)\sqrt{n_0^2-\sin^2\theta}} \tag{D-58}
$$

Subsequently,

$$
1/T_p = \left|\left(\frac{1}{2}+\frac{H}{4}+\frac{1}{4H}\right)\exp\left[i\gamma_1(1)t\right]+\left(\frac{1}{2}-\frac{H}{4}-\frac{1}{4H}\right)\exp\left[-i\gamma_1(1)t\right]\right|^2 \tag{D-59}
$$

$$
1/R_p = \left|\frac{\left(\frac{1}{2}+\frac{H}{4}+\frac{1}{4H}\right)\exp\left[i\gamma_1(1)t\right]+\left(\frac{1}{2}-\frac{H}{4}-\frac{1}{4H}\right)\exp\left[-i\gamma_1(1)t\right]}{\left(\frac{H}{4}-\frac{1}{4H}\right)\exp\left[i\gamma_1(1)t\right]-\left(\frac{H}{4}-\frac{1}{4H}\right)\exp\left[-i\gamma_1(1)t\right]}\right|^2 \tag{D-60}
$$

APPENDIX E

EXPERIMENTAL PROOF OF THROUGH-PLANE UNIFORMITY OF OPTICAL ANISOTROPY IN SPIN-COATED POLY (BIPHENYL DIANHYDRIDE-P-PHENYLENEDIAMINE) (BPDA-PDA) FILMS

This appendix experimentally establishes the uniformity of optical anisotropy in the BPDA-PDA film thickness direction (through-plane). Flitsch and Shih reported that reactive ion etching (RIE) of BPDA-PDA films using an oxygen plasma at 300mTorr with a power density of 0.28W/cm^2 only affected a shallow surface region (~10-20nm), while the bulk properties of the films were unaffected [98]. In this study, BPDA-PDA films were thinned gradually using O_2 plasma RIE. Since the damage by RIE to the bulk properties of the films was negligible, a prism wave guide coupler could be used to measure the in-plane and through-plane refractive indices of a series of "controllably-thinned" films. In this way, the depth dependence of optical anisotropy in BPDA-PDA films was studied.

E.1. Sample preparation

BPDA-PDA films were spin-coated on 4-inch silicon wafers following the procedure described in Section 3.1.1. Four wafers were coated with BPDA-PDA films, one at 1500rpm (PI1500_1) and three at 2000rpm (PI2000_1, PI2000_2 and PI2000_3). PI2000_1 and PI2000_3 were broken to small pieces of 15mm×15mm samples for subsequent studies. Color fringes were observed across the BPDA-PDA films after curing, which was an indication of non-uniformity in thickness and/or optical properties

across the wafer. Because both film thickness and optical properties of the BPDA-PDA films are sensitive to preparation conditions and may vary from wafer to wafer even if the same conditions are used to prepare the films, only pieces broken from a single wafer were used in RIE studies. For convenience, a 4-inch silicon wafer with two flats was conceptually divided into three regions: a central region (≤1 inch from the center), an annular region (>1 inch but <1.5 inch from the center) and an edge region (≥1.5 inch from the center) (Figure E-1).

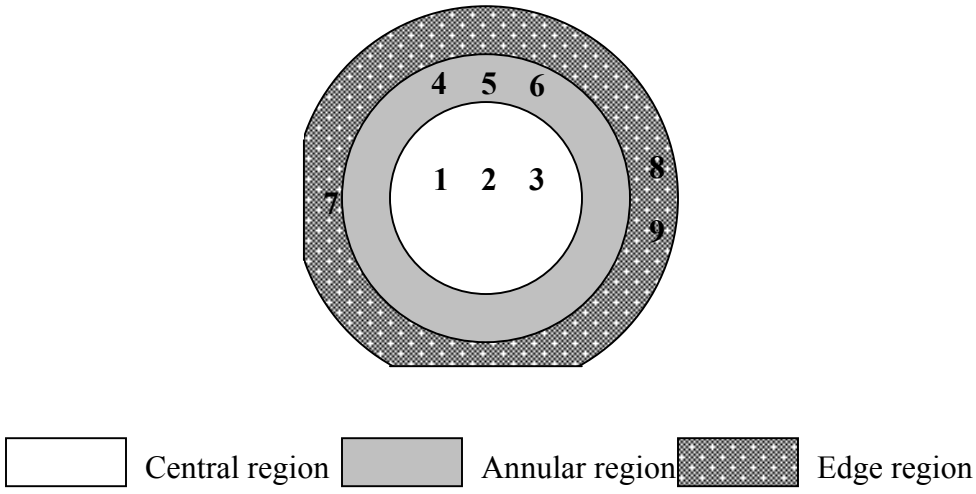

Figure E-1 Sample location on 4-inch silicon wafers

RIE of BPDA-PDA films were carried out following procedures described in Section 3.1.3. The initial BPDA-PDA film thickness, measured with a Tencor Alpha Step profilometer, was ~3μm. All 15mm×15mm samples were initially placed in the etching chamber. After each batch (etching for 40s or 50s), one sample was removed while the

other samples remained in the RIE chamber for next etch run. The sequential removal of samples from the chamber produced a series of films with different thicknesses. Since the precision of refractive index and thickness measurements will be compromised when the film thickness is below 1.5μm for the prism coupler, only films with thicknesses in the range between 1.5μm and 3μm were used for prism coupler measurements. The surface roughness of BPDA-PDA films before and after RIE (270s) was measured with atomic force microscopy (AFM) (Section 3.3.2).

E.2. Thickness measurement

The information obtained from prism waveguide coupler measurements include the in-plane refractive index ($n_{//}$), through-plane refractive index ($n_{\perp}$) and thickness calculated from TE (transverse electric) and TM (transverse magnetic) modes (Section 3.3.4). The average refractive index $\overline{n}$ and birefringence Δn are calculated by $\overline{n} = (2n_{//} + n_{\perp})/3$ and $\Delta n = n_{//} - n_{\perp}$, respectively.

The thickness values generated from the prism coupler were compared to those obtained from measurement on the same film (PI2000_1) with a Tencor Alpha Step profilometer. For films with a thickness of ~3μm, the difference was always less than 0.1um (data are given in Table E-1). In the following paragraphs, only thickness values generated by the prism coupler are discussed.

Table E-1 Comparison between thickness values from a prism coupler and a profilometer

Point #	Prism wave guide coupler					Profilometer
	$n_{//}$	$n_{\perp}$	Δn	$\overline{n}$	Thickness, μm	Thickness, μm
1	1.83565	1.63105	0.20460	1.76745	3.2462	3.33600
2	1.83518	1.63081	0.20437	1.76706	3.2837	3.36300
3	1.83573	1.63078	0.20495	1.76741	3.2802	3.34200
4	1.83587	1.63080	0.20507	1.76751	3.2795	3.35700
5	1.83573	1.63080	0.20493	1.76742	3.2793	3.35700

E.3. Repeatability of prism coupler measurement

Twenty-five measurements were performed on the same spot on sample PI2000_1 on different days; results are summarized in Table E-2. Clearly, very good repeatability was obtained. The standard deviations for $n_{//}$, $n_{\perp}$, $\overline{n}$ and Δn are all ~0.0003; the standard deviation for thickness is ~0.01um. We have observed that ambient temperature has a slight influence on the measurement results and thus in part, accounts for the data scatter.

Table E-2 Results from repeated measurement on the same spot of a film on different days

Control #	$n_{//}$	$n_{\perp}$	Δn	$\overline{n}$	Thickness, μm
1	1.83610	1.63093	0.20517	1.76771	3.3095
2	1.83597	1.63072	0.20525	1.76755	3.3011
3	1.83583	1.63091	0.20492	1.76752	3.3072
4	1.83583	1.63092	0.20491	1.76753	3.3072
5	1.83583	1.63092	0.20491	1.76753	3.3072
6	1.83583	1.63091	0.20492	1.76752	3.3072
7	1.83596	1.63056	0.20540	1.76749	3.3154
8	1.83555	1.63074	0.20481	1.76728	3.3137
9	1.83555	1.63108	0.20447	1.76739	3.3151
10	1.83540	1.63089	0.20451	1.76723	3.3243
11	1.83557	1.63092	0.20465	1.76735	3.3010
12	1.83540	1.63092	0.20448	1.76724	3.3181
13	1.83556	1.63089	0.20467	1.76734	3.3094
14	1.83555	1.63114	0.20441	1.76741	3.3151
15	1.83542	1.63073	0.20469	1.76719	3.3102
16	1.83530	1.63038	0.20492	1.76699	3.2980
17	1.83515	1.63041	0.20474	1.76690	3.3086
18	1.83529	1.63076	0.20453	1.76711	3.3072
29	1.83514	1.63021	0.20493	1.76683	3.3128
20	1.83514	1.63003	0.20511	1.76677	3.3128
21	1.83518	1.62987	0.20531	1.76674	3.2896
22	1.83518	1.63021	0.20497	1.76686	3.2896
23	1.83558	1.63039	0.20519	1.76718	3.2904
24	1.83571	1.63057	0.20514	1.76733	3.2980
25	1.83543	1.63038	0.20505	1.76708	3.3026
Average	1.83554	1.63067	0.20488	1.76725	3.30703
Standard deviation	0.00029	0.00034	0.00029	0.00028	0.0090

E.4. Optical anisotropy and in-plane isotropy of BPDA-PDA films

Optical anisotropy of BPDA-PDA films is indicated by large birefringence. For films in this study, $\overline{n}$ and Δn are approximately 1.768 and 0.216, respectively. Because the spin coating process is isotropic in the film plane, the resulting film should possess in-plane isotropy regardless of the birefringence. In order to establish the in-plane isotropy of BPDA-PDA films, PI2002_2 was mounted on a protractor and rotated at an interval of 45°; in this way, $n_{//}$ values in different directions can be obtained. Such measurements

should yield constant $n_{\perp}$ values; results are shown in Table E-3. The standard deviations for $n_{//}$ in all directions are smaller than 0.0003, indicating that the film is isotropic in the plane. As expected, $n_{\perp}$ shows little variation. Because it is difficult to ensure that the same area is measured each time after the proctor is rotated, the thickness variation is larger than that obtained in Section E.3.

Table E-3 In-plane isotropy of a BPDA-PDA film

Sample rotation	$n_{//}$	$n_{\perp}$	Δn	$\overline{n}$	Thickness, μm
0º	1.83968	1.62369	0.21599	1.76768	3.1818
45º	1.83951	1.62387	0.21564	1.76763	3.1993
90º	1.83946	1.62368	0.21578	1.76753	3.1535
135º	1.83951	1.62365	0.21586	1.76756	3.1975
180º	1.83923	1.62367	0.21556	1.76738	3.2043
225º	1.83968	1.62368	0.21600	1.76768	3.1760
270º	1.83968	1.62371	0.21597	1.76769	3.1760
315º	1.83968	1.62369	0.21599	1.76768	3.1760
Average	1.83955	1.62371	0.21585	1.76760	3.18305
Standard deviation	0.00015	0.00006	0.00016	0.00010	0.016

E.5. Spin speed influence and wafer-to-wafer differences

The anisotropy of BPDA-PDA results from preferential orientation of polymer chains during spin coating and curing. Therefore, the concentration and viscosity of the polymer solution, spin speed and cure temperature will have a large influence on the optical anisotropy of the films. PI2610 resins were stored in a refrigerator at -18°C and thus brought to room temperature prior to spin coating. Because there is no strict control over warming time before spin coating, differences in resin temperature are possible. Also, after the resin was dispensed onto the wafer, the amount of time that was needed for the

resin to spread out before wafer rotation was different for different samples. This may cause variation in solvent evaporation. As a result, these factors may have resulted in differences in solution viscosity. Therefore, wafer-to-wafer differences in optical anisotropy can be expected even if the same spin coating and curing conditions are used. Table E-4 shows typical measurement results from films prepared at two different spin speeds: 1500rpm and 2000rpm. Results from three films, PI2000_1, PI2000_2 and PI2000_3, prepared on two different days using the same spin speed (2000rpm), are also shown. Indeed, wafer-to-wafer variations under essentially the same preparation conditions occur. To ensure that RIE results can be compared directly, only samples broken from wafer PI2000_3 were used in the RIE studies described in Sections E.7, E.8 and E.9.

Table E-4 Influence of spin speed and wafer-to-wafer variation

Spin speed	$n_{//}$	$n_{\perp}$	Δn	$\overline{n}$	Thickness, μm
1500rpm (PI1500_1)	1.82786	1.64085	0.18701	1.76552	4.8697
2000rpm (PI2000_1)	1.83615	1.62787	0.20829	1.76672	3.2203
2000rpm (PI2000_2)	1.83968	1.62371	0.21597	1.76769	3.1760
2000rpm (PI2000_3)	1.84057	1.62343	0.21714	1.76819	3.2079

E.6. With-in sample non-uniformity of BPDA-PDA films

The optical properties of a film are not completely uniform across a 4-inch wafer (See Section E.7). However, the non-uniformities should be much smaller across a 15mm×15mm sample than across a 4-inch wafer. Measurements were performed at five points (left, top, right, bottom, center) of a 15mm×15mm sample from PI2000_1 and the

results are shown in Table E-5. The standard deviations for refractive indices obtained from 5 different points on a small square are smaller than 0.0003, indicating that the film is optically uniform across the sample. Furthermore, the thickness variation is more pronounced than are the optical properties for the small sample.

Table E-5 Non-uniformity across a 15mm×15mm die

Position	$n_{//}$	$n_{\perp}$	Δn	$\overline{n}$	Thickness, μm
Left	1.83687	1.63040	0.20647	1.76805	3.3332
Top	1.83684	1.63018	0.20666	1.76795	3.3586
Right	1.83718	1.62992	0.20726	1.76809	3.3130
Bottom	1.83691	1.62956	0.20735	1.76779	3.3073
Center	1.83687	1.63005	0.20682	1.76793	3.3373
Average	1.83693	1.63002	0.20691	1.76796	3.3299
Standard deviation	0.00014	0.00031	0.00038	0.00012	0.021

E.7. With-in wafer non-uniformity of BPDA-PDA films

In central, annular and edge regions of the wafer, three points were chosen in each, and two measurements were performed at each point. (Points 1, 2 and 3 are in the central region, 4, 5 and 6 in the annular region and 7, 8 and 9 in the edge region; positions of the points are shown in Figure E-1). The results are summarized in Table E-6. Figure E-2 shows $\overline{n}$ and Δn in different wafer regions. Clearly, $\overline{n}$ does not vary significantly from region to region, but Δn in the edge region is obviously larger than that in the central and annular regions. Since the difference between central and annular regions is small, samples from these two regions were used in RIE studies. The average and standard deviations for $\overline{n}$ and Δn in the combined region of central and annular are also listed in Table E-6.

Table E-6 Measurement results from different regions on a 4-inch wafer

Central Region

Point #	$n_{//}$	$n_{\perp}$	Δn	$\overline{n}$	Thickness, μm
1	1.84076	1.62347	0.21729	1.76833	3.17650
1	1.84004	1.62329	0.21675	1.76779	3.20160
2	1.84047	1.62327	0.2172	1.76807	3.18840
2	1.84005	1.62309	0.21696	1.76773	3.19440
3	1.84057	1.62343	0.21714	1.76819	3.20790
3	1.84048	1.62274	0.21774	1.7679	3.18300
Average	1.84040	1.62322	0.21718	1.76800	3.19197
Standard deviation	0.00029	0.00027	0.00034	0.00024	0.012

Annular Region

Point #	$n_{//}$	$n_{\perp}$	Δn	$\overline{n}$	Thickness, μm
4	1.84025	1.62360	0.21665	1.768033	3.07970
4	1.83962	1.62321	0.21641	1.767483	3.12960
5	1.84025	1.62365	0.2166	1.76805	3.15590
5	1.84001	1.62354	0.21647	1.767853	3.13690
6	1.84000	1.62380	0.2162	1.767933	3.06150
6	1.83988	1.62331	0.21657	1.76769	3.05590
Average	1.84000	1.62352	0.21648	1.76784	3.10325
Standard deviation	0.00024	0.00022	0.00016	0.00022	0.043

Edge Region

Point #	$n_{//}$	$n_{\perp}$	Δn	$\overline{n}$	Thickness, μm
7	1.84282	1.61989	0.22293	1.76851	2.99630
7	1.84227	1.61974	0.22253	1.768093	3.00160
8	1.84027	1.62244	0.21783	1.76766	2.80050
8	1.84103	1.62169	0.21934	1.767917	2.88360
9	1.84118	1.62132	0.21986	1.767893	2.81190
9	1.84068	1.62164	0.21904	1.767667	2.91780
Average	1.84138	1.62112	0.22026	1.76796	2.90195
Standard deviation	0.00098	0.0011	0.0020	0.00032	0.087

Central and Annular Regions Combined

	$n_{//}$	$n_{\perp}$	Δn	$\overline{n}$	Thickness, μm
Average	1.840198	1.623367	0.216832	1.767921	3.147608
Standard deviation	0.00033	0.00028	0.00044	0.00023	0.055

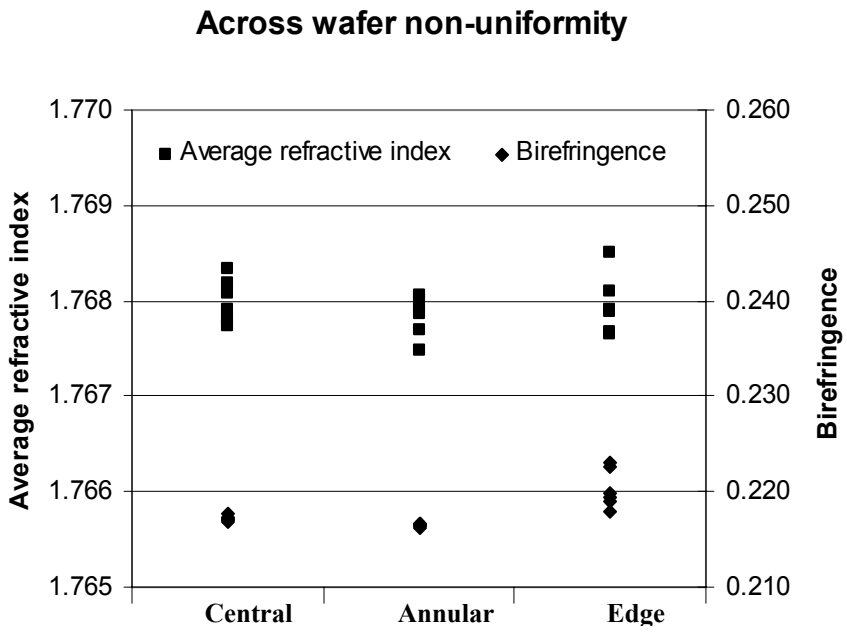

Figure E-2 Average refractive index and birefringence across a 4-inch wafer

E.8. Roughening of the BPDA-PDA surface due to RIE

The surface roughness values of a BPDA-PDA film before and after RIE (4.5 min) were determined by AFM to be ~1nm and ~15nm, respectively; thus, the BPDA-PDA film surface was roughened by the RIE process. Since the surface roughness of BPDA-PDA films is still significantly less than the wavelength of the laser light used in the prism coupler measurement (632.8nm), the roughness will not have a detectable impact on the optical measurement.

E.9. With-in sample non-uniformity after RIE

Although the film is uniform across a 1.5mm×1.5mm sample prior to RIE, non-uniformity develops during RIE; this effect was obvious from the interference color

fringes on the film after RIE. Generally, the film etched faster on one of the sample edges. Measurements were performed at 9 different positions across a sample and the results are shown in Table E-7. The thickness variation across the sample is larger than that before RIE, while the optical properties remain uniform and the standard deviations are comparable to those in Table E-2 and Table E-5. All the data in Section E.10 were collected at the center of each etched sample.

Table E-7 Non-uniformity across a 15mm×15mm die after RIE

Position	$n_{//}$	$n_{\perp}$	Δn	$\overline{n}$	Thickness, μm
Center	1.83979	1.62344	0.21635	1.767673	1.45260
Bottom	1.83954	1.62339	0.21615	1.76749	1.45100
Left	1.83980	1.62352	0.21628	1.767707	1.43470
Top	1.83945	1.62383	0.21562	1.767577	1.38280
Right	1.83971	1.62377	0.21594	1.76773	1.44030
Left Bottom	1.83976	1.62317	0.21659	1.767563	1.45440
Left Top	1.83987	1.62305	0.21682	1.767597	1.38230
Right Top	1.83960	1.62374	0.21586	1.767647	1.36740
Right Bottom	1.83992	1.62385	0.21607	1.767897	1.44430
Average	1.83972	1.62353	0.21619	1.76765	1.42331
Standard deviation	0.00016	0.00029	0.00037	0.00012	0.035

E.10. Depth dependence of optical anisotropy in a BPDA-PDA film

Seven samples from the central and annular regions of a wafer were etched by RIE for different times; measurement results after RIE are shown in Table E-8. The etching time is expressed as 40s×*i*+50s×*j*, where *i* designates the number of 40 second runs and *j* designates the number of 50 second runs. Figure E-3 shows average refractive index and birefringence as a function of film thickness after etching. Both $\overline{n}$ and Δn remain within the range defined by average value (m) ± 2 times standard deviation (σ) across the central

and annular regions (See Table E-6). Since $\overline{n}$ is directly related to the chemical structure and density of a material, the small change in $\overline{n}$ is consistent with the assumption that the bulk BPDA-PDA film is not affected during RIE.

Table E-8 Optical properties of BPDA-PDA films after RIE

Etching Time	$n_{//}$	$n_{\perp}$	Δn	$\overline{n}$	Thickness, μm
40s	1.83983	1.62331	0.21652	1.767657	2.87560
40s×2	1.84022	1.62271	0.21751	1.767717	2.70840
40s×3	1.83968	1.62349	0.21619	1.767617	2.60600
40s×4	1.83975	1.62368	0.21607	1.767727	2.41450
40s×4+50s	1.83984	1.62355	0.21629	1.767743	2.22310
40s×4+50s×2	1.83971	1.62303	0.21668	1.767483	1.87320
40s×4+50s×3	1.83996	1.62250	0.21746	1.767473	1.45050

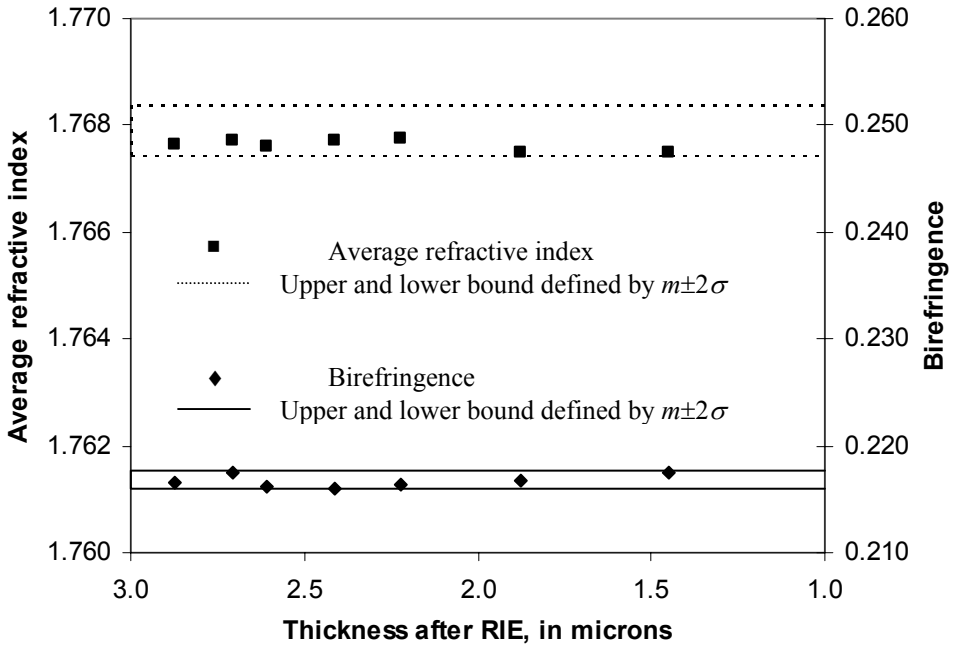

Figure E-3 Optical properties of BPDA-PDA films after RIE

Hasegawa *et al.* studied spontaneous molecular orientation of BPDA-PDA induced by thermal imidization [63]. Trirefringence in cured BPDA-PDA films ($\overline{n}$=1.7710) was observed when the corresponding polyamic acid films were stretched prior to curing. The refractive index difference in the two perpendicular directions normal to the stretching direction approached zero as the draw ratio increased. By following the dependence of trirefringence of cured BPDA-PDA films on the draw ratio of polyamic acid films, the intrinsic birefringence for the BPDA-PDA system was determined to be 0.66. If we use $n_{//}^0$ and $n_{\perp}^0$ to denote the refractive indices parallel and perpendicular, respectively, to the perfectly oriented polymer chains (denoted by the ideal system shown in Figure E-4a), the above results can be expressed as $n_{//}^0 - n_{\perp}^0 = 0.66$ and $(n_{//}^0 + 2n_{\perp}^0)/3 = 1.7710$. Thus, $n_{//}^0 = 2.211$ and $n_{\perp}^0 = 1.551$.

However, if all polymer backbones lie in the same plane but with random in-plane orientation (limiting case for spin coating, Figure E-4b), the in-plane and through-plane refractive indices $n_{//}$ and $n_{\perp}$ can be calculated from:

$$n_{//} = (n_{//}^0 - n_{\perp}^0) f(n_{//}) + n_{\perp}^0 \qquad \text{(E-1)}$$

and

$$n_{\perp} = (n_{//}^0 - n_{\perp}^0) f(n_{\perp}) + n_{\perp}^0 \qquad \text{(E-2)}$$

respectively, where $f(n_{//})$=0.5 and $f(n_{\perp})$=0 if the polymer chains are randomly distributed in-plane [187]. Therefore, $n_{//} = 1.881$ and $n_{\perp} = 1.551$. The birefringence for the latter case is 0.33. Since the force that can be exerted on the polymer chain is limited

in spin coating relative to mechanical stretching, it is difficult for the birefringence of the spin cast BPDA-PDA film to approach 0.3.

Therefore, for the spin coated BPDA-PDA films, the theoretical range for Δn is between 0 (random alignment in all directions) and 0.33 (limiting case in Figure E-4b). The variation in Δn shown in Figure E-3 only accounts for a very small portion of the possible range. Thus it can be safely concluded that the optical anisotropy is uniform in the through-plane direction for spin coated BPDA-PDA films.

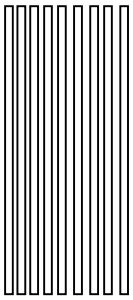

(a) All backbones aligned in the same direction

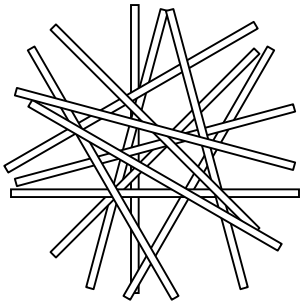

(b) All backbones aligned in the same plane with random in-plane orientation

Figure E-4 Ideal cases of molecular alignment (polymer backbones are represented as hollow strips)

APPENDIX F

RELATION BETWEEN POLARIZER EFFICIENCY AND FRACTION OF POLARIZED LIGHT INTENSITY PARALLEL TO THE POLARIZER ELECTRIC VECTOR DIRECTION

Polarizer efficiency (*PE*), or degree of polarization, is defined as [188]:

$$PE(\nu) = \frac{T_{//}(\nu) - T_{\perp}(\nu)}{T_{//}(\nu) + T_{\perp}(\nu)} \tag{F-1}$$

where $T_{//}(\nu)$ is the transmittance at wavelength ν when the polarizer electric vector direction is aligned parallel to a fully polarized beam and $T_{\perp}(\nu)$ is the transmittance at wavelength ν when the polarizer electric vector direction is aligned perpendicular to the fully polarized beam. Figure F-1 schematically shows light passing a polarizer.

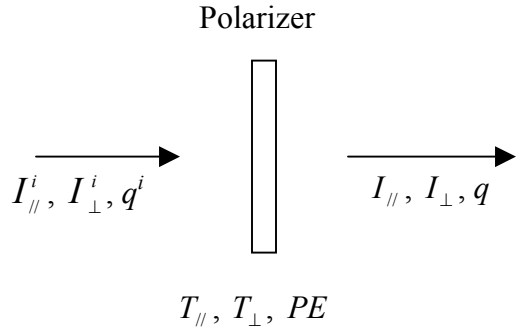

Figure F-1 A schematic representation of light passing through a polarizer

$I^i_{//}$ and $I^i_{\perp}$ are used to denote the intensity component of the two directions (one parallel and the other perpendicular to the polarizer electric vector direction) of incident light prior to striking the polarizer. The corresponding fraction of polarized light intensity parallel to the polarized electric vector direction q^i is defined in a similar way as in Equation (5-67).

$$q^i = \frac{I^i_{//}}{I^i_{//} + I^i_{\perp}} \tag{F-2}$$

Therefore:

$$I_{//} = I^i_{//} T_{//} \tag{F-3}$$

$$I_{\perp} = I^i_{\perp} T_{\perp} \tag{F-4}$$

$$q = \frac{I^i_{//} T_{//}}{I^i_{//} T_{//} + I^i_{\perp} T_{\perp}} = \frac{I^i_{//} / I^i_{\perp}}{I^i_{//} / I^i_{\perp} + T_{\perp} / T_{//}} = \frac{q^i + q^i PE}{1 - PE + 2q^i PE} \tag{F-5}$$

Equation (F-5) relates q, q^i and PE. If the light is randomly polarized before hitting the polarizer, q^i=0.5. In this case, q=(1+PE)/2. If the polarizer is an ideal polarizer (PE=1) or the incident beam is fully polarized (q^i=1), q will also be 1. In an infrared spectrometer, although the radiation produced by the infrared source tends to be randomly polarized, the randomness in polarization cannot be guaranteed when the radiation passes through the mirror sets in the spectrometer due to the difference in reflectivity of p- and s-polarized light on the mirrors. Therefore, in a common infrared spectrometer, q cannot be solely determined by PE; it depends on q^i as well.

APPENDIX G

SENSITIVITY ANALYSIS FOR R/T RATIO METHOD

Figure G-1 shows the operational procedure for the sensitivity analysis.

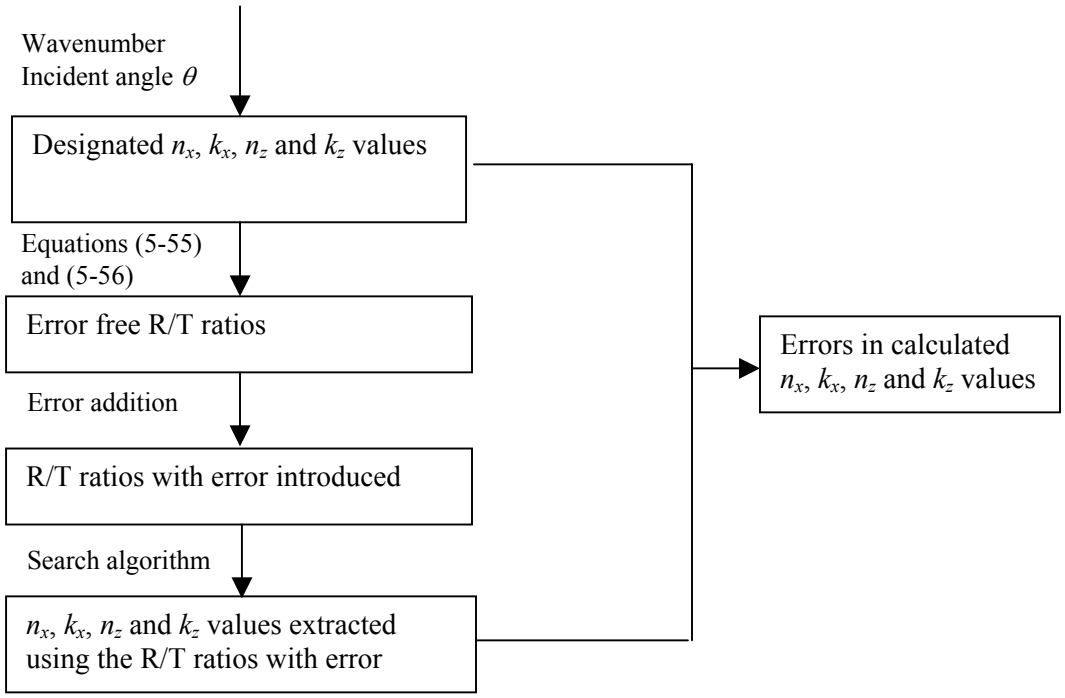

Figure G-1 Operational procedure for the sensitivity analysis

The sensitivity analysis was performed for two wavenumbers (1500 and 1900cm^{-1}) and three incident angles (θ =15°, 45° and 75°). From the n and k spectra of BPDA-PDA shown in Figure 5-7, n_x varies between 1.3 and 2.3, n_z varies between 1.1 and 2.1, and

both k_x and k_z are less than 1 in the spectra range of 1200-1900cm^{-1}. In the sensitivity analysis, n_x, k_x, n_z and k_z were so chosen that the influence of R/T ratio errors could be studied under different combinations of smaller and larger n and k values. In choosing n_x and n_z values, anisotropy was taken into account and the difference between n_x and n_z was fixed at 0.2. R/T ratios were then calculated using Equations (5-55) and (5-56). The same thickness pairings shown in Table 5-2b were used to calculate R/T ratios. Subsequently, errors were intentionally added to the R/T ratios. Six different levels of error were studied (-4%, -2%, -1%, 1%, 2% and 4%). It was assumed that the error associated with all R/T ratios is the same for a certain level of error. Finally, the algorithm described in Section 5.3.2 was used to extract n and k values and the results compared with the initially designated n and k values. Tables G-1 to G-4 list the sensitivity analysis results. In Tables G-1 to G-4, Δ denotes the error of calculated values, that is, the calculated value minus the designated value.

Table G-1 Sensitivity analysis results at 1500cm^{-1} wavenumber (positive R/T ratio errors)

θ	Designated values				Errors in calculated values from R/T ratios with error											
					R/T ratio error: +4%				R/T ratio error: +2%				R/T ratio error: +1%			
	n_x	k_x	n_z	k_z	Δn_x	Δk_x	Δn_z	Δk_z	Δn_x	Δk_x	Δn_z	Δk_z	Δn_x	Δk_x	Δn_z	Δk_z
15	1.3	1	1.1	1	-0.034	0.068	-0.046	-0.064	-0.014	0.034	-0.052	-0.162	-0.016	0.018	-0.016	0.156
15	1.3	0	1.1	1	0	0.002	0.062	0.058	0	0	0	0.004	0	0	0	0.002
15	1.3	1	1.1	0	-0.034	0.068	0.028	0	-0.014	0.034	0.016	0	-0.016	0.018	0.008	0
15	1.3	0	1.1	0	0	0.002	0	0	0	0	0	0.01	0	0	0	0.008
15	2.3	1	2.1	1	-0.038	0.064	-0.042	0.15	-0.02	0.032	0.016	0.148	-0.01	0.016	0.01	0.074
15	2.3	0	2.1	1	-0.004	0.03	0.816	-0.498	-0.002	0.022	0.802	-0.584	0	0.006		-0.028
15	2.3	1	2.1	0		0.064	0.06	0.054	-0.02	0.032	0.082	0.008	-0.01		0.042	0.004
15	2.3	0	2.1	0		0.03	-0.018	0	-0.002	0.022	-0.02	0	0		-0.21	0.428
Maximum Δ values					0	0.068		0.15	0	0.034	0.802	0.148	0	0.018	0.042	0.428
Minimum Δ values					-0.038		-0.046	-0.498	-0.02	0	-0.052	-0.584	-0.016	0	-0.21	
45	1.3	1	1.1	1	0.014	0.066	0.004	-0.048	-0.008	0.032	-0.018	0.062	-0.004		-0.01	0.044
45	1.3	0	1.1	1	0	0.004	-0.004	0.018	0	0.002	-0.002	0.01	0	0.002		0.008
45	1.3	1	1.1	0	0.014	0.066	0.01	0	-0.008	0.032	0.008	0	-0.004	0.016	0.004	0
45	1.3	0	1.1	0	0	0.004	-0.01	0	0	0.002	-0.004	0	0	0.002	-0.002	0
45	2.3	1	2.1	1	-0.042	0.064	-0.058	0.018	-0.022	0.032	-0.036	0	-0.012	0.016	-0.014	0.006
45	2.3	0	2.1	1	0	0.006	-0.018	-0.086	0	0.004	0	-0.046	0	0.004	0.02	-0.028
45	2.3	1	2.1	0	-0.042	0.064	-0.002	0.036	-0.022	0.032	-0.012	0.02	-0.012	0.016	-0.008	0.01
45	2.3	0	2.1	0	0	0.006	-0.01	0	0	0.004	-0.006	0	0	0.004	-0.002	0
Maximum Δ values					0.014	0.066	0.01	0.036	0	0.032	0.008	0.062	0	0.016	0.02	0.044
Minimum Δ values					-0.042	0.004	-0.058	-0.086	-0.022	0.002	-0.036	-0.046	-0.012	0.002	-0.014	-0.028
75	1.3	1	1.1	1	0.04	0.072	0.026	0.03	0.032	0.038	0.022	0.022	0.022	0.02	0.016	0.012
75	1.3	0	1.1	1	-0.012	0	-0.068	0.016	-0.006	0	-0.034	0.008	-0.002	0.014	0.004	0.04
75	1.3	1	1.1	0	0.04	0.072	-0.032	0.02	0.032	0.038	-0.02	0.012	0.022	0.02	-0.008	0.006
75	1.3	0	1.1	0	-0.012	0	-1.1	0.038	-0.006	0	-0.012	0	-0.002	0.014	-0.006	0
75	2.3	1	2.1	1	-0.034	0.064	-0.026	0.07	-0.018	0.032	-0.022	0.02	-0.01	0.016	-0.01	0.012
75	2.3	0	2.1	1	-0.004	0	-0.038	-0.046	-0.002	0	-0.02	-0.024	-0.002	0	-0.01	-0.006
75	2.3	1	2.1	0	-0.034	0.064	0.102	0.008	-0.018	0.032	0.048	0.004	-0.01	0.016	0.022	0.002
75	2.3	0	2.1	0	-0.004	0	-0.012	0.022	-0.002	0	-0.006	0.004	-0.002	0	0	0.014
Maximum Δ values					0.04	0.072	0.102	0.07	0.032	0.038	0.048	0.022	0.022	0.02		0.04
Minimum Δ values					-0.034	0	-1.1	-0.046	-0.018	0	-0.034	-0.024		0	-0.01	-0.006

Table G-2 Sensitivity analysis results at 1500cm^{-1} wavenumber (negative R/T ratio errors)

θ	Designated values				Errors in calculated values from R/T ratios with error											
					R/T ratio error: -1%				R/T ratio error: -2%				R/T ratio error: -4%			
	n_x	k_x	n_z	k_z	Δn_x	Δk_x	Δn	Δk_z	Δn_x	Δk_x	Δn_z	Δk_z	Δn_x		Δn_z	Δk_z
15	1.3	1	1.1	1		-0.018	0.016	0.01	0.026	-0.036	0.008	0.304	-0.182	-0.054	-0.126	-0.058
15	1.3	0	1.1	1		0	0	-0.002	0	0	0	-0.004	0	0	0.002	-0.006
15	1.3	1	1.1	0	0.014	-0.018	-0.158	0.1	0.026	-0.036	-0.41	0.154	-0.182	-0.054	0.042	0
15	1.3	0	1.1	0	0	0	-0.006	0.048	0	0	-0.012	0.068	0	0	-0.026	0.098
15	2.3	1	2.1	1	0.01	-0.016	-0.018	-0.078	0.018	-0.032	0.052	-0.056	0.034	-0.066	0.044	0.052
15	2.3	0	2.1	1	0		0.894	-1	0	0	0.868	-1	0	0		-1
15	2.3	1	2.1	0	0.01	-0.016	-0.052	0	0.018	-0.032	-0.094	0	0.034	-0.066		0
15	2.3	0	2.1	0	0	0	-0.01	0.016	0	0	-0.018	0	0	0		0
Maximum Δ values					0.014		0.894	0.1	0.026	0	0.868	0.304	0.034	0	0.816	
Minimum Δ values					0	-0.018		-1	0	-0.036	-0.41	-1	-0.182	-0.066	-0.126	-1
45	1.3	1	1.1	1	-0.034	-0.018	-0.028	0.022	-0.064	-0.036	-0.044	-0.054	-0.128	-0.074	-0.09	-0.098
45	1.3	0	1.1	1	0	0		0	0.004	0.01	0.06	0.024	0.004	0.01	0.07	0.02
45	1.3	1	1.1	0	-0.034	-0.018	0	0	-0.064	-0.036	-0.002	0	-0.128		-0.004	0
45	1.3	0	1.1	0	0		0.006	0.044	0.004	0.01	0.01	0.048	0.004	0.01	0.024	
45	2.3	1	2.1	1	0.012	-0.016	0.018		0.024	-0.032	0.038	0.002	0.054	-0.062	0.06	-0.056
45	2.3	0	2.1	1	0.002	0.01	0.126	-0.026	0.004	0.014	0.192	-0.044	0.014	0.024		-0.188
45	2.3	1	2.1	0	0.012	-0.016		0	0.024	-0.032	-0.018	0	0.054	-0.062	-0.05	0
45	2.3	0	2.1	0	0.002	0.01	0.004	0.038	0.004	0.014	0.01	0.06	0.014		-0.018	0.046
Maximum Δ values						0.01	0.126	0.044	0.024	0.014	0.192	0.06	0.054	0.024		0.074
Minimum Δ values					-0.034		-0.028	-0.026	-0.064	-0.036	-0.044	-0.054	-0.128	-0.074	-0.09	
75	1.3	1	1.1	1	-0.032	-0.022	-0.024	-0.016	-0.05	-0.042	-0.03	-0.068	-0.09	-0.084		-0.114
75	1.3	0	1.1	1	0.008	0.036		0.082	0.014	0.046	0.144	0.096	0.028	0.064	0.262	0.102
75	1.3	1	1.1	0	-0.032	-0.022	-0.016	0	-0.05	-0.042	-0.03	0	-0.09	-0.084		0
75	1.3	0	1.1	0	0.008	0.036		0.056	0.014	0.046	0.018	0.07	0.028	0.064	0.036	0.094
75	2.3	1	2.1	1	0.012	-0.016	0.014		0.032	-0.03	0.03	-0.03	0.068	-0.06	0.076	-0.034
75	2.3	0	2.1	1	0.002	0.014	0.088	-0.004	0.004	0.02	0.136	-0.004	0.008	0.028	0.214	-0.004
75	2.3	1	2.1	0	0.012	-0.016	-0.022	0	0.032	-0.03	-0.05	0	0.068	-0.06	-0.056	0
75	2.3	0	2.1	0	0.002	0.014	0	0	0.004	0.02	0	0	0.008	0.028		0
Maximum Δ values					0.012	0.036	0.092	0.082	0.032	0.046	0.144	0.096	0.068		0.262	
Minimum Δ values					-0.032	-0.022	-0.024	-0.016	-0.05	-0.042	-0.05	-0.068	-0.09		-0.056	-0.114

Table G-3 Sensitivity analysis results at 1900cm^{-1} wavenumber (positive R/T ratio errors)

θ	Designated values				Errors in calculated values from R/T ratios with error											
					R/T ratio error: +4%				R/T ratio error: +2%				R/T ratio error: +1%			
	n_x	k_x	n_z	k_z	Δn_x	Δk_x	Δn_z	Δk_z	Δn_x	Δk_x	Δn_z	Δk_z	Δn_x	Δk_x	Δn_z	Δk_z
15	1.3	1	1.1	1	0.004	0.056	-0.006	0.014	0.002	0.028	-0.012	0.006	0.002	0.014	-0.008	-0.024
15	1.3	0	1.1	1	0	0	0.224	0.39	0	0	0.08	0.134	0	0	0.034	0.056
15	1.3	1	1.1	0	0.004	0.056	-0.042	0.056	0.002	0.028	-0.018	0.032	0.002	0.014	-0.018	0.024
15	1.3	0	1.1	0	0	0		0.002	0	0	0	0.002	0	0	0	0
15	2.3	1	2.1	1	0.016		-0.058		0.01	0.026	-0.044	0.01	0.004	0.014	0.112	
15	2.3	0	2.1	1	0	0.004	-0.14	-0.014	0	0.002	-0.094	-0.002	0		0.028	-0.018
15	2.3	1	2.1	0	0.016		0.044	0.038	0.01	0.026	0.024	0.028	0.004	0.014	-0.074	0
15	2.3	0	2.1	0	0	0.004	-0.16	0.398	0	0.002	-0.106	0.34	0	0.002	-0.044	0.22
Maximum Δ values					0.016	0.056		0.398	0.01	0.028	0.08	0.34	0.004	0.014	0.112	0.22
Minimum Δ values					0	0	-0.16	-0.014	0	0	-0.106	-0.002	0	0	-0.074	-0.024
45	1.3	1	1.1	1	-0.012	0.054	-0.012		-0.022	0.026	-0.028	0.062	0	0.014		-0.006
45	1.3	0	1.1	1	0	0	-0.002	0.026	0	0	-0.002	0.014	0	0	0	0.006
45	1.3	1	1.1	0	-0.012	0.054		0.014	-0.022	0.026	0.014	0	0		0.002	0.002
45	1.3	0	1.1	0	0	0	0	0	0	0	0	0	0	0	0	0
45	2.3	1	2.1	1	0.022		0.044	0.102	0.01	0.026	0.032	0.07	0.014	0.014	-0.02	-0.038
45	2.3	0	2.1	1		0	-0.004	-0.004	0	0	-0.002	-0.002	0	0		-0.002
45	2.3	1	2.1	0	0.022	0.052	0.036		0.01	0.026	0.028	0.002	0.014	0.014		0.018
45	2.3	0	2.1	0	0	0	0.002	0.036	0	0	0	0.002	0	0	0	0.002
Maximum Δ values					0.022	0.054	0.044	0.102	0.01	0.026	0.032	0.07	0.014	0.014	0.002	0.018
Minimum Δ values					-0.012	0	-0.012	-0.004	-0.022	0	-0.028	-0.002	0	0	-0.042	-0.038
75	1.3	1	1.1	1	-0.056	0.046	-0.06	0.054	-0.022	0.024	-0.02	0.006	-0.012	0.012	-0.012	0.01
75	1.3	0	1.1	1	0	0	0	0.034	0	0	0	0.018	0	0	0	0.008
75	1.3	1	1.1	0	-0.056	0.046	0.008	0.004	-0.022	0.024	0.004	0.002	-0.012		0	0.002
75	1.3	0	1.1	0	0	0	-0.012	0	0	0	-0.006	0	0	0	-0.002	0.01
75	2.3	1	2.1	1	0.016	0.052	0.026	0.076	0.006	0.026	0.016	0.046	0.012	0.014	-0.008	-0.016
75	2.3	0	2.1	1	0	0.006	0.028	-0.002	0	0.004	0.02	-0.002	0	0.002	0.01	0
75	2.3	1	2.1	0		0.052	-0.006	0.026	0.006	0.026	0.002	0.012	0.012	0.014		0.014
75	2.3	0	2.1	0	0	0.006	0	0	0	0.004	0	0.002	0	0.002	0	0.004
Maximum Δ values					0.016		0.028	0.076	0.006	0.026	0.02	0.046	0.012	0.014	0.01	0.014
Minimum Δ values					-0.056	0	-0.06		-0.022	0	-0.02	-0.002	-0.012	0	-0.026	-0.016

Table G-4 Sensitivity analysis results at 1900cm^{-1} wavenumber (negative R/T ratio errors)

θ	Designated values				Errors in calculated values from R/T ratios with error											
					R/T ratio error: -1%				R/T ratio error: -2%				R/T ratio error: -4%			
	n_x	k_x	n_z	k_z	Δn_x	Δk_x	Δn_z	Δk_z	Δn_x	Δk_x	Δn_z	Δk_z	Δn_x	Δk_x	Δn_z	Δk_z
15	1.3	1	1.1	1	-0.002		0.014	0.032	0.002	-0.03	-0.028	-0.106	-0.004	-0.058	0.03	0.026
15	1.3	0	1.1	1	0	0		-0.046	0	0	-0.054	-0.088	0	0	-0.092	-0.15
15	1.3	1	1.1	0	-0.002	-0.014	-0.016	0	0.002	-0.03	-0.006	0.002	-0.004	-0.058	-0.046	0
15	1.3	0	1.1	0	0	0	-0.006	0.036	0	0	-0.018	0.06	0	0	-0.038	0.082
15	2.3	1	2.1	1	-0.006	-0.014	-0.07	-0.024	-0.016	-0.026	0.082	-0.006	-0.036		-0.072	-0.1
15	2.3	0	2.1	1	0	0	0.16	-0.036	0	0	0.394	-0.136	0	0	0.9	-0.858
15	2.3	1	2.1	0	-0.006	-0.014	-0.036	0.046	-0.016	-0.026	-0.118	0	-0.036	-0.054	-0.054	
15	2.3	0	2.1	0	0		0	0.026	0	0	0.002	0	0	0		0.012
Maximum Δ values					0	0	0.16	0.046	0.002	0	0.394	0.06		0	0.9	0.082
Minimum Δ values					-0.006	-0.014	-0.07	-0.046	-0.016	-0.03	-0.118	-0.136	-0.036	-0.058	-0.092	-0.858
45	1.3	1	1.1	1	0.002		0.002	0.002	0.004	-0.028	0.004	0.01	0.014	-0.056	0.018	-0.024
45	1.3	0	1.1	1	0	0	0	-0.006	0	0	0.002	-0.012	0	0	0.002	-0.026
45	1.3	1	1.1	0	0.002	-0.014	-0.004	0	0.004	-0.028	-0.042	0.028	0.014	-0.056	-0.116	0.064
45	1.3	0	1.1	0	0	0		0	0	0	0	0	0	0	0	0
45	2.3	1	2.1	1	-0.012	-0.014		0.02	-0.01	-0.026	-0.038	-0.078	-0.032	-0.054	-0.03	
45	2.3	0	2.1	1	0	0	0.002	0.002	0	0	0.002	0.002	0	0	0.004	0.004
45	2.3	1	2.1	0	-0.012	-0.014	-0.002	0	-0.01	-0.026	-0.04	0	-0.032	-0.054	-0.052	0
45	2.3	0	2.1	0	0	0		0	0	0	0	0	0	0	0	0
Maximum Δ values					0.002	0	0.008	0.02	0.004	0	0.004	0.028	0.014	0	0.018	0.064
Minimum Δ values					-0.012	-0.014	-0.004	-0.006	-0.01	-0.028	-0.042	-0.078	-0.032	-0.056	-0.116	-0.066
75	1.3	1	1.1	1	0.012	-0.012	0.012	-0.008	0.026	-0.024	0.026	-0.022	0.042	-0.05	0.042	-0.03
75	1.3	0	1.1	1	0	0	0	-0.008	0	0	0	-0.016	0	0	-0.954	-0.45
75	1.3	1	1.1	0	0.012	-0.012	-0.004	0	0.026	-0.024	-0.006	0	0.042	-0.05	-0.014	0
75	1.3	0	1.1	0		0	0.004	0.026	0	0	0.01	0.044		0	0.018	0.056
75	2.3	1	2.1	1	-0.012	-0.014	0.008	0.016	-0.004	-0.026	-0.018	-0.052	-1.16	-0.204	-1.028	-0.318
75	2.3	0	2.1	1	0	0	0	0	0	0	0.002	0	0	0		-0.002
75	2.3	1	2.1	0	-0.012	-0.014	-0.006		-0.004	-0.026	-0.03	0	-1.16	-0.204	-0.818	0.404
75	2.3	0	2.1	0	0	0	0	0	0	0	0	0	0	0	0	0
Maximum Δ values					0.012	0	0.012	0.026	0.026	0	0.026	0.044	0.042	0	0.042	0.404
Minimum Δ values					-0.012	-0.014	-0.006		-0.004	-0.026	-0.03	-0.052	-1.16	-0.204	-1.028	-0.45

REFERENCES

1 Lee, J. A.; Moinpour, M.; Liou, H. C.; Abell, T., Integration Challenges for Chemical Mechanical Polishing of Cu/Low-k interconnects, *Materials Research Society Symposium Proceedings*, 767, F7.4 - F7.5, 2003.

2 Campbell, S.A., *The Science and Engineering of Microelectronic Fabrication*, 2nd Ed., Oxford University Express, New York, 2001.

3 Singh, R. K and Bajaj, R., Advances in Chemical Mechanical Planarization, *MRS Bulletin*, 27, p743-751, 2002.

4 Weling, M.; Dunton, V.; Zhang, L.; Annapragada, R., CMP Integration Issues for Sub-0.15μm Process Technologies, *Electrochemical Society Proceedings*, 99-37, p517-533, 2000.

5 Oliver, M. R., CMP Fundamentals and Challenges, *Materials Research Society Symposium Proceedings*, 566, p73-79, 2000.

6 Basim, G. B.; Vakarelski, I. U.; Moudgil, B. M., Role of Interaction Forces in Controlling the Stability and Polishing Performance of CMP Slurries, *Journal of Colloidal and Interface Science*, 263, p506-515, 2003.

7 Zhou, C; Lei, S.; Hight, J. R.; Ng, S. H.; Danyluk, S., Fluid Pressure and Its Effects on Chemical Mechanical Polishing, *Wear*, 253, p430-437, 2002.

8 Shan, L; Levert, J.; Meade, L.; Tichy, J.; Danyluk, S., Interfacial Fluid Mechanics and Pressure Prediction in Chemical Mechanical Polishing, *Journal of Tribology*, 122, p539-543, 2000.

9 Schlueter J., Trench Warfare: CMP and Shallow Trench Isolation, *Semiconductor International*, 22, p123-130, 1999 (October).

10 Jeng S. P.; Havemann R.; Chang M., Advanced Metallization and Interconnect Systems for ULSI Applications, *Materials Research Society Symposium Proceedings*, 337, p25-31, 1996.

11 Steigerwald J. M., Murarka S. P., Gutmann R. J., *Chemical Mechanical Planarization of Microelectronic Materials*, John Wiley & Sons, Inc., New York, 1997.

12 Singer P., Dual-Damascene Challenges Dielectric-Etch, *Semiconductor International*, 22, p68-72, 1999 (August).

13 Singer P., Tantalum, Copper and Damascene: The Future of Interconnects, *Semiconductor International*, 21, p91-98, 1998 (June).

14 Sheih B., Saraswat K., Deal M., McVittie., Air Gaps Lower k of Interconnects Dielectrics, *Solid State Technology*, 42, p51-58, 1999 (Feburary).

15 Morgen, M.; Ryan, E. T.; Zhao, J. H.; et al., Low Dielectric Constant Materials for ULSI Interconnects, *Annual Review of Material Science*, 30, p645-680, 2000.

16 Tai, Y. L; Dai, B. T.; Tsai, M. S.; Tung, I. C.; Feng, M. S., CMP of Polyimide for Low-k Dielectric Application in ULSI, *Proceedings of International Symposium on VLSI Technology, Systems, and Applications*, p139-142, 1999.

17 Tai, Y. L.; Tsai, M. S.; Tung, I. C.; Dai, B. T.; Feng, M. S., Study on Chemical Mechanical Polishing of Low Dielectric Constant Polyimide Thin Films, *Electrochemical Society Proceedings*, Vol. 99-7, p15-23, 1999.

18 Kim, H. G.; An, Y. M.; Moon, D. K.; Park, J. G., Effect of Chemicals and Slurry Particles on Chemical Mechanical Polishing of Polyimide, *Japanese Journal of Applied Physics Part I*, 39 (3A), p1085-1090, 2000.

19 Murarka, S. P, Chemical-Mechanical Planarization of the Polymer Interlayer Dielectrics, *Material Research Society Symposium Proceedings*, 511, p277-290, 1998.

20 Neirynck, J. M.; Muraka, S. P.; Gutmann, R. J., Investigations of the Chemical Mechanical Polishing of Polymer Films for ILD Applications, *Materials Research Society Symposium Proceedings*, 381, p229-235, 1995.

21 Neirynck, J. M.; Yang, G. R.; Muraka, S. P.; Gutmann, R. J., The addition of Surfactant to Slurry for Polymer CMP: Effects on Polymer Surface, Removal Rate and Underlying Cu, *Thin Solid Films*, 290-291, p447-452, 1996.

22 Borst, C. L.; Thakurta, D. G.; Gill, W. N.; Gutmann, R. J., Chemical Mechanical Polishing Mechanisms of Low Dielectric Constant Polymers in Copper Slurries, *Journal of the Electrochemical Society*, 146, p4309-4315, 1999.

23 Borst, C. L.; Korthuis, V.; Shinn, G. B.; Luttmer, J. D.; Gutmann, R. J.; Gill, W. N., Chemical – Mechanical Polishing of SiOC Organosilicate Glasses: the Effect of Film Carbon Content, *Thin Solid Films*, 385, p281-292, 2001.

24 Borst, C. L.; Thakurta, D. G.; Gill, W. N.; Gutmann, R. J., Chemical Mechanical Planarization of Low k Polymers for Advanced IC Structures, *Transactions of ASME*, 124, p362-366, 2002.

25 Yang, G. R.; Zhao, Y. P.; Neirynck, J. M.; Merarka, S. P.; Gutmann, R. J., Chemical-Mechanical Polishing of Polymer Films: Comparison of Benzocyclobutene (BCB) and Parylene-N Films by XPS and AFM, *Materials Research Society Symposium Proceedings*, 476, p161-172, 1997.

26 Yang, G. R.; Zhao, Y. P.; Neirynck, J. M.; Murarka, S. P.; Gutmann, R. J., Chemical-Mechanical Polishing of Parylene N and Benzocyclobutene Films, *Journal of the Electrochemical Society*, 144, p3249-3255, 1997.

27 Kuchenmeister, F.; Schubert, U.; Wenzel, C., SiLK Dielectric Planarization by Chemical Mechanical Polishing, *Microelectronic Engineering*, 50, p47-52, 2000.

28 Block, K. H.; Rayle, H. L., Integration of CMP with Low-k Materials, *Semiconductor International*, 25, p115-p122, 2002 (June).

29 Heeg, J.; Schubert, U.; Huchenmeister, Surface Chemistry of Planarized SiLK-Films Studied by XPS, *Mikrochim Acta*, 133, p113-117, 2000.

30 Wang, S. and Grover, G., Integrating Cu/Ultra-Low-k with CMP, *Solid State Technology*, 45, S7-S8, S10, S24, 2002 (September).

31 Zantye, P. B.; Sikder, A. K.; Kumar, A., Polishing Behavior of the Various Interconnect Thin Films in Cu Damascene Process with Different Slurries, *Materials Research Society Symposium Proceedings*, 767, p291-296, 2003.

32 Towery, D.; Fury, M. A., Chemical Mechanical Polishing of Polymer Films, *Journal of Electronic Materials*, 27, p1088-1094, 1998.

33 Hara, T.; Tomisawa, T.; Kurosu, T.; Doy, T. K., Chemical Mechanical Polishing of Polyarylether Low Dielectric Constant Layers by Manganese Oxide Slurry, *Journal of the Electrochemical Society*, 146, p2333-2336, 1999.

34 Hara, T.; Tomisawa, T.; Kurosu, T.; Doy, T. K.; Sakai, K., Chemical Mechanical Polishing of a Fluorinated Carbon Low Dielectric Constant Interlayer and a Tantalum Nitride Barrier Layer by Magnesium Oxide Slurry, *Electrochemical and Solid-State Letters*, 2, p339-341, 1999.

35 Tseng, W. T.; Hsieh, Y. T.; Lin, C. F., CMP of Fluorinated Silicon Dioxide: Is It Necessary and Feasible, *Solid State Technology*, 40, p61-66, 1997 (February).

36 Tseng, W. T.; Lin, C. C. F.; Hsieh, Y. T.; Feng, M. S., Material Characterization and Chemical Mechanical Polishing of Low-Dielectric Constant Fluorinated Silicon Dioxide Films, *Materials Research Society Symposium Proceedings*, 427, p441-447, 1996.

37 Chen, W. C; Lin, S. C.; Dai, B. T.; Tsai, M. S., Chemical Mechanical Polishing of Low-Dielectric-Constant Polymers: Hydrogen Silsesquioxane and Methyl Silsesquioxane, *Journal of the Electrochemical Society*, 146, p3004-3008, 1999.

38 Chen, W. C.; Yen, C. T., Effects of Slurry Formulations on Chemical Mechanical Polishing of Low Dielectric Constant Polysiloxanes: Hydrido-Organo Siloxane and Methyl Silsesquioxane, *Journal of Vacuum Science and Technology B*, 18, p201-207, 2000.

39 Wang, Y. L.; Liu, C.; Chang, S. T.; Tsai, M. S.; Feng, M. S.; Tseng, W. T., Chemical-Mechanical Polishing of Low-Dielectric-Constant Spin-On-Glasses: Film Chemistries, Slurry Formulation and Polish Selectivity, *Thin Solid Films*, 308-309, p550-554, 1997.

40 Chang, T. C.; Liu, P. T.; Tasi, T. M.; Yeh, F. S.; Tseng, T. Y.; Tasi, M. S.; Chen, B. C.; Yang, Y. L.; Sze, S. M., Elimination of Dielectric Degradation for Chemical Mechanical Planarization of Low-K Hydrogen Silsesquioxane, *Japanese Journal of Applied Physics Part I*, 40 (5A), p3143-3146, 2001.

41 Chang, T. C.; Tsai, T. M.; Liu, P. T.; Chen, C. W.; Yan, S. T.; Aoki, H.; Chang, Y. C.; Tseng, T. Y., CMP of Ultra Low-k Material Porous-Polysilanes (PPSZ) for Interconnect Applications, *Thin Solid Films*, 447-448, p524-530, 2004.

42 Chang, T. C.; Tsai, T. M.; Liu, P. T.; Yan, S. T.; Chang, Y. C.; Aoki, H.; Sze, S. M.; Tseng, T. Y., Method to Improve Chemical Mechanical Planarization Polishing Rate of Low k Methyl-Silsesquiazane for Ultralarge Scale Integrated Interconnect Application, *Journal of Vacuum Science and Technology B*, 22, p1196-1201, 2004.

43 Chang, T. C.; Tsai, T. M.; Liu, P. T.; Chen, C. W.; Yan, S. T.; Aoki, H.; Chang, Y. C; Tseng, T. Y., CMP of Low-k Methylsilsesquiazane with Oxygen Plasma Treatment for Multilevel Interconnect Applications, *Electrochemical and Solid-State Letters*, 7, G122-G124, 2004.

44 Liu, P. T.; Chang, T. C.; Huang, M. C.; Yang, Y. L.; Mor, Y. S.; Tsai, M. S., Chung, H.; Hou, J.; Sze, S. M., Improvement of Post-Chemical Mechanical Planarization Characteristics on Organic Low K Methylsilsesquioxane as Intermetal Dielectric, *Journal of The Electrochemical Society*, 147, p4313-4317, 2000

45 Liu, P. T.; Chang, T. C.; Huang, M. C.; Tsai, M. S.; Sze, S. M., Highly Reliable Chemical-Mechanical Polishing Process for Organic Low-K Methylsilsesquioxane, *Journal of Vacuum Science and Technology B*, 19, p1212-1218, 2001.

46 Liu, P. T.; Chang, T. C.; Tsai, T. M.; Yan, S. T.; Chang, Y. C.; Aoki, H.; Tseng, T. Y., Characteristics of Low-k Methyl-silsesquiazane (MSZ) for CMP Process using Oxygen Plasma Treatment, *Electrochemical Society Proceedings*, 2003-13, p237-243, 2003.

47 Cui, H.; Bhat, I. B.; Murarka, S. P.; Lu, H; Li, W.; Hsia, W. J.; Catabay, W., Chemical Mechanical Polishing of Low Dielectric Constant Oxide Films Deposited Using Flowfill Chemical Vapor Deposition Technology, *Journal of the Electrochemical Society*, 147, p3816-3819, 2000.

48 Beaud, P; Bouvet, D.; Fazan, P.; Jacquinot, E.; Aoki, H.; Aoki, T., Ta/low-k CMP with Colloidal Silica Particles, *Materials Research Society Symposium Proceedings*, 767, p141-151, 2003.

49 Block, K. H.; CHen, W.; Gray, W. D., Chemical Mechanical Polishing of Amorphous Silicon Carbide and Low-k Carbon Doped Oxide Films, *Electrochemical Society Proceedings*, 2002-22, p302-309, 2003.

50 Cohen, S. A.; Jaso, M. A.; Bright, A. A., Electrical Properties of Chemical Mechanical Polished Tetraethyl Orthosilicate Films With and Without Capping Layers, *Journal of the Electrochemical Society*, 139, p3572-3574, 1992.

51 Doy, T. K.; Seshimo, K.; Suzuki, K.; Phillipossian, A.; Kinoshita, M., Impact of Novel Pad Groove Designs on Removal Rate and Uniformity of Dielectric and Copper CMP, *Journal of Electrochemical Society*, 151, G196-G199, 2004.

52 E. P. Guyer, R. H. Dauskardt, Effect of CMP slurry environments on subcritical crack growth in ultra low-k dielectric materials, *IEEE International Interconnect Technology Conference Proceedings*, p89-91, June 2003.

53 Hara, T.; Togoh, F.; Kurosu, T.; Sakamoto, K.; Shioya, Y.; Ishimaru, T.; Doy, T. K., Mechanism of Mechanical and Chemical Polishing in Low Dielectric Constant Plasma-Enhanced Chemical Vapor Deposition SiOC Layer from Hexamethyldisiloxane, *Electrochemical and Solid State Letters*, 4, G65-G67, 2001.

54 Kim, J.; Park, U.; Jung, Y. G.; Katoh, T.; Park, J. G., The Stability of Nano Fumed Silica Particles and Its Influence on Chemical Mechanical Planarization for Interlayer Dielectrics, *Japanese Journal of Applied Physics Part I*, 41 (7A), p4509-4512, 2002.

55 Lin, W. J.; Yang, C. J.; Chen, W. C., Processing, Properties, and CMP characteristics of a Spin-on Polymer: HSQ, *Materials Research Society Symposium Proceedings*, 612, D5.1.1-D5.1.6, 2001.

56 Lu, H.; Cui, H.; Bhat, I.; Muraka, S.; Lanford, W.; Hsia, W. J.; Li, W., Characterization of Methyl-doped Silicon Dioxide Film Deposited using FlowfillTM Chemical Vapor Deposition and Technology, *Journal of Vacuum Science and Technology B*, 20, p828-833, 2002.

57 Thagella, S.; Sikder, A. K.; Kumar, A., Thibological Issues and Modeling of Removal Rate of Low-k Films in CMP, *Journal of the Electrochemical Society*, 151, G205-G215, 2004.

58 Wang, Y.; Bajaj, R.; Moon, Y.; Mai, D.; Wijekoon, K.; Chen, Y.; Redeker, F.; Sugiarto, D.; Xia, L. Q., Polishing and Cleaning of Low k Dielectric Material for ILD and Damascene, *Materials Research Society Symposium Proceedings*, 671, M7.3.1-M7.3.7, 2001.

59 Zhang, F.; Wake, R. W.; Cook, L.; Busnaina, A. A., Evaluation of Commercialized Slurries and Pads for Polymer CMP (Chemical Mechanical Polishing), *Electrochemical Society Proceedings*, 98-7, p246-254, 1998.

60 Harmannsgruber, E.; Zwicker, G.; Beekmann, K., A Selective CMP Process for Stacked Low-k CVD Oxide Films, *Microelectronic Engineering*, 50, p53-58, 2000.

61 Hasegawa, M.; Shindo, Y.; Sugimura, T.; Yokota, R.; Kochi, M.; Mita, I., Spontaneous Molecular Orientation of Polyimides Induced by Thermal Imidization. I. Uniaxial Stretching of Polyamic Acid Film, *Journal of Polymer Science: Part B: Polymer Physics*, 32, p1299-1303, 1994.

62 Hasegawa, M.; Matano, T.; Shindo, Y.; Sugimura, T., Spontaneous Molecular Orientation of Polyimides Induced by Thermal Imidization. 2. In-Plane Orientation, *Macromolecules*, 29, p7879-7909, 1996.

63 Hasegawa, M.; Okuda, K.; Horimoto, M.; Shindo, Y.; Yokota, R.; Kochi, M., Spontaneous Molecular Orientation of Polyimides Induced by Thermal Imidization. 3. Component Chain Orientation in Binary Polyimide Blends, *Macromolecules*, 70, p5745-5752, 1997.

64 Hietpas, G. D. and Allara, D. L., The Molecular Structure of Poly (biphenyl dianhydride-p-phenylenedianmine) Polyimide Thin Films by Infrared Spectroscopy: Thickness Dependence of Structure in the Nano- to Micrometer Range, *Journal of Polymer Science: Part B: Polymer Physics*, 36, p1247-1260, 1998.

65 Hietpas, G. D.; Sands, J. M.; Allara, D. L., Formation of Molecularly Reconstructed Surface Layer during Unidirectional Rubbing of Polyimide Films, *Macromolecules*, 31, p3374-3378, 1998.

66 Boses, D.; Lee, H.; Yoon, D. Y.; Swalen, J. D.; Rabolt, J. F., Chain Orientation and Anisotropies in Optical and Dieletric Properties in Thin Films of Stiff Polyimides, *Journal of Polymer Science: Part B: Polymer Physics*, 30, p1321-1327, 1992.

67 Chung, H.; Jang, W.; Hwang, J.; Han, H., Analysis of Dimensionally Stable Copolyimide with a Low-Level Residual Stress, *Journal of Polymer Science: Part B: Polymer Physics*, 39, p796-810, 2001.

68 Chung, H.; Joe, Y.; Han, H., The Effect of Curing History on the Residual Stress Behavior of Polyimide Thin Films, *Journal of Applied Polymer Science*, 74, p3287-3298, 1999.

69 Chung, H.; Lee, J.; Jang, W.; Shul, Y.; Han, H., Stress Behaviors and Thermal Properties of Polyimide Thin Films Depending on the Different Curing Process, *Journal of Polymer Science: Part B: Polymer Physics*, 38, p2879-2890, 2000.

70 Heminghaus, S.; Boese, D.; Yoon, D. Y.; Smith, B. A., Large Anisotropy in Optical Properties of Thin Polyimide Films of Poly (p-phenylene biphenyltetracarboximide), *Applied Physics Letters*, 59, p1043-1045, 1991.

71 Liou, H. C.; Willecke, R.; Ho, P. S., Study of Out-of-plane Elastic Properties of PMDA-ODA and BPDA-PDA Polyimide Thin Films, *Thin Solid Films*, 323, p203-208, 1998.

72 Liou, H. C.; Ho, P. S.; Stierman, R., Thickness Dependence of the Anisotropy in Thermal Expansion of PMDA-ODA and BPDA-PDA thin films, *Thin Solid Films*, 339, p68-73, 1999.

73 Nishino, T.; Miki, N.; Mitsuoka, Y.; Nakamae, K.; Saito, T.; Kikuchi, T., Elastic Modulus of the Crystalline Regions of Polyimide Derived from Poly (amic acid)-Biphtalic Diamine, *Journal of Polymer Science: Part B: Polymer Physics*, 37, p3294-3301, 1999.

74 Nunes, T. L. and Sachdev, K. G., WAXD Study of Low TCE Polyimide Films Formed from Polyamic Acid Blends and Copolymers, *Materials Research Society Symposium Proceedings*, 264, p213-218, 1992.

75 Ree, M.; Park, Y. H.; Kim, K.; Kim, S. I.; Cho, C. K.; Park, C. E., Effect of Film Formation Process on Residual Stress of Poly(p-phenylene biphenyltetracarboximide) in Thin Films, *Polymer*, 38 (26), p6333-6345, 1997.

76 Seo, J. and Han, H., Water Sorption Behavior of Polyimide Films with Various Internal Linkages in the Dianhydride Component, *Polymer Degradation and Stability*, 77, p477-482, 2002.

77 Seo, J.; Jeon, J.; Lee, C.; Park, S.; Han, H., Water Sorption Behaviors of the BPDA-Based Polyimide Films Depending Upon the Structural Isomers of Diamine, *Journal of Applied Polymer Science*, 79, p2121-2127, 2001.

78 Seo, J.; Jeon, J.; Shul, Y. G.; Han, H., Water Sorption and Activation Energy in Polyimide Thin Films, *Journal of Polymer Science: Part B: Polymer Physics*, 38, p2714-2720, 2000.

79 Seo, J.; Lee, A.; Lee, C.; Han, H., Water-Sorption Behavior of p-Phenylene Diamine-Based Polyimide Films, *Journal of Applied Polymer Science*, 76, p1315-1323, 2000.

80 Alford, T. L.; Zou, Y. L.; Gadre, K. S.; Theodore, N. D.; Chen, W., Characterization of Thin Photosensitive Polyimide Films for Future Metallization Schemes, *Journal of Vacuum Science and Technology B*, 19, p1253-1258, 2001.

81 Terui, Y. and Ando, S., Anisotropy in Thermo-optic Coefficients of Polyimide Films Formed on Si Substrates, *Applied Physics Letters*, 83, p4755-4757, 2003.

82 Lee, C.; Kwon, J.; Park, S.; Sundar, S.; Min, B.; Han, H., Nanoindentation Studies of Polyimide Thin Films with Various Internal Linkages in the Diamine Component, *Journal of Polymer Science: Part B: Polymer Physics*, 42, p861-870, 2004.

83 Kim, Y.; Ree, M.; Chang, T.; Ha, C. S.; Nunes, T. L.; Lin, J. S., Rodlike/Flexible Polyimide Composite Films Prepared from Soluble Poly(amic diethyl Ester) Precursors: Miscibility, Structure and Properties, *Journal of Polymer Science: Part B: Polymer Physics*, 33, p2075-2082, 1995.

84 L. Lin, S. A. Bidstrup, Effect of Molecular Orientation on the Dielectric Properties of Spin Coated Polyimide Films, *Journal of Applied Polymer Science*, 54, p553-560, 1994.

85 Ree, M.; Kim, K.; Woo, S. H.; Chang, H., Structure, Chain Orientation, and Properties in Thin Films of Aromatic Polyimides with Various Chain Rigidities, *Journal of Applied Physics*, 81, p698-708, 1997.

86 Chen, S. T. and Wagner, H. H., Out-of-Plane Thermal Expansion Coefficient of Biphenyldianhydride-Phenylenediamine Polyimide Film, *Journal of Electronic Materials*, 22, p797-799, 1993.

87 Poon, T. W.; Leu, J.; Kang, Y. S.; Liou, H. C.; Ho, P. S., Morphological Effects on the Materials Properties of Polyimides, *Materials Research Society Symposium Proceedings*, 323, p333-344, 1994.

88 Bidstrup, S. A.; Hodge, T. C.; Lin, L.; Kohl, P. A.; Lee, J. B.; Allen, M. G., Anisotropy in Thermal, Electrical and Mechanical Properties of Spin-Coated Polymer Dielectrics, *Materials Research Society Symposium Proceedings*, 338, p577-587, 1994.

89 Ree, M.; Nunes, T. L.; Lin, J. S., X-ray Scattering Studies of Thin Films of Photosensitive Polyimides, *Polymer*, 35, p1148-1156, 1994.

90 Coburn, J. C.; Pottiger, M. T.; Pryde, C. A., Structure Development in Polyimide Films, *Materials Research Society Symposium Proceedings*, 308, p475-487, 1993.

91 Ree, M.; Nunes, T. L.; Lin, J. S., X-ray Scattering Study of Polyimide Thin Films from Poly(amic acid)s Functionalized with a Methyacrylate, *Proceedings of 4th International Conference on Polyimides*, p415-432, 1993.

92 Ho, P.S.; Poon, T. W.; Leu, J., Molecular Structure and Thermal/Mechanical Properties of Polymer Thin Films, *Journal of Physics and Chemistry of Solids*, 55, p1115-1124, 1994.

93 Leu, J.; Kang, Y. S.; Liou, H. C.; Ho, P. S., Effect of Curing on the Thermomechanical Properties of BPDA-PDA Polyimide Thin Films, *Materials Research Society Symposium Proceedings*, 323, p283-288, 1994.

94 Coburn, J. C.; Pottiger, M. T.; Nader, A. E.; Pryde, C. A., The Effect of Photoreactive Substituents on the Morphological Structure and Properties of BPDA-PPD Based Polyimides, *Materials Research Society Symposium Proceedings*, 264, p107-115, 1992.

95 Ree, M.; Chu, C. W.; Goldberg, M. J., Influences of Chain Rigidity, In-plane Orientation, and Thickness on Residual Stress of Polymer Films, *Journal of Applied Physics*, 75, p1410-1419, 1994.

96 Goeschel, U.; Lee, H.; Yoon, D. Y.; Siemens, R. L.; Smith, B. A.; Volksen, W., Effects of Chemical Structure and Precursor on Optical Properties, Thermo-mechanical Properties, and Molecular Orientation and Order of Thin Films of Stiff Aromatic Polyimides, *Colloid and Polymer Science*, 272, p1388-1395, 1994.

97 Ektessabi, A. M. and Hakamata, S., XPS Study of Ion Beam Modified Polyimide Films, *Thin Solid Films*, 377-378, p621-625, 2000.

98 Flitsch, R. and Shih, D. Y., An XPS Study of Argon-Ion Beam and Oxygen RIE Modified BPDA-PDA Polyimide as Related to Adhesion, *Journal of Adhesion Science and Technology*, 10, p1241-1253, 1996.

99 Lee, K. W.; Kowalczyk, S. P.; Shaw, J. M., Surface Modification of BPDA-PDA Polyimide, *Langmuir*, 7, p2450-2453, 1991.

100 Lee, K. W., Modification of Polyimide Surface-Morphology Relationship between Modification Depth and Adhesion Strength, *Journal of Adhesion Science and Technology*, 8, p1077-1092, 1994.

101 Stoffel, N. C.; Hsieh, M.; Chandra, S.; Kramer, E. J., Surface Modification Studies of Polyimide Films Using Rutherford Backscattering and Forward Recoil Spectrometry, *Chemistry of Materials*, 8, p1035-1041, 1996.

102 Yu, W. and Ko, T. M., Surface Characterization of Potassium-Hydroxide-Modified Upilex-S Polyimide at an Elevated Temperature, *European Polymer Journal*, 37, p1791-1799, 2001.

103 Samant, M. G.; Stohr, J.; Brown, H. R.; Russell, T. P.; Sands, J. M.; Kumar, S. K., NEXAFS Studies on the Surface Orientation of Buffed Polyimides, *Macromolecules*, 29, p8334-8342, 1996.

104 Cossy-Favre, A.; Diaz, J.; Liu, Y.; Brown, H. R.; Samant, M. G.; Stohr, J.; Hanna, A. J.; Anders, S.; Russell, T. P., X-PEEM Study on Surface Orientation of Stylized and Rubbed Polyimides, *Macromolecules*, 31, p4957-4962, 1998.

105 Devlin, C. L.; Glab, S. D.; Chiang, S.; Russell, T. P., Atomic Force Microscopy Study of Rubbed Polyimide Films, *Journal of Applied Polymer Science*, 80, p1470-1477, 2001.

106 M. P. Seah, in D. Briggs and M. P. Seah (Eds), *Practical Surface Analysis, 2nd Edition, Volume 1 – Auger and X-ray Photoelectron Spectroscopy*, John Wiley & Sons, New York, 1990 (Chapter 5).

107 Poggi, M. A.; Bottomley, L. A.; Lilehei, P. T., Scanning Probe Microscopy, *Analytical Chemistry*, 74, 2851-2862, 2002.

108 Lin-Vien D.; Colthup N. B.; Fateley W. G., *The Handbook of Infrared and Raman Characteristic Frequencies of Organic Molecules*, Academic Press, Inc., 1991.

109 Hardaker, S. S.; Moghazy, S.; Cha, C. Y.; Samuels, R. J., Quantitative Characterization of Optical Anisotropy in High Refractive Index Films, *Journal of Polymer Science: Part B: Polymer Physics*, 31, p1951-1963, 1993.

110 Liu, T.; Samuels. R. J., Improved Refractive Index from a Planar Leaky Wave-Guide Coupler, *Materials Research Society Symposium Proceedings*, v597, p57-62, 2000.

111 Tompkins, H. G.; McGahan, W. A., *Spectroscopic Ellipsometry and Reflectometry A User's Guide*, John Wiley & Sons Inc., New York, 1999.

112 Akhter, S.; Cannon, K. C., White, J. M., Distribution of Compositional Defects in Solvent Cast Polyvinyl Alcohol Films, Angular Dependent XPS and Reactivity Study, *Applied Surface Science*, 44, p49-57, 1990.

113 Ton-That, C.; Shard, A. G.; Bradley, R. H., Thickness of Spin-Cast Polymer Thin Films Determined by Angle-Resolved XPS and AFM Tip-Scratch Methods, *Langmuir*, 16, p2281-2284, 2000.

114 Paynter, R. W., Angle-Resolved X-Ray Photoelectron Spectroscopy Studies of the Evolution of Plasma-Treated Surfaces with Time, *Surface and Interface Analysis*, 27, p103-113, 1999.

115 Palacio, C. and Arranz, A., Spectroscopic Characterization of the Surface Nano-structure of Ti during Deposition on Polycrystalline Aluminum, *Surface and Interface Analysis*, 27, p871-879, 1999.

116 Verpoort, F.; De Doncker, G.; Bossuyt, A. R.; Fiermans, L.; Verdonck, L., Angle-Resolved and Depth Profiling XPS Investigation of a Monolayer Niobium Oxide Catalyst, *Journal of Electron Spectroscopy and Related Phenomena*, 73, p271-281, 1995.

117 Chen, L. and Hoffman, R. W., Angle-Resolved X-Ray Photoelectron Spectroscopy Method for the Thickness Measurement of Metal Oxide/Metal Ultrathin Films, *Journal of Vacuum Science and Technology A*, 11 (4), p2303-2307, 1993.

118 Hill, J. M.; Royce, D. G.; Fadley, C. S.; Wagner, L. F.; Grunthaner, F. J., Properties of Oxidized Silicon as Determined by Angular-Dependent X-Ray Photoelectron Spectroscopy, *Chemical Physics Letters*, 44 (2), p225-231, 1976.

119 Aarnink, W. A. M.; Weishaupt, A.; van Silfhout, A., Angle-Resolved X-Ray Photoelectron Spectroscopy (ARXPS) and a Modified Levenberg-Marguardt Fit Procedure: A New Combination for Modeling Thin Layers, *Applied Surface Science*, 45, 37-48, 1990.

120 Kallury, K. M. R.; Brennan, J. D.; Krull, U. J., Depth Profiling of Functionalized Silane Films on Quartz and Silicon Substrates and of Urease Immobilized on Such Films by Angle-Resolved X-Ray Photoelectron Spectroscopy, *Analytical Chemistry*, 67, p2625-2634, 1995.

121 Spruytte, S.; Coldren, C.; Harris, J.; Pantelidis, D.; Lee, H. J.; Bravman, J.; Kelly, M., Use of Angle Resolved X-Ray Photoelectron Spectroscopy for Determination of Depth and Thickness of Compound Layer Structures, *Journal of Vacuum Science and Technology A*, 19 (2), p603-608, 2001.

122 Seah, M. P.; Qiu, J. H.; Cumpson, P. J.; Castle, J. E., Simple Method of Depth Profiling (Stratifying) Contamination Layers, Illustrated by Studies on Stainless Steel, *Surface and Interface Analysis*, 21, p336-341, 1994.

123 Fulghum, J. E., Determination of Overlayer Thickness by Angle-Resolved XPS: A Comparison of Algorithms, *Surface and Interface Analysis*, 20, p161-173, 1993.

124 Fadley, C. S.; Baird, R. J.; Siekhaus, W.; Novakov, T.; Bergstrom, S. A. L., Review: Surface Analysis and Angular Distribution in X-Ray Photoelectron Spectroscopy, *Journal of Electron Spectroscopy and Related Phenomena*, 4, p93-137, 1974.

125 Fadley, C. S., Angle-Resolved X-Ray Photoelectron Spectroscopy, *Progress in Surface Science*, 16, p275-388, 1984.

126 Nefedov, V. I., X-Ray Photoelectron Analysis of Surface Layers with Composition Gradients, *Surface and Interface Analysis*, 3 (2), p72-75, 1981.

127 Fischer, H.; Svagera, R.; Ebel, H.; Ebel, M. F.; Schobmann, B., Depth Profiling by ARXPS in Surface Analysis, *Fresenius Journal of Analytical Chemistry*, 353, p473-477, 1995.

128 Grabherr, M. G.; Ebel, H.; Ebel, M. F.; Svagera, R.; Baron, G., Investigation of Concentration Depth Profiles by Means of Angle-Resolved XPS, A Polynomial Model, *Journal of Electron Spectroscopy and Related Phenomena*, 63, 43-52, 1993.

129 Siuda, R., A Procedure for Non-Destructive Depth Profiling of Smooth Profiles with ARXPS, *Vacuum*, 48 (3/4), p391-394, 1997.

130 Ebel, H.; Ebel, M. F.; Svagera, R.; Winklmayr, E., A Comparison of Two XPS Methods for Quantification of Concentration Profiles, *Journal of Electron Spectroscopy and Related Phenomena*, 57, p15-32, 1991.

131 Perruchot, C; Watts, J. F.; Lowe, C.; White, R. G.; Cumpson, P. J., Angle-Resolved XPS Characterization of Urea Formaldehyde-Epoxy Systems, *Surface and Interface Analysis*, 33, p869-878, 2002.

132 Asami, K.; Akiyama, E.; Hashimoto, K., Angle-Resolved XPS for Determination of Diffusion Coefficients and Mobilities of Cations in Thin Passive Films, *Surface and Interface Analysis*, 30, p106-111, 2000.

133 Akiyama, E.; Kawashima, A.; Asami, K.; Hashimoto, K., A Study of the Structure of a Passive Film Using Angle-Resolved X-Ray Photoelectron Spectroscopy, *Corrosion Science*, 38, p1127-1140, 1996.

134 Akiyama, E.; Kawashima, A.; Asami, K.; Hashimoto, K., An Angle-Resolved XPS Study of the In-Depth Structure of Passivated Amorphous Aluminum Alloys, *Corrosion Science*, 39, p1351-1364, 1997.

135 Popovici, D.; Piyakis, K.; Meunier, M.; Sacher, E., Angle-Resolved X-Ray Photoelectron Spectroscopy Comparison of Copper/Teflon AF1600 and Aluminum/Kapton metal Diffusion, *Journal of Applied Physics*, 83, p108-111, 1998.

136 Pijolat, M. and Hollinhger, G., New Depth-Profiling Method by Angular-Dependent X-Ray Photoelectron Spectroscopy, *Surface Science*, 105, p114-128, 1981.

137 Hazell, L. B.; Brown, I. S.; Freisinger, F., A Model for Determining the Composition of Layer Structured Samples Using XPS Electron Take-Off Angle Experiments, *Surface and Interface Analysis*, 8, p25-31, 1986.

138 Cherkashinin, G. Y., Inverse Problem: The Concentration Depth Profile of Elements from ARXPS Data, *Journal of Electron Spectroscopy and Related Phenomena*, 74, p67-75, 1995.

139 Borodyansky, S. E. and Abashkin, Y. G., Determination of Concentration Depth-Profiles by Angle-Dependent XPS and AES Data, *Surface Science*, 251/252, p325-329, 1991.

140 Nefedov, V. I. and Baschenko, O. A., Relative Intensities in ESCA and Quantitative Depth Profiling, *Journal of Electron Spectroscopy and Related Phenomena*, 47, p1-25, 1988.

141 Baschenko, O. A. and Nefedov, V. I., Depth Profiling of Elements in Surface Layers of Solids Based on Angular Resolved X-Ray Photoelectron Spectroscopy, *Journal of Electron Spectroscopy and Related Phenomena*, 53, p1-18, 1990.

142 Baschenko, O. A., Photoelectron Mean Free Path Chemical Composition Dependence and Elastic Scattering and Analyzer Acceptance Angle Finiteness Effects in Restoring Concentration Profiles from Angular Resolved X-Ray Photoelectron Spectroscopy Data, *Journal of Electron Spectroscopy and Related Phenomena*, 57, p297-305, 1991.

143 Bussing, T. D. and Holloway, P. H., Deconvolution of Concentration Depth Profiles from Angle Resolved X-Ray Photoelectron Spectroscopy Data, *Journal of Vacuum Science and Technology A*, 3, p1973-1981, 1985.

144 Bussing, T. D.; Holloway, P. H., Wang, Y. X.; Moulder, J. F.; Hammond, J. S., Composition Depth Profiles of Oxidized Silicon and Sputtered GaAs from Angle-Resolved X-Ray Photoelectron Spectroscopy, *Journal of Vacuum Science and Technology B*, 6, p1514-1518, 1988.

145 Flinn, B. J. and McIntyre, N. S., Studies of the UV/Ozone Oxidation of GaAs Using Angle-Resolved X-Ray Photoelectron Spectroscopy, *Surface and Interface Analysis*, 15, p19-26, 1990.

146 Holloway, P. H. and Bussing, T. D., Quantitative Surface Analysis of Layered Materials, *Surface and Interface Analysis*, 18, p251-256, 1992.

147 Smith, G. C. and Livesey, A. K., Maximum Entropy: A New Approach to Non-Destructive Deconvolution of Depth Profiles from Angle-Dependent XPS, *Surface and Interface Analysis*, 19, p175-180, 1992.

148 Livesey, A. K. and Smith, G. C., The Determination of Depth Profiles from Angle-Dependent XPS Using Maximum Entropy Data Analysis, *Journal of Electron Spectroscopy and Related Phenomena*, 67, p439-461, 1994.

149 Jisl, R., Restoration of the Depth-Concentration Profile from the Angle-Resolved Relative Intensities of X-Ray Photoelectron Spectra, *Surface and Interface Analysis*, 15, p719-726, 1990.

150 Paynter, R. W., Angle-Resolved XPS Study of the Effect of X-Radiation on the Aging of Polystyrene Exposed to An Oxygen/Argon Plasma, *Surface and Interface Analysis*, 33, p14-22, 2002.

151 Williams, J. M. and Beebe, T. P. Jr., High-Resolution Algorithm for Quantitative Elemental Depth Profiling by Angle-Resolved X-Ray Photoelectron Spectroscopy, *Journal of Vacuum Science and Technology A*, 15(4), p2122-2133, 1997.

152 Iwasaki, H.; Nishitani, R.; Nakamura, S., Determination of Depth Profiles by Angular Dependent X-Ray Photoelectron Spectra, *Japanese Journal of Applied Physics*, 17, p1519-1523, 1978.

153 Paynter, R. W., Modification of the Beer-Lambert Equation for Application to Concentration Gradients, *Surface and Interface Analysis*, 3, p186-187, 1981.

154 Tyler, B. J.; Castner, D. G.; Ratner, B. D., Regularization: A Stable and Accurate Method for Generation Depth Profiles from Angle-Dependent XPS Data, *Surface and Interface Analysis*, 14, p443-450, 1989.

155 Ro, C. U., Simulation Study on Regeneration of Depth Profiles from Angle-Resolved XPS Data, *Surface and Interface Analysis*, 25, p869-877, 1997.

156 Yih, R. S. and Ratner, B. D., A Comparison of Two Angular Dependent ESCA Algorithms Useful for Constructing Depth Profiles of Surfaces, *Journal of Electron Spectroscopy and Related Phenomena*, 43, p61-82, 1987.

157 McCaslin, P. C. and Young, V., Numerical Approaches to Non-Destructive Depth Profiling by Variable Angle X-Ray Photoelectron Spectroscopy, *Scanning Microscopy*, 1, p1545-1556, 1987.

158 Seelmann-Eggebert, M. and Richter, H. J., Theoretical Aspects for Depth Profiling by XPS, *Journal of Electron Spectroscopy and Related Phenomena*, 52, p273-283, 1990.

159 Seelmann, M. and Keller, R. C., Information on Compositional Depth Profiles Conveyed by Angle-Resolved XPS, *Surface and Interface Analysis*, 23, p589-600, 1995.

160 Tielsch, B. J. and Fulghum, J. E., Application of Angle-Resolved XPS Algorithms to Overlayers and Concentration Gradients, *Surface and Interface Analysis*, 21, p621-630, 1994.

161 Gries, W. H., A General Procedure for Extracting Quantitative Depth Information from Take-Off-Angle-Resolved XPS and AES, *Applied Surface Science*, 100/101, p41-46, 1996.

162 Tilinin, I. S.; Jablonski, A.; Werner, W. S. M., Quantitative Surface Analysis by Auger and X-Ray Photoelectron Spectroscopy, *Progress in Surface Science*, 52, p193-335, 1996.

163 Opila, R. L. and Eng, J., Thin Films and Interfaces in Microelectronics: Composition and Chemistry as Function of Depth, *Progress in Surface Science*, 69, p125-163, 2002.

164 Cumpson, P. J., Angle-Resolved XPS and AES: depth-resolution limits and a general comparison of properties of depth-profile reconstruction methods, *Journal of Electron Spectroscopy and Related Phenomena*, 73, p25-32, 1995.

165 McWhirter, J. G. and Pike, E. R., On the Numerical Inversion of the Laplace Transform and Similar Fredholm Integral Equations of the First Kind, *Journal of Physics A*, 11 (9), p1729-1745, 1978.

166 Bertero, M.; Boccacci, P.; Pike, E. R., On the Recovery and Resolution of Exponential Relaxation Rates from Experimental Data: A Singular Value Analysis of the Laplace Transform Inversion in the Presence of Noise, *Proceedings of the Royal Society of London. Series A, Mathematical and Physical Sciences*, 383, p15-29, 1982.

167 Cumpson, P. J., Angle-Resolved XPS Depth-Profiling Strategies, *Applied Surface Science*, 144-145, p16-20, 1999.

168 Tyler, B. J.; Castner, D. G.; Ratner, B. D., Determining Depth Profiles from Angle Dependent X-Ray Photoelectron Spectroscopy: The Effects of Analyzer Lens Aperture Size and Geometry, *Journal of Vacuum Science and Technology A*, 7 (3), p1646-1654, 1989.

169 Seelmann, M., Photoemission Spectroscopic Techniques to Assess Physical and Chemical Properties of Mercury Cadmium Telluride, *Journal of Vacuum Science and Technology B*, 10 (4), p1515-1524, 1992.

170 Lisowski, W.; van den Berg, A. H. J.; Smithers, M., Characterization of Titanium Hydride Film after Long-Term Air Interaction: SEM, ARXPS and AES Depth Profile Studies, *Surface and Interface Analysis*, 26, p213-219, 1998.

171 Gosset, L. G.; Ganem, J. J.; Trimaille, I.; Rigo, S.; Rochet, F.; Dufour, G.; Jolly, F.; Stedile, F. C.; Baumvol, I. J. R., High Resolution Depth Profiling in Silicon Oxynitride Films Using Narrow Nuclear Reaction Resonances, *Nuclear Instruments and Methods in Physics Research B*, 136-138, p521-527, 1998.

172 Butcher, K. S. A.; Tansley, T. L.; Li, X., X-Ray Photoelectron Spectroscopy Depth Profiling of Aluminum Nitride Thin Films, *Surface and Interface Analysis*, 25, p99-104, 1997.

173 Chaparro, A. M.; Maffiotte, C.; Herrero, J.; Gutierrez, M. T., XPS Analysis with Depth Resolution of Chemical Bath-Deposited ZnSe Thin Films, *Surface and Interface Analysis*, 30, p522-526, 2000.

174 Palacio, C.; Gomez-Aleixandre, C.; Diaz, D.; Garcia, M. M., Carbon Nitride Thin Films Formation by N2+ Ion Implantation, *Vacuum*, 48 (7), p709-713, 1997.

175 Rickman, J. T., Surface and Depth Profiling Techniques using XPS Applied to the Study of Nickel-Containing Environmental Particles, *Applied Surface Science*, 68, 375-393, 1993.

176 Asami, K. and Hashimoto, K., X-Ray Photoelectron Spectroscopy for Corrosion Studies, *Langmuir*, 3, p897-904, 1987.

177 Wong, H. Y.; Ong, C. W.; Kwok, R. W. M.; Wong, K. W.; Wong, S. P.; Cheung, W. Y., Effects of Ion Beam Bombardment on Electrochromic Tungsten Oxide Films Studied by X-Ray Photoelectron Spectroscopy and Rutherford Back-Scattering, *Thin Solid Films*, 376, p131-139, 2000.

178 Seah, M. P. and Anthony M. T., Quantitative XPS: The Calibration of Spectrometer Intensity - Energy Response Functions, *Surface and Interface Analysis*, 6, p230-241, 1984.

179 Jablonski A. and Powell C. J., The Electron Attenuation Length Revisited, *Surface Science Reports*. 47, p33-91, 2002.

180 J. Crank, *The Mathematics of Diffusion*, 2nd Ed., Oxford University Press, New York, 1975.

181 Yeh, P., *Optical Waves in Layered Media*, John Wiley & Sons, Inc., New York, 1988.

182 Parikh, A. N. and Allara, D. L. J., Quantitative Determination of Molecular Structure in Multilayered Thin Films of Biaxial and Lower Symmetry from Photon Spectroscopies. I. Reflection Infrared Vibrational Spectroscopy, *Journal of Chemical Physics*, 96, p927-945, 1992.

183 Poelman, D. and Smet, P. F., Methods for the Determination of the Optical Constants of Thin Films from Single Transmission Measurements: A Critical Review, *Journal of Physics D: Applied Physics*, 36, p1850-1857, 2003.

184 Lagarias, J.C., Reeds J. A.; Wright M. H.; Wright P. E. Convergence Properties of the Nelder-Mead Simplex Method in Low Dimensions, *SIAM Journal of. Optimization*, 9, p112-147, 1998.

185 C. J. Powell and A. Jablonski, *NIST Electron Effective-Attenuation-Length Database – Version 1.0*, National Institute of Standards and Technology, Gaithersburg, MD, 2001.

186 S. A. Kafafi, The Ionization Potential, Electron Affinity and Energy Gap of Polyimide, *Chemical Physics Letters*, 169, p561-563, 1990.

187 R. E. Pepper and R. J. Samuels, in Craver C. D. and Provder T. (Eds), *Polymer Characterization*, ACS Publishers, Washington, D.C., 1990, p315.

188 Bennett, J. M. and Bennett, H. E. in: Driscoll, W. G. and Vaughan, W. (Eds.) *Handbook of Optics*, McGraw-Hill, New York, 1978 (Section 10).

189 Hong, S. C.; Oh-e, M.; Zhuang, X.; Shen, Y. R., Orientations of Side Chains and Adsorbed Liquid Crystal Molecules on a Rubbed Polyimide Surface Studied by Optical Second Harmonic Generation, *Physical Review E*, 63, p051706(1-7), 2001.

190 Meister, R. and Jerome, B., The Conformation of a Rubbed Polyimide, *Macromolecules*, 32, p480-486, 1999.

191 Van Aerle, N. A. J. M.; Barmentlo, M.; Hollering, R. W. J., Effect of Rubbing on the Molecular Orientation within Polyimide Orienting Layers of Liquid-Crystal Displays, *Journal of Applied Physics*, 74 (5), p3111-3120, 1993.

192 Van Aerle, N. A. J. M. and Tol, A. J. W., Molecular Orientation in Rubbed Polyimide Alignment Layers Used for Liquid Crystal Displays, *Macromolecules*, 27, p6520-6526, 1994.

193 Tsang, O. C.; Xie, F.; Tsui, O. K. C.; Yang, Z.; Zhang, J.; Shen, D., Rubbing-Induced Molecular Alignment and Its Relaxation in Polystyrene Thin Films, *Journal of Polymer Science: Part B: Polymer Physics*, 39, p2906-2914, 2001.

194 Wei, X.; Zhuang, X.; Hong, S. C.; Goto, T.; Shen, Y. R., Sum-Frequency Vibrational Spectroscopic Study of a Rubbed Polymer Surface, *Physical Review Letters*, 82, p4256-4259, 1999.

195 Oh-e, M.; Lvosky, A. I.; Wei, X.; Shen, Y. R., Sum-Frequency Generation (SFG) Vibrational Spectroscopy of Side Alkyl Chain Structures of Polyimide Surfaces, *Journal of Chemical Physics*, 113, p8827-8832, 2000.

196 Adachi, S., *Optical Constants of Crystalline and Amorphous Semiconductors*, Kluwer Academic Publishers, Boson, 1999.

197 Shimoo, T.; Okamura, K.; Itoh, M., Interaction of Si3N4 with Ni-Cr Alloy under N2 or Ar Atmosphere, *Journal of Materials Science*, 33, p5169-5175, 1998.

198 Shimoo, T.; Okamura, K.; Yamasaki, T., Reaction between Si3N4 and Fe-Ni Alloy, *Journal of Materials Science*, 34, p5525-5532, 1999.

199 Neter, J.; Kutner, M. H.; Nachtsheim, C. J.; Wasserman, W., *Applied Linear Statistical Models*, 4th Ed., WCB/McGraw-Hill, New York, 1996.

200 Lamkin, M. A.; Riley, F. L; Fordham, R. J., Oxygen Mobility in Silicon Dioxide and Silicate Glasses: a Review, *Journal of the European Ceramic Society*, 10, p347-367, 1992.

201 Liu, T. and Samuels, R., The Influence of Hydrogen Chloride Doping Level on the Complex Refractive Indices of Anisotropic Polyaniline Film: Application of a New Internal Reflection Waveguide Coupling Technique, *Journal of Polymer Science: Part B: Polymer Physics*, 39, p2481-2490, 2001.

202 Liu, T.; Henderson, C. L.; Samuels, R., Quantitative Characterization of the Optical Properties of Absorbing Polymer Films: Comparative Investigation of the Internal Reflection Intensity Analysis Method, *Journal of Polymer Science: Part B: Polymer Physics*, 41, p842-855, 2003.

203 Elman, J. F.; Greener,J.; Herzinger, C. M.; Johs, B., Characterization of Biaxially-Stretched Plastic Films by Generalized Ellipsometry, *Thin Solid Films*, 313-314, p814-818, 1998.

204 Tammer, M. and Monkman, A. P., Measurement of the Anisotropic Indices of Spin Cast Thin Poly (2-methoxy-5-(2'-ethyl-hexyloxy)-p-phenyl-enevinylene) (MEH-PPV) Films, *Advanced Materials*, 14, p210-212, 2002.

205 Losurdo, M.; Giangregorio, M. M.; Capezzuto, P.; Bruno, G.; Babudri, F.; Colangiuli, D.; Farinola, G. M.; Naso, F., Study of Anisotropic Optical Properties of Poly (arylenephenylene) Thin Films: Dependence on Polymer Backbone, *Macromolecules*, 36, p4492-4497, 2003.

206 Kirov, K. R. and Assender, H. E., Quantitative ATR-IR Analysis of Anisotropic Polymer Films: Extraction of Optical Constants, *Macromolecules*, 37, 894-904, 2004.

207 Buffeteau, T.; Blaudez, D.; Pere, E.;Desbat, B., Optical Constants Determination in the Infrared of Uniaxially Oriented Monolayers from Transmittance and Reflectance Measurements, *Journal of Physical Chemistry B*, 103, 5020-5027, 1999.

VITA

Jie Diao was born on April 10, 1976, in Gansu Province, China. He spent his childhood on the Loess Plateau. He graduated from Fengxian Middle School in 1993 and obtained his B.S. in Chemical Engineering from East China University of Science and Technology in 1997. After that, he pursued graduate study in Tsinghua University and obtained his M.S. in Chemical Engineering in 2000. In August 2000, he began pursuing his Ph.D. in Chemical Engineering at Georgia Institute of Technology under the guidance of Dr. Dennis W. Hess and Dr. Jeffrey F. Morris. He is receiving his Ph.D. in Chemical Engineering in December 2004.